

MICROWAVE ENABLED SYNTHESIS OF CARBON BASED MATERIALS
WITH CONTROLLED STRUCTURES: APPLICATIONS FROM
MULTIFUNCTIONAL DRUG DELIVERY TO METAL FREE CATALYSTS

by

Mehulkumar Patel

A Dissertation submitted to the

Graduate School-Newark

Rutgers, The State University of New Jersey

in partial fulfillment of the requirements

for the degree of

Doctor of Philosophy

Graduate Program in Chemistry

written under the direction of

Professor Huixin He

and approved by

Newark, New Jersey

October, 2016

Copyright Page

Copyright

© 2016

Mehulkumar Patel

ALL RIGHTS RESERVED

ABSTRACT OF THE DISSERTATION

MICROWAVE ENABLED SYNTHESIS OF CARBON BASED MATERIALS WITH CONTROLLED STRUCTURES: APPLICATIONS FROM MULTIFUNCTIONAL DRUG DELIVERY TO METAL FREE CATALYSIS

By Mehulkumar Patel

Dissertation Director:

Prof. Huixin He

Graphene is a single-layered sheet of sp^2 -bonded carbon atoms arranged in a honeycomb structure, whose discovery won the 2010 Nobel Prize in physics. Due to its excellent electronic, optical, thermal and mechanical properties, and its large surface area and low mass, graphene holds great potential for a broad range of applications. It seems that the research in graphene has now proceeded from the initial phase of developing myriad strategies for the synthesis of graphene sheets to the use of graphene in various research fields. However, it is still challenging to controllably produce solution processable highly conductive graphene sheets in large quantity, at low cost, and energy saving process, with optimal sheet size, layer thickness, defects (vacancies and holes) and molecular structures (oxygen-containing groups and non-defective graphene domains). All these structural parameters determine their electronic, thermal and mechanical properties of graphene, which are key warrants for their practical application in various devices. As examples, fundamental studies and high-frequency electronics require pristine graphene. However, “bulk” applications such as flexible macro-electronics, and mechanically and electronically reinforced composites, require large quantities of solution-processable highly conductive large graphene sheets manufactured at low cost. On the other hand, holey graphene, referring to graphene with nanoholes in their basal plane, demonstrates

much better performance in their application as metal-free catalysts and in energy storage. Finally, there is a surge of interests in nanosized graphene sheets for various biological applications due to their unique size effects, edge effects, and even quantum confinement effects.

As one part of this thesis, we have demonstrated that by understanding the oxidation mechanism of nitronium ions and KMnO_4 , which were both used in the widely used Hummers method for fabrication of graphene oxides, we developed various microwave chemistries for rapid (30-40 seconds) and controllable fabrication of graphene with controlled lateral sizes, holey structures, and oxidation levels. As examples, by intentionally excluding KMnO_4 in the reaction system while controlling the concentration of nitronium ions and microwave irradiation power and time, we can rapidly and directly fabricate graphene nanosheets with uniform lateral sizes. The as-fabricated graphene nanosheets largely retain the intrinsic properties of graphene. These nanosheets exhibit strong and wavelength-independent absorption in NIR regions, which ensures their applications in Near-Infrared (NIR) photoacoustic imaging, photothermal treatment, and multifunctional drug delivery. On the other hand, by including KMnO_4 in the recipe and still taking advantage of the unique thermal and kinetic effects of microwave heating, we developed approaches to directly fabricate micrometer sized graphene oxide with controlled holey structures. Taking one step further; we have also developed microwave chemistry to dope these graphene oxide sheets with/without holes in their basal planes with N controllable bond configurations. We have shown that the N-doping and holey structure of graphene is important for their excellent electrochemical catalytic performance in oxygen reduction reaction (ORR).

In the drive towards green and sustainable chemistry, there is an ever-increasing interest in developing the heteroatom-doped carbon-based catalysts to replace the metal-based catalysts for organic reactions. Compared to ORR, studies that use doped and/or co-doped carbon materials as catalysts for selective organic synthesis is in the early stages of development. This might be due to lack of systematic studies about how the electronic and geometrical structures, surface functionalities, and therefore, the interface properties of graphene-based materials determine their catalytic performance. Also lacking is the inability to synthesize these doped carbon catalysts in bulk quantity with simple and cost effective approaches. In the second part of this dissertation, we have reported extremely simple and rapid (seconds) approaches to directly synthesize gram quantities of single or multiple heteroatom-doped graphitic porous carbon materials from abundant and cheap biomass molecules (inositol or phytic acid) with controlled doping configuration. The porous structure of the catalyst is beneficial for efficient mass transport and dramatically increases edges and surface area, and therefore creates more accessible catalytic centers. Furthermore, we have also explored the catalytic center of these heteroatom-doped carbon catalysts (especially phosphorus-doped and phosphorus, sulfur-codoped) to gain a fundamental understanding of how the heteroatom (P and S) configuration affect the catalytic properties of carbon material in ORR and industry oxidation reactions, such as benzyl alcohol oxidation. This fundamental understanding will help us to design more efficient heteroatom-doped carbon catalysts.

Preface

Chapter 1. **Figure 1.1.1** is reprinted with permission from the “Mineralogical Society of America” **Figure 1.2.2-A** is reprinted with permission from “Akhavan, O. Graphene nanomesh by ZnO nanorod photocatalysts. *ACS nano* 2010, 4, 4174-4180”. Copyright ©2014, American Chemical Society. **Figure 1.2.2-B** is reprinted with permission from “Mao, S.; Wen, Z.; Kim, H.; Lu, G.; Hurley, P.; Chen, J. A general approach to one-pot fabrication of crumpled graphene-based nanohybrids for energy applications. *ACS nano* 2012, 6, 7505-7513”. Copyright ©2012, American Chemical Society. **Figure 1.2.2-C** and **D** is reprinted with permission from “Wu, Z.-S.; Winter, A.; Chen, L.; Sun, Y.; Turchanin, A.; Feng, X.; Müllen, K. Three-Dimensional Nitrogen and Boron Co-doped Graphene for High-Performance All-Solid-State Supercapacitors. *Adv. Mater.* 2012, 24, 5130-5135”. Copyright ©2012, WILEY-VCH Verlag GmbH & Co. **Figure 1.4.1** and **1.4.2.** are reprinted with permission from “Microwave synthesis: chemistry at the speed of light. Hayes, Brittany L. (2002)”. Copyright ©2002, CEM Publishing.

Chapter 2. A large portion of this material has been published as a full journal article in “*ACS Nano*”. All the figures and text of this published article are reprinted in this chapter with permission from “Patel, M.; Yang, H.; Chiu, P.; Mastrogiovanni, D.; Flach, C.; Savaram, K.; Gomez, L.; Hemnarine, A.; Mendelsohn, R.; Garfunkel, E.; Jiang, H. and He, H., 2013. Direct production of graphene nanosheets for near infrared photoacoustic imaging. *ACS nano*, 7(9), pp.8147-8157”. Copyright © 2013, American Chemical Society. **Figure 2.12** is reprinted with permission from the “Taratula, O.; Patel, M.; Schumann, C.; Naleway, M.; Pang, A.; He, H. and Taratula, O., 2015. Phthalocyanine-loaded graphene nanoplatform for imaging-guided combinatorial

phototherapy. *International journal of nanomedicine*, 10, pp.2347-2362”. Copyright © 2015, Taratula et al.

Chapter 3. A full portion of this material has been published as a full journal article in “Small”. All the figures and text of this published article are reprinted in this chapter with permission from “Patel, M.; Feng, W.; Savaram, K.; Khoshi, M.R.; Huang, R.; Sun, J.; Rabie, E.; Flach, C.; Mendelsohn, R.; Garfunkel, E. and He, H., 2015. Microwave Enabled One-Pot, One-Step Fabrication and Nitrogen Doping of Holey Graphene Oxide for Catalytic Applications. *Small*, 11(27), pp.3358-3368.”. Copyright © 2015, John Wiley & Sons, Inc.

Chapter 4. A full portion of this material has been published as a full journal article in “ACS Nano”. All the figures and text of this published article are reprinted in this chapter with permission from “Patel, M.A.; Luo, F.; Khoshi, M.R.; Rabie, E.; Zhang, Q.; Flach, C.R.; Mendelsohn, R.; Garfunkel, E.; Szostak, M. and He, H., 2015. P-Doped Porous Carbon as Metal Free Catalysts for Selective Aerobic Oxidation with an Unexpected Mechanism. *ACS nano*, 10 (2), 2305-2315”. Copyright © 2016, American Chemical Society.

Chapter 5. A full portion of this material has been published as a full journal article in “Journal of Natural Products Research Updates”. All the figures and text in this chapter are reprinted with permission from “Patel, M.; Savaram, K.; Keating, K. and He, H., 2015. Rapid Transformation of Biomass Compounds to Metal Free Catalysts via Short Microwave Irradiation. *Journal of Natural Products Research Updates*, 1, 18-28”. Copyright © 2015, Synchro Publisher.

Dedication

**This dissertation is dedicated to all my family members for their
abundant love, patience and continuous support
to fulfill my dream.**

Acknowledgement

It is with immense gratitude that I acknowledge my Professor, Dr. Huixin He for giving me a golden opportunity to pursue a Ph.D. research in her lab to fulfill my dream. I would also like to thank for her invaluable assistance, motivation, advice and guidance throughout in all phase of my Ph.D. studies. She has always inspired me to become independent researcher and planted a seed for developing scientific reasoning in my mind. I would also like to thank her for encouraging and allowing me to grow as a research scientist.

My sincere thanks also go to all my thesis committee members: Dr. Phillip Huskey, Dr. Jenny Lockard, and Dr. Xianqin Wang for agreeing to be a member for my Ph.D. defense committee. I really appreciate all of them for devoting their precious time in reading and valuable comments to improve my thesis.

I am also more grateful to the collaborators, who have always advice and helped me with their expertise to solve my scientific and technical problems. So would like share the credit of my success with them: Prof. Eric Garfunkel and his students (Dr. Daniel Mastrogiovanni, Dr. Wenchun Feng, Dr. Feixiang Luo and Ms. Qing Zhang) for X-ray photoelectron spectroscopy (XPS) measurement and data analysis. Prof. Richard Mendelsohn, Dr. Carol R Flach and their lab members (Ms. Emann Rabie and Dr. Qihong Zhang) for their help in FT-IR and Raman measurement and analysis of our graphene samples. Prof. Jenny Lockard and her student (Dr. Pavel Kucheryavy and Mr. Qiaoqiao Xie) for X-ray absorption spectroscopy (XAS) measurement and data analysis. Prof. Huabei Jiang and Dr. Hao Yang for their help in photoacoustic measurement. Prof.

Michal Szostak and Dr. Feng Hu for their fruitful collaboration in usefulness of graphene based material for organic catalysis. Prof. Kristina Keating for surface area measurement of graphene samples by Brunauer–Emmett–Teller (BET) method. Prof. Theresa Li-Yun Chang and her group members (Ms. Carley Tasker and Ms. Kimyata Valere) for help in anti-HIV activity measurement of graphene nanosheets. Prof. Oleh Taratula and Dr. Olena Taratula for the study of graphene nanosheets in cancer treatment. Dr. Roman Brukh for his help in Gas Chromatography Mass Spectrometry (GC-MS) and Scanning electron microscope (SEM) training and measurements.

I cannot forget my friends cum colleagues cum lab mates (Dr. William Cheung, Dr. Pui Lam Chiu, Ms. Keerthi Savaram, Mr. M Reza Khoshi and Dr. Ruiming Huang) who not only cheered me for each of my accomplishment but also helped me and inspired me in my research. My sincere thanks also goes to all the faculties and staff members in chemistry department for their kind support and making my Ph.D. journey memorable.

I would like to acknowledge the financial support from our chemistry department, Rutgers university-Newark and National Science Foundation (CHE-0750201, CHE-1229030, CBET-0933966, CBET 1438493, STTR 1346496, DMR 1507812, and MRI-1039828).

A special thanks to my family. Words cannot express how grateful I am to my parents (Arvindbhai and Jayaben), my parents-in-law (Rameshchandra and Aartibahen), my dear sisters (Nisha and Dharmishtha), and brother-in-law (Parth) for their trust, constant inspiration and unconditional support. Their prayers for me was what sustained me thus far. I also want to thank my school time mentor(Mr. Pravinbhai), my uncle Mr.

(Parsottambhai) and aunty (Sunitaben), who has always encouraged me by his moral support and by his unconditional financial support during my transition from India to USA. I would also like to thanks all my friends for their emotional support.

Finally, this thesis would have remained a dream and had not been possible without support from my beautiful, lovely wife (Monal). She has always motivated, loved, supported, entertained me and even digested my frustration. Thanks to her (and her alone) I have been able to maintain a sustainable level of work/life balance throughout my Ph.D. You are truly the best companion that I can ever have in my life.

Table of Contents

Copyright Page.....	i
Abstract of The Dissertation	ii
Preface.....	v
Dedication	vii
Acknowledgement	viii
List of Figures	xiv
List of Schematic Drawings.....	xxv
List of Tables	xxvi
Chapter-1. Introduction.....	1
1.1. Graphene: Background and its properties.	1
1.1.1. Background of graphene.	1
1.1.2. The unique properties of graphene.	2
1.2. Graphene with controlled morphology	4
1.2.1. The importance of controlling the morphology of graphene sheet.....	4
1.2.2. Properties and application of graphene nanosheets:	6
1.2.3. Synthesis of graphene nanosheets.....	8
1.2.4. Properties and application of porous/holey graphene.....	10
1.2.5. Synthesis of holey graphene sheets.....	12
1.3. Chemical modification of graphene.	16
1.3.1. The Importance of heteroatoms doped graphene and its application.	17
1.3.2. Synthesis of heteroatom-doped graphene/carbon.	20
1.3.3. Catalytic applications of heteroatom-doped graphene/carbon material.....	27
1.4. Microwave Chemistry.	37
1.5. References.	40
Chapter 2. Direct Production of Graphene Nanosheets for Near Infrared Photoacoustic Imaging	56
2.1. Introduction.....	56
2.2. Results and Discussion	58
2.3. Conclusions.....	80

2.4. Experimental Section	82
2.4.1. Materials	82
2.4.2. Fabrication of ME-LOGr nanosheets.....	82
2.4.3. Control experiments.....	83
2.4.4. Material Characterization.....	84
2.4.5. Photoacoustic characterization.....	85
2.5. References.....	86
Chapter 3. Microwave Enabled One-Pot, One-Step Fabrication and Nitrogen Doping of Holey Graphene Oxide for Catalytic Applications.....	91
3.1 Introduction.....	91
3.2 Results and Discussion	93
3.3. Conclusions.....	122
3.4. Experimental Section.....	123
3.4.1. Synthesis of GO and HGO.....	123
3.4.2. N doping of GO and HGO	124
3.4.3. Material Characterization.....	124
3.4.4. Surface area measurement of GO, HGO, N-rGO-10 and N-HrGO-10:	125
3.4.5. Electrochemical Measurements	126
3.5. References.....	128
Chapter 4. P-Doped Porous Carbon as Metal Free Catalysts for Selective Aerobic Oxidation with an Unexpected Mechanism.....	133
4.1. Introduction.....	133
4.2. Results and Discussion	137
4.3. Conclusions.....	162
4.4. Experimental Section.....	163
4.4.1. PGc (Phosphorus doped graphitic carbon) fabrication	163
4.4.2. Fabrication of PGc-30 and PGc-180.....	164
4.4.3. Synthesis of GO and rGO for catalysis.....	165
4.4.4. Catalytic oxidation of primary and secondary alcohol Reaction.	165
4.4.5. Material Characterization.....	167
4.5. References.....	173

Chapter 5. Rapid Transformation of Biomass Compounds to Metal Free Catalysts via Short Microwave Irradiation.....	178
5.1. Introduction.....	178
5.2. Results and Discussion	183
5.3. Conclusions.....	199
5.4. Experimental Section	200
5.4.1. Synthesis of the PGc (Phosphorus doped graphitic carbon), PGc-30 and PGc-180:	200
5.4.2. Synthesis of P and other heteroatoms (N, B, S and Si) co-doped catalysts:..	201
5.4.3. Synthesis of P-doped and Non-carbon catalysts using Inositol and phosphoric acid/sulfuric acid for control experiment.	203
5.4.4. Synthesis of sole heteroatoms (B, N, S, or Si) doped carbon materials using Inositol as carbon (C) source.	203
5.4.5. Electrochemical Characterization:	204
5.4.6. Material Characterization:	206
5.5. References.....	207
Chapter 6. Phosphorus and Sulfur Dual-Doped Graphitic Porous Carbon Metal-Free Catalysts for Aerobic Oxidation Reactions: Enhanced Catalytic Activity and Active Sites.	211
6.1. Introduction.....	211
6.2. Results and Discussion	213
6.3. Conclusions.....	239
6.4. Experimental Section	240
6.4.1. Synthesis of catalysts	240
6.4.2. Catalytic oxidation of primary and secondary alcohol Reaction.	241
6.4.3. Material characterization	242
6.5. References.....	244

List of Figures

Figure 1.1.1. The structures of different carbon allotropes.....	1
Figure 1.2.1. Schematics of graphene structure with highlighting different type of edge and hole defect. Carbon atoms on the edges are highlighted with red color to differentiate it from bulk C atom (gray color).....	6
Figure 1.2.2. A) AFM image of holey graphene sheets B) SEM image of Crumpled graphene sheet C) is a digital photograph and D) SEM image of graphene foam.....	10
Figure 1.3.1. The schematic for N-doped graphene (A) and P-doped graphene (B) with different dopant configurations. Inset of (B) is showing the side view of P-doped graphene to show that P atom is protruding out of graphene plane.....	19
Figure 1.3.2. Schematics of Fuel cell design.	30
Figure 1.4.1. Electric and magnetic field of Microwave.	37
Figure 1.4.2. The electromagnetic spectrum of Microwave.	38
Figure 2.1. Digital photographs of stable ME-LOGr solutions in water, N, N-dimethylformamide (DMF), acetone, pyridine, and acetonitrile.	59
Figure 2.2. (A) AFM images of ME-LOGr nanosheets, (B) UV-Vis-NIR spectra of ME-LOGr nanosheets with concentrations of 20 (pink), 10 (olive), 6.7 (blue), is 5 (red), and 3.3 mg/L (black), respectively. Inset B, a digital picture of an aqueous suspension of ME-LOGr nanosheets (left) and graphene oxide (GO) nanosheets (right) shows different colors, indicating they are in different oxidation states. The GO nanosheets were obtained <i>via</i> Control-A Experiment in which nitronium ions and KMnO_4 both act as an oxidant.	60
Figure 2.3. Statistical analysis of the AFM pictures of ME-LOGr nanosheets.	60
Figure 2.4. An x-ray photoelectron spectrum (XPS) of ME-LOGr nanosheets.	61

Figure 2.5. Raman spectra of ME-LOGr nanosheets (red) and GO nanosheets (blue). GO nanosheets were obtained *via* Control- A experiment where nitronium ions and KMnO_4 both act as an oxidant..... 63

Figure 2.6. (A) AFM image of graphene oxide nanosheets obtained *via* Control-A experiment. Some of the nanometer gaps between nanosheets and nanoholes generated during the oxidation reaction were labeled with arrows and circles, respectively. (B) UV-Vis-NIR spectra of the GO sheets at different concentrations of 133.3 (Wine), 66.7 (olive), 53.3 (blue), 44.4 (red), and 33.3 mg/L (black), respectively. For better comparison, the pink curve (20mg/L of ME-LOGr nanosheets) in **Figure 2.2B** is also displayed in panel B with the same color. Inset (B) shows the linear relationships between the absorption at 984 nm and the concentration of ME-LOGr nanosheets and GO. The mass coefficient of the ME-LOGr is 40 fold higher than that of GO..... 67

Figure 2.7. (A) UV-Vis-NIR spectrum of the nanosheets obtained *via* KMnO_4 oxidation (Control-B experiment). The maximum plasmon peak is around 235 nm. Inset (A) is a picture of the dispersed nanosheet solution. The brownish yellow color and the plasmon peak at 235 nm collectively demonstrated that the product is highly oxidized. (B) An AFM image of the nanosheets, majority of which have multiple layers. 68

Figure 2.8. (A) Raman spectra of different concentrations of nitronium ions produced with different ratios of concentrated HNO_3 , H_2SO_4 , and H_2O with ratios of (1) 1:1:0; (2) 1:42:7 ; (3) 1:2.5:0.07; (4) 1:17.5:1.5 and (5) 1:4:0, respectively. (B) Digital pictures of filtrates obtained after graphite particles were oxidized in microwave with different ratios of $\text{HNO}_3\text{:H}_2\text{SO}_4\text{:H}_2\text{O}$ of (1) to (5), and therefore different concentrations of nitronium ions. 5-K was obtained with the same ratio as (5), except that KMnO_4 was included. (C

and D) AFM images of porous graphene sheets dispersed with magnetic stirring instead of sonication to avoid sonication-induced tearing. The graphene sheets in panels C, and D were obtained with ratio (3) and (4), respectively. 70

Figure 2.9. Raman spectra of the mixture of concentrated H_2SO_4 and HNO_3 and H_2O with different volume ratios of concentrated HNO_3 , H_2SO_4 , and H_2O with ratios of (1) 1:1:0; (2) 1:42:7 ; (3) 1:2.5:0.07; (4) 1:17.5:1.5 and (5) 1:4:0, respectively. The concentration of the generated nitronium ions by the acid mixtures increases as the ratio of H_2SO_4 , HNO_3 , and H_2O changes. Peak assignments are labeled on the spectra and listed in the following **Table 2.1**..... 71

Figure 2.10. (A) An AFM image of nanosheets obtained with traditional heating (Control-C Experiment). (B)UV-Vis-NIR spectrum of the nanosheets indicates that these sheets are more oxidized than the ME-LOGr nanosheets fabricated *via* microwave heating..... 73

Figure 2.11. Photoacoustic (PA) signal of GO and graphene nanosheets of different concentrations, illuminated with 700nm and 800nm laser. The color coded vertical bar represents the strength of the photoacoustic signal generated. GO nanosheets were obtained *via* Control-A experiment. 79

Figure 2.12.Schematic illustration of the multifunctional nanoplatform based on ME-LOGr nanosheets. A) In Vivo NIR fluorescence imaging of nude mice 12 hours after injection of saline ME-LOGr-Pc-LHRH. B) Combinatorial (PDT-PTT) therapeutic effects of ME-LOGr-Pc-LHRH (cyan color) on A2780/AD cell pellets (2,000,000) irradiated for 10 minutes using a 690 nm laser diode (0.95 W/cm^2), compared with controls- ME-LOGr-LHRH (black) and Pc-LHRH (sky blue).⁶⁹ 80

Figure 2.13. Schematic of the experimental setup for PA imaging	85
Figure 3.1. (A) AFM and (C) STEM of GO sheets obtained via 30seconds of microwave irradiation. (B) AFM and (D) STEM images of HGO sheets obtained via 40 seconds of microwave irradiation. (E) UV-Vis-NIR spectra of GO sheets (black line) and N-rGO-10 (red line). Inset (E) is a digital picture of an aqueous dispersion of GO (left) and N-rGO-10(right) shows different colors, indicating they are in different oxidation states. (F) UV-Vis-NIR spectra of HGO sheets (black line) and N-HrGO-10 (red line). Inset (F) is a digital picture of an aqueous dispersion of HGO (left), N-HrGO-10(right) shows different color, indicating their different oxidation states. The red arrows in (B and D) shows hole on HGO sheet.....	95
Figure 3.2. (A) XPS survey scan and (B) O 1s peak of GO, N-rGO-10, HGO and N-HrGO-10. XPS high resolution C 1s peak analysis of HGO (C), GO (D), N-HrGO-10 (E) and N-rGO-10(F), where 10 denotes microwave treatment time (in minutes) of HGO/GO with NH ₄ OH at 120 °C.	97
Figure 3.3. (A) AFM and (B) Uv-Vis-NIR spectrum of an aqueous dispersion of HGO sheets obtained via 45seconds of microwave heating. The inset of (B) shows its digital picture. (C) is the digital pictures and (D) is the fluorescence emission spectra ($\lambda_{exc} = 335nm$) of the filtrates, produced after graphite particles were oxidized with different microwave time: (I) 30seconds, (II) 40seconds, (III) 45seconds, respectively. (IV) is the filtrate obtained with the same experimental conditions as (I), except that KMnO ₄ was excluded and (V) is the filtrate obtained with the same experiment condition as (II), except the graphite was excluded.	100

Figure 3.4. AFM images of the products obtained with different control experimental conditions. Microwave heating of the mixture of H_2SO_4 , HNO_3 and graphite (300W and 30 seconds) in the absence of KMnO_4 (A); in the presence of KMnO_4 (125wt% of graphite) (B); traditional heating of the mixture of H_2SO_4 , HNO_3 and graphite with KMnO_4 (500wt% of graphite) (C). (D) shows their corresponding UV-VIS-NIR spectrum: black curve for (A), red curve for (B) and blue curve for (C). The UV peak at 264 nm and the strong NIR absorption indicate the intrinsic properties of graphene are largely maintained in product (A); the blue shift of the UV peak to 240 nm and the decrease in NIR absorption suggest that the product (B) is partially oxidized. The product (C) shows a typical UV-VIS-NIR spectrum of a highly oxidized graphene oxide. 102

Figure 3.5. Microwave heating temperature ($^{\circ}\text{C}$) profile with time during GO (black line) and HGO (red line) synthesis..... 104

Figure 3.6. (A) FTIR spectrum of GO and N-rGO-10. (B) FTIR spectrum of HGO and N-HrGO-10. 107

Figure 3.7. Raman spectra of HGO and N-HrGO-5, N-HrGO-10 and N-HrGO-30. 109

Figure 3.8. Scanning electron microscopic (SEM) images of N-rGO-10(A and B), N-HrGO-5(C and D), N-HrGO-10(E and F) and N-HrGO-30(G and H). The yellow arrow shows hole on N-HrGO's surface. 110

Figure 3.9. XPS high resolution N1s peak analysis of N-rGO-10 (A), N-HrGO-10 (c) and N-HrGO-30 (d), where 10 and 30 denotes microwave treatment time (in minutes) of GO/HGO with NH_4OH at 120°C 111

Figure 3.10. (A) and (B) is CV and LSV curves of Pt/C, EC-HrGO, N-HrGO-10, N-rGO-10 and bare electrode in O_2 saturated 0.1M KOH electrolyte at a scan rate of 50

mV/s and 10 mV/s, respectively. Inset (B) is zoomed in LSV curve of bare electrode, N-rGO-10 and N-HrGO-10. All potentials are measured using Ag/AgCl as a reference electrode. (C) CVs of N-HrGO-10 in N₂ and O₂ saturated 0.1M KOH electrolyte at a scan rate of 50mv/s. (D) Tafel plots of Pt/C, N-HrGO-10, N-rGO-10, EC-HrGO and bare electrode derived by the mass-transport correction of corresponding RDE data (**Figure 3.10B**)..... 113

Figure 3.11. CV curves (A) and onset potential (B) of N-HrGO-x electrode in O₂ saturated 0.1M KOH electrolyte at a scan rate of 50mv/s, where “x” is different microwave time (0, 5, 10, 15, 30 minutes) used for synthesis of different N-HrGO. All potentials are measured using Ag/AgCl as a reference electrode..... 115

Figure 3.12. (a) RRDE voltammogram of N-HrGO-10, N-HrGO-30, EC-HrGO, N-rGO-10 and Pt/C modified electrode in oxygen saturated 0.1M KOH at a scan rate of 10mV/s and 1600rpm rotation speed. (b) and (c) is the number of electron transfer and relative peroxide %, respectively, for all catalyst calculated from RRDE voltammogram. All potentials are measured using Ag/AgCl as a reference electrode..... 118

Figure 3.13. LSV curves of N-HrGO-10(a), N-rGO-10(b) and Pt/C(c) at different rotation speed in O₂ saturated 0.1M KOH solution at 10mV/s. (d) is K-L plot of Pt/C, obtained based on the LSV data(c).All potentials are measured using Ag/AgCl as a reference electrode..... 119

Figure 3.14. (A) and (B) are K-L plot of N-HrGO-10 and N-rGO-10, obtained based on the LSV curves at different rotating speeds (**Figure 3.13**), respectively. (C) is calculated oxygen diffusion coefficient and (D) is calculated rate constant for ORR, using slope and

intercept from K-L plot of N-HrGO-10, N-rGO-10 and Pt/C. All potentials are measured using Ag/AgCl as a reference electrode..... 120

Figure 3.15. (A) is Nyquist plot of EIS for the oxygen reduction on the bare electrode, EC-HrGO, N-rGO-10, N-HrGO-10 and Pt/C. (B) is durability testing of the Pt/C and N-HrGO-10 electrode for ~7 hours at -0.38V and 1000rpm speed. (C) is chronoamperometric response of the N-HrGO-10 and Pt/C modified electrode for ORR upon addition of methanol after about ~300seconds at -0.38V. All potentials are measured using Ag/AgCl as a reference electrode. 121

Figure 3.16. Linear relationships between the concentration of MB and its absorption at 664 nm. 126

Figure 4.1. Scanning electron microscope (SEM) images of the as-fabricated PGc catalyst. 138

Figure 4.2. (A) XPS and (B) EDS spectra of PGc, PGc-30 and PGc-180 catalysts. (C) The Raman spectra of different catalysts. (D) 12-point BET plot of PGc catalyst. 140

Figure 4.3. TGA (Thermo Gravimetric Analysis) spectra of different phosphorus doped carbon catalyst and graphite..... 141

Figure 4.4. (A) Molarity of benzaldehyde vs reaction time plot at different reaction temperatures to study the rate of oxidation of benzyl alcohol. Reaction conditions: 7 mg benzyl alcohol, 10.5 mg PGc catalyst, 10 ml water, 1 atm O₂. (B) Arrhenius plot for the benzyl alcohol oxidation. The rate constant (k) values at different temperature were regarded as the pseudo-zero-order rate constants (k_{obs}) because the plot of the molarity of benzaldehyde produced versus time is linear. 143

Figure 4.5. HPLC chromatogram of blank (No catalyst), PGc catalyst with an oxygen oxidant (B) and PGc catalyst with an H ₂ O ₂ oxidant(C). Reaction condition for (A) and (B) can be found in Table 4.3- entry no. 1 and 4. Reaction condition for (C) can be found in Table 4.8 entry no. 4.	143
Figure 4.6. (A) Recycling the PGc catalyst for benzyl alcohol oxidation. Reaction condition: 50mg catalyst, 100mg benzyl alcohol, 1atm O ₂ , 80°C, 48hours. (B) Time conversion plot of a fresh and used PGc catalyst. Reaction condition: 10 mg catalyst, 50 mg benzyl alcohol, 1 atm O ₂ , 100°C. The used catalyst is recycled twice (at reaction conditions specified in Figure 4.6A before the time conversion measurement.	146
Figure 4.7. Scanning electron microscope image of the fabricated PGc-30 and PGc-180 catalysts.	146
Figure 4.8. (A, C) topography and (B, D) PF-KPFM images of PGc and PGc-180 catalysts, respectively.	150
Figure 4.9. P 2p (A, C, E) and O 1s (B, D, F) Peak deconvolution of different PGc catalysts, PGc, PGc-30 and PGc-180, respectively.	153
Figure 4.10. The FT-IR spectrum comparison of PGc with GO and rGO catalysts.	154
Figure 4.11. The FT-IR spectrum of PGc, PGc-30 and PGc-180 catalysts.	156
Figure 4.12. H-NMR spectrum of reaction mixture (Table2- entry no. 4) containing benzyl alcohol (2H, 4.62 ppm), Benzaldehyde (1H, 9.95 ppm) and trace amount of water (2.12 ppm).	157
Figure 4.13. Hammett plot of Plot of log k vs. σ for the oxidation of 4-substituted benzyl alcohols with PGc catalyst.	160

Figure 4.14. The FT-IR spectrum of the fresh and used PGc catalyst. The used catalyst was recycled twice (the reaction conditions were specified in Figure 4.6A caption) before this FT-IR measurement.	160
Figure 4.15. (A, C) AFM Topography and (B, D) PF-KPFM images for the PGc and the PGc-180 catalysts.....	172
Figure 4.16. X-ray fluorescence spectroscopic (XRF) analysis of standard mixture (rGO with different % P). The used catalyst is recycled twice (at reaction conditions specified in the caption of Figure 4.6) before XRF measurement.	172
Figure 5.1. The SEM images and EDS spectra of (A) PN-Gc, (B) PS-Gc, (C)PB-Gc, (D)PSi-Gc, (E)PBN-Gc. The EDS spectra were taken by drop casting each of the co-doping carbon materials on a Cu tape.....	186
Figure 5.2. The SEM image and EDS spectrum of the PGc (A), Non doped-Gc (B), Si-Gc (C), N-Gc (D), B-Gc (E), S-Gc (F), which were fabricated by heating the mixture of inositol and phosphoric acid, inositol and sulfuric acid, inositol + sulfuric acid + tetraethyl orthosilicate (TES), inositol + sulfuric acid + NH ₄ OH, inositol + sulfuric acid + boric acid, and inositol + sulfuric acid + amorphous sulfur in microwave, respectively. The scale bar shown in all SEM images is 2 μ m.	189
Figure 5.3. (A) is Cyclic voltammetry (CV) and (B) is Linear sweep voltammetry (LSV) curves of different phosphorus doped carbon catalyst in O ₂ saturated 0.1M KOH. LSV measurements were performed using rotating ring disc (RRDE) electrode at 2000 rpm.	190
Figure 5.4. N ₂ adsorption/desorption isotherms for different phosphorus doped carbon catalysts.....	192

Figure 5.5. (A, B and C) are Linear sweep voltammetry (LSV) curves for PGc, PGc-30 and PGc-180 carbon catalysts, respectively, at different rotating speed in O₂ saturated 0.1M KOH solution at 10mV/s. (D) is RRDE curve comparison of PGc, PGc-30 and PGc-180 modified electrode at 2000 rpm in O₂ saturated 0.1M KOH solution at 10mV/s. Inset (D) is zoom out of ring current comparison of PGc, PGc-30 and PGc-180 catalysts.

..... 194

Figure 5.6. Koutecky-Levich (K-L) plots of PGc, PGc-30 and PGc-180 catalysts at different potentials, calculated from their respective LSV curves at different rotating speed (rpm). 194

Figure 5.7. The Tafel plot and respective Tafel slopes (b₁ and b₂) of different P doped carbon catalysts (A), P and other heteroatoms co-doped carbon catalysts (B), Pt/C catalyst (C) and Bare electrode(D). 196

Figure 5.8. (A) Cyclic voltammetry (CV) and (B) is RRDE curves of different phosphorus (P)and other heteroatoms (B, N, S) co-doped carbon catalysts in O₂ saturated 0.1M KOH electrolyte. The RRDE experiment was performed at 2000 rpm using rotating ring disc (RRDE) electrode in O₂ saturated 0.1M KOH solution at 10 mV/s. 197

Figure 5.9. (A) is Durability testing of the Pt/C, PGc-180 and PN-Gc catalyst modified electrode for ~ 7 hours at -0.35V and 2000 rpm rotating speed. (B) is Methanol tolerance test of the Pt/C, PN-Gc and PGc-180 catalysts, where methanol was added at about 300 seconds of amperometric analysis at -0.35 V. All potentials were measured using Ag/AgCl as the reference electrode. 198

Figure 6.1. (A) is scanning electron microscopic (SEM) of PS-Gc and (B) Energy Dispersive X-ray Spectra (EDS) of PS-Gc. 216

Figure 6.2. C1s, O 1s and P2p XPS peak deconvolution of PS-Gc catalyst (A) and PS-Gc-used catalyst (B).....	218
Figure 6.3. S 2p XPS peak deconvolution of PS-Gc catalyst (A), PS-Gc-used catalyst (B), PS-Gc-TA catalyst (C) and PS-Gc-TA-used (D).	219
Figure 6.4. The FT-IR spectra of GO, P-Gc, S-Gc and PS-Gc.....	220
Figure 6.5. The Raman spectra of PS-Gc, PS-Gc-used, PS-Gc-TA and PS-Gc-TA-used.	221
Figure 6.6. (A) The plot of different reaction temperatures versus benzaldehyde concentration in molarity. Reaction conditions: 10 mg benzyl alcohol, 5 mg PS-Gc catalyst, 10 ml water, 1 atm O ₂ . (B) Arrhenius plot for the Benzyl alcohol oxidation. The rate constant (k) values at different temperature were regarded as the pseudo-zero-order rate constants (k obs) because the plot of the molarity of benzaldehyde versus reaction time is linear.....	228
Figure 6.7. The FT-IR spectra of fresh and used PS-Gc catalysts (A) and PS-GC-TA catalysts (B).	234
Figure 6.8. The deconvolution of normalized S K-edge XANES spectra of fresh and used PS-Gc catalysts.	235

List of Schematic Drawings

Scheme 2.1. Schematic of the possible cutting mechanisms by microwave assisted nitronium oxidation in the presence and absence of KMnO_4 . v_c and v_G are referred to $v_{\text{consumption}}$ (reaction rate of defect consumption) and $v_{\text{generation}}$ (reaction rate of defect generation), respectively.	76
Scheme 3.1. Schematic drawing of proposed mechanism of HGO synthesis.....	104
Scheme 4.1. Schematic drawing of PGc synthesis from Phytic acid by microwave heating.	137
Scheme 4.2. Proposed mechanism of benzyl alcohol oxidation catalyzed by PGc in presence of oxygen as an oxidant.	156
Scheme 5.1. The General Scheme of P and other heteroatom co-doped carbon fabrication.	181
Scheme 6.1. The proposed mechanism for benzylic alcohol oxidation by exocyclic S active center.	232

List of Tables

Table 1.2.1. Summary of synthetic approaches for holey graphene.	14
Table 1.3.1. Summary of synthetic approaches for heteroatom doping into graphene /carbon matrix.	25
Table 2.1. An assigned name and position of the peaks from the above Raman spectra of the mixture of concentrated H_2SO_4 and HNO_3 and H_2O	71
Table 2.2. Different volume ratio of $HNO_3:H_2SO_4:H_2O$	83
Table 3.1 Atomic ratio of C, N and O calculated from high resolution C 1s, N 1s and O 1s XPS peak analysis of different catalysts.	97
Table 3.2 The measured surface area of GO, HGO, N-rGO-10 and N-HrGO-10 via MB adsorption method.	98
Table 3.3. The calculated relative % of different kind of carbon from XPS high resolution C1s deconvolution in different catalysts.	108
Table 3.4. Relative % ratio of different kind of N-dopant in N-HrGO-10, N-HrGO-30 and N-rGO-10.	111
Table 3.5. Electrochemical parameters (onset potential, peak potential, current density at - 0.4V and Tafel slopes- b1 and b2- calculated at low and high current density region, respectively) of different catalysts for ORR estimated from CV and RDE polarization curves in 0.1M KOH solution. All potential are measured using Ag/AgCl as a reference electrode.	111
Table 4.1. Calculated atomic % of C, P and O for PGc, PGc-30 and PGc-180 catalysts.	138
Table 4.2. Benzyl alcohol oxidation catalyzed by PGc in water.	139

Table 4.3. Optimization experiments for solvent free alcohol oxidation catalyzed by PGc	142
Table 4.4. The catalytic activity of PGc in the oxidation of different alcohols	146
Table 4.5. Recycling the PGc catalyst in benzyl alcohol oxidation in presence of different environment.	149
Table 4.6. The benzyl alcohol oxidation in presence of radical quencher.	149
Table 4.7. Calculated % of different type of oxygen present in PGc, PGc-30 and PGc-180 catalysts.....	152
Table 4.8. Calculated % of P-C and P-O present in PGc, PGc-30 and PGc-180 catalysts.	153
Table 4.9. The benzyl alcohol oxidation catalyzed by PGc in the presence of H ₂ O ₂ and TBHP oxidants.....	159
Table 5.1. Atomic composition of different atoms in all co-doped carbon materials as determined from EDS measurements.	182
Table 5.2. Electrochemical parameters (onset potential, peak potential, current density, no of electrons, % HO ₂ ⁻ , rate constant k and Tafel slopes-b1 and -b2 of different catalysts for ORR estimated from CV and RRDE polarization curves in 0.1 m KOH solution. b1 and b2 are calculated at low and high current density region, respectively. All potentials were measured using Ag/AgCl as the reference electrode.	188
Table 5.3. BET analysis summary of different phosphorus doped carbon catalysts.	190
Table 6.1. Comparison of various heteroatom-doped porous carbon for its catalytic efficiency towards selective benzylic alcohol oxidation	211
Table 6.2. Calculated atomic % of C, O, P and S from EDS and XPS analysis.	212

Table 6.3. Calculated atomic % different type of O present in catalyst by XPS analysis.	212
Table 6.4. Calculated atomic % different type of P and S present in catalyst by XPS analysis.	214
Table 6.5. Optimization experiments for solvent free alcohol oxidation catalyzed by PS-Gc at 1atm O ₂ .	218
Table 6.6. The scope of PS-Gc in the oxidation of different alcohols	220
Table 6.7. The catalytic performance of the PS-Gc and S-Gc in benzyl alcohol oxidation in presence of different environment	224
Table 6.8. The benzyl alcohol oxidation in presence of BHT (radical quencher)	225
Table 6.9. Recycling the catalyst at different reaction conditions.	226
Table 6.10. Calculated atomic % of the different type of S functionalities from S K-edge XANES peak deconvolution analysis.	230

Chapter-1. Introduction

1.1. Graphene: Background and its properties.

1.1.1. Background of graphene.

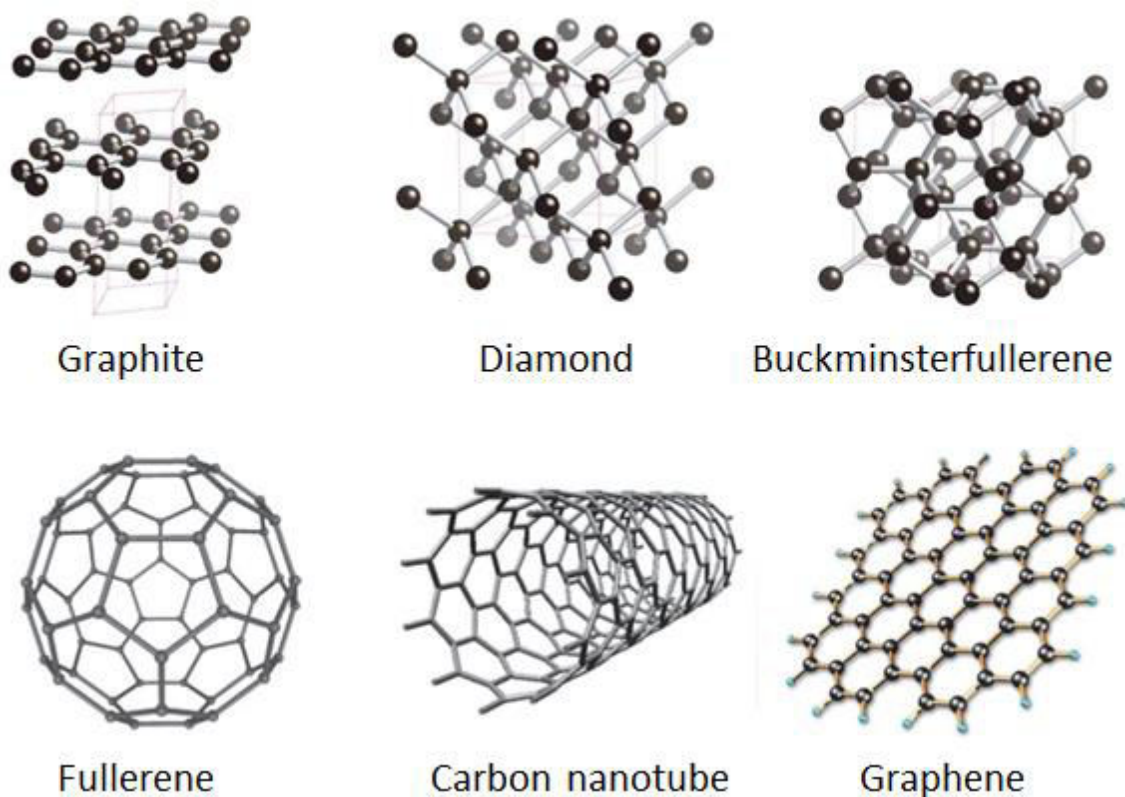


Figure 1.1.1. The structures of different carbon allotropes.¹

Carbon is a unique element on the earth. This is attributed to the four valence electrons in its valence shell which endow carbon to form many different elemental allotropes such as diamond, graphite, graphene, amorphous carbon, glassy carbon, fullerene, buckminsterfullerene, carbon nanotubes, carbon nanobuds, Lonsdaleite etc.¹⁻³ Among the different elemental carbon allotropes, sp^3 hybridized diamond and sp^2 hybridized graphite and graphene are very well-known forms of carbon. For more than a decade, extensive research has been contributed on graphene because of its superior physico-chemical

properties. Graphene is a two-dimensional (2D) monolayer sheet consisting of one atom thick sp^2 hybridized carbon atoms arranged in a honeycomb crystal lattice while graphite is a three-dimensional (3D) crystal made of stacked layers of graphene that interact through hydrophobic or van der Waals forces (**Figure 1.1.1**).

1.1.2. The unique properties of graphene.

For an extended period of time, it was believed that this excellent 2D system (graphene) was thermodynamically unstable and could not exist in free state.^{4, 5} But, a groundbreaking experiment in graphene research was achieved in 2004 by Dr. A. Geim and Dr. K. Novoselov at the University of Manchester, where they discovered that a monolayer graphene can be isolated from the highly oriented pyrolytic graphite (HOPG) by mechanical exfoliation using a simple Scotch-tape approach.⁶ Since then, graphene has spawned enormous research interest over the past decade due to its many fascinating physical and chemical properties, which originate from the presence of extensive π -conjugation in its structure.^{6, 7} Graphene exhibits many extraordinary physicochemical properties such as high electric conductivity or charge carrier mobility (theoretically $200,000 \text{ cm}^2 \text{ V}^{-1} \text{ s}^{-1}$)³, very large theoretical surface area ($2630 \text{ m}^2/\text{g}$)⁸, high thermal conductivity ($\sim 5000 \text{ W/mK}$)^{9, 10} and exceptional mechanical strength of 130 GPa (Young's modulus $\sim 1.0 \text{ TPa}$)¹¹. In addition, graphene also shows excellent stretchability^{12, 13}, optical transparency (97.7% for single layer graphene below 3 eV light)¹⁴ and complete impermeability to any gases¹⁵. Because of these exceptional properties of graphene^{6, 7}, Dr. A. Geim and Dr. K. Novoselov were awarded a Nobel Prize in Physics in 2010 for their discovery.

The phenomenal properties of graphene offers a vast scope of applications in the flexible electronic fields such as supercapacitors^{16, 17}, transparent conductors in solar cells^{13, 18, 19}, organic light emitting diodes (OLEDs)²⁰, touch screens²¹, field effect transistors (FETs)^{22, 23}, photodetectors^{24, 25} etc. Moreover, due to its strong mechanical properties, chemical inertness and large surface area, graphene can also be used as supports for catalyst such as metals and metal oxides nanoparticles²⁶ and sensor²⁷ applications. The above-mentioned properties justify graphene to be the “wonder” or “miracle” material.

The unique properties of graphene, as described above, are not only ideal for electronics applications but also can be advantageous for other applications such as biomedical fields, organo, and electrocatalysis.²⁸⁻³⁰ For example, a high theoretical surface area (2630 m²/g for single layer graphene), the ease of surface functionalization, chemical inertness and strong wavelength independent absorption in near infra-red (NIR) properties of graphene are very important for biomedical applications such as drug/gene carrier, targeted delivery, photothermal treatment, photodynamic treatment and bio-imaging applications.^{28, 29} In addition, the large surface area, great mechanical stability, excellent electrical and thermal conductivity properties of graphene are also beneficial in the development of graphene-based catalysts for electrochemical reactions and organic synthesis.^{26, 31, 32} Even though graphene shows great potential for the above biomedical and catalytic applications, pure graphene sheets cannot be used as such for these applications due to some challenges which needed to be overcome. For example, drug delivery and bio-imaging applications require uniform nanosized graphene sheets (lateral size 10-50 nm) with all the intrinsic properties of graphene preserved. Furthermore, the lack of an intrinsic bandgap near to its Fermi level makes the graphene inert and so largely restricts graphene's

potential in imaging and catalysis fields.^{7, 26, 28, 32, 33} But, by controlling the morphology and/or chemical structure of graphene, the physico-chemical properties of graphene can be tuned, which can help in expanding the potential of graphene in various applications. In short, the electronic structure of graphene provides both challenges and opportunities for its potential in catalysis and biomedical field.

In general, the approaches to tune the electronic structures and chemical properties of graphene can be divided into two categories: 1) Controlling the morphologies of graphene such as size and shape of the graphene, number of layers, different edges of the graphene and the presence of vacancy/hole in graphene sheets and 2) Chemical modification of graphene sheets such as insertion of heteroatoms (N, B, S, P, etc.) into graphene's matrix or modification of graphene with different functional groups.³¹ In the following sections, the modern development of these approaches will be summarized.

1.2. Graphene with controlled morphology

1.2.1. The importance of controlling the morphology of graphene sheet.

The synthesis of graphene with controlled morphology is one way to satisfy the need for different applications and thus to expand the graphene's potential in the different field. For example, a graphene sheet with larger lateral size (microns to millimeter) is more suitable for electronics and conductive coating applications, while a nanosized graphene sheet (10-50 nm lateral size) is important for biomedical applications such as delivery vehicle for hydrophobic drugs/genes applications.³⁴ Moreover, the chemical and physical properties of graphene can be tuned by controlling the morphology of graphene such as the size, shape, thickness or number of layer, edges and presence of vacancies in the graphene plane. For example, by decreasing the lateral size of graphene to nanometer range (less

than 10 nm), the electronic confinement effect occurs and opens the bandgap of graphene. The bandgap opening effect depends on the lateral size of the graphene sheet (smaller the size results into larger the bandgap).^{35, 36} It is also reported that nanosized graphene or graphene sheets with holes create more edges, which are more reactive for catalytic applications such as in oxygen reduction reaction in fuel cells.³¹ Furthermore, the presence of holes/vacancies induces additional electronic states and affects the electron transfer rate in graphene.^{37, 38} Moreover, the electron density of states can be strongly enhanced at the edges compared to the plane of graphene and so graphene sheets with different edges (armchair and zigzag edges) (**Figure 1.2.1**) have different electronic structures.^{35, 36, 39} The different types of edges generated by cutting of the graphene, also affects its electronic structure.⁴⁰ For example, zigzag edges in graphene sheet give rise to the magnetism and localized states at the edge site, which is entirely absent in armchair edge and makes graphene more reactive.^{41, 42} In addition, the electronic effect of the zigzag edge becomes more pronounced by decreasing the lateral size of the graphene sheet to a sub-nanometer range. Thus, by controlling the morphology of graphene, one can tune the properties of graphene for desired applications.

In this section, we will focus on properties, applications, and synthesis of nanosized graphene sheets (also known as graphene nanosheets) and holey graphene sheets.

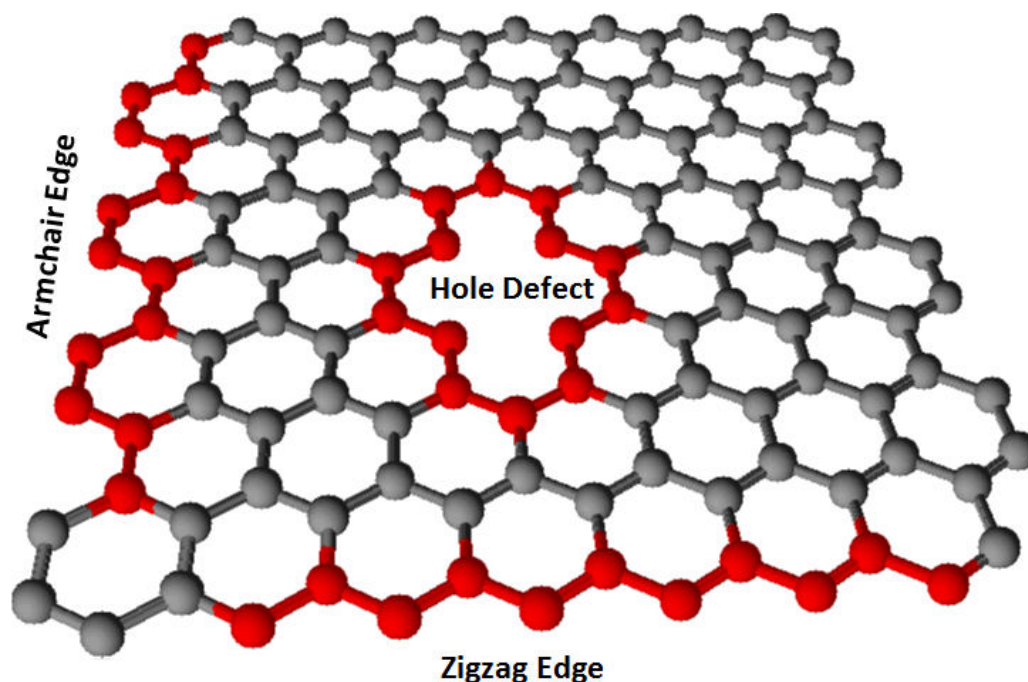


Figure 1.2.1. Schematics of graphene structure with highlighting different type of edge and hole defect. Carbon atoms on the edges are highlighted with red color to differentiate it from bulk C atom (gray color).

1.2.2. Properties and application of graphene nanosheets:

Graphene nanosheets or nano-sized graphene derivatives such as graphene oxide or reduced graphene oxide possess many intrinsic properties of pure graphene, which is important for various biomedical applications. For example, a very large surface area and hydrophobic surface of graphene nanosheets offer high loading and delivery of the aromatic chemotherapy/anti-cancer drug molecules such as doxorubicin⁴³, camptothecin⁴⁴ and SN 38⁴⁵. The surface of graphene nanosheets also provides facile conjugation/functionalization with various targeting ligands (such as an antibody) via covalent (using the presence of oxygen functionalities of graphene's surface) and non-covalent (using hydrophobic interaction) method for target delivery of the anticancer drug³⁴, gene^{44, 46}, other macromolecules,^{28, 29, 47, 48} and even for co-delivering multiple

targeting agents/drug molecules for enhanced or synergistic biomedical effects.⁴⁹ In addition to that, the drug/gene loaded graphene surface can be further functionalized with fluorescent dye for tracking the graphene and its uptake at targeting sites by in vivo fluorescence imaging.⁵⁰ Another important property of graphene is its intrinsic strong and wavelength independent near IR (NIR) absorption property, which has been useful in photothermal treatment of cancer tumors.⁵¹⁻⁵³ The strong NIR absorption properties of graphene and its hydrophobic surface has also been used for a treatment of cancer by the synergistic effect of a drug molecule and photothermal therapy.⁵¹ In addition, nanosized graphene or graphene oxide sheet also shows photo-luminescent properties due to the bandgap opening from size/edge effect or due to the presence of defects,²⁸ thus making possible applications in biological imaging and image-guided therapy.²⁸ Graphene nanosheets have also been useful in the detection of small biological molecules, credited to the intrinsic electronic properties of graphene.²⁹ The graphene's surface is very sensitive to foreign molecules, and its electronic structure largely depends on its interaction with foreign molecules. Based on this principle, it has been used in detection of many biological substances such as oligonucleotides^{54, 55}, pathogens⁵⁶, heavy metal ions⁵⁷, glucose⁵⁸, dopamine⁵⁹, enzymes and proteins⁴⁷ and many others.²⁹

The advance of graphene in biomedical applications makes it necessary to study its long-term fate and toxicity in the human body. Many researchers have tried to study the in vivo toxicity of graphene nanosheets in an animal model and found that the toxicity of graphene mainly depends on the surface functionalization and lateral size of graphene sheets.^{50, 60-62} It was found that functionalization of graphene with biocompatible molecules or polymers such as polyethyleneimine, polyethylene glycol, chitosan, etc.³⁴ renders it non-

toxic. However, graphene sheets with larger lateral sizes (hundreds of nanometers) can dominantly be accumulated in the lung, resulting in toxic effects after its intravenous injection into mice/rats.^{50, 60-62} It was also reported that, if the lateral size of graphene sheets is well controlled to 10-50 nm, the biocompatibility of graphene sheets was dramatically improved, and no visible sign of toxic effects were found in cured mice for 40 days.⁵⁰ Moreover, the radio-isotope labeling of graphene nanosheets shows that the graphene nanosheets (10 to 50nm) were mainly localized in liver and spleen with negligible lung accumulation and gradually were excreted from mice within a few months.^{48, 60}

1.2.3. Synthesis of graphene nanosheets.

In past decade, a tremendous amount of effort has been devoted to developing a straightforward and cheap approach for the large-scale synthesis of graphene nanosheets for biomedical applications. Graphene nanosheets can be synthesized by two general methods, bottom-up approach and top-down approach. In bottom-up approach, graphene nanosheet is synthesized from small carbon molecules (such as methane) by chemical vapor deposition (CVD) or organic chemical synthesis.⁶³⁻⁶⁶ The bottom-up approach gives precise control on the lateral size of graphene but leads to difficulties in scaling up the graphene nanosheets synthesis due to complex handling and high-cost issues. In the top-down approach, firstly, the graphite particles are exfoliated into graphene sheets by mechanical or chemical approaches.⁶⁶ Among them, a chemical approach, especially Hummers or modified Hummers approach, is the most obvious way to exfoliate the graphite particles into graphene oxide in bulk quantity.⁶⁷ In the Hummers or modified Hummers method, the oxidization of graphite powder is performed using the strong oxidant ($\text{KMnO}_4 + \text{NaNO}_3$ in H_2SO_4), which results into heavily oxidized graphene sheets termed

as graphene oxide (GO).⁶⁷ This oxidation reaction is a lengthy process (from hours to several days) and the aggressive oxidation chemistry also leads to uncontrollable cutting of graphene sheets into small pieces of different sizes and shapes with extensive defects.⁶⁸ ⁶⁹ To reach predefined nanometer-sized GO sheets, an extended oxidation and sonication⁷⁰ or other simultaneous oxidative cutting reactions are required.^{71, 72} Alternatively, nanosized GO sheets can also be synthesized using precursors which are already small in lateral sizes such as graphite nanofibers or carbon fibers.^{73, 74} Most importantly, in GO, most of the exotic properties of graphene have vanished due to the high density of oxygen-containing groups that heavily distort and break up the π -conjugated structure. The π -conjugated structure of graphene can be partially recovered in GO by reducing the GO sheets via chemical, electrochemical, or hydrothermal methods.⁷⁵⁻⁸⁰

In Hummers' method, both KMnO_4 and NO_2^+ (nitronium ions) in concentrated H_2SO_4 solutions act as oxidants *via* different oxidation mechanisms. From both experimental observations and theoretical calculations, it appears that KMnO_4 plays a major role in the observed oxidative cutting and unzipping processes. In **Chapter-2**, we find that by intentionally excluding KMnO_4 and exploiting pure nitronium ion oxidation, aided by the unique thermal and kinetic effects induced by microwave heating, graphite particles can be transformed into graphene nanosheets with their π -conjugated aromatic structures and properties largely retained. Unlike GO, the as-fabricated graphene nanosheets exhibit strong absorption in the visible and near-infrared (NIR) regions, which is nearly wavelength independent. This optical property is typical for intrinsic graphene sheets. Moreover, for the first time, we demonstrated that strong photoacoustic signals can be generated from these graphene nanosheets with NIR excitation. The photo-to-acoustic

conversion is weakly dependent on the wavelength of the NIR excitation, which is different from all other NIR photoacoustic contrast agents previously reported. This work has been published in ACS Nano journal (*ACS Nano* 7.9 (2013): 8147-8157) under the title, “Direct production of graphene nanosheets for near infrared photoacoustic imaging”.

1.2.4. Properties and application of porous/holey graphene.

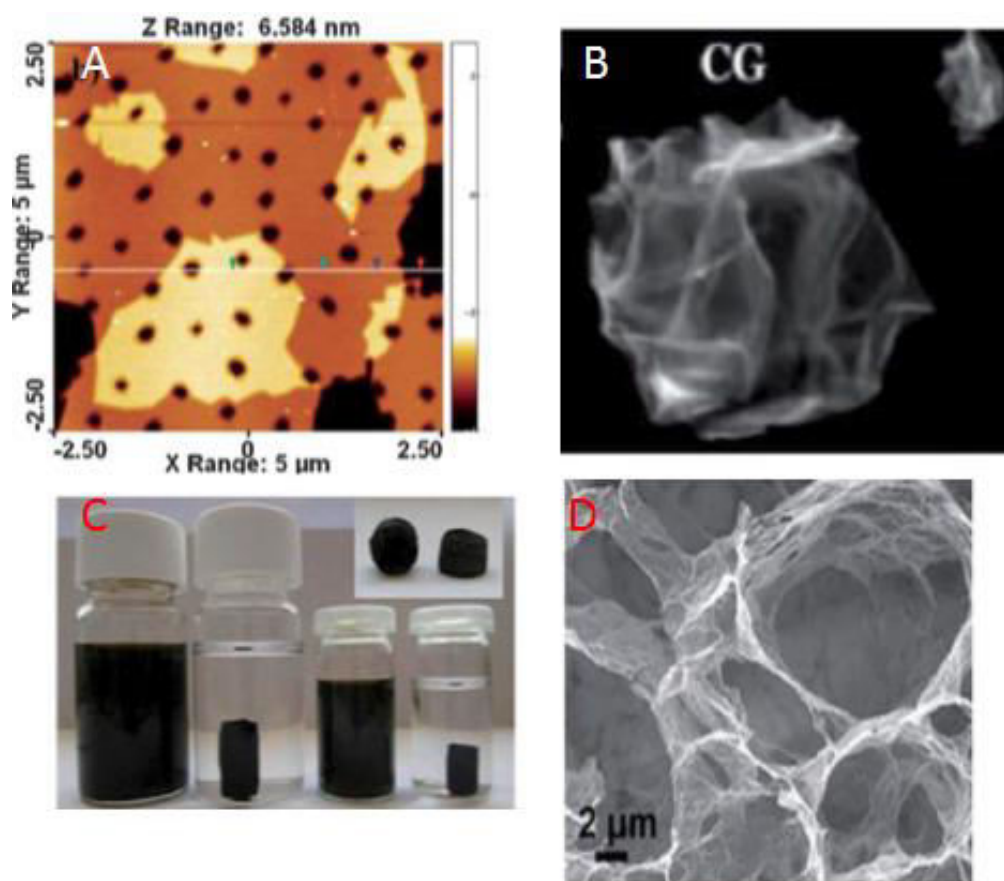


Figure 1.2.2. A) AFM image of holey graphene sheets⁸¹ B) SEM image of Crumpled graphene sheet⁸² C) is a digital photograph and D) SEM image of graphene foam.⁸³

The high surface area of graphene along with its intrinsic properties is a very critical factor for ion/electron/molecule transportation and to make electrochemical devices with optimum performance such as supercapacitors with high energy and power density. However, due to strong $\pi - \pi$ interaction or hydrophobic interaction and van der Waals

interaction between the graphene sheets, it forms irreversible graphite-like agglomerates.⁸⁴ This results in drastic decrease in the surface area of graphene and limits the cross-plane ion diffusion or mass transport of reactants or ions. So, to fully utilize the unique properties of graphene, the morphology of graphene must be tuned such that a high surface area of graphene can be readily accessible without destroying its inherent properties.

Recently, porous graphene materials such as holey graphene or graphene nanomesh (graphene sheets with holes in its basal plane), crumpled graphene (bent or folded graphene sheet) and graphene foam have attracted tremendous research interest due to their high surface area and the presence of porous structure with inherent properties of graphene.⁸⁴ Depending on the size of the pore/hole, these porous materials can be microporous (pore size < 2 nm), mesoporous (2 - 50 nm), and/or macroporous (pore size > 50 nm).^{84, 85} The presence of macroporous structure in crumpled graphene and graphene foam makes it very difficult to gain control of its pore size and volume. Moreover, because of the microporous structure, the surface area of crumpled graphene and graphene foam cannot be achieved near to the theoretical surface area of graphene.⁸⁴ However, the holey graphene (or sometimes called graphene nanomesh) can have microporous or mesoporous structure depending on the experimental synthesis technique.⁸⁴ The presence of porous structure in the graphene sheets not only provides improved transportation of electrolytes and ions but also drastically improves its dispersibility in many solvents.⁸⁴ Because of these unique advantages of holey graphene compared to original graphene sheet, it has dramatically enhanced the performance of electronic and energy storage devices.^{84, 85} For example, Dr. Ruoff demonstrated that by using the holey graphene for a supercapacitor, they can achieve ultra-high energy density (70 W.h.kg^{-1}), power density (250 kW.kg^{-1}) and specific

capacitance to 166 F/g at 5.7 A/g current density).⁸⁶ At the same time, Wang *et al.* reported that by using a porous structure of graphene as an electrode for the lithium-ion battery, it can deliver 116 kW.kg⁻¹ power density and 322 W.h.kg⁻¹ energy density.⁸⁷ Other than its application in energy-related application, the presence of holes/pore in the graphene sheet also opens up graphene's potential in new fields such as gas storage applications⁸⁸, gas separation (such as H₂⁸⁹, He⁹⁰, N₂⁹¹, NO⁹², CO₂⁹³ and CH₄⁹⁴), electrochemical sensors⁹⁵, high oil absorption⁹⁶, catalyst support^{8, 97, 98} and others.⁸⁴

1.2.5. Synthesis of holey graphene sheets.

Many reports were published to synthesize holey graphene and are summarized in **Table 1.2.1**. These synthetic approaches can be divided into two main categories 1) bottom-up approach and 2) top-down approach.

In bottom-up approach, holey graphene sheets are synthesized from small organic molecules, serving as a carbon source and can be grown on the catalytic template/substrate at a high temperature in the presence of inert environment.⁸⁴ The bottom-up approach gives better control on pore size and pore structure by selecting either specific molecule for graphene precursor or catalyst substrate or by process parameters. For instance, Bieri *et al.* have shown that the holey graphene sheet can be synthesized by aryl- aryl coupling of the hexa-iodo-substituted macrocycle cyclohexa-m-phenylene (CHP) molecules in the presence of a silver (Ag) crystal and the hole size can be controlled by the molecular design of the aryl molecule.⁹⁹ At the same time, Ning *et al.* have shown that the holey graphene can be synthesized by growing the graphene on porous MgO template by chemical vapor deposition (CVD) technique and the hole size can be control by selecting the MgO template of varying pore size/structure.¹⁰⁰ The surface area and the pore volume of the holey

graphene, synthesized by the bottom-up approach, can go up to 3300 m²/g and ~2.4 cm³/g.¹⁰¹ Other reports are summarized in the **Table 1.2.1**. Even though these bottom-up approaches gives better control on pore size and structure, it suffers from several disadvantages such as high energy and inert atmosphere requirement, toxic chemicals/precursors, high cost and low production yield.

Recently, many reports have been published to synthesize the holey graphene sheet in a scalable amount from the top-down approach using graphene, graphene oxide (GO) or reduced graphene oxide (rGO) as a starting material. In this method, the holey graphene is synthesized via oxidation or degradation of defects, present on graphene sheets, by using the metal particles¹⁰², chemicals^{86, 103-105}, enzymes¹⁰⁶, photon⁸¹, electron beam¹⁰⁷ or oxygen plasma¹⁰⁸ and other porous template⁸⁷ based etching methods. In the above-listed methods, photo-, electron beam- and plasma etching approaches are environment-friendly because they do not require any toxic chemicals. However, these approaches suffer from a limitation on large scale synthesis, high cost, uncontrollable pore size and its distribution in the holey graphene. The precise control of the size and shape can be achieved by a template-based methods. However, the requirement of complex experimental setup and multiple step procedure impose challenges for the template-based approach. Recently, chemical based etching of graphene/GO/rGO approaches, which involves KOH or HNO₃ activation, are available to synthesize holey graphene in large scale production. Nevertheless, all these top-down approaches requires either graphene/graphene oxide/reduced graphene oxide as a precursor, which adds additional steps to synthesize these precursors for holey graphene fabrication. In summary, these top-down approaches give ease for the large scale synthesis but also impart several challenges such as multiple

steps synthesis, chemical waste and high-cost, along with a lack of control on pore size and shape.⁸⁴

In **Chapter-3**, we have reported that GO with or without holes can be controllably, directly and rapidly (tens of seconds) fabricated from graphite powder via a one-step-one-pot microwave assisted synthesis with a production yield of 120 wt% of graphite. Furthermore, a fast and low-temperature approach is also developed for simultaneous nitrogen (N) doping and reduction of GO sheets. The N-doped holey rGO sheets demonstrated remarkable electro-catalytic capabilities towards electrochemical oxygen reduction reaction (ORR). The existence of the nanoholes not only provides a “short cut” for efficient mass transport but also dramatically increase edges and surface area, therefore, creating more catalytic centers. The capability of rapid fabrication and simultaneous N doping as well as reduction of holey GO can lead us to develop efficient catalysts, which can replace previous coin metals for energy generation and storage, such as fuel cells and metal –air batteries. This work has been published in Small journal (*Small* 11.27 (2015): 3358-3368) under the title “Microwave Enabled One-Pot, One-Step Fabrication and Nitrogen Doping of Holey Graphene Oxide for Catalytic Applications”.

Table 1.2.1. Summary of synthetic approaches for holey graphene.

Ref.	Holey Graphene precursor	Synthetic method	Experimental condition
Bottom Up Approach			
99	hexaiodo-substituted macrocycle cyclohexa-m-phenylene (CHP)	aryl–aryl coupling	aryl–aryl coupling of CHP on the Ag (111) catalyst surface
101	Aromatic poly nitriles (1,2 dicyano benzene)	Polymerization of poly nitriles	1,2 dicyano benzene + 5 mole equivalent anhydrous ZnCl ₂ -

			400 to 700 °C for ~ 20 to 96 hours- in vacuum
109	CH ₄ + H ₂	CVD growth of graphene on SiO ₂ substrate containing porous layer of Au catalyst	Graphene growth by CVD at 950 °C for 10 minutes and removal of metal via acid wash
110	CH ₄ + H ₂	CVD growth of graphene on Cu substrate containing silica sphere on its surface	CVD growth of graphene at 900 to 1000 °C, 30 minutes and removal of silica sphere by HF acid.
100	CH ₄ + H ₂	Porous MgO template	CVD growth of graphene on porous MGO template at 900C, 10min and Etch MgO by HCl
111	Coal tar Pitch	Thermal annealing on Porous MgO sheets template	carbonization at 900°C, 2 hours under N ₂ and removal of MgO by HCl.
Top Down Approach			
112	Graphite	Microwave assisted oxidative etching	HNO ₃ , H ₂ SO ₄ , and KMnO ₄ - 300Watt, 40sec
81	GO on Quartz substrate	Uv assisted etching by ZnO nanorods	Uv (5mW/cm ²) treatment of 10 Hours
107	Multilayered graphene sheets on porous silicon nitride substrate	Electron beam assisted etching	creating holes in graphene by TEM imaging electron beam
113	Graphene film on SiO ₂ substrate	Oxygen plasma-assisted etching of graphene	Step-1: Oxygen plasma etching of polymer from graphene /SiO ₂ / block co-polymer assembly Step-2 CHF ₃ -based reactive-ion etch (RIE) process to remove underlying SiO ₂ Step-3 repeat Oxygen plasma to etch exposed graphene
108	rGO film on PMMA/AAO/SiO ₂	Oxygen plasma assisted etching	Oxygen Plasma (10.5 W, 160 mTorr) for 30 to 120s and etching of AAO/PMMA by NaOH
87	GO film on Nickle (Ni) foam.	Porous template etching	Thermal annealing at 400 °C 2Hr in N ₂ and remove Ni by HCl
114	GO	Chemical etching KMnO ₄	GO + KMnO ₄ - Microwave 5 minute (700Watt)

106	GO	Enzymatic oxidation	GO + Peroxidase + H ₂ O ₂ - Room temp, ~ 8- 10 days.
115	GO	Catalytic oxidation by Au + thermal annealing	GO + albumin, NaOH, gold nanoparticle mixture on PEI-modified quartz- 900 °C 2Hrs in N ₂ and 340 °C, 2Hr in air
102	Graphene	Catalytic oxidation by Ag nanoparticles	Thermal annealing at 250°C to 400 °C- 1Hr and remove Ag particles by HNO ₃
116	GO	Steam etching	Water- 200°C for 5 to 20Hours.
104	GO	Chemical oxidative etching by HNO ₃	GO + Fuming HNO ₃ -1 Hour- Bath sonication (100 W, 50/60 Hz).
105	rGO	Chemical oxidative etching by HNO ₃	GO +HNO ₃ - reflux at 100°C, 4-11 hour
117	rGO	Activation by CO ₂ /Thermal treatment	Thermal annealing of GO under CO ₂ -800°C for 25 to 75 min
103	GO	KOH activation by Hydrothermal+ thermal treatment	GO +Biomass(PVA/resin), KOH, Ar gas- Hydrothermal180°C, 12 Hour + thermal annealing 800°C for 1hour
86	rGO	KOH activation etching by thermal annealing	KOH, Ar Gas +vacuum 800°C, 3 Hour (1 in Ar and 2 in vacuum)
87	GO	Mesoporous Ni substrate based	GO deposited on Ni foam- thermal annealing 400°C 2Hr and 800°C 2Hr

1.3. Chemical modification of graphene.

Other than morphological control in graphene, the electronic structure of graphene can also be tuned by either introducing heteroatom dopants such as nitrogen (N), boron (B), phosphorus (P), sulfur (S) and others into the graphene matrix¹¹⁸ or by modifying the graphene surface with different functional groups such as oxygen and halogen containing functional groups.¹¹⁹ Out of these, the heteroatom doping is the most efficient way of tuning the graphene's properties, and this will be discussed in detail.

1.3.1. The Importance of heteroatoms doped graphene and its application.

It is reported that the heteroatom doping into graphene matrix opens up the bandgap by increasing the density of states near to the Fermi level of graphene. An increase in the density of states (especially around the Fermi energy) usually results in the enhanced catalytic activity of the material.¹¹⁸ In addition to that, it also augments some new properties like spin density and/or charge density and magnetic moments into graphene. These electronic, magnetic and physico-chemical properties of the doped graphene mostly depend on the heteroatom's unique electronic properties, atomic size, and the type of doping configuration.

The most commonly studied heteroatoms are N and B atoms due to their similar atomic size with C atom, which helps them to dope easily into the graphene matrix without destroying the planar structure of graphene.¹¹⁸ However, the properties of B-doped and N-doped graphene are very different due to their different electronegativity. In B-doped graphene, electron transfer happened from B to C due to the lower electronegativity of B (2.04) than C (2.55). This will result in a generation of partial positive charge on B atom, which becomes the active centers for the catalytic activity.¹²⁰ Moreover the B-doping in graphene results in p-type doping with the bandgap opening of ~ 0.14 eV (at 2 atomic % doping), which transforms the semi-metallic behavior of graphene to semiconductor.^{121, 122} It is also reported that, unlike N-doping, B-doping into graphene cannot induce localized states, and thus magnetism.¹²³ On the other hand, in the case of N-doped graphene, N can be doped into graphene with three different configurations, graphitic (or quaternary)-N, pyridinic-N and pyrrolic-N as shown in **Figure 1.3.1**. The polarity of N-C bond have reverse polarity than that of B-C bond due to higher electronegativity of N (3.04) than C.

This leads to the transfer of the electron from C to N atom and generate the positive on C atom adjacent to N dopant and so C atom (adjacent to N dopant) is considered to be the active site for catalytic reaction.¹²⁴ Moreover, N doping also opens up a bandgap of graphene and imparting it with semiconductor properties. However, the semiconductor properties of N-doped graphene largely depends on the type of N doping configuration.¹²⁵ For example, in graphitic N, the fifth electron of N is involved in the π^* state of conductance and resulting into n-type doping effect due to its electron donating effect.¹²⁶ However, the pyridinic and pyrrolic type of N doping impose the p-type doping effect in graphene due to their electron withdrawing effect.¹²⁷ Recently it is also reported that, unlike pyridinic and pyrrolic N, graphitic N doping can result in lowering the work function of graphene, which is very useful for organic field effect transistors (OFETs) and light emitting diodes (LEDs).¹²⁸ Furthermore, it is also reported that pyrrolic N can create the strong magnetic moments ($0.32\mu_B$) in graphene due to the formation of π and π^* states by a nonbonding electron of pyrrolic N, which leads to spin polarization in graphene and can be used in spintronic applications.¹²⁹ This type of magnetic effects cannot be achieved by the graphitic type of N doping due to lack of nonbonding electrons on N atom. In addition to the above electronic and magnetic properties, N doping into graphene nanosheets can also tailor its optical properties by making graphene photo luminescent.¹³⁰

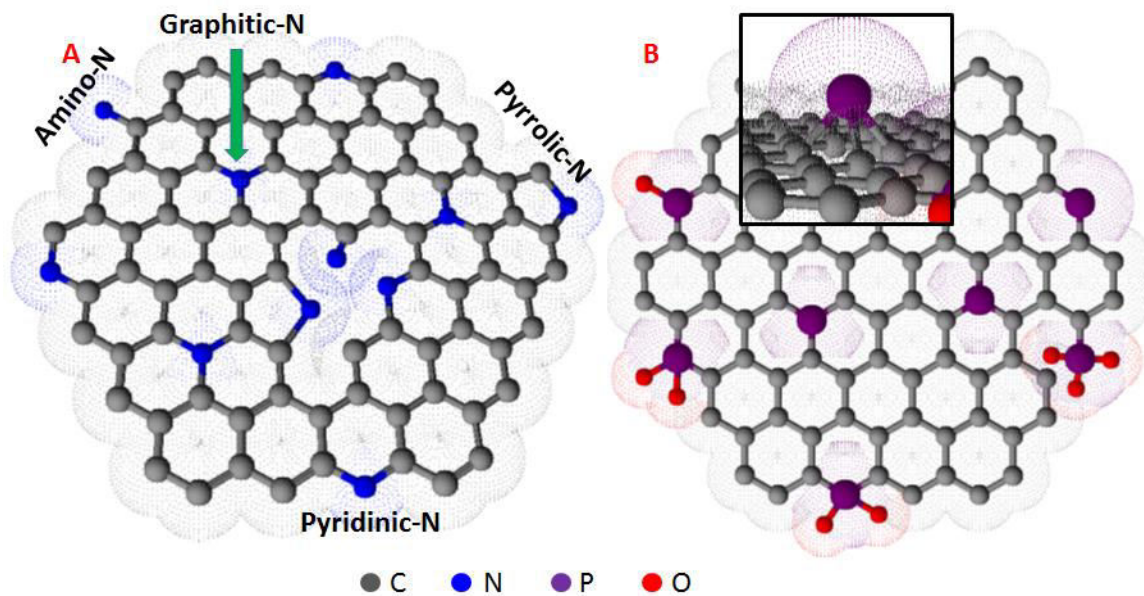


Figure 1.3.1. The schematic for N-doped graphene (A) and P-doped graphene (B) with different dopant configurations. Inset of (B) is showing the side view of P-doped graphene to show that P atom is protruding out of graphene plane.

Recently, besides N and B dopants, other heteroatoms such as P and S have also received great attention in doping due to their unique properties, which are different than N and B dopants^{120, 131}. Unlike N and B, the P doping in the graphene creates the structural distortion and local curvature due to the larger atomic size of P than C atom and also greater C-P bond length (1.77 Å) than C-C bond (1.40 Å). P doping into graphene transforms the sp^2 hybridized C to sp^3 state at the dopant site, which results in the pyramidal type bonding configuration of P with three C atoms, where P is protruding out of the graphene plane by 1.33 Å. A theoretical calculation shows that the bandgap opening in P-doped graphene is dependent on the P doping level (~0.3 to 0.4 eV for 0.5 atomic % P-doping).¹³² Moreover unlike N doping, the polarity of P-C bond is similar to B-C bond but opposite then that of C-N bond due to the lower electronegativity of P (2.19) than C atom (2.55). In addition to that, P-doping results in stronger n-type behavior, and a much strong magnetic moment (1.02 μ_B) than N doping due to the breaking of the symmetry of the P-doped graphene's π -

electron framework.^{133, 134} In addition to above effects, the distinct effect from P doping may also arise due to presence of additional phosphorus's p orbital.¹¹⁸

The doping of S into graphene matrix also results in the formation of local curvature due to the larger atomic size of S than C atom and larger C-S bond length (1.78 Å) than C-C bond (1.40 Å). Similar to other heteroatoms, Sulfur doping into graphene can result in different doping configurations such as C-S-C, C-S(O)_x-C, C-S(O)_x (where x = 2,3 or 4) and C-SH. However, unlike other heteroatoms (such as B, N, and P), S doping cannot induce polarity or charge transfer in C-S bond due to the similar electronegativity of S (2.58) and C atom (2.55). But at the same time, S doping into graphene induces a non-uniform spin density due to mismatch of the outermost orbitals of C and S, which is thought to play a vital role in many catalytic applications of S-doped graphene such as in ORR.^{131, 135} Besides, P and S, recently, other heteroatoms such as Se¹³⁶, Si¹³⁷ and Sb (antimony)¹³⁸ doped graphene are also reported for its catalytic applications but the properties of those heteroatom-doped graphene remains largely unexplored.¹³⁹

1.3.2. Synthesis of heteroatom-doped graphene/carbon.

The synthetic approaches for heteroatom-doped graphene can be divided into two categories: post-treatment synthesis and direct synthesis (also known as in-situ or bottom-up approach). Both approaches are summarized in **Table 1.3.1**.

Post-treatment synthesis approach

In this approach, heteroatom-doped graphene is synthesized by thermal heat treatment of graphene materials such as single or few-layer graphene/graphene oxide/reduced graphene oxide with a heteroatom source. This method is named as a post

treatment synthesis approach because the carbon source needs to be synthesized in the first step and then used for the synthesis of heteroatom-doped graphene. It is reported that the presence of defects and oxygen functionality in the carbon source is playing a major role in doping of the heteroatom into graphene. As a result, the heteroatom doping content is low if the graphene or graphite, which have fewer defects and oxygen functionalities, is used as a carbon source.³⁰ Apart from graphene, graphene oxide is the most widely used precursor of carbon due to the presence of abundant oxygen functionalities and defects which help in the heteroatom doping in an efficient way. The control of doping level and doping configuration of heteroatom dopant in the graphene plane can be controlled by varying different precursors, thermal annealing temperature and time, and the mass ratio of graphene oxide with heteroatom precursor.³⁰ For example, it is reported that by heating GO with melamine, ~10 atomic % N can be doped in N-doped graphene.¹⁴⁰ But by using ammonia as a N precursor, N-doping content is decreased to 5 atomic %.¹⁴¹ For sulfur doped graphene synthesis, a mixture of graphene oxide and benzyl disulfide (BDS) is thermally annealed at high temperature under argon environment.¹³¹ The thermal annealing not only helps in heteroatom doping into graphene structure but also helps in reducing the graphene oxide (due to the high annealing temperature ~ 700 to 1000 °C) to restore the intrinsic properties of graphene partially in the heteroatom-doped graphene. Other than thermal annealing, plasma treatment has also been used to synthesize heteroatom-doped graphene such as N-doped graphene by treating GO/graphene with nitrogen plasma or NH₃ plasma. In this approach, even by using graphene as a carbon source, it results in high atomic heteroatom doping (such as 8.5 atomic % N¹⁴²) because plasma treatment not only helps into N doping but also create the defects and oxygen functionalities into graphene.¹⁴³

Recently, the use of strong reducing agents such as N_2H_4 has been used as a doping agent for the synthesis of N-doped graphene at relatively low temperature (80 to 160 °C).¹⁴⁴ The post treatment approach often results into agglomeration or restacking of graphene sheets and thus decreases the specific surface area of the resultant heteroatom-doped graphene due to the reduction of graphene sheet at high temperature.¹⁴⁵ This problem can be solved by using holey GO as the starting graphene source in heteroatom-doped graphene due to its unique advantages as described in holey graphene section.

Direct Synthesis Approach

The direct synthesis approach is a type of bottom-up approach where small molecules of carbon source and heteroatom source are mixed and heated together at high temperature by different heating approaches such as chemical vapor deposition (CVD), solvothermal approach, arc discharge approach and microwave approach. In CVD approach, a carbon and heteroatom precursor (usually gas form) are heated at high temperature in the presence of a metal substrate, typically Cu or Ni^{146, 147} in the inert environment. The CVD method usually results in single or few layer of heteroatom-doped graphene. Moreover, in CVD approach, the heteroatom doping level can be adjusted by controlling the flow rate of heteroatom precursor gas or pre-set ratio of carbon and heteroatom source. While the doping configuration of heteroatom can be controlled by varying the growth temperature and/or by changing the carbon/heteroatom source and/or even by selecting appropriate metal substrate.³⁰ For example, It has been reported that by heating the CH_4/NH_3 (1:1) precursor on Cu substrate yields N-doped graphene with mainly graphitic N doping type, while on Ni substrate, pyridinic and pyrrolic type of N doping become prominent.¹⁴⁷ At the same time it is also reported that by changing the C source to

C_2H_4 while keeping Cu as the catalyst, pyridinic-N becomes more prominent.¹⁴⁸ Even though, this CVD approach mostly results in high quality of graphene, the complex operational procedure, the requirement of an inert environment, use of toxic chemicals along with high energy demand makes this approach non-scalable, time-consuming and costly, and hence makes this approach not suitable to synthesize cheap carbon-based catalysts for catalytic applications. Other than CVD approach, segregation growth approach and Arc discharge approach are also reported but face similar problems as CVD approach. Recently, gram scale synthesis of heteroatom-doped graphene is reported by the solvothermal approach. For example, N-doped graphene can be synthesized by heating a mixture of lithium nitride with tetrachloromethane at 300 °C.¹⁴⁹ However, it is still in development phase and also requires relatively high temperature and pressure for synthesis, which raises concern for safety and cost of the catalyst. To solve the above problems, recently, heating the biomass molecules (such as glucose, fructose, alginate and tannic acid) with a heteroatom source by thermal annealing are reported.¹⁵⁰⁻¹⁵² These methods result in the fabrication of heteroatom-doped porous graphene-like carbon materials. These materials are catalytically active due to the presence of graphene-like domains along with heteroatom doping. In addition, the porous structure of this heteroatom-doped carbon material can provide a larger surface area, easy access to the active sites and better mass transport for catalytic applications. Even though these porous heteroatom-doped carbon materials are synthesized from cheap biomass, it still requires very long synthesis time (hours), inert environment and high temperature to afford stable materials with the desired performance. This phenomenon deviates from the original concept of energy saving and sustainability. To avoid the problems mentioned above, recently, the use of microwave

(MW) heating instead of traditional annealing is reported to synthesize heteroatom-doped porous carbon materials rapidly. However, in these reported approaches, either pre-heating of the reaction mixture (carbon source and heteroatom source) by thermal treatment or addition of MW absorbing materials (such as mineral oxides or polyphosphoric acid) is required because of weak MW absorbing capacity of the biomass molecules.¹⁵³⁻¹⁵⁵ However, these microwave-absorbing materials may introduce unintentional contaminations to the obtained carbon materials, which is not desirable for catalytic applications in organic synthesis. Therefore, choosing the right microwave-adsorbing biomass material is important to avoid this problem.

In chapter-4, an incredibly simple and rapid (40 seconds) microwave-assisted carbonization approach is reported to directly synthesize gram quantities of P-doped graphitic porous carbon materials from the anti-nutrient compound, phytic acid. Phytic acid strongly absorbs microwave energy and hence the as-purchased phytic acid solution can be directly used for the fabrication of P-doped graphitic carbon product (PGc) with microwave energy without the requirement of preheating, drying treatment and without adding additional microwave absorber. Moreover, by just changing the microwave irradiation time, PGc with different P bond configurations were fabricated, as determined by combined FTIR and X-ray photoelectron spectroscopy (XPS). Using microwave heating instead of traditional heating ensures that this approach is both sustainable and energy efficient. Furthermore, the fabrication can be performed under ambient conditions without the requirements of an inert environment, which makes this approach, even more, cost efficient and convenient.

In **chapter-5**, we have demonstrated that the above microwave-assisted carbonization approach can be extended to fabricate co-doped carbon catalysts such as P-N, P-S, P-Si, and P-B co-doped carbon materials, by simply adding a suitable dopant precursor into phytic acid solution prior to microwave irradiation. In addition to that we have also demonstrated that by changing the carbon resource to inositol (a biomass compound similar to phytic acid but without the phosphate arms), and using H₂SO₄ as a microwave absorber and dehydrating agent, carbon materials without doping or sole doping with one type of heteroatom were successfully fabricated.

Table 1.3.1. Summary of synthetic approaches for heteroatom doping into graphene /carbon matrix.

No .	Carbon Source	Heteroatom Source	Synthetic Method	Experimental condition	Atomic % doping
Post treatment synthesis approaches					
1	GO ^{131, 140, 156-159} rGO ^{160, 161} Graphite ¹⁶²	BCl ₃ ¹⁶⁰ , NH ₃ ^{156, 157, 159, 160} , melamine ¹⁴⁰ , H ₂ S ¹⁵⁹ , ionic liquid ^{158, 162} , N ₂ plasma ¹⁶¹ , benzyl disulfide ¹³¹	Thermal Annealing	(550 - 1100 °C, 0.5 to 2 h) ^{131, 156-160} , (15V, 3Hrs, 400°C, 4Hrs) ¹⁶²	N: 2.4 - 10% ^{140, 156, 159-161} P: 1.16% ¹⁵⁸ S: 0.5–1.7% ^{131, 159}
2	GO ^{112, 163-165}	Cyanamide ¹⁶³ , B ₂ O ₃ ¹⁶³ NH ₄ OH ^{112, 165} Pyroll ¹⁶⁴	Microwave heating	1h microwave + 900°C, 30min ¹⁶³ 120°C, 5 to 30 min ¹¹² 800W, 1 to 8 min ¹⁶⁵	N: 1.7 – 10.5% ^{112, 163-165} B: 3.9% ¹⁶³

				150Watt, 2 - 10 min ¹⁶⁴	
3	graphene ¹⁶⁶ CCl ₄ ¹⁴⁹ GO ¹⁶⁷⁻¹⁶⁹	BBr ₃ +K ¹⁶⁶ Lithium nitride ¹⁴⁹ Hydrazine ¹⁶⁷ , Urea ¹⁶⁸ , NH ₄ SCN ¹⁶⁹	Wet Chemical method	150–210 °C, 10–30 min ¹⁶⁶ , 350°C, 6 Hrs ¹⁴⁹ , 50°C, 24 h ¹⁶⁷ , 180 °C for 12 h ¹⁶⁸ , 180°C, 10 h ¹⁶⁹	N: 4 to 10% ^{149, 168, 169} B: 1.02% ¹⁶⁶ S: 4 - 18wt% ¹⁶⁹
4	graphite ¹⁷⁰⁻¹⁷²	N ₂ ¹⁷⁰ sulfur ¹⁷¹ B ₂ H ₆ ¹⁷² pyridine ¹⁷²	Ball Milling ^{170, 171} Arc discharge ¹⁷²	500rpm 48Hrs ^{170, 171}	N: ~13% ¹⁷⁰ , 0.6-1.4% ¹⁷² S: ~7.4% ¹⁷¹ B: 1.2 - 3.1% ¹⁷²
Bottom up/in situ treatment/direct synthesis approaches					
5	CH ₄ ^{146, 173} , polystyrene ¹⁷⁴ , phenylboronic acid ¹⁷⁵ , hexane ¹⁷⁶ , pyrimidine ¹⁷⁷ , thiophene ¹⁷⁷ ethylene ¹⁴⁸	H ₃ NBH ₃ ¹⁷³ , NH ₃ ^{146, 148} , Urea ¹⁷⁴ , Boric acid ¹⁷⁴ phenylboronic acid ¹⁷⁵ sulfur ¹⁷⁶ pyrimidine ¹⁷⁷ thiophene ¹⁷⁷	CVD	700 – 1100 °C, 10 - 40 min ^{146, 148, 173-176}	N: 0.9 - 5% ¹⁷⁴ , 4 -10% ^{146, 177} B: 0.7- 4.3% ¹⁷⁴ S: 0.6 - 3.2% ^{176, 177}
6	Dicyandiamide ^{178, 179}	Dicyandiamide ¹⁷⁸	Thermal Annealing	800 - 900°C for 2 to 6 h ^{150-152, 178, 179}	N: 3.6 - 9.1% ^{178, 179}

	Alginate ¹⁵⁰ Fruit stone/styrene based copolymer ¹⁵¹ resourcinol ¹⁵²	Boric acid ^{152, 178} Phosphoric acid ^{150-152, 178, 179}			B: 0.2 - 4.3% ^{152, 178} P: 0.6 - 2.8% ^{152, 178, 179}
7	Tannin ^{153, 154} Phytic acid ^{180, 181} Inositol ³⁶	Melamine + polyphosphoric acid ¹⁵³ Silicone + polyphosphoric acid ¹⁵⁴ Phytic acid ^{180, 181} , sulfur ³⁶ , boric acid ³⁶ , NH ₄ OH ³⁶	Microwave heating	1250Watt, 30min ^{153, 154} 1100Watt, 40 to 150s ^{180, 181}	N: 2 - 8.3% ¹⁵³³⁶ P: 3 - 6.6% ^{153, 154, 180, 181} Si: 8.8% ³⁵³⁶ B: 8.3% ³⁶ S: 2.6 - 6% ³⁶

1.3.3. Catalytic applications of heteroatom-doped graphene/carbon material.

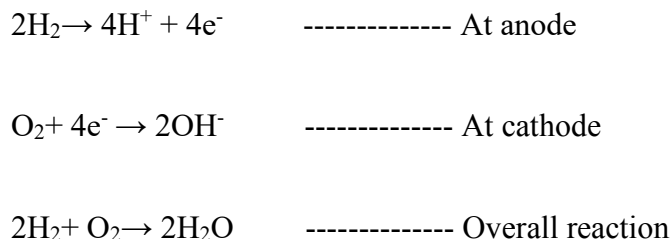
Catalysts play an imperative role in our life by accelerating the reactions to satisfy essentials such as in pharmaceutical chemicals, fuel, oil refineries, energy storage, batteries and much more.¹⁸²⁻¹⁸⁵ But most of the catalysts are based on precious rare earth metals such as Pd, Pt, Au, etc. These precious metals are not only expensive but are also toxic to human health and environment and require additional cost to handle, destroy or to dispose of them.^{145, 183, 186} These drawbacks suggest an urgent need for metal-free catalysts which are cheap, environmentally friendly, sustainable and highly efficient in catalytic performance. Out of all other carbon allotropes, graphene possesses many unique properties which are suitable for an ideal metal-free catalyst. For example, graphene has a very high theoretical surface area (2630 m²/g) which is double that of single walled carbon nanotubes and much

greater than carbon black and activated carbon.¹⁴⁵ Moreover, graphene also has a highly conjugated structure which can promote the unique substrate-substrate interaction during catalytic reactions. Another reason is that the structure of graphene and its electronic properties can be easily tuned based on their specific applications. Moreover, unlike carbon nanotubes, graphene-based materials have evitable metal impurities and so graphene purely catalyzes catalytic performance rather than metal contaminants.¹⁴⁵ In addition to that, the superior electronic and thermal conductivity can facilitate the heat and electron transfer easily on its surface during the catalytic reaction. Last but not least, the strong mechanical properties, thermal and chemical stability ensure its long lifetime in catalytic fields. Since the last decade, graphene or chemically modified graphene have shown promising catalytic performance in the different catalytic applications, which includes energy-related devices such as fuel cells^{147, 183, 187-189}, solar cells¹⁹⁰, water splitting¹⁵⁰, organic synthesis¹⁸⁶, photochemical reactions¹⁹¹, electrochemical sensors^{142, 143, 190, 192-194} and environmental protections. Herein we will mainly focus on catalytic applications in fuel cell and organic synthesis.

1.3.3.1. Carbon-based Catalysts in Fuel Cells.

A fuel cell is a type of electrochemical energy conversion device that generates the clean energy by converting the chemical energy from the fuel, where fuel is oxidized at the anode, and simultaneously oxygen is being reduced at the cathode to generate electricity.¹⁹⁵ In the typical fuel cells, hydrogen or methanol, is used as a fuel source and oxygen as an oxidant. At the anode, a catalyst oxidizes the fuel (usually hydrogen or methanol) to a positively charged proton/ CO₂ (if methanol is used as a fuel source) and negatively charged electron. The proton ion moves to the cathode through electrolyte where it reacts

with oxygen to reduce it to water. The equations for hydrogen/oxygen type fuel cells are written as follow.



Out of both reactions, oxygen reduction reaction (ORR) ($E^0 = 1.23 \text{ V}$) is more energy extensive than hydrogen oxidation reaction ($E^0 = 0.00 \text{ V}$), and expensive Pt-based catalysts usually catalyze these reactions. However, commercialization of Pt catalyst in fuel cells are limited due to its limited reserves, high cost, agglomerations, instability in the presence of methanol or CO and time-dependent drift.¹⁹⁶ To promote the large-scale commercialization of fuel cells in our daily life, the precious metal based catalyst should be replaced with other cheap and sustainable nonmetal based catalysts. Recent studies have proven that the heteroatoms (N, B, S, P or Se) doped carbon catalysts shows excellent electrocatalytic performance for ORR and become a potential candidate for replacing Pt-based catalysts.³² Due to low cost, excellent durability and environment friendliness of heteroatom-doped carbon catalysts, they are considered as a great candidate for replacement of Pt-based catalysts.

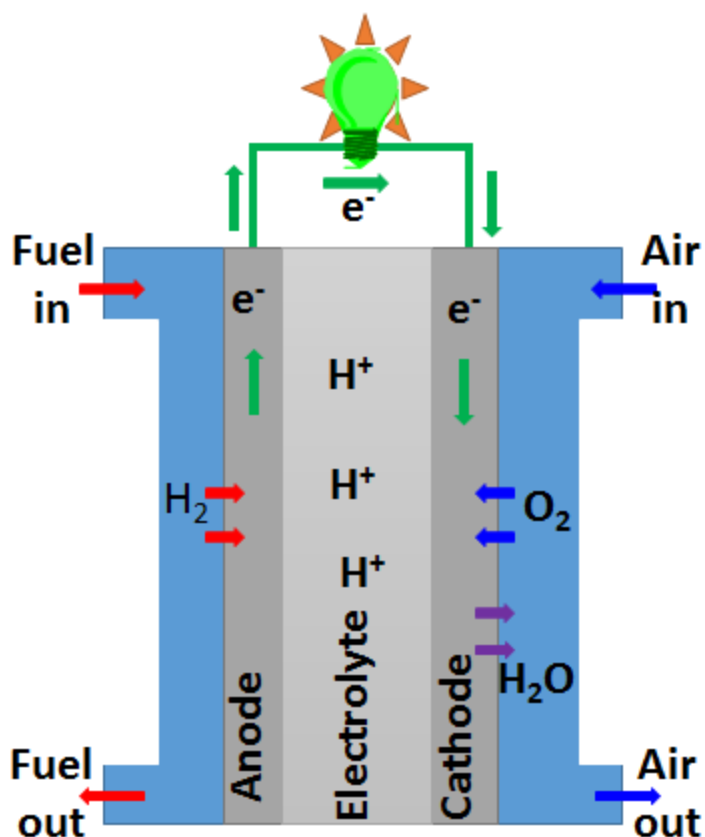


Figure 1.3.2. Schematics of Fuel cell design.

The ORR can occur via two different pathways. One involves four-electron pathway where oxygen is reduced to water or OH^- depending on the acidic or basic environments. Another pathway involves two-electron pathway where oxygen is first partially reduced to H_2O_2 or OOH^- depending on the acidic or basic environments. For fuel cell applications, the four-electron pathway is more preferred to avoid any safety issue and toxic effects of peroxides. It is reported that pristine graphene catalyzes the oxygen reduction reaction by the two-electron pathway, while by inserting the heteroatoms into graphene, it follows the direct four-electron pathway. Mostly, all types of heteroatoms (B, N, P, S, etc.) doped carbon catalysts are capable of catalyzing ORR in the fuel cell with similar or slightly better catalytic performance than Pt-based catalysts.^{32, 147, 197, 198}

However, the ORR performance of heteroatom-doped carbon primarily depends on the type of dopant configuration while the mechanism of ORR in different heteroatom-doped carbon depends on the unique electronic properties of heteroatoms dopant configuration.¹⁹⁸ For example, some research groups reported that the better ORR performance in N-doped graphene is mainly attributed to the pyridinic-N, which introduces the high positive spin density and asymmetric atomic charge density into graphene,^{140, 157, 187, 189, 199} Whereas others found that graphitic-N plays a crucial role in ORR $4e^-$ pathway by decreasing the energy cost at the intermediate steps of ORR. In the latter case, the carbon atom adjacent to the graphitic-N is considered to act as a catalytic active center.^{197, 200-202} In short, the mechanism of ORR on these N-doped carbon catalysts is not clearly understood and still in debate.¹⁹⁸ In the case of B-doped graphene, B plays crucial role in adsorption of O_2 and OOH^- either due to its strong electron withdrawing property or due to the formation of partial positive charge (because of smaller electronegativity of B than C).^{172, 203} Other than N and B, P and S-doped carbon catalysts have also been studied for ORR. However, there are few results reported. This may be because of the difficulty in doping of P and S due to their relatively large atomic size compared to C atom.¹⁹⁸ In S-doped graphene, S can be doped in two forms- reduced S (or sulfide S) and oxidized S. Both types of doped S can catalyze ORR by introducing the electronic spin density in graphene matrix due to mismatch of the outer shell of S and C atoms.^{32, 145, 188} P-doped graphene is also able to catalyze the ORR by introducing the larger band gap energy into graphene.²⁰ Other than the type of the heteroatom dopant, the amount of heteroatom doping is also playing an important role. For example, one study suggests that N-doped graphene with 16 atomic %

of N doping shows poorer ORR activity than the one having 2 atomic % of N doping. This may be due to high affinity of oxygen to N which may poison the ORR active center.²⁰⁴

Other than individual heteroatom-doped graphene, co-doping of different heteroatoms together in the graphene/carbon matrix is also reported to create special synergistic effects from multiple heteroatom doping. For example, theoretical and experimental results show that by co-doping B and N into graphene matrix, whose electronegativity is lower and higher than C atom, respectively, can result in enhanced ORR catalytic performance.²⁰⁵ similar to that, S, N-codoped graphene and P, N-codoped graphene also shows improved ORR catalytic performance due to a synergistic effect by the enhancement of spin density attained by multiple heteroatom co-doping.^{177, 206} However, the detailed mechanistic study about the co-doping effect is in the primary stage and needs extensive experiments to understand the effect of co-dopant in graphene.

1.3.3.2. Carbon-based catalysts in organic synthesis.

In the past few years, the carbon-based material has also attracted growing interest in the organic synthesis of valuable chemicals due to their several advantages over the traditional transition/noble metal based catalysts.²⁰⁷ For example, carbon-based catalysts are sustainable, cheap, and can be synthesized from biomass material. In addition to that, the existence of giant π structures and feasibility of tuning the physicochemical and electronic properties of carbon materials gives the advantage to promote the interaction of various organic reactant on the surface of carbon materials.

A majority of the research has been focused on graphene oxide (GO), possibly due to its easy availability and large scale synthesis.²⁰⁸⁻²¹⁰ GO is the oxidized form of graphene sheet which can be synthesized in large scale by exfoliation of graphite in the presence of

strong oxidant in acidic media.²¹¹ GO contains a high density of oxygen functionalities such as epoxide, hydroxyl, ketones and carboxylic groups on its surface, which makes GO easy to disperse in many aqueous and organic solvents.²⁰⁷ The first example of a carbon-based material for metal-free catalyst in organic synthesis was reported by Bielawski and coworkers, where they reported that GO can catalyze the oxidation of alcohols and the hydration of various alkynes under a relatively mild condition with high selectivity to aldehydes/ketones.²¹² In addition to that, Bielawski and coworkers have further explored the catalytic role of GO for different organic reactions such as oxidation of sulfides and thiols,²¹³ C–H oxidation²¹⁴ and Claisen–Schmidt condensation²¹⁵. After these great results, other researchers have also explored the applications of GO catalyst in the various organic synthesis such as photocatalytic oxidative C–H functionalization of tertiary amines to generate imines²¹⁶, oxidation coupling of amines to imines^{114, 217}, aerobic oxidation of SO₂²¹⁸, ring opening of epoxides²¹⁹, acetalization of aldehydes²²⁰, aza-Michael addition of amines to activated alkenes²²¹, Friedel–Crafts addition of indoles to α , β -unsaturated ketones²²², Friedel–Crafts alkylation of arenes with styrenes and alcohols²²³ and oxidative dehydrogenation of propane²²⁴ and isobutane²²⁵. In addition, GO modified with other functional groups can further extend its catalytic application in organic synthesis. For example, GO modified with abundant carboxylic groups can mimic the catalytic activity similar to that of natural horseradish peroxidase.⁵⁸

In all the above applications, the role of the oxygen containing functionalities is proved to be crucial in catalytic applications.²⁰⁷ Some of these functionalities such as hydroxyl and epoxide are not stable at high temperature and so during many catalytic reactions, GO would undergo partial reduction during the catalytic conversion.³² And at

the same time the catalytic activity of GO is also decreased during the recycling/reuse of GO catalyst in catalytic reactions due to loss of oxygen functionalities, which were playing an important catalytic role in GO.^{32, 226, 227} So the biggest problem in GO-based catalyst is its stability and reusability.²⁰⁷

Due to interesting catalytic applications of GO in the organic reactions, recently, other carbon materials such as N-doped and/or co-doped with other heteroatoms (B, S) carbon materials have also been explored for their catalytic ability in organic syntheses such as for C-H activation^{186, 228} and aerobic alcohol oxidation²²⁹⁻²³¹, epoxidation of trans-stilbene and styrene^{186, 232}, reduction of nitro compounds such as nitrophenols²³³ and nitrotoluene²³⁴. Among three types of nitrogen species doped into the graphene lattice, pyridinic-N, pyrrolic-N, and graphitic-N, the graphitic sp^2 N species were reported to be important for the observed catalytic performance in oxidation reactions,^{228, 230} while pyridinic-N was found to be playing a crucial role in catalyzing reduction reaction such as reduction of nitro compounds.^{194, 234} However, it was also reported that due to the planar structure of graphitic sp^2 N, it brings difficulties in overcoming substrate steric hindrance effects and leads to the problem in oxidizing secondary benzylic alcohol.^{139, 229} Compared to GO-based catalysts, the use of heteroatom-doped carbon catalysts in organic reactions are in a very early stage.²⁰⁷ Especially, the potential of other heteroatom-doped carbon such as P and S-doped or codoped carbon catalysts are still yet to be explored in the field of organic reaction catalysis.

In chapter- 4, for the first time, we have demonstrated that the P-doped carbon materials can be used as a selective metal-free catalyst for aerobic oxidation reactions. The work function of P-doped carbon materials, its connectivity to the P bond configuration,

and the correlation with its catalytic efficiency are studied and established. In direct contrast to N-doped graphene, the P-doped carbon materials with higher work function show high activity in catalytic aerobic oxidation. The selectivity trend for the electron donating and withdrawing properties of the functional groups attached to the aromatic ring of benzyl alcohols is also different from other metal-free carbon-based catalysts. A unique catalytic mechanism is demonstrated, which differs from both GO and N-doped graphene obtained by high-temperature nitrification. The unique and unexpected catalytic pathway endows that P-doped carbon materials exhibit not only good catalytic efficiency but also recyclability. This, combined with a rapid, energy saving approach that permits fabrication on a large scale, suggests that the P-doped porous materials are promising materials for “green catalysis” due to their higher theoretical surface area, sustainability, environmental friendliness and low cost. This work has been published in ACS Nano journal (*ACS Nano* **2016** *10* (2), 2305-2315) title as “P-Doped Porous Carbon as Metal Free Catalysts for Selective Aerobic Oxidation with an Unexpected Mechanism”.

In **chapter-5**, the electrocatalytic performance of P-doped carbon material in oxygen reduction reaction (ORR) was carefully studied. The correlation between their ORR performance, aerobic catalytic performance, and the P bond configuration in their carbon matrix was revealed. It was found that the PGc catalyst with prominent P-C bonding, which exhibits inferior aerobic oxidation, is more facile to kinetically catalyze the ORR via a four-electron pathway. Whereas, the PGc with P-O bonding exhibits the reverse phenomenon (two-electron pathway in ORR and superior aerobic catalytic oxidation). Besides, we have also analyzed the ORR characteristic of the co-doped

catalysts (PN-, PB-, PS-, and PSi-co-doped) and found that N co-doped with P is the most beneficial for ORR catalysis toward $4e^-$ pathway among all co-doped carbon catalysts.

In **chapter-6**, we have further explored and compared the catalytic activity of the P co-doped catalysts (such as PN-, PB-, PS-, and PSi-co-doped), as synthesized in chapter-5, for selective oxidation of benzylic alcohols to corresponding aldehydes/ketone. Herein, we found that a P and S co-doped carbon catalyst shows the better catalyst performance compared to other single heteroatom-doped (S-Gc and P-Gc) and co-doped carbon catalysts (PB-Gc and PN-Gc) for benzylic alcohol oxidations. Moreover, similar to PGc, the PS-Gc catalyst can also selectively oxidize a variety of primary and secondary benzylic alcohols to corresponding aldehydes/ketone without the steric hindrance. The calculated activation energy for benzyl alcohol oxidation is 32 kJ/mol for the PS-Gc, which is much lower than P doped, N-doped carbon catalyst as well as Ru metal based catalysts. From the various control experiments and the detailed characterization of fresh and used PS-Gc catalysts we have concluded that 1) PS-Gc catalyst probably contains two distinct type of catalyst centers, dominated by individual doping of P and S. 2) S-doped active site requires oxygen activation as the first step of oxidation, which is different than P-doped carbon. 3) S is mainly doped as an exocyclic sulfur (C-S-C) and plays a major role in activating the oxygen molecule as well as selectively oxidizing the benzylic alcohols.

1.4. Microwave Chemistry.

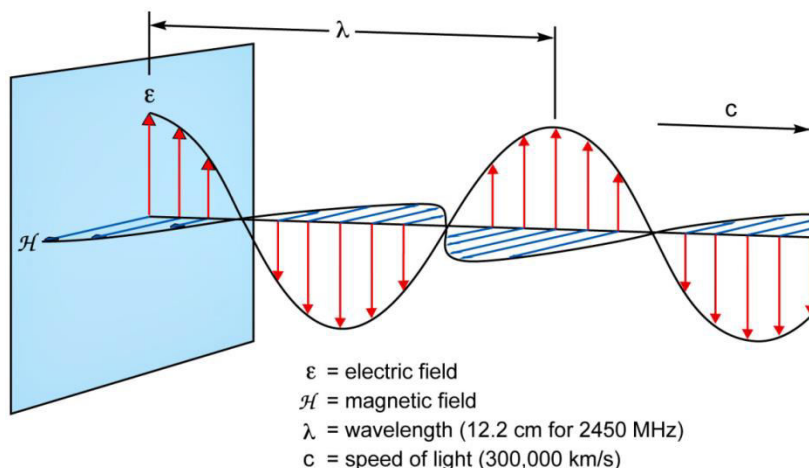


Figure 1.4.1. Electric and magnetic field of Microwave.²³⁵

Microwave irradiations are very energy efficient and a green heating source, which has already shown its potential usefulness in many synthetic applications such as in the synthesis of many organic molecules²³⁶, polymers²³⁷, nanoparticles or nanomaterials²³⁸⁻²⁴¹ along with food processing^{242, 243} applications. Microwaves are electromagnetic waves with a wavelength of 0.01m to 1m and frequency of 300MHz to 300GHz, which lies between the infrared and radio frequency.²⁴⁴ The microwave radiation is made up of two components, electric and magnetic field component. The mechanism of microwave assisted reactions is not entirely understood. But during the microwave heating, molecules in solid or liquid phase absorb the microwave radiations and transform the electromagnetic portion of microwave energy into heat. The energy of the microwave radiation can be transferred to molecules via two mechanisms: 1) dipole rotation and/or 2) ionic conduction.²³⁵ The dipole rotation mechanism applies to polar molecules/reactant, who tries to rearrange in the direction of alternating electric field at very high speed during

the microwave heating and create the internal friction between the molecules, which results in localized heat generation.²⁴⁵ So the magnitude of heating strongly depends on the dielectric properties of the molecules/reactant and its ability to align with the electric field. The ionic conduction mechanism plays an important role when there are free ions or ionic species present in the substance. In this mechanism, the oscillatory migration of ions in the material/substance occurs under the rapidly changing electric field of microwave radiation. This phenomenon results in increased collision rate of ions and converts the kinetic energy of ions into heat.²⁴⁵ This mechanism results in much stronger heating (also called superheating) than that of the dipolar mechanism. Moreover, the ionic conductance depends on the temperature, and hence the energy transfer from microwave to a substance becomes stronger with higher temperature.²³⁵ From both mechanisms of heating, it can be concluded that the electric component of the electromagnetic field is playing an important role in wave- material interaction.

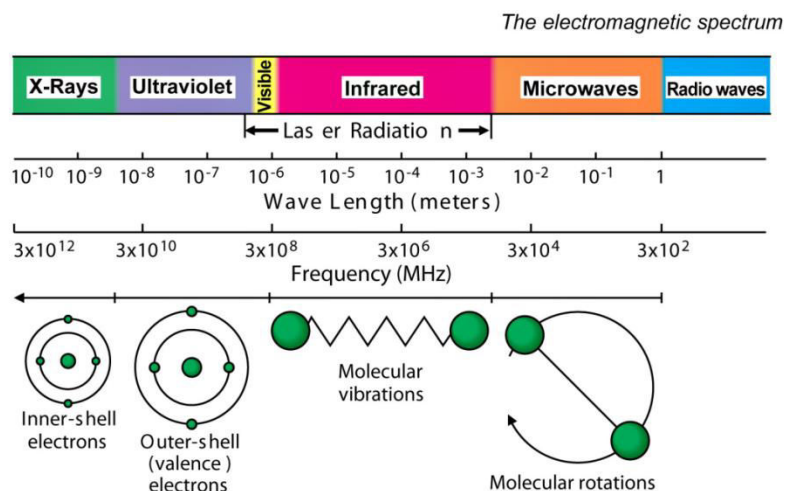


Figure 1.4.2. The electromagnetic spectrum of Microwave.²³⁵

This rapid and unique local superheating effect generated by microwave heating differs from the traditional or conventional heating methods.^{246, 247} In conventional heating,

such as refluxing or oil bath heating, the energy has to pass through the wall of the vessel and then to the solvent to reach the reactant. Due to this energy flow direction the temperature of a vessel is higher than the reaction mixture until it reaches the thermal equilibrium and makes the heating process slow and inefficient. While in the case of microwave heating, the microwave irradiation can directly interact with the molecules/reactant and produce rapid and uniform heating without the interference of reaction vessel or solvent (microwave transparent). Moreover, It should also be noted that the energy of microwave irradiation is ~ 37 cal/mole, which is just enough for molecular rotation but much lower than the typical energy required to break any molecular bonds ($\sim 80,000$ to $120,000$ cal/mole),²⁴⁸ so it does not affect the chemical structure of the molecule. Due to these quick energy transfer properties of microwave heating, it not only results in the rapid rise of the local reaction temperature but also enhances the reaction rate significantly. Microwave heating method can also be useful in solid phase reactions because of its superior penetration power and selective heating at adsorption site without the need for any mechanical agitation and energy loss.^{236, 238} In addition to that, it is also possible to selectively heat one material over another due to the different microwave wave-adsorption ability of different materials.

Even though the microwave radiation covers a broad spectrum of frequency (300MHz to 300GHz), a microwave oven uses only specific frequency as defined by ISM (industrial, scientific, medical) bands to avoid the high cost and its interference with other vital radio services. For example, the domestic microwave owns a frequency of 2.45 GHz (a wavelength of 12.25 cm), while the industrial microwave usually owns frequencies of 915 MHz and 2.45 GHz.⁹

In summary, microwave assisted heating methods have several advantages such as quick and time efficient, simple experimental setup, cost-effective and controllable /selective heating of molecules and unique reaction rate enhancement.^{246, 247} Due to the above advantages, microwave heating, has rapidly grown as one of the important heating sources in the field of materials science.^{249, 250}

1.5. References.

1. Oganov, A. R.; Hemley, R. J.; Hazen, R. M.; Jones, A. P. Structure, bonding, and mineralogy of carbon at extreme conditions. *Rev Mineral Geochem* 2013, 75, 47-77.
2. Tripathi, A. C.; Saraf, S. A.; Saraf, S. K. Carbon Nanotropes: A Contemporary Paradigm in Drug Delivery. *Materials* 2015, 8, 3068-3100.
3. Morozov, S.; Novoselov, K.; Katsnelson, M.; Schedin, F.; Elias, D.; Jaszczak, J.; Geim, A. Giant intrinsic carrier mobilities in graphene and its bilayer. *Phys. Rev. Lett.* 2008, 100, 016602.
4. Boehm, H. P.; Setton, R.; Stumpp, E. Nomenclature and terminology of graphite intercalation compounds (IUPAC Recommendations 1994). *Pure Appl. Chem.* 1994, 66, 1893-1901.
5. Lu, X.; Yu, M.; Huang, H.; Ruoff, R. S. Tailoring graphite with the goal of achieving single sheets. *Nanotechnology* 1999, 10, 269.
6. Novoselov, K. S.; Geim, A. K.; Morozov, S.; Jiang, D.; Zhang, Y.; Dubonos, S. a.; Grigorieva, I.; Firsov, A. Electric field effect in atomically thin carbon films. *science* 2004, 306, 666-669.
7. Geim, A. K.; Novoselov, K. S. The rise of graphene. *Nature materials* 2007, 6, 183-191.
8. Stoller, M. D.; Park, S.; Zhu, Y.; An, J.; Ruoff, R. S. Graphene-based ultracapacitors. *Nano letters* 2008, 8, 3498-3502.
9. Balandin, A. A.; Ghosh, S.; Bao, W.; Calizo, I.; Teweldebrhan, D.; Miao, F.; Lau, C. N. Superior thermal conductivity of single-layer graphene. *Nano Lett.* 2008, 8, 902-907.
10. Balandin, A. A. Thermal properties of graphene and nanostructured carbon materials. *Nature materials* 2011, 10, 569-581.
11. Lee, C.; Wei, X.; Kysar, J. W.; Hone, J. Measurement of the elastic properties and intrinsic strength of monolayer graphene. *science* 2008, 321, 385-388.
12. Erickson, K.; Erni, R.; Lee, Z.; Alem, N.; Gannett, W.; Zettl, A. Determination of the local chemical structure of graphene oxide and reduced graphene oxide. *Adv. Mater.* 2010, 22, 4467-72.
13. Gomez De Arco, L.; Zhang, Y.; Schlenker, C. W.; Ryu, K.; Thompson, M. E.; Zhou, C. Continuous, highly flexible, and transparent graphene films by chemical vapor deposition for organic photovoltaics. *ACS nano* 2010, 4, 2865-2873.

14. Nair, R.; Blake, P.; Grigorenko, A.; Novoselov, K.; Booth, T.; Stauber, T.; Peres, N.; Geim, A. Fine structure constant defines visual transparency of graphene. *Science* 2008, 320, 1308-1308.
15. Bunch, J. S.; Verbridge, S. S.; Alden, J. S.; Van Der Zande, A. M.; Parpia, J. M.; Craighead, H. G.; McEuen, P. L. Impermeable atomic membranes from graphene sheets. *Nano Lett.* 2008, 8, 2458-2462.
16. Wu, Z. S.; Parvez, K.; Feng, X.; Müllen, K. Graphene-based in-plane micro-supercapacitors with high power and energy densities. *Nature communications* 2013, 4.
17. Yoo, J. J.; Balakrishnan, K.; Huang, J.; Meunier, V.; Sumpter, B. G.; Srivastava, A.; Conway, M.; Mohana Reddy, A. L.; Yu, J.; Vajtai, R. Ultrathin planar graphene supercapacitors. *Nano Lett.* 2011, 11, 1423-1427.
18. Wang, X.; Zhi, L.; Müllen, K. Transparent, conductive graphene electrodes for dye-sensitized solar cells. *Nano Lett.* 2008, 8, 323-327.
19. Su, Q.; Pang, S.; Alijani, V.; Li, C.; Feng, X.; Müllen, K. Composites of graphene with large aromatic molecules. *Adv. Mater.* 2009, 21, 3191-3195.
20. Matyba, P.; Yamaguchi, H.; Eda, G.; Chhowalla, M.; Edman, L.; Robinson, N. D. Graphene and mobile ions: the key to all-plastic, solution-processed light-emitting devices. *Acs Nano* 2010, 4, 637-642.
21. Bae, S.; Kim, H.; Lee, Y.; Xu, X.; Park, J.-S.; Zheng, Y.; Balakrishnan, J.; Lei, T.; Kim, H. R.; Song, Y. I. Roll-to-roll production of 30-inch graphene films for transparent electrodes. *Nature nanotechnology* 2010, 5, 574-578.
22. Pang, S.; Tsao, H. N.; Feng, X.; Müllen, K. Patterned Graphene Electrodes from Solution- Processed Graphite Oxide Films for Organic Field- Effect Transistors. *Adv. Mater.* 2009, 21, 3488-3491.
23. Parvez, K.; Li, R.; Puniredd, S. R.; Hernandez, Y.; Hinkel, F.; Wang, S.; Feng, X.; Müllen, K. Electrochemically exfoliated graphene as solution-processable, highly conductive electrodes for organic electronics. *ACS nano* 2013, 7, 3598-3606.
24. Cao, Y.; Liu, S.; Shen, Q.; Yan, K.; Li, P.; Xu, J.; Yu, D.; Steigerwald, M. L.; Nuckolls, C.; Liu, Z. High- Performance Photoresponsive Organic Nanotransistors with Single- Layer Graphenes as Two- Dimensional Electrodes. *Adv. Funct. Mater.* 2009, 19, 2743-2748.
25. Pang, S.; Yang, S.; Feng, X.; Müllen, K. Coplanar asymmetrical reduced graphene oxide-titanium electrodes for polymer photodetectors. *Adv. Mater.* 2012, 24, 1566-1570.
26. Machado, B. F.; Serp, P. Graphene-based materials for catalysis. *Catalysis Science & Technology* 2012, 2, 54-75.
27. Kuila, T.; Bose, S.; Khanra, P.; Mishra, A. K.; Kim, N. H.; Lee, J. H. Recent advances in graphene-based biosensors. *Biosens. Bioelectron.* 2011, 26, 4637-4648.
28. Li, J.-L.; Tang, B.; Yuan, B.; Sun, L.; Wang, X.-G. A review of optical imaging and therapy using nanosized graphene and graphene oxide. *Biomaterials* 2013, 34, 9519-9534.
29. Shao, Y.; Wang, J.; Wu, H.; Liu, J.; Aksay, I. A.; Lin, Y. Graphene based electrochemical sensors and biosensors: a review. *Electroanalysis* 2010, 22, 1027-1036.
30. Wang, H.; Maiyalagan, T.; Wang, X. Review on recent progress in nitrogen-doped graphene: synthesis, characterization, and its potential applications. *Acs Catalysis* 2012, 2, 781-794.

31. Deng, D.; Novoselov, K.; Fu, Q.; Zheng, N.; Tian, Z.; Bao, X. Catalysis with two-dimensional materials and their heterostructures. *Nature nanotechnology* 2016, 11, 218-230.
32. Kong, X.-K.; Chen, C.-L.; Chen, Q.-W. Doped graphene for metal-free catalysis. *Chem. Soc. Rev.* 2014, 43, 2841-2857.
33. Neto, A. C.; Guinea, F.; Peres, N.; Novoselov, K. S.; Geim, A. K. The electronic properties of graphene. *Reviews of modern physics* 2009, 81, 109.
34. Yang, K.; Feng, L.; Shi, X.; Liu, Z. Nano-graphene in biomedicine: theranostic applications. *Chem. Soc. Rev.* 2013, 42, 530-547.
35. Enoki, T.; Kobayashi, Y.; Fukui, K.-I. Electronic structures of graphene edges and nanographene. *Int. Rev. Phys. Chem.* 2007, 26, 609-645.
36. Fujii, S.; Enoki, T. Nanographene and Graphene Edges: Electronic Structure and Nanofabrication. *Acc. Chem. Res.* 2013, 46, 2202-2210.
37. Zhong, J.-H.; Zhang, J.; Jin, X.; Liu, J.-Y.; Li, Q.; Li, M.-H.; Cai, W.; Wu, D.-Y.; Zhan, D.; Ren, B. Quantitative correlation between defect density and heterogeneous electron transfer rate of single layer graphene. *J. Am. Chem. Soc.* 2014, 136, 16609-16617.
38. Banhart, F.; Kotakoski, J.; Krasheninnikov, A. V. Structural defects in graphene. *ACS nano* 2010, 5, 26-41.
39. Girit, Ç. Ö.; Meyer, J. C.; Erni, R.; Rossell, M. D.; Kisielowski, C.; Yang, L.; Park, C.-H.; Crommie, M.; Cohen, M. L.; Louie, S. G. Graphene at the edge: stability and dynamics. *science* 2009, 323, 1705-1708.
40. Zhou, S.; Gweon, G.-H.; Fedorov, A.; First, P.; De Heer, W.; Lee, D.-H.; Guinea, F.; Neto, A. C.; Lanzara, A. Substrate-induced bandgap opening in epitaxial graphene. *Nature materials* 2007, 6, 770-775.
41. Nakada, K.; Fujita, M.; Dresselhaus, G.; Dresselhaus, M. S. Edge state in graphene ribbons: Nanometer size effect and edge shape dependence. *Physical Review B* 1996, 54, 17954-17961.
42. Jiang, D.-e.; Sumpter, B. G.; Dai, S. Unique chemical reactivity of a graphene nanoribbon's zigzag edge. *The Journal of chemical physics* 2007, 126, 134701.
43. Yang, X.; Zhang, X.; Liu, Z.; Ma, Y.; Huang, Y.; Chen, Y. High-efficiency loading and controlled release of doxorubicin hydrochloride on graphene oxide. *The Journal of Physical Chemistry C* 2008, 112, 17554-17558.
44. Bao, H.; Pan, Y.; Ping, Y.; Sahoo, N. G.; Wu, T.; Li, L.; Li, J.; Gan, L. H. Chitosan- functionalized graphene oxide as a nanocarrier for drug and gene delivery. *Small* 2011, 7, 1569-1578.
45. Liu, Z.; Robinson, J. T.; Sun, X.; Dai, H. PEGylated nanographene oxide for delivery of water-insoluble cancer drugs. *J. Am. Chem. Soc.* 2008, 130, 10876-10877.
46. Yang, X.; Niu, G.; Cao, X.; Wen, Y.; Xiang, R.; Duan, H.; Chen, Y. The preparation of functionalized graphene oxide for targeted intracellular delivery of siRNA. *J. Mater. Chem.* 2012, 22, 6649-6654.
47. Lu, C. H.; Yang, H. H.; Zhu, C. L.; Chen, X.; Chen, G. N. A graphene platform for sensing biomolecules. *Angew. Chem.* 2009, 121, 4879-4881.
48. Liu, Z.; Robinson, J. T.; Tabakman, S. M.; Yang, K.; Dai, H. Carbon materials for drug delivery & cancer therapy. *Mater. Today* 2011, 14, 316-323.

49. Zhang, L.; Lu, Z.; Zhao, Q.; Huang, J.; Shen, H.; Zhang, Z. Enhanced chemotherapy efficacy by sequential delivery of siRNA and anticancer drugs using PEI-grafted graphene oxide. *Small* 2011, 7, 460-464.
50. Yang, K.; Zhang, S.; Zhang, G.; Sun, X.; Lee, S.-T.; Liu, Z. Graphene in mice: ultrahigh in vivo tumor uptake and efficient photothermal therapy. *Nano Lett.* 2010, 10, 3318-3323.
51. Zhang, W.; Guo, Z.; Huang, D.; Liu, Z.; Guo, X.; Zhong, H. Synergistic effect of chemo-photothermal therapy using PEGylated graphene oxide. *Biomaterials* 2011, 32, 8555-8561.
52. Markovic, Z. M.; Harhaji-Trajkovic, L. M.; Todorovic-Markovic, B. M.; Kepić, D. P.; Arsin, K. M.; Jovanović, S. P.; Pantovic, A. C.; Dramićanin, M. D.; Trajkovic, V. S. In vitro comparison of the photothermal anticancer activity of graphene nanoparticles and carbon nanotubes. *Biomaterials* 2011, 32, 1121-1129.
53. Robinson, J. T.; Tabakman, S. M.; Liang, Y.; Wang, H.; Sanchez Casalongue, H.; Vinh, D.; Dai, H. Ultrasmall reduced graphene oxide with high near-infrared absorbance for photothermal therapy. *J. Am. Chem. Soc.* 2011, 133, 6825-6831.
54. Mohanty, N.; Berry, V. Graphene-based single-bacterium resolution biodevice and DNA transistor: interfacing graphene derivatives with nanoscale and microscale biocomponents. *Nano Lett.* 2008, 8, 4469-4476.
55. Nelson, T.; Zhang, B.; Prezhd, O. V. Detection of nucleic acids with graphene nanopores: ab initio characterization of a novel sequencing device. *Nano Lett.* 2010, 10, 3237-3242.
56. Jung, J. H.; Cheon, D. S.; Liu, F.; Lee, K. B.; Seo, T. S. A Graphene Oxide Based Immuno- biosensor for Pathogen Detection. *Angew. Chem. Int. Ed.* 2010, 49, 5708-5711.
57. Wen, Y.; Xing, F.; He, S.; Song, S.; Wang, L.; Long, Y.; Li, D.; Fan, C. A graphene-based fluorescent nanoprobe for silver (I) ions detection by using graphene oxide and a silver-specific oligonucleotide. *Chem. Commun.* 2010, 46, 2596-2598.
58. Song, Y.; Qu, K.; Zhao, C.; Ren, J.; Qu, X. Graphene oxide: intrinsic peroxidase catalytic activity and its application to glucose detection. *Adv. Mater.* 2010, 22, 2206-2210.
59. Wang, Y.; Li, Y.; Tang, L.; Lu, J.; Li, J. Application of graphene-modified electrode for selective detection of dopamine. *Electrochem. Commun.* 2009, 11, 889-892.
60. Yang, K.; Wan, J.; Zhang, S.; Zhang, Y.; Lee, S.-T.; Liu, Z. In vivo pharmacokinetics, long-term biodistribution, and toxicology of PEGylated graphene in mice. *ACS nano* 2010, 5, 516-522.
61. Wang, K.; Ruan, J.; Song, H.; Zhang, J.; Wo, Y.; Guo, S.; Cui, D. Biocompatibility of graphene oxide. *Nanoscale Res Lett* 2011, 6, 1.
62. Zhang, X.; Yin, J.; Peng, C.; Hu, W.; Zhu, Z.; Li, W.; Fan, C.; Huang, Q. Distribution and biocompatibility studies of graphene oxide in mice after intravenous administration. *Carbon* 2011, 49, 986-995.
63. Yan, X.; Cui, X.; Li, L.-s. Synthesis of large, stable colloidal graphene quantum dots with tunable size. *J. Am. Chem. Soc.* 2010, 132, 5944-5945.
64. Liu, R.; Wu, D.; Feng, X.; Müllen, K. Bottom-up fabrication of photoluminescent graphene quantum dots with uniform morphology. *J. Am. Chem. Soc.* 2011, 133, 15221-15223.
65. Zhu, S.; Tang, S.; Zhang, J.; Yang, B. Control the size and surface chemistry of graphene for the rising fluorescent materials. *Chem. Commun.* 2012, 48, 4527-4539.

66. Park, S.; Ruoff, R. S. Chemical methods for the production of graphenes. *Nature nanotechnology* 2009, 4, 217-224.
67. Hummers, W. S.; Offeman, R. E. Preparation of Graphitic Oxide. *J. Am. Chem. Soc.* 1958, 80, 1339.
68. Erickson, K.; Erni, R.; Lee, Z.; Alem, N.; Cannett, W.; A., Z. Determination of the Local Chemical Structure of Graphene Oxide and Reduced Graphene Oxide. *Adv. Mater.* 2010, 22, 4467-4472.
69. Li, J.-L.; Kudin, K. N.; McAllister, M. J.; Prud'homme, R. K.; Aksay, I. A.; Car, R. Oxygen-Driven Unzipping of Graphitic Materials *Phys. Rev. Lett.* 2006, 96, 176101.
70. Zhang, L.; Liang, J. J.; Huang, Y.; Ma, Y. F.; Wang, Y.; Chen, Y. S. Size-controlled synthesis of graphene oxide sheets on a large scale using chemical exfoliation. *Carbon* 2009, 47, 3365-3368.
71. Zhou, X. J.; Zhang, Y.; Wang, C.; Wu, X. C.; Yang, Y. Q.; Zheng, B.; Wu, H. X.; Guo, S. W.; Zhang, J. Y. Photo-Fenton Reaction of Graphene Oxide: A New Strategy to Prepare Graphene Quantum Dots for DNA Cleavage. *Acs Nano* 2012, 6, 6592-6599.
72. Wang, D.; Wang, L.; Dong, X. Y.; Shi, Z.; Jin, J. Chemically tailoring graphene oxides into fluorescent nanosheets for Fe³⁺ ion detection. *Carbon* 2012, 50, 2147-2154.
73. Luo, J. Y.; Cote, L. J.; Tung, V. C.; Tan, A. T. L.; Goins, P. E.; Wu, J. S.; Huang, J. X. Graphene Oxide Nanocolloids. *J. Am. Chem. Soc.* 2010, 132, 17667-17669.
74. Peng, J.; Gao, W.; Gupta, B. K.; Liu, Z.; Romero-Aburto, R.; Ge, L. H.; Song, L.; Alemany, L. B.; Zhan, X. B.; Gao, G. H.; Vithayathil, S. A.; Kaipparattu, B. A.; Marti, A. A.; Hayashi, T.; Zhu, J. J.; Ajayan, P. M. Graphene Quantum Dots Derived from Carbon Fibers. *Nano Lett.* 2012, 12, 844-849.
75. Tian, B.; Wang, C.; Zhang, S.; Feng, L. Z.; Liu, Z. Photothermally Enhanced Photodynamic Therapy Delivered by Nano-Graphene Oxide. *Acs Nano* 2011, 5, 7000-7009.
76. Yang, K.; Wan, J. M.; Zhang, S.; Tian, B.; Zhang, Y. J.; Liu, Z. The influence of surface chemistry and size of nanoscale graphene oxide on photothermal therapy of cancer using ultra-low laser power. *Biomaterials* 2012, 33, 2206-2214.
77. Robinson, J. T.; Tabakman, S. M.; Liang, Y. Y.; Wang, H. L.; Casalongue, H. S.; Vinh, D.; Dai, H. J. Ultrasmall Reduced Graphene Oxide with High Near-Infrared Absorbance for Photothermal Therapy. *J. Am. Chem. Soc.* 2011, 133, 6825-6831.
78. Pan, D. Y.; Zhang, J. C.; Li, Z.; Wu, M. H. Hydrothermal Route for Cutting Graphene Sheets into Blue-Luminescent Graphene Quantum Dots. *Adv. Mater.* 2010, 22, 734-+.
79. Li, Y.; Hu, Y.; Zhao, Y.; Shi, G. Q.; Deng, L. E.; Hou, Y. B.; Qu, L. T. An Electrochemical Avenue to Green-Luminescent Graphene Quantum Dots as Potential Electron-Acceptors for Photovoltaics. *Adv. Mater.* 2011, 23, 776-+.
80. Zhang, M.; Bai, L. L.; Shang, W. H.; Xie, W. J.; Ma, H.; Fu, Y. Y.; Fang, D. C.; Sun, H.; Fan, L. Z.; Han, M.; Liu, C. M.; Yang, S. H. Facile synthesis of water-soluble, highly fluorescent graphene quantum dots as a robust biological label for stem cells. *J. Mater. Chem.* 2012, 22, 7461-7467.
81. Akhavan, O. Graphene nanomesh by ZnO nanorod photocatalysts. *ACS nano* 2010, 4, 4174-4180.

82. Mao, S.; Wen, Z.; Kim, H.; Lu, G.; Hurley, P.; Chen, J. A general approach to one-pot fabrication of crumpled graphene-based nanohybrids for energy applications. *ACS nano* 2012, 6, 7505-7513.
83. Wu, Z.-S.; Winter, A.; Chen, L.; Sun, Y.; Turchanin, A.; Feng, X.; Müllen, K. Three-Dimensional Nitrogen and Boron Co-doped Graphene for High-Performance All-Solid-State Supercapacitors. *Adv. Mater.* 2012, 24, 5130-5135.
84. Jiang, L.; Fan, Z. Design of advanced porous graphene materials: from graphene nanomesh to 3D architectures. *Nanoscale* 2014, 6, 1922-1945.
85. Liang, C.; Li, Z.; Dai, S. Mesoporous carbon materials: synthesis and modification. *Angew. Chem. Int. Ed.* 2008, 47, 3696-3717.
86. Zhu, Y.; Murali, S.; Stoller, M. D.; Ganesh, K.; Cai, W.; Ferreira, P. J.; Pirkle, A.; Wallace, R. M.; Cychosz, K. A.; Thommes, M. Carbon-based supercapacitors produced by activation of graphene. *Science* 2011, 332, 1537-1541.
87. Wang, Z.-L.; Xu, D.; Wang, H.-G.; Wu, Z.; Zhang, X.-B. In situ fabrication of porous graphene electrodes for high-performance energy storage. *Acs Nano* 2013, 7, 2422-2430.
88. Ning, G.; Xu, C.; Mu, L.; Chen, G.; Wang, G.; Gao, J.; Fan, Z.; Qian, W.; Wei, F. High capacity gas storage in corrugated porous graphene with a specific surface area-lossless tightly stacking manner. *Chem. Commun.* 2012, 48, 6815-6817.
89. Li, Y.; Zhou, Z.; Shen, P.; Chen, Z. Two-dimensional polyphenylene: experimentally available porous graphene as a hydrogen purification membrane. *Chem. Commun.* 2010, 46, 3672-3674.
90. Schrier, J. Helium separation using porous graphene membranes. *The Journal of Physical Chemistry Letters* 2010, 1, 2284-2287.
91. Du, H.; Li, J.; Zhang, J.; Su, G.; Li, X.; Zhao, Y. Separation of hydrogen and nitrogen gases with porous graphene membrane. *The Journal of Physical Chemistry C* 2011, 115, 23261-23266.
92. Si, C.; Zhou, G. Size-dependent chemical reactivity of porous graphene for purification of exhaust gases. *The Journal of chemical physics* 2012, 137, 184309.
93. Shan, M.; Xue, Q.; Jing, N.; Ling, C.; Zhang, T.; Yan, Z.; Zheng, J. Influence of chemical functionalization on the CO₂/N₂ separation performance of porous graphene membranes. *Nanoscale* 2012, 4, 5477-5482.
94. Hauser, A. W.; Schwerdtfeger, P. Methane-selective nanoporous graphene membranes for gas purification. *PCCP* 2012, 14, 13292-13298.
95. Dong, X.; Wang, X.; Wang, L.; Song, H.; Zhang, H.; Huang, W.; Chen, P. 3D graphene foam as a monolithic and macroporous carbon electrode for electrochemical sensing. *ACS applied materials & interfaces* 2012, 4, 3129-3133.
96. Li, H.; Liu, L.; Yang, F. Covalent assembly of 3D graphene/polypyrrole foams for oil spill cleanup. *Journal of Materials Chemistry A* 2013, 1, 3446-3453.
97. Kou, R.; Shao, Y.; Mei, D.; Nie, Z.; Wang, D.; Wang, C.; Viswanathan, V. V.; Park, S.; Aksay, I. A.; Lin, Y. Stabilization of electrocatalytic metal nanoparticles at metal-metal oxide-graphene triple junction points. *J. Am. Chem. Soc.* 2011, 133, 2541-2547.
98. Luo, J.; Jang, H. D.; Sun, T.; Xiao, L.; He, Z.; Katsoulidis, A. P.; Kanatzidis, M. G.; Gibson, J. M.; Huang, J. Compression and aggregation-resistant particles of crumpled soft sheets. *Acs Nano* 2011, 5, 8943-8949.

99. Bieri, M.; Treier, M.; Cai, J.; Ait-Mansour, K.; Ruffieux, P.; Gröning, O.; Gröning, P.; Kastler, M.; Rieger, R.; Feng, X. Porous graphenes: two-dimensional polymer synthesis with atomic precision. *Chem. Commun.* 2009, 6919-6921.
100. Ning, G.; Fan, Z.; Wang, G.; Gao, J.; Qian, W.; Wei, F. Gram-scale synthesis of nanomesh graphene with high surface area and its application in supercapacitor electrodes. *Chem. Commun.* 2011, 47, 5976-5978.
101. Kuhn, P.; Forget, A.; Su, D.; Thomas, A.; Antonietti, M. From microporous regular frameworks to mesoporous materials with ultrahigh surface area: dynamic reorganization of porous polymer networks. *J. Am. Chem. Soc.* 2008, 130, 13333-13337.
102. Lin, Y.; Watson, K. A.; Kim, J.-W.; Baggett, D. W.; Working, D. C.; Connell, J. W. Bulk preparation of holey graphene via controlled catalytic oxidation. *Nanoscale* 2013, 5, 7814-7824.
103. Zhang, L.; Zhang, F.; Yang, X.; Long, G.; Wu, Y.; Zhang, T.; Leng, K.; Huang, Y.; Ma, Y.; Yu, A. Porous 3D graphene-based bulk materials with exceptional high surface area and excellent conductivity for supercapacitors. *Scientific reports* 2013, 3.
104. Zhao, X.; Hayner, C. M.; Kung, M. C.; Kung, H. H. Flexible holey graphene paper electrodes with enhanced rate capability for energy storage applications. *ACS nano* 2011, 5, 8739-8749.
105. Wang, X.; Jiao, L.; Sheng, K.; Li, C.; Dai, L.; Shi, G. Solution-processable graphene nanomeshes with controlled pore structures. *Scientific reports* 2013, 3.
106. Kotchey, G. P.; Allen, B. L.; Vedala, H.; Yanamala, N.; Kapralov, A. A.; Tyurina, Y. Y.; Klein-Seetharaman, J.; Kagan, V. E.; Star, A. The enzymatic oxidation of graphene oxide. *ACS nano* 2011, 5, 2098-2108.
107. Fischbein, M. D.; Drndić, M. Electron beam nanosculpting of suspended graphene sheets. *Appl. Phys. Lett.* 2008, 93, 113107.
108. Zeng, Z.; Huang, X.; Yin, Z.; Li, H.; Chen, Y.; Li, H.; Zhang, Q.; Ma, J.; Boey, F.; Zhang, H. Fabrication of graphene nanomesh by using an anodic aluminum oxide membrane as a template. *Adv. Mater.* 2012, 24, 4138-4142.
109. Jung, I.; Jang, H. Y.; Park, S. Direct growth of graphene nanomesh using a Au nano-network as a metal catalyst via chemical vapor deposition. *Appl. Phys. Lett.* 2013, 103, 023105.
110. Yi, J.; Lee, D. H.; Lee, W. W.; Park, W. I. Direct synthesis of graphene meshes and semipermanent electrical doping. *The Journal of Physical Chemistry Letters* 2013, 4, 2099-2104.
111. Fan, Z.; Liu, Y.; Yan, J.; Ning, G.; Wang, Q.; Wei, T.; Zhi, L.; Wei, F. Template-Directed Synthesis of Pillared- Porous Carbon Nanosheet Architectures: High-Performance Electrode Materials for Supercapacitors. *Advanced Energy Materials* 2012, 2, 419-424.
112. Patel, M.; Feng, W.; Savaram, K.; Khoshi, M. R.; Huang, R.; Sun, J.; Rabie, E.; Flach, C.; Mendelsohn, R.; Garfunkel, E. Microwave Enabled One- Pot, One- Step Fabrication and Nitrogen Doping of Holey Graphene Oxide for Catalytic Applications. *small* 2015, 11, 3358-3368.
113. Bai, J.; Zhong, X.; Jiang, S.; Huang, Y.; Duan, X. Graphene nanomesh. *Nature nanotechnology* 2010, 5, 190-194.
114. Fan, Z.; Zhao, Q.; Li, T.; Yan, J.; Ren, Y.; Feng, J.; Wei, T. Easy synthesis of porous graphene nanosheets and their use in supercapacitors. *Carbon* 2012, 50, 1699-1703.

115. Xi, Q.; Chen, X.; Evans, D. G.; Yang, W. Gold nanoparticle-embedded porous graphene thin films fabricated via layer-by-layer self-assembly and subsequent thermal annealing for electrochemical sensing. *Langmuir* 2012, 28, 9885-9892.
116. Han, T. H.; Huang, Y.-K.; Tan, A. T.; Dravid, V. P.; Huang, J. Steam etched porous graphene oxide network for chemical sensing. *J. Am. Chem. Soc.* 2011, 133, 15264-15267.
117. Peng, W.; Liu, S.; Sun, H.; Yao, Y.; Zhi, L.; Wang, S. Synthesis of porous reduced graphene oxide as metal-free carbon for adsorption and catalytic oxidation of organics in water. *Journal of Materials Chemistry A* 2013, 1, 5854-5859.
118. Wang, X.; Sun, G.; Routh, P.; Kim, D.-H.; Huang, W.; Chen, P. Heteroatom-doped graphene materials: syntheses, properties and applications. *Chem. Soc. Rev.* 2014, 43, 7067-7098.
119. Kuila, T.; Bose, S.; Mishra, A. K.; Khanra, P.; Kim, N. H.; Lee, J. H. Chemical functionalization of graphene and its applications. *Prog. Mater. Sci.* 2012, 57, 1061-1105.
120. Jiao, Y.; Zheng, Y.; Jaroniec, M.; Qiao, S. Z. Origin of the electrocatalytic oxygen reduction activity of graphene-based catalysts: A roadmap to achieve the best performance. *J. Am. Chem. Soc.* 2014, 136, 4394-4403.
121. Rani, P.; Jindal, V. Designing band gap of graphene by B and N dopant atoms. *RSC Advances* 2013, 3, 802-812.
122. Miwa, R. H.; Martins, T. B.; Fazzio, A. Hydrogen adsorption on boron doped graphene: an ab initio study. *Nanotechnology* 2008, 19, 155708.
123. Faccio, R.; Fernández-Werner, L.; Pardo, H.; Goyenola, C.; Ventura, O. N.; Mombrú, Á. W. Electronic and structural distortions in graphene induced by carbon vacancies and boron doping. *The Journal of Physical Chemistry C* 2010, 114, 18961-18971.
124. Yu, L.; Pan, X.; Cao, X.; Hu, P.; Bao, X. Oxygen reduction reaction mechanism on nitrogen-doped graphene: A density functional theory study. *J. Catal.* 2011, 282, 183-190.
125. Lherbier, A.; Botello-Mendez, A. R.; Charlier, J.-C. Electronic and transport properties of unbalanced sublattice N-doping in graphene. *Nano Lett.* 2013, 13, 1446-1450.
126. Jalili, S.; Vaziri, R. Study of the electronic properties of li-intercalated nitrogen doped graphite. *Mol. Phys.* 2011, 109, 687-694.
127. Schiros, T.; Nordlund, D.; Pálková, L.; Prezzi, D.; Zhao, L.; Kim, K. S.; Wurstbauer, U.; Gutiérrez, C.; Delongchamp, D.; Jaye, C. Connecting dopant bond type with electronic structure in N-doped graphene. *Nano Lett.* 2012, 12, 4025-4031.
128. Hwang, J. O.; Park, J. S.; Choi, D. S.; Kim, J. Y.; Lee, S. H.; Lee, K. E.; Kim, Y.-H.; Song, M. H.; Yoo, S.; Kim, S. O. Workfunction-tunable, N-doped reduced graphene transparent electrodes for high-performance polymer light-emitting diodes. *ACS Nano* 2011, 6, 159-167.
129. Liu, Y.; Feng, Q.; Tang, N.; Wan, X.; Liu, F.; Lv, L.; Du, Y. Increased magnetization of reduced graphene oxide by nitrogen-doping. *Carbon* 2013, 60, 549-551.
130. Chiou, J.; Ray, S. C.; Peng, S.; Chuang, C.; Wang, B.; Tsai, H.; Pao, C.; Lin, H.-J.; Shao, Y.; Wang, Y. Nitrogen-functionalized graphene nanoflakes (GNFs: N): tunable photoluminescence and electronic structures. *The Journal of Physical Chemistry C* 2012, 116, 16251-16258.
131. Yang, Z.; Yao, Z.; Li, G.; Fang, G.; Nie, H.; Liu, Z.; Zhou, X.; Chen, X. a.; Huang, S. Sulfur-doped graphene as an efficient metal-free cathode catalyst for oxygen reduction. *ACS nano* 2011, 6, 205-211.

132. Denis, P. A. Concentration dependence of the band gaps of phosphorus and sulfur doped graphene. *Computational Materials Science* 2013, 67, 203-206.
133. Wang, H.-m.; Wang, H.-x.; Chen, Y.; Liu, Y.-j.; Zhao, J.-x.; Cai, Q.-h.; Wang, X.-z. Phosphorus-doped graphene and (8, 0) carbon nanotube: Structural, electronic, magnetic properties, and chemical reactivity. *Appl. Surf. Sci.* 2013, 273, 302-309.
134. Some, S.; Kim, J.; Lee, K.; Kulkarni, A.; Yoon, Y.; Lee, S.; Kim, T.; Lee, H. Highly air- stable phosphorus- doped n- type graphene field- effect transistors. *Adv. Mater.* 2012, 24, 5481-5486.
135. Liang, J.; Jiao, Y.; Jaroniec, M.; Qiao, S. Z. Sulfur and nitrogen dual- doped mesoporous graphene electrocatalyst for oxygen reduction with synergistically enhanced performance. *Angew. Chem. Int. Ed.* 2012, 51, 11496-11500.
136. Choi, C. H.; Chung, M. W.; Jun, Y. J.; Woo, S. I. Doping of chalcogens (sulfur and/or selenium) in nitrogen-doped graphene–CNT self-assembly for enhanced oxygen reduction activity in acid media. *RSC Advances* 2013, 3, 12417-12422.
137. Chen, Y.; Liu, Y.-j.; Wang, H.-x.; Zhao, J.-x.; Cai, Q.-h.; Wang, X.-z.; Ding, Y.-h. Silicon-Doped Graphene: An Effective and Metal-Free Catalyst for NO Reduction to N₂O? *ACS Applied Materials & Interfaces* 2013, 5, 5994-6000.
138. Jeon, I.-Y.; Choi, M.; Choi, H.-J.; Jung, S.-M.; Kim, M.-J.; Seo, J.-M.; Bae, S.-Y.; Yoo, S.; Kim, G.; Jeong, H. Y. Antimony-doped graphene nanoplatelets. *Nature communications* 2015, 6.
139. Wang, X.; Sun, G.; Routh, P.; Kim, D. H.; Huang, W.; Chen, P. Heteroatom-doped graphene materials: syntheses, properties and applications. *Chem. Soc. Rev.* 2014, 43, 7067-98.
140. Sheng, Z.-H.; Shao, L.; Chen, J.-J.; Bao, W.-J.; Wang, F.-B.; Xia, X.-H. Catalyst-free synthesis of nitrogen-doped graphene via thermal annealing graphite oxide with melamine and its excellent electrocatalysis. *ACS nano* 2011, 5, 4350-4358.
141. Li, X.; Wang, H.; Robinson, J. T.; Sanchez, H.; Diankov, G.; Dai, H. Simultaneous nitrogen doping and reduction of graphene oxide. *J. Am. Chem. Soc.* 2009, 131, 15939-15944.
142. Shao, Y.; Zhang, S.; Engelhard, M. H.; Li, G.; Shao, G.; Wang, Y.; Liu, J.; Aksay, I. A.; Lin, Y. Nitrogen-doped graphene and its electrochemical applications. *J. Mater. Chem.* 2010, 20, 7491-7496.
143. Wang, Y.; Shao, Y.; Matson, D. W.; Li, J.; Lin, Y. Nitrogen-doped graphene and its application in electrochemical biosensing. *ACS nano* 2010, 4, 1790-1798.
144. Long, D.; Li, W.; Ling, L.; Miyawaki, J.; Mochida, I.; Yoon, S.-H. Preparation of nitrogen-doped graphene sheets by a combined chemical and hydrothermal reduction of graphene oxide. *Langmuir* 2010, 26, 16096-16102.
145. Huang, C.; Li, C.; Shi, G. Graphene based catalysts. *Energy & Environmental Science* 2012, 5, 8848-8868.
146. Wei, D.; Liu, Y.; Wang, Y.; Zhang, H.; Huang, L.; Yu, G. Synthesis of N-doped graphene by chemical vapor deposition and its electrical properties. *Nano Lett.* 2009, 9, 1752-1758.
147. Qu, L.; Liu, Y.; Baek, J.-B.; Dai, L. Nitrogen-doped graphene as efficient metal-free electrocatalyst for oxygen reduction in fuel cells. *ACS nano* 2010, 4, 1321-1326.

148. Luo, Z.; Lim, S.; Tian, Z.; Shang, J.; Lai, L.; MacDonald, B.; Fu, C.; Shen, Z.; Yu, T.; Lin, J. Pyridinic N doped graphene: synthesis, electronic structure, and electrocatalytic property. *J. Mater. Chem.* 2011, 21, 8038-8044.
149. Deng, D.; Pan, X.; Yu, L.; Cui, Y.; Jiang, Y.; Qi, J.; Li, W.-X.; Fu, Q.; Ma, X.; Xue, Q. Toward N-doped graphene via solvothermal synthesis. *Chem. Mater.* 2011, 23, 1188-1193.
150. Latorre- Sánchez, M.; Primo, A.; García, H. P- Doped Graphene Obtained by Pyrolysis of Modified Alginate as a Photocatalyst for Hydrogen Generation from Water–Methanol Mixtures. *Angew. Chem. Int. Ed.* 2013, 52, 11813-11816.
151. Hulicova-Jurcakova, D.; Puziy, A. M.; Poddubnaya, O. I.; Suárez-García, F.; Tascón, J. M.; Lu, G. Q. Highly stable performance of supercapacitors from phosphorus-enriched carbons. *J. Am. Chem. Soc.* 2009, 131, 5026-5027.
152. Zhao, X.; Wang, A.; Yan, J.; Sun, G.; Sun, L.; Zhang, T. Synthesis and electrochemical performance of heteroatom-incorporated ordered mesoporous carbons. *Chem. Mater.* 2010, 22, 5463-5473.
153. Nasini, U. B.; Gopal Bairi, V.; Kumar Ramasahayam, S.; Bourdo, S. E.; Viswanathan, T.; Shaikh, A. U. Oxygen Reduction Reaction Studies of Phosphorus and Nitrogen Co- Doped Mesoporous Carbon Synthesized via Microwave Technique. *ChemElectroChem* 2014, 1, 573-579.
154. Ramasahayam, S. K.; Nasini, U. B.; Bairi, V.; Shaikh, A. U.; Viswanathan, T. Microwave assisted synthesis and characterization of silicon and phosphorous co-doped carbon as an electrocatalyst for oxygen reduction reaction. *RSC Advances* 2014, 4, 6306-6313.
155. Guiotoku, M.; Rambo, C. R.; Hotza, D. Charcoal produced from cellulosic raw materials by microwave-assisted hydrothermal carbonization. *J. Therm. Anal. Calorim.* 2014, 117, 269-275.
156. Jun, G. H.; Jin, S. H.; Lee, B.; Kim, B. H.; Chae, W.-S.; Hong, S. H.; Jeon, S. Enhanced conduction and charge-selectivity by N-doped graphene flakes in the active layer of bulk-heterojunction organic solar cells. *Energy & Environmental Science* 2013, 6, 3000-3006.
157. Lai, L.; Potts, J. R.; Zhan, D.; Wang, L.; Poh, C. K.; Tang, C.; Gong, H.; Shen, Z.; Lin, J.; Ruoff, R. S. Exploration of the active center structure of nitrogen-doped graphene-based catalysts for oxygen reduction reaction. *Energy & Environmental Science* 2012, 5, 7936-7942.
158. Li, R.; Wei, Z.; Gou, X.; Xu, W. Phosphorus-doped graphene nanosheets as efficient metal-free oxygen reduction electrocatalysts. *Rsc Advances* 2013, 3, 9978-9984.
159. Yang, S.; Zhi, L.; Tang, K.; Feng, X.; Maier, J.; Müllen, K. Efficient synthesis of heteroatom (N or S)- doped graphene based on ultrathin graphene oxide- porous silica sheets for oxygen reduction reactions. *Adv. Funct. Mater.* 2012, 22, 3634-3640.
160. Wu, Z.-S.; Ren, W.; Xu, L.; Li, F.; Cheng, H.-M. Doped graphene sheets as anode materials with superhigh rate and large capacity for lithium ion batteries. *ACS nano* 2011, 5, 5463-5471.
161. Jeong, H. M.; Lee, J. W.; Shin, W. H.; Choi, Y. J.; Shin, H. J.; Kang, J. K.; Choi, J. W. Nitrogen-doped graphene for high-performance ultracapacitors and the importance of nitrogen-doped sites at basal planes. *Nano Lett.* 2011, 11, 2472-2477.

162. Liu, J.-Y.; Chang, H.-Y.; Truong, Q. D.; Ling, Y.-C. Synthesis of nitrogen-doped graphene by pyrolysis of ionic-liquid-functionalized graphene. *Journal of Materials Chemistry C* 2013, 1, 1713-1716.
163. Yang, G.-H.; Zhou, Y.-H.; Wu, J.-J.; Cao, J.-T.; Li, L.-L.; Liu, H.-Y.; Zhu, J.-J. Microwave-assisted synthesis of nitrogen and boron co-doped graphene and its application for enhanced electrochemical detection of hydrogen peroxide. *RSC Advances* 2013, 3, 22597-22604.
164. Liu, C. L.; Hu, C.-C.; Wu, S.-H.; Wu, T.-H. Electron transfer number control of the oxygen reduction reaction on nitrogen-doped reduced-graphene oxides using experimental design strategies. *J. Electrochem. Soc.* 2013, 160, H547-H552.
165. Kim, I. T.; Shin, M. W. Synthesis of nitrogen-doped graphene via simple microwave-hydrothermal process. *Mater. Lett.* 2013, 108, 33-36.
166. Lü, X.; Wu, J.; Lin, T.; Wan, D.; Huang, F.; Xie, X.; Jiang, M. Low-temperature rapid synthesis of high-quality pristine or boron-doped graphene via Wurtz-type reductive coupling reaction. *J. Mater. Chem.* 2011, 21, 10685-10689.
167. Wu, P.; Cai, Z.; Gao, Y.; Zhang, H.; Cai, C. Enhancing the electrochemical reduction of hydrogen peroxide based on nitrogen-doped graphene for measurement of its releasing process from living cells. *Chem. Commun.* 2011, 47, 11327-11329.
168. Sun, L.; Wang, L.; Tian, C.; Tan, T.; Xie, Y.; Shi, K.; Li, M.; Fu, H. Nitrogen-doped graphene with high nitrogen level via a one-step hydrothermal reaction of graphene oxide with urea for superior capacitive energy storage. *Rsc Advances* 2012, 2, 4498-4506.
169. Su, Y.; Zhang, Y.; Zhuang, X.; Li, S.; Wu, D.; Zhang, F.; Feng, X. Low-temperature synthesis of nitrogen/sulfur co-doped three-dimensional graphene frameworks as efficient metal-free electrocatalyst for oxygen reduction reaction. *Carbon* 2013, 62, 296-301.
170. Jeon, I.-Y.; Choi, H.-J.; Ju, M. J.; Choi, I. T.; Lim, K.; Ko, J.; Kim, H. K.; Kim, J. C.; Lee, J.-J.; Shin, D. Direct nitrogen fixation at the edges of graphene nanoplatelets as efficient electrocatalysts for energy conversion. *Scientific reports* 2013, 3.
171. Jeon, I. Y.; Zhang, S.; Zhang, L.; Choi, H. J.; Seo, J. M.; Xia, Z.; Dai, L.; Baek, J. B. Edge- selectively sulfurized graphene nanoplatelets as efficient metal- free electrocatalysts for oxygen reduction reaction: the electron spin effect. *Adv. Mater.* 2013, 25, 6138-6145.
172. Panchakarla, L.; Subrahmanyam, K.; Saha, S.; Govindaraj, A.; Krishnamurthy, H.; Waghmare, U.; Rao, C. Synthesis, structure, and properties of boron-and nitrogen-doped graphene. *Adv. Mater.* 2009, 21, 4726.
173. Ci, L.; Song, L.; Jin, C.; Jariwala, D.; Wu, D.; Li, Y.; Srivastava, A.; Wang, Z.; Storr, K.; Balicas, L. Atomic layers of hybridized boron nitride and graphene domains. *Nature materials* 2010, 9, 430-435.
174. Wu, T.; Shen, H.; Sun, L.; Cheng, B.; Liu, B.; Shen, J. Nitrogen and boron doped monolayer graphene by chemical vapor deposition using polystyrene, urea and boric acid. *New J. Chem.* 2012, 36, 1385-1391.
175. Wang, H.; Zhou, Y.; Wu, D.; Liao, L.; Zhao, S.; Peng, H.; Liu, Z. Synthesis of Boron- Doped Graphene Monolayers Using the Sole Solid Feedstock by Chemical Vapor Deposition. *Small* 2013, 9, 1316-1320.

176. Gao, H.; Liu, Z.; Song, L.; Guo, W.; Gao, W.; Ci, L.; Rao, A.; Quan, W.; Vajtai, R.; Ajayan, P. M. Synthesis of S-doped graphene by liquid precursor. *Nanotechnology* 2012, 23, 275605.
177. Xu, J.; Dong, G.; Jin, C.; Huang, M.; Guan, L. Sulfur and Nitrogen Co- Doped, Few- Layered Graphene Oxide as a Highly Efficient Electrocatalyst for the Oxygen-Reduction Reaction. *ChemSusChem* 2013, 6, 493-499.
178. Choi, C. H.; Park, S. H.; Woo, S. I. Binary and ternary doping of nitrogen, boron, and phosphorus into carbon for enhancing electrochemical oxygen reduction activity. *ACS nano* 2012, 6, 7084-7091.
179. Choi, C. H.; Park, S. H.; Woo, S. I. Phosphorus–nitrogen dual doped carbon as an effective catalyst for oxygen reduction reaction in acidic media: effects of the amount of P-doping on the physical and electrochemical properties of carbon. *J. Mater. Chem.* 2012, 22, 12107-12115.
180. Patel, M.; Savaram, K.; Keating, K.; He, H. Rapid Transformation of Biomass Compounds to Metal Free Catalysts via Short Microwave Irradiation. *Journal of Natural Products Research Updates* 2015, 1, 18-28.
181. Patel, M. A.; Luo, F.; Khoshi, M. R.; Rabie, E.; Zhang, Q.; Flach, C. R.; Mendelsohn, R.; Garfunkel, E.; Szostak, M.; He, H. P-Doped Porous Carbon as Metal Free Catalysts for Selective Aerobic Oxidation with an Unexpected Mechanism. *ACS nano* 2015.
182. Herrmann, W. A. N- Heterocyclic Carbenes: A New Concept in Organometallic Catalysis. *Angew. Chem. Int. Ed.* 2002, 41, 1290-1309.
183. Zhao, X.; Yin, M.; Ma, L.; Liang, L.; Liu, C.; Liao, J.; Lu, T.; Xing, W. Recent advances in catalysts for direct methanol fuel cells. *Energy & Environmental Science* 2011, 4, 2736-2753.
184. Bond, G. C.; Thompson, D. T. Catalysis by gold. *Catalysis Reviews* 1999, 41, 319-388.
185. Du, P.; Eisenberg, R. Catalysts made of earth-abundant elements (Co, Ni, Fe) for water splitting: recent progress and future challenges. *Energy & Environmental Science* 2012, 5, 6012-6021.
186. Dhakshinamoorthy, A.; Primo, A.; Concepcion, P.; Alvaro, M.; Garcia, H. Doped Graphene as a Metal-Free Carbocatalyst for the Selective Aerobic Oxidation of Benzylic Hydrocarbons, Cyclooctane and Styrene. *Chemistry-a European Journal* 2013, 19, 7547-7554.
187. Zhang, L.; Niu, J.; Dai, L.; Xia, Z. Effect of microstructure of nitrogen-doped graphene on oxygen reduction activity in fuel cells. *Langmuir* 2012, 28, 7542-7550.
188. Zhang, L.; Niu, J.; Li, M.; Xia, Z. Catalytic mechanisms of sulfur-doped graphene as efficient oxygen reduction reaction catalysts for fuel cells. *The Journal of Physical Chemistry C* 2014, 118, 3545-3553.
189. Zhang, L.; Xia, Z. Mechanisms of oxygen reduction reaction on nitrogen-doped graphene for fuel cells. *The Journal of Physical Chemistry C* 2011, 115, 11170-11176.
190. Xue, Y.; Liu, J.; Chen, H.; Wang, R.; Li, D.; Qu, J.; Dai, L. Nitrogen- doped graphene foams as metal- free counter electrodes in high- performance dye- sensitized solar cells. *Angew. Chem. Int. Ed.* 2012, 51, 12124-12127.

191. Hsu, H.-C.; Shown, I.; Wei, H.-Y.; Chang, Y.-C.; Du, H.-Y.; Lin, Y.-G.; Tseng, C.-A.; Wang, C.-H.; Chen, L.-C.; Lin, Y.-C. Graphene oxide as a promising photocatalyst for CO₂ to methanol conversion. *Nanoscale* 2013, 5, 262-268.
192. Zeng, F.; Sun, Z.; Sang, X.; Diamond, D.; Lau, K. T.; Liu, X.; Su, D. S. In situ one- step electrochemical preparation of graphene oxide nanosheet- modified electrodes for biosensors. *ChemSusChem* 2011, 4, 1587-1591.
193. Wu, P.; Qian, Y.; Du, P.; Zhang, H.; Cai, C. Facile synthesis of nitrogen-doped graphene for measuring the releasing process of hydrogen peroxide from living cells. *J. Mater. Chem.* 2012, 22, 6402-6412.
194. Wu, P.; Du, P.; Zhang, H.; Cai, C. Microscopic effects of the bonding configuration of nitrogen-doped graphene on its reactivity toward hydrogen peroxide reduction reaction. *PCCP* 2013, 15, 6920-6928.
195. Steele, B. C.; Heinzel, A. Materials for fuel-cell technologies. *Nature* 2001, 414, 345-352.
196. Yu, Y.; Hu, Y.; Liu, X.; Deng, W.; Wang, X. The study of Pt@ Au electrocatalyst based on Cu underpotential deposition and Pt redox replacement. *Electrochim. Acta* 2009, 54, 3092-3097.
197. Geng, D.; Chen, Y.; Chen, Y.; Li, Y.; Li, R.; Sun, X.; Ye, S.; Knights, S. High oxygen-reduction activity and durability of nitrogen-doped graphene. *Energy & Environmental Science* 2011, 4, 760-764.
198. Wu, Z.; Iqbal, Z.; Wang, X. Metal-free, carbon-based catalysts for oxygen reduction reactions. *Frontiers of Chemical Science and Engineering* 2015, 9, 280-294.
199. Lee, K. R.; Lee, K. U.; Lee, J. W.; Ahn, B. T.; Woo, S. I. Electrochemical oxygen reduction on nitrogen doped graphene sheets in acid media. *Electrochem. Commun.* 2010, 12, 1052-1055.
200. Niwa, H.; Horiba, K.; Harada, Y.; Oshima, M.; Ikeda, T.; Terakura, K.; Ozaki, J.-i.; Miyata, S. X-ray absorption analysis of nitrogen contribution to oxygen reduction reaction in carbon alloy cathode catalysts for polymer electrolyte fuel cells. *J. Power Sources* 2009, 187, 93-97.
201. Wang, P.; Wang, Z.; Jia, L.; Xiao, Z. Origin of the catalytic activity of graphite nitride for the electrochemical reduction of oxygen: geometric factors vs. electronic factors. *PCCP* 2009, 11, 2730-2740.
202. Lin, Z.; Waller, G. H.; Liu, Y.; Liu, M.; Wong, C.-p. 3D Nitrogen-doped graphene prepared by pyrolysis of graphene oxide with polypyrrole for electrocatalysis of oxygen reduction reaction. *Nano Energy* 2013, 2, 241-248.
203. Kong, X.; Chen, Q.; Sun, Z. Enhanced Oxygen Reduction Reactions in Fuel Cells on H- Decorated and B- Substituted Graphene. *ChemPhysChem* 2013, 14, 514-519.
204. Okamoto, Y. First-principles molecular dynamics simulation of O₂ reduction on nitrogen-doped carbon. *Appl. Surf. Sci.* 2009, 256, 335-341.
205. Zheng, Y.; Jiao, Y.; Ge, L.; Jaroniec, M.; Qiao, S. Z. Two- Step Boron and Nitrogen Doping in Graphene for Enhanced Synergistic Catalysis. *Angew. Chem.* 2013, 125, 3192-3198.
206. Choi, C. H.; Chung, M. W.; Kwon, H. C.; Park, S. H.; Woo, S. I. B, N-and P, N-doped graphene as highly active catalysts for oxygen reduction reactions in acidic media. *Journal of Materials Chemistry A* 2013, 1, 3694-3699.

207. Navalon, S.; Dhakshinamoorthy, A.; Alvaro, M.; Garcia, H. Carbocatalysis by Graphene-Based Materials. *Chemical Reviews* 2014, 114, 6179-6212.
208. Jia, H. P.; Dreyer, D. R.; Bielawski, C. W. Graphite Oxide as an Auto-Tandem Oxidation-Hydration-Aldol Coupling Catalyst. *Adv. Synth. Catal.* 2011, 353, 528-532.
209. Jia, H. P.; Dreyer, D. R.; Bielawski, C. W. C-H oxidation using graphite oxide. *Tetrahedron* 2011, 67, 4431-4434.
210. Dreyer, D. R.; Jia, H. P.; Bielawski, C. W. Graphene oxide: a convenient carbocatalyst for facilitating oxidation and hydration reactions. *Angew. Chem. Int. Ed. Engl.* 2010, 49, 6813-6.
211. Dreyer, D. R.; Park, S.; Bielawski, C. W.; Ruoff, R. S. The chemistry of graphene oxide. *Chem. Soc. Rev.* 2010, 39, 228-240.
212. Dreyer, D. R.; Jia, H. P.; Bielawski, C. W. Graphene oxide: a convenient carbocatalyst for facilitating oxidation and hydration reactions. *Angewandte Chemie* 2010, 122, 6965-6968.
213. Dreyer, D. R.; Jia, H.-P.; Todd, A. D.; Geng, J.; Bielawski, C. W. Graphite oxide: a selective and highly efficient oxidant of thiols and sulfides. *Organic & biomolecular chemistry* 2011, 9, 7292-7295.
214. Jia, H.-P.; Dreyer, D. R.; Bielawski, C. W. C-H oxidation using graphite oxide. *Tetrahedron* 2011, 67, 4431-4434.
215. Jia, H. P.; Dreyer, D. R.; Bielawski, C. W. Graphite Oxide as an Auto- Tandem Oxidation-Hydration-Aldol Coupling Catalyst. *Adv. Synth. Catal.* 2011, 353, 528-532.
216. Pan, Y.; Wang, S.; Kee, C. W.; Dubuisson, E.; Yang, Y.; Loh, K. P.; Tan, C.-H. Graphene oxide and Rose Bengal: oxidative C-H functionalisation of tertiary amines using visible light. *Green chemistry* 2011, 13, 3341-3344.
217. Su, C.; Acik, M.; Takai, K.; Lu, J.; Hao, S.-j.; Zheng, Y.; Wu, P.; Bao, Q.; Enoki, T.; Chabal, Y. J. Probing the catalytic activity of porous graphene oxide and the origin of this behaviour. *Nature communications* 2012, 3, 1298.
218. Long, Y.; Zhang, C.; Wang, X.; Gao, J.; Wang, W.; Liu, Y. Oxidation of SO₂ to SO₃ catalyzed by graphene oxide foams. *J. Mater. Chem.* 2011, 21, 13934-13941.
219. Dhakshinamoorthy, A.; Alvaro, M.; Concepción, P.; Fornés, V.; Garcia, H. Graphene oxide as an acid catalyst for the room temperature ring opening of epoxides. *Chem. Commun.* 2012, 48, 5443-5445.
220. Dhakshinamoorthy, A.; Alvaro, M.; Puche, M.; Fornes, V.; Garcia, H. Graphene oxide as catalyst for the acetalization of aldehydes at room temperature. *ChemCatChem* 2012, 4, 2026-2030.
221. Verma, S.; Mungse, H. P.; Kumar, N.; Choudhary, S.; Jain, S. L.; Sain, B.; Khatri, O. P. Graphene oxide: an efficient and reusable carbocatalyst for aza-Michael addition of amines to activated alkenes. *Chem. Commun.* 2011, 47, 12673-12675.
222. Kumar, A. V.; Rao, K. R. Recyclable graphite oxide catalyzed Friedel-Crafts addition of indoles to α , β -unsaturated ketones. *Tetrahedron Lett.* 2011, 52, 5188-5191.
223. Hu, F.; Patel, M.; Luo, F.; Flach, C.; Mendelsohn, R.; Garfunkel, E.; He, H.; Szostak, M. Graphene-Catalyzed Direct Friedel-Crafts Alkylation Reactions: Mechanism, Selectivity, and Synthetic Utility. *J. Am. Chem. Soc.* 2015, 137, 14473-14480.
224. Tang, S.; Cao, Z. Site-dependent catalytic activity of graphene oxides towards oxidative dehydrogenation of propane. *PCCP* 2012, 14, 16558-16565.

225. Schwartz, V.; Fu, W.; Tsai, Y. T.; Meyer, H. M.; Rondinone, A. J.; Chen, J.; Wu, Z.; Overbury, S. H.; Liang, C. Oxygen- Functionalized Few- Layer Graphene Sheets as Active Catalysts for Oxidative Dehydrogenation Reactions. *ChemSusChem* 2013, 6, 840-846.
226. Patel, M. A.; Luo, F.; Khoshi, M. R.; Rabie, E.; Zhang, Q.; Flach, C. R.; Mendelsohn, R.; Garfunkel, E.; Szostak, M.; He, H. P-Doped Porous Carbon as Metal Free Catalysts for Selective Aerobic Oxidation with an Unexpected Mechanism. *ACS Nano* 2016, 10, 2305-2315.
227. Boukhvalov, D. W.; Dreyer, D. R.; Bielawski, C. W.; Son, Y. W. A computational investigation of the catalytic properties of graphene oxide: Exploring mechanisms by using DFT methods. *ChemCatChem* 2012, 4, 1844-1849.
228. Gao, Y.; Hu, G.; Zhong, J.; Shi, Z.; Zhu, Y.; Su, D. S.; Wang, J.; Bao, X.; Ma, D. Nitrogen- Doped sp²- Hybridized Carbon as a Superior Catalyst for Selective Oxidation. *Angew. Chem. Int. Ed.* 2013, 52, 2109-2113.
229. Long, J. L.; Xie, X. Q.; Xu, J.; Gu, Q.; Chen, L. M.; Wang, X. X. Nitrogen-Doped Graphene Nanosheets as Metal-Free Catalysts for Aerobic Selective Oxidation of Benzylic Alcohols. *Acs Catalysis* 2012, 2, 622-631.
230. Watanabe, H.; Asano, S.; Fujita, S.-i.; Yoshida, H.; Arai, M. Nitrogen-Doped, Metal-Free Activated Carbon Catalysts for Aerobic Oxidation of Alcohols. *ACS Catalysis* 2015, 5, 2886-2894.
231. Meng, Y.; Voiry, D.; Goswami, A.; Zou, X.; Huang, X.; Chhowalla, M.; Liu, Z.; Asefa, T. N-, O-, and S-Tridoped Nanoporous Carbons as Selective Catalysts for Oxygen Reduction and Alcohol Oxidation Reactions. *J. Am. Chem. Soc.* 2014, 136, 13554-13557.
232. Li, W. J.; Gao, Y. J.; Chen, W. L.; Tang, P.; Li, W. Z.; Shi, Z. J.; Su, D. S.; Wang, J. G.; Ma, D. Catalytic Epoxidation Reaction over N-Containing sp(2) Carbon Catalysts. *Acs Catalysis* 2014, 4, 1261-1266.
233. Kong, X.-k.; Sun, Z.-y.; Chen, M.; Chen, Q.-w. Metal-free catalytic reduction of 4-nitrophenol to 4-aminophenol by N-doped graphene. *Energy & Environmental Science* 2013, 6, 3260-3266.
234. Chen, T.-W.; Xu, J.-Y.; Sheng, Z.-H.; Wang, K.; Wang, F.-B.; Liang, T.-M.; Xia, X.-H. Enhanced electrocatalytic activity of nitrogen-doped graphene for the reduction of nitro explosives. *Electrochem. Commun.* 2012, 16, 30-33.
235. Hayes, B. L. Microwave synthesis: chemistry at the speed of light. 2002.
236. Kappe, C. O. Controlled microwave heating in modern organic synthesis. *Angew. Chem. Int. Ed.* 2004, 43, 6250-6284.
237. Wiesbrock, F.; Hoogenboom, R.; Schubert, U. S. Microwave- assisted polymer synthesis: state- of- the- art and future perspectives. *Macromol. Rapid Commun.* 2004, 25, 1739-1764.
238. Roberts, B. A.; Strauss, C. R. Toward rapid, "green", predictable microwave-assisted synthesis. *Acc. Chem. Res.* 2005, 38, 653-661.
239. Gerbec, J. A.; Magana, D.; Washington, A.; Strouse, G. F. Microwave-enhanced reaction rates for nanoparticle synthesis. *J. Am. Chem. Soc.* 2005, 127, 15791-15800.
240. Motasemi, F.; Afzal, M. T. A review on the microwave-assisted pyrolysis technique. *Renewable and Sustainable Energy Reviews* 2013, 28, 317-330.

241. Mutyala, S.; Fairbridge, C.; Paré, J. J.; Bélanger, J. M.; Ng, S.; Hawkins, R. Microwave applications to oil sands and petroleum: A review. *Fuel Process. Technol.* 2010, 91, 127-135.
242. Abubakar, Z.; Salema, A. A.; Ani, F. N. A new technique to pyrolyse biomass in a microwave system: effect of stirrer speed. *Bioresour. Technol.* 2013, 128, 578-585.
243. Mudgett, R. Microwave food processing. *Food technology (USA)* 1989.
244. Zlotorzynski, A. The application of microwave radiation to analytical and environmental chemistry. *Crit. Rev. Anal. Chem.* 1995, 25, 43-76.
245. Datta, A. K.; Davidson, P. M. Microwave and radio frequency processing. *J. Food Sci.* 2000, 65, 32-41.
246. Galema, S. A. Microwave chemistry. *Chem. Soc. Rev.* 1997, 26, 233-238.
247. Thostenson, E.; Chou, T.-W. Microwave processing: fundamentals and applications. *Composites Part A: Applied Science and Manufacturing* 1999, 30, 1055-1071.
248. Kingston, H. M.; Jassie, L. B. *Introduction to microwave sample preparation: theory and practice*. American Chemical Society: 1988.
249. Vázquez, E.; Giacalone, F.; Prato, M. Non-conventional methods and media for the activation and manipulation of carbon nanoforms. *Chem. Soc. Rev.* 2014, 43, 58-69.
250. Faraji, S.; Ani, F. N. Microwave-assisted synthesis of metal oxide/hydroxide composite electrodes for high power supercapacitors—a review. *J. Power Sources* 2014, 263, 338-360.

Chapter 2. Direct Production of Graphene Nanosheets for Near Infrared Photoacoustic Imaging

2.1. Introduction

Recently, there has been a surge of interest in nanosized graphene sheets due to their unique size effects,¹⁻⁴ edge effects,⁵⁻⁷ and even quantum confinement effects,⁸ in addition to the intrinsic exotic properties of graphene. Several strategies have been developed to fabricate nanosized graphene sheets.⁸⁻¹⁰ Most of them rely on chemical oxidation *via* Hummers' method or other modified Hummers' methods, which always involve the oxidization of graphite powder to produce heavily oxidized graphene sheets termed graphene oxide (GO).¹¹ The oxidation reaction is a lengthy process (from hours to several days) and the aggressive chemistry also leads to uncontrollable cutting/unzipping of graphene sheets into small pieces of different sizes and shapes with extensive defects.^{12,}

13

To reach predefined nanometer-sized GO sheets, extended oxidation and sonication¹⁴ or other oxidative cutting reactions are required.^{10, 15} Alternatively, nanosized GO sheets can be synthesized using starting materials which are already small such as graphite nanofibers or carbon fibers.^{16, 17} In GO, most of the exotic properties of graphene have vanished due to the high density of oxygen containing groups that heavily distort and break up the π -conjugated structure. Various approaches to reduce GO including chemical, electrochemical, and hydrothermal methods have been explored with only a fraction of the graphene properties recovered.^{4, 8, 9, 18-20} No strategy has been reported to directly fabricate graphene nanosheets (instead of GO nanosheets) in a one-pot reaction. Theoretical studies

of graphite oxidation have demonstrated that the activation barrier to initiate the oxidation of pristine graphene is much greater than the energy requirement for additional oxidation at those defect sites.²¹ It is the latter oxidation process is responsible for cutting graphene sheets into small pieces.^{1, 22, 23} Therefore, from a thermodynamic point of view, it is a daunting challenge to directly produce graphene nanosheets (instead of graphene oxide) with their π conjugated structures and properties of graphene largely retained in a one-pot oxidation reaction.²³

Microwave chemistry, due to the different heating mechanism compared to traditional convection heating, has been well known for high speed synthesis, shortening reaction times from days to minutes, even to seconds.²⁴ Even though the observed rate enhancements have been ascribed to purely thermal/kinetic effects, *i.e.* a consequence of the high reaction temperatures that can be attained so rapidly, these unique effects can also lead to reaction selectivity to enable fabrication of desired products.²⁵ Herein we report an unexpected discovery that monodispersed graphene nanosheets can be directly and rapidly (30s) fabricated *via* microwave assisted nitronium oxidation chemistry. The graphene nanosheets as-fabricated have strong NIR absorption and high efficiency in the generation of photoacoustic signals without the need of any post-reduction processes. Furthermore, from previous experimental reports on the oxidation of carbon nanotubes (CNTs)^{1, 22, 23} and recent theoretical studies on the mechanism of graphene unzipping/cutting,^{13, 26} it can be concluded that KMnO_4 in Hummer's method plays a major role in the experimentally observed cutting/unzipping. We reveal that KMnO_4 may also protect the already oxidized sites from gasification (CO_2 and/or CO) and hole generation, and thereby slowing down the subsequent global fracture of graphene sheets into nanosized pieces. At the same time,

KMnO₄ may also initiate its own oxidative cutting leading to highly oxidized graphene sheets with much larger lateral dimensions and straight edges compared to graphene nanosheets obtained *via* nitronium oxidation. Understanding the roles and molecular cutting mechanisms of these oxidants allows us to fabricate graphene sheets in a controlled fashion with different morphological and electronic structures to accommodate different applications.

2.2. Results and Discussion

We recently developed a rapid, microwave enabled, scalable approach to produce large, highly-conductive graphene sheets directly from graphite powder.²⁷ We intentionally excluded KMnO₄ (as is used in Hummer's methods) with the aim of avoiding cutting and exploited the advantage of aromatic oxidation by nitronium ions (NO₂⁺) combined with microwave heating. This unique combination promotes rapid and simultaneous oxidation of multiple non-neighboring carbon atoms across an entire graphene sheet, so that a minimum concentration of oxygen moieties enables the separation and dispersion of relatively large graphene sheets (several tens of micrometers) into solutions without cutting them into small pieces.²⁷ Due to the essential role of microwave heating during the production, we refer to these dispersed graphene sheets as microwave-enabled low oxygen graphene (ME-LOGr). High resolution transmission electron microscopy shows that the ME-LOGr consists of many different crystalline-like domains, which are uniformly distributed across the entire ME-LOGr sheets.

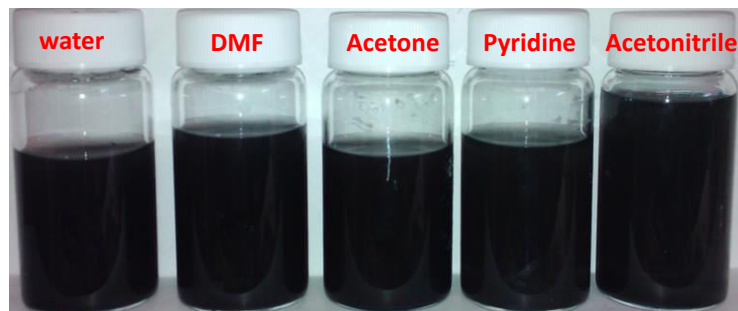


Figure 2.1. Digital photographs of stable ME-LOGr solutions in water, N, N-dimethylformamide (DMF), acetone, pyridine, and acetonitrile.

In this work²⁸, we discovered that high concentrations of graphene nanosheets can be rapidly obtained by simply increasing the NO_2^+ concentration. In a typical experiment, graphite powder is mixed with concentrated nitric acid, sulfuric acid, and a small amount of water (volume ratio of $\text{HNO}_3\text{:H}_2\text{SO}_4\text{:H}_2\text{O}$ of 1: 2.5: 0.07) and then subjected the solution to 30 seconds of microwave irradiation (300 watts). The reaction results in a dispersed slurry, which is significantly easier to clean and handle than the sticky paste obtained from Hummer's method.¹¹ Vacuum filtration was used to remove the acid residues and the possible byproducts. With the help of bath sonication (30 min), the cleaned cake on the filter paper can be re-dispersed in a wide range of polar solvents to form graphene colloidal solutions without the use of surfactants or stabilizers. The concentration of the nanosheets in water is 0.4 mg/ml, and is much higher in other organic solvents, such as N, N-dimethylformamide (DMF), acetone, pyridine, and acetonitrile (**Figure 2.1**). These solutions are stable, showing no precipitation for several months. From atomic force microscopy (AFM) measurements (**Figure 2.2A**), the nanosheets have a lateral diameter of 10 ± 4 nm and an average thickness of 0.75 ± 0.23 nm (**Figure 2.3**). This result demonstrates that the microwave assisted oxidation reaction directly converted the large graphene sheets in graphite particles into graphene nanosheets with a thickness of one or

two layers, which is in stark contrast to previous approaches that require a separate step for cutting the GO sheets to the nanometer scale.^{14, 15}

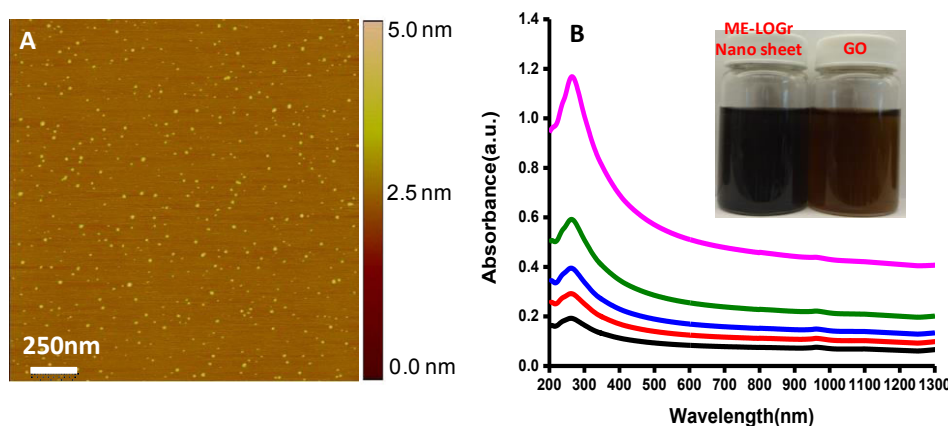


Figure 2.2. (A) AFM images of ME-LOGr nanosheets, (B) UV-Vis-NIR spectra of ME-LOGr nanosheets with concentrations of 20 (pink), 10 (olive), 6.7 (blue), 5 (red), and 3.3 mg/L (black), respectively. Inset B, a digital picture of an aqueous suspension of ME-LOGr nanosheets (left) and graphene oxide (GO) nanosheets (right) shows different colors, indicating they are in different oxidation states. The GO nanosheets were obtained *via* Control-A Experiment in which nitronium ions and KMnO_4 both act as an oxidant.

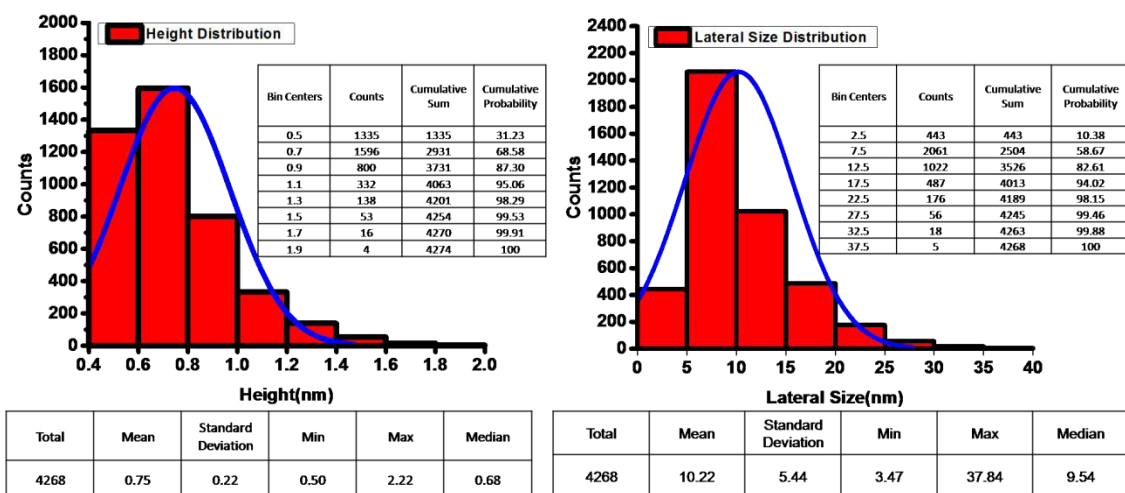


Figure 2.3. Statistical analysis of the AFM pictures of ME-LOGr nanosheets.

The color of the nanosheet suspensions is grayish black, similar to the suspensions of the larger ME-LOGr sheets,²⁷ which qualitatively suggests that we have directly obtained graphene nanosheets with small amounts of oxygen-containing groups instead of

heavily oxidized GO nanosheets (**Figure 2.2B**, inset). The plasmon band in the UV region (**Figure 2.2B**) is centered at ~ 262 nm, slightly blue-shifted compared to the larger ME-LOGr sheets (267 nm), but still much higher than GO (~ 230 nm).²⁹ Additionally, unlike GO, the UV-Vis-NIR spectrum of the solution of graphene nanosheets displayed strong while nearly wavelength independent absorption in the visible and NIR regions, which suggests that the π -conjugation within the graphene sheets is largely retained.³⁰⁻³² The molecular absorption coefficient of the nanosheets at 984 nm is 21.7 L/g.cm and at 808 nm is 22.7 L/g.cm, which is very close to that of reduced GO (rGO) nanosheets (24.6 L/g.cm at 808 nm) as reported by Dai *et al.*¹⁹ It should be noted that the molecular absorption coefficient of the rGO nanosheets was measured after they were PEGylated due to the insolubility of rGO in aqueous solutions.

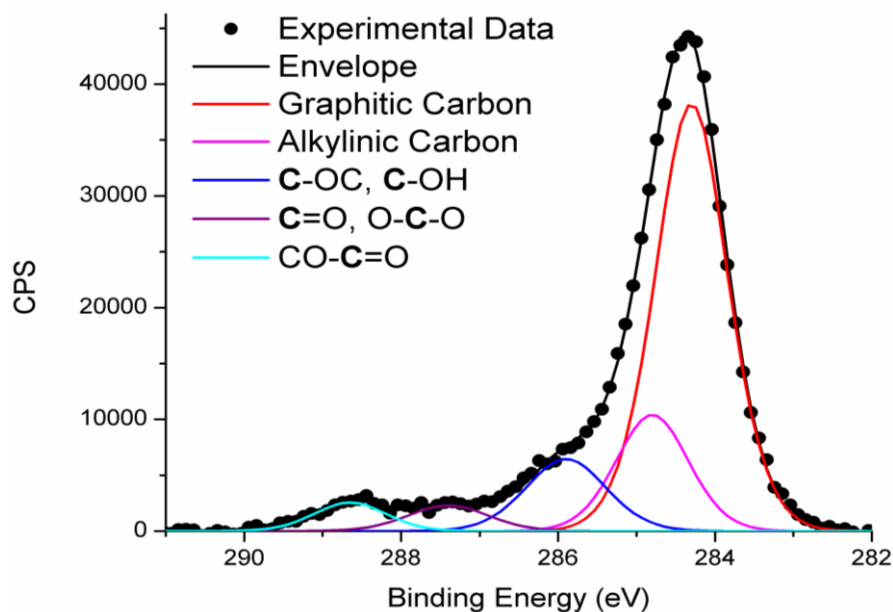


Figure 2.4. An x-ray photoelectron spectrum (XPS) of ME-LOGr nanosheets.

The chemical functionalities of the nanosheets were studied with X-ray photoelectron spectroscopy (XPS) (**Figure 2.4**). The nanosheets have a large amount of carbon that is not bound to oxygen ($\sim 80\%$ of the total carbon), similar to the larger-sized

ME-LOGr sheets,²⁷ and those of reduced GO sheets.^{33, 34} Due to the similar production procedures and oxidation levels of the larger-sized ME-LOGr sheets, we refer to these nanosheets as ME-LOGr nanosheets. With careful fitting, we found that the nanosheets contained more oxygen functional groups of higher oxidation levels, such as –COOH, than was observed in larger ME-LOGrsheets.²⁷ This is consistent with the observation that –COOH groups are normally located on the edges of the graphene sheets.^{35, 36} The nanosheets obviously contain a higher edge/center ratio when compared to larger ME-LOGr sheets.

Even though the ME-LOGr nanosheets contain a similar quantity of oxygen-free carbon compared to that reported for rGO,³³⁻³⁵ they may have different molecular structures, which leads to different physical chemical properties. As an example, most of the rGO sheets are not stable in aqueous solution without the help of surfactants or stabilizers. Furthermore, it was reported that GO and rGO nanosheets obtained *via* further oxidation and/or reduction of large GO sheets fabricated by Hummers method are highly luminescent, which has been attributed to special edge effects and/or the existence of small and isolated graphene domains.^{35, 37-40} In contrast, ME-LOGr nanosheets can form stable aqueous colloidal solutions without the necessity of surfactants and stabilizers (**Figure 2.1**). They are not photo-luminescent, suggesting that either the intact graphene domains are much larger than those in GO or rGO nanosheets, or they possess different electronic structures at their edges.⁴⁰

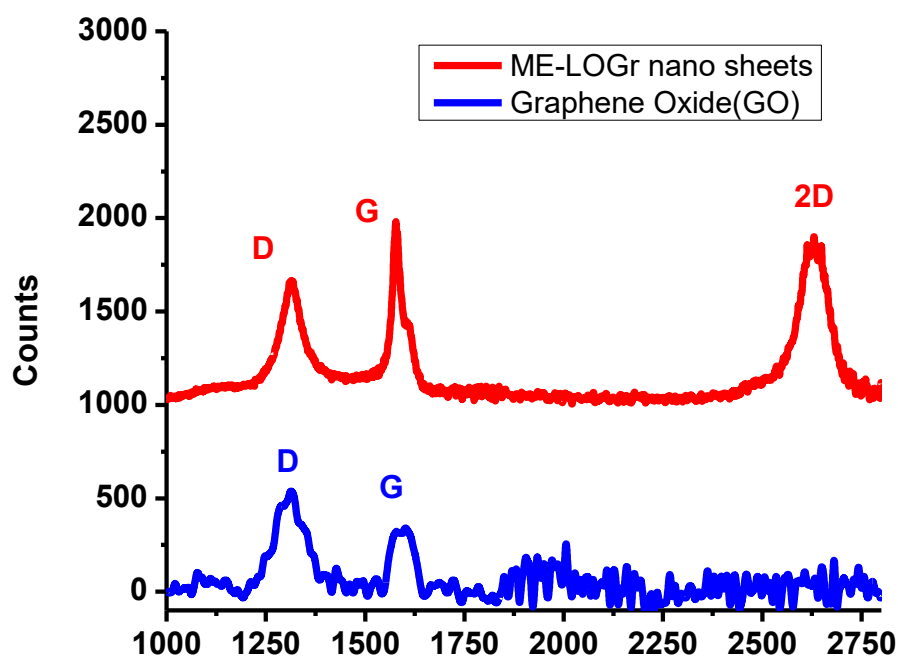


Figure 2.5. Raman spectra of ME-LOGr nanosheets (red) and GO nanosheets (blue). GO nanosheets were obtained *via* Control- A experiment where nitronium ions and KMnO_4 both act as an oxidant.

Raman spectroscopy was utilized to estimate the intact graphene domain sizes in the ME-LOGr nanosheets. The typical features of G band, defect D band, and 2D band are shown in the Raman spectrum of ME-LOGr (**Figure 2.5**). The D to G band intensity ratio (I_D/I_G) is 0.65, which is slightly higher than that from larger ME-LOGr as we reported earlier,²⁷ but much lower than GO (1.65). The reported I_D/I_G ratios for r-GO are similar to, or even higher than that for GO, which has been explained by the fact that chemical reduction preferentially generates a greater number of smaller crystalline domains rather than increasing the size of existing graphitic domains.^{41, 42} Using the empirical Tuinstra-Koenig relation,⁴³ we estimated that the size of the ordered crystallite graphitic domains was ≈ 6.7 nm, much larger than those in GO and rGO (1-3 nm). Therefore, although the apparent electronic structure and the graphitic carbon components of the ME-LOGr

nanosheets are similar to rGO, as demonstrated by their color, UV-Vis-NIR and XPS spectra, the ME-LOGr sheets have unique molecular structures that differ from both GO and r-GO.^{42, 44}

It has been reported that the 2D band in GO is absent.^{34, 42} Additionally, the reduction of GO results in only a small increase in the 2D band intensity, presumably due to the defects in the graphitic structures.⁴¹ A decrease of the 2D band intensity has also been associated with the modification of pristine graphene through chemisorption⁴⁵ and physisorption.^{46, 47} However, for ME-LOGr nanosheets, the intensity of the 2D band is similar to that of the G band. The small intensity ratio of D/G bands and the high intensity of 2D band are in contrast to the larger D/G band ratio and the absence of the 2D band in GO and rGO, indicating that the intrinsic structure and properties of graphene were largely retained in ME-LOGr nanosheets, and these nanosheets are clean without adsorbent-induced surface modification.⁴¹

All of these results collectively demonstrate that with microwave heating and nitronium oxidation of graphite particles directly leads to relatively “clean” graphene nanosheets instead of GO nanosheets as produced *via* Hummer’s method.¹¹ The molecular mechanism for the experimentally observed graphite oxidation and the accompanied graphene sheet cutting *via* Hummer’s method remains elusive. From density functional calculations, it has been reported that graphene cutting is likely initiated by the formation of an epoxy group. The strain associated with epoxy group formation on graphene facilitates the generation of another epoxy group at its nearest neighbor, and finally leads to linearly aligned epoxy groups on the surface as the oxidation progresses.^{13, 26, 48} These aligned epoxy groups co-operatively strain the graphene sheets, which accounts for the GO

cutting. In Hummer's method, both HNO_3 and KMnO_4 in concentrated H_2SO_4 act as oxidants *via* different mechanisms (NaNO_3 converts to HNO_3 under acidic conditions),¹¹ so it is not immediately clear which oxidant played a more important role in the observed graphene sheet cutting.

Due to the chemical similarity of graphene and carbon nanotubes (CNTs), additional insight into the mechanism of oxidative cutting of graphene/GO sheets may also be derived from the extensive experimental studies of shortening and longitudinal unzipping of CNTs. Both $\text{KMnO}_4/\text{H}_2\text{SO}_4$ and $\text{HNO}_3/\text{H}_2\text{SO}_4$ have been used for oxidative cutting of CNTs. An important common feature for these two oxidation systems is that the initiation, which produces various oxygen containing groups, is the rate determining step. Further local oxidation of the oxidized carbon atoms and their near neighbors (the key procedure in cutting and unzipping) under the same reaction conditions is favored over oxidation on defect-free graphene regions in these two cases.²³ Both methods produced highly oxidized products, indicating further oxidation of the defect-free graphene regions is still continuing during the cutting step.^{1, 22, 49}

While the oxidation processes that occur *via* nitronium ions (produced by the mixture of concentrated HNO_3 and H_2SO_4) leads mainly to CNT shortening,^{22, 49} the oxidation by KMnO_4 in anhydrous H_2SO_4 predominantly induces longitudinal unzipping of CNTs to produce graphene nanoribbons.¹ It was reported that nitronium ions not only attack the existing defects on the graphene, but also randomly attack the relatively inert defect-free graphene basal planes, producing various oxygen containing groups,¹ which is the first step in oxidative cutting. As the oxidation progresses, it can further etch these oxidized sites, leading to vacancies, holes and finally fracturing the CNTs into short

pieces.^{22, 49} The mechanism for the longitudinal unzipping has been explained by the oxidation being initiated with permanganate ions attacking predominantly existing defects in CNTs (such as alkenes) to form a cyclic manganate ester. With further oxidation, the esters can form dione structures, which distort the β,α -alkenes making the neighboring sites more prone to further attacks. It is in this step-wise manner that the longitudinal unzipping of the tubes into ribbons occurs. Note that most of the GO sheets formed *via* Hummers methods have straight edges³⁰ similar to the graphene ribbons obtained by longitudinal unzipping of CNTs *via* $\text{KMnO}_4/\text{H}_2\text{SO}_4$. Combined with the theoretical studies described above,^{13, 26} it is easy to conclude that KMnO_4 plays a major role in the observed cutting/unzipping in Hummers oxidation processes.

As a control experiment (which is referred as Control-A), KMnO_4 (5 times of the weight of graphite particles, the same ratio has been used to unzip CNTs¹) was introduced to the reaction mixture with the same previously used volume ratio of $\text{H}_2\text{SO}_4/\text{HNO}_3/\text{H}_2\text{O}$ (which we assume, to first order, will result in the same concentration of nitronium ions in solution). Applying the same microwave power and irradiation time, a highly oxidized product is obtained. Similar vacuum filtration procedures were performed to clean the residues of KMnO_4 , acids, and other reaction byproducts. The resulting filtrate cake appeared quite similar to GO prepared by traditional Hummers' methods, and was sticky and time consuming to clean.⁵⁰ When the cleaned filtrate cake was re-dispersed into water solution, the dispersed solution showed a brownish color (**Figure 2.2B** inset). The plasmon band of the control suspension in the UV region is centered at ~ 230 nm (**Figure 2.6B**), similar to that of GO prepared by Hummers' method.⁵¹ The absorption in the visible and NIR region dramatically decreased. The mass absorption coefficient at 808 nm and 984 nm

decreased to 0.76 and 0.54 L/g.cm, respectively. Compared to the ME-LOGr nanosheets at the same wavelengths (22.7 and 21.78 L/g.cm, respectively), this represents more than 30 and 40-fold decreases, suggesting that the addition of KMnO_4 to the system caused extensive oxidation of the graphene sheets. The much larger D/G ratio (1.65) and the complete absence of the 2D band in the Raman spectrum shown in **Figure 2.5** provided further evidence that the product was heavily oxidized.

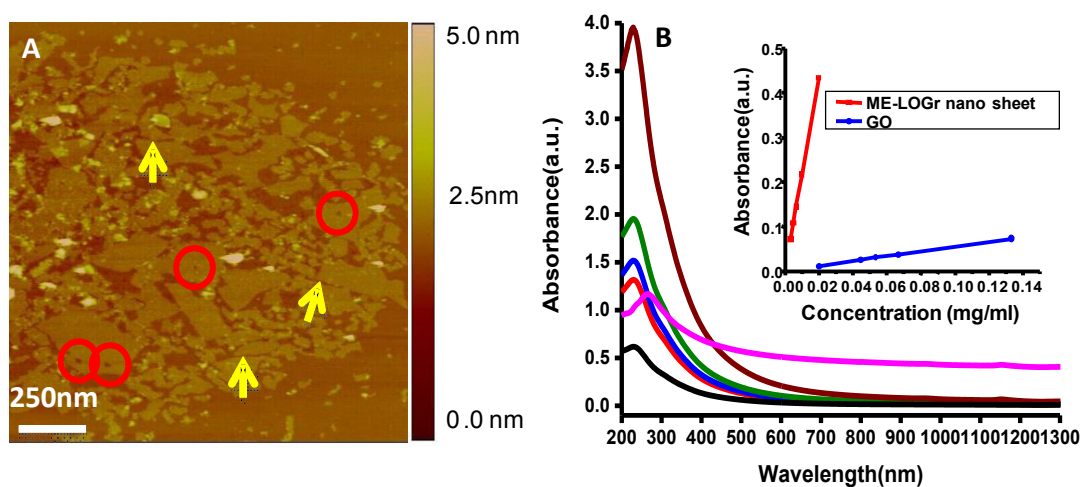


Figure 2.6. (A) AFM image of graphene oxide nanosheets obtained *via* Control-A experiment. Some of the nanometer gaps between nanosheets and nanoholes generated during the oxidation reaction were labeled with arrows and circles, respectively. (B) UV-Vis-NIR spectra of the GO sheets at different concentrations of 133.3 (Wine), 66.7 (olive), 53.3 (blue), 44.4 (red), and 33.3 mg/L (black), respectively. For better comparison, the pink curve (20mg/L of ME-LOGr nanosheets) in **Figure 2.2B** is also displayed in panel B with the same color. Inset (B) shows the linear relationships between the absorption at 984 nm and the concentration of ME-LOGr nanosheets and GO. The mass coefficient of the ME-LOGr is 40 fold higher than that of GO.

Surprisingly, the size of the control sheets is much larger than the ME-LOGr nanosheets obtained without KMnO_4 present (**Figure 2.6A**). We observe a significant proportion of sheets in the range of 200 - 400 nm among smaller sheets of several tens of nanometers. Additionally, a large majority of the sheets have straight edges, quite similar to GO sheets obtained *via* Hummer's method. For the first time, we observed some GO

sheets with straight edges separated with small gaps of only several nanometers (indicated by arrows in **Figure 2.6A**). These nanogaps provide strong evidence that molecular cutting/unzipping has occurred during the oxidation. Since these nanogaps are only observed when KMnO_4 is present during the reaction, it is apparent that KMnO_4 plays a major role in cutting and unzipping graphene sheets to small pieces, similar to those observed in Hummer's method.¹³

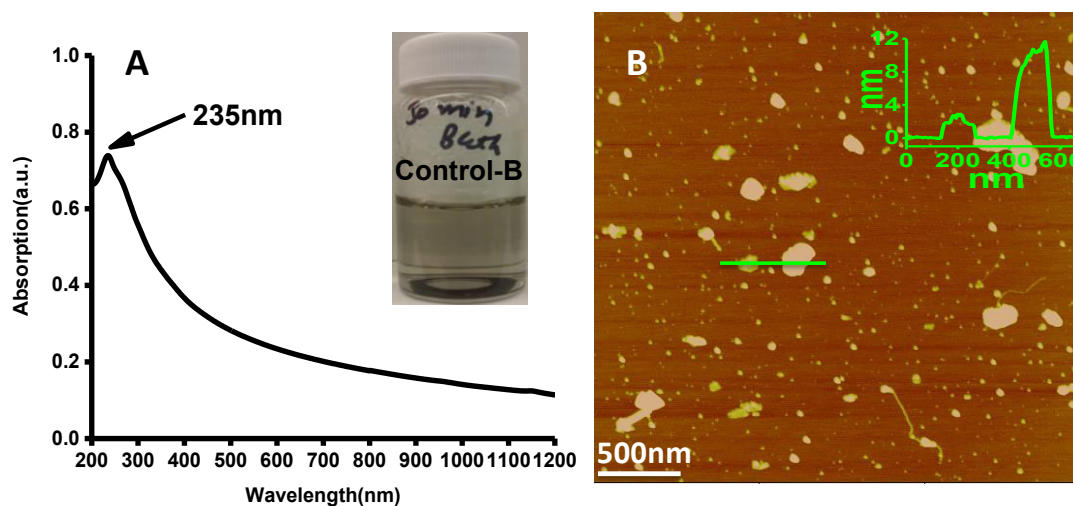


Figure 2.7. (A) UV-Vis-NIR spectrum of the nanosheets obtained *via* KMnO_4 oxidation (Control-B experiment). The maximum plasmon peak is around 235 nm. Inset (A) is a picture of the dispersed nanosheet solution. The brownish yellow color and the plasmon peak at 235 nm collectively demonstrated that the product is highly oxidized. (B) An AFM image of the nanosheets, majority of which have multiple layers.

To further understand the role of KMnO_4 as the sole oxidant, another control experiment (referred as Control-B) was conducted. In this experiment, NO_2^+ was excluded and the same weight ratio (5:1) between KMnO_4 and graphite particles in H_2SO_4 was used. Applying the same microwave power and irradiation time, Similar to the product obtained with both KMnO_4 and NO_2^+ (Control-A), the dispersed graphene sheets were highly oxidized in the reaction mixture, indicated by its yellowish-brownish color, and the maximum absorption at 235 nm in its UV-Vis spectrum (**Figure 2.7A**). However, the

concentration of the dispersed sheets is about 10 times lower than that achieved in Control A. Furthermore, a large majority of the dispersed sheets are multiple layered as observed by AFM measurements (**Figure 2.7B**). Most of the graphite particles were not exfoliated and they settled on the bottom of the vial, suggesting that the capability of KMnO_4 in anhydrous H_2SO_4 to intercalate into and oxidize the inner parts of graphite is not as efficient as NO_2^+ ions.

The molecular mechanisms leading to these significantly different results need further study. We hypothesize that it is due to the different initiation oxidation capabilities and the following oxidization pathways of KMnO_4 and NO_2^+ . Nitronium ions not only attack the existing defects on the graphene, but also randomly attack the relatively inert defect-free graphene basal planes.¹ In the following oxidation step, NO_2^+ continues to attack the already oxidized carbon atoms and carbon atoms far away from those already oxidized. An important consequence of these differences is that oxidation by NO_2^+ can naturally produce intact graphene domains separated by regions of oxygen containing groups.²⁷ With the increased speed of the second etching step, nanosheets with retained structures can be obtained. Alternatively, KMnO_4 starts oxidation at existing defect sites and the following oxidation preferentially attack the neighboring carbons which are already oxidized. While the high temperature reached by microwave heating selectively speeds up the cutting/unzipping process, the unzipped sheets are still more oxidized.

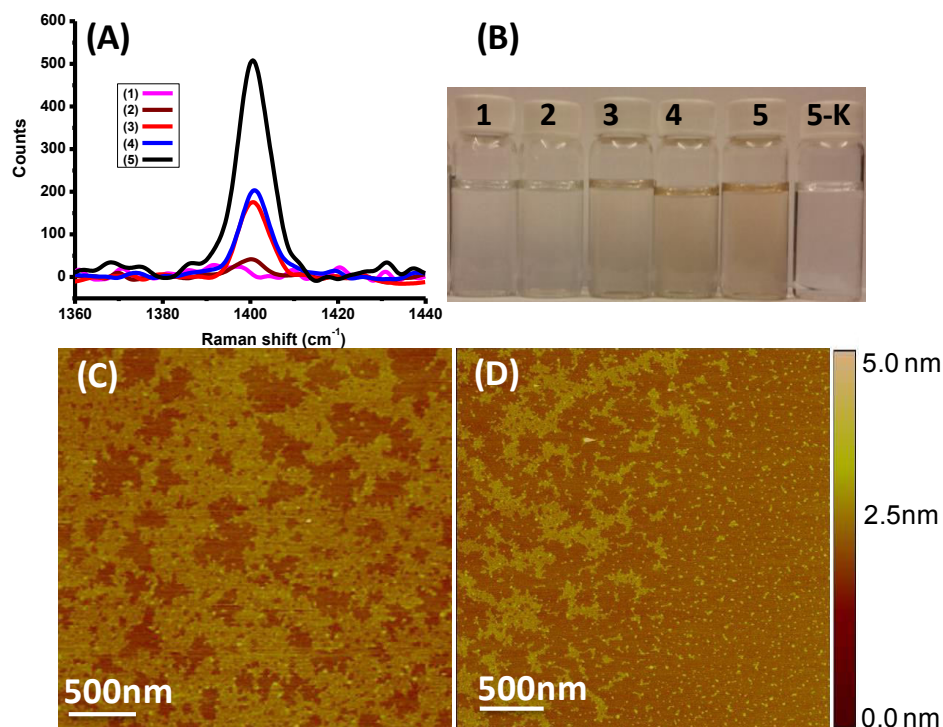


Figure 2.8. (A) Raman spectra of different concentrations of nitronium ions produced with different ratios of concentrated HNO₃, H₂SO₄, and H₂O with ratios of (1) 1:1:0; (2) 1:42:7 ; (3) 1:2.5:0.07; (4) 1:17.5:1.5 and (5) 1:4:0, respectively. (B) Digital pictures of filtrates obtained after graphite particles were oxidized in microwave with different ratios of HNO₃:H₂SO₄:H₂O of (1) to (5), and therefore different concentrations of nitronium ions. 5-K was obtained with the same ratio as (5), except that KMnO₄ was included. (C and D) AFM images of porous graphene sheets dispersed with magnetic stirring instead of sonication to avoid sonication-induced tearing. The graphene sheets in panels C, and D were obtained with ratio (3) and (4), respectively.

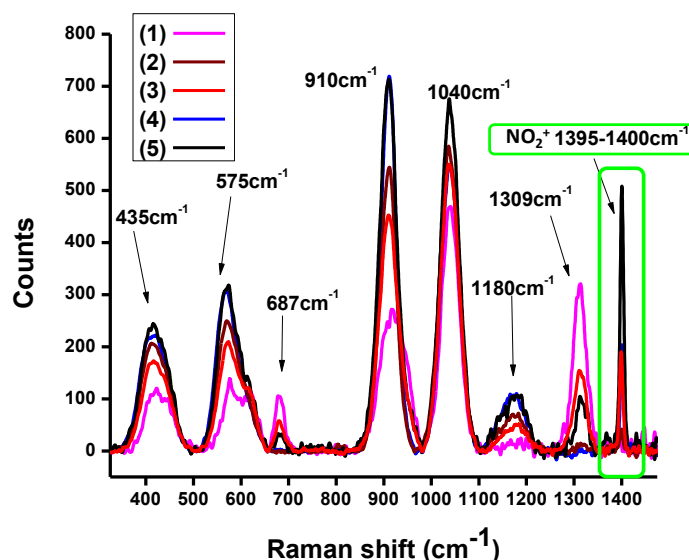


Figure 2.9. Raman spectra of the mixture of concentrated H_2SO_4 and HNO_3 and H_2O with different volume ratios of concentrated HNO_3 , H_2SO_4 , and H_2O with ratios of (1) 1:1:0; (2) 1:42:7 ; (3) 1:2.5:0.07; (4) 1:17.5:1.5 and (5) 1:4:0, respectively. The concentration of the generated nitronium ions by the acid mixtures increases as the ratio of H_2SO_4 , HNO_3 , and H_2O changes.⁵² Peak assignments are labeled on the spectra and listed in the following **Table 2.1**.

Table 2.1. An assigned name and position of the peaks from the above Raman spectra of the mixture of concentrated H_2SO_4 and HNO_3 and H_2O .

Peak name	Approximate peak position(vibrational band)
Concentrated H_2SO_4 peaks	$\sim 435\text{cm}^{-1}$, $\sim 575\text{cm}^{-1}$, $\sim 910\text{cm}^{-1}$, $\sim 1180\text{cm}^{-1}$,
Concentrated HNO_3 peaks	$\sim 687\text{cm}^{-1}$, $\sim 1309\text{cm}^{-1}$
Nitronium Ion Peak	$\sim 1400\text{cm}^{-1}$
Reference peak(bath acids)	$\sim 1040\text{cm}^{-1}$

To understand the formation pathways of graphene nanosheets *via* nitronium oxidation under microwave irradiation, different concentrations of nitronium ions were used for the microwave oxidation. The microwaved product was dispersed with mild magnetic stirring to avoid sonication-induced tearing. In our previous report,²⁷ a much lower concentration of nitronium ions (**Figure 2.8A**, line 1, volume ratio of H_2SO_4 : HNO_3 : H_2O =1:1:0) was used during microwave assisted oxidation. The graphene sheets obtained were large and free of nanometer sized holes.²⁷ In this work,²⁸ different concentrations of nitronium ions were produced with different ratios of H_2SO_4 , HNO_3 and H_2O . Raman spectroscopy was used to measure the relative concentrations of the nitronium ions as the solution ratios change (**Figure 2.8A**, and **Figure 2.9**).⁵² With a high concentration of nitronium ions, a large number of holes were generated in the basal plane of the graphene sheets (**Figure 2.8C**). These large porous sheets were obtained using the same oxidation conditions (line 3 in **Figure 2.8A**) as those shown in **Figure 2.2A**. With further increasing the concentration of nitronium ions, more holes were generated with some of the holes becoming much larger. Eventually, the big sheets fractured into nanosized sheets. (**Figure**

2.8D). At the same time, we also found that the weight of the cleaned filtrate cake on the filter paper gradually decreased, and the color of the filtrate gradually changed from colorless to light yellow and brown (**Figure 2.8B**), indicating a large amount of carbon lost either in the form of small organic compounds or CO₂, as previously reported.³³ The yellow colored filtrate was found to be fluorescent upon excitation at 335 nm and contains flavanol derivatives, confirmed by its fluorescence spectroscopy and GC-MS analysis.^{53, 54} In contrast, when KMnO₄ was introduced into the reaction system, the filtrate was almost colorless (**Figure 2.8B**, vial 5-K), suggesting much less carbon was lost during oxidation. At the same time, we found that the sheets have fewer holes (**Figure 2.6A** indicated by circles), suggesting that KMnO₄ protects the graphene sheets from being damaged by hole formation.

To understand the mechanism of nitronium oxidation under microwave irradiation, a control experiment (referred as Control-C) was performed using the same concentration of nitronium ions (line 3 in **Figure 2.8A**), however, this time with traditional heating. The temperature was controlled at 85 °C by a water bath as reported for CNT oxidative cutting.^{22, 49} As expected, 30-second heating did not lead to any observable reaction. When the reaction time was extended to 4 hours, small uniform graphene nanosheets (15 ± 5.3 nm in diameter and 1.5 ± 0.6 nm in height) were observed by AFM (**Figure 2.10A**). When compared to the nanosheets produced with microwave heating for 30 seconds, these nanosheets show an additional plasmon band at 235 nm in the UV-Vis spectrum (**Figure 2.10B**). This is an indication that the nanosheets are oxidized to a greater extent, which is consistent with previous reports showing that nitronium ions cut carbon nanotubes into highly oxidized short pipes.^{22, 49}

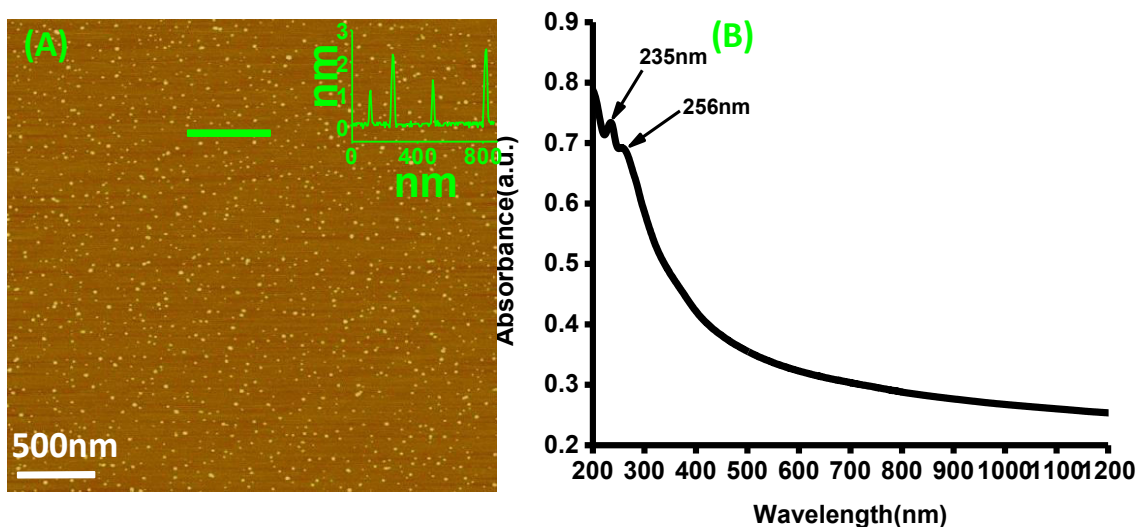


Figure 2.10. (A) An AFM image of nanosheets obtained with traditional heating (Control-C Experiment). (B) UV-Vis-NIR spectrum of the nanosheets indicates that these sheets are more oxidized than the ME-LOGr nanosheets fabricated *via* microwave heating.

The exact mechanism behind these results remains inconclusive. Based on the observations, we assume that microwave heating changes the relative speeds of the various competitive parallel (and sequential) reactions that can occur during graphite oxidation (**Scheme 2.1**). It has been reported that nitronium ions interact with graphene surfaces to form multiple aromatic radical-ion pairs *via* a single electron transfer (SET) pathway.⁵⁵ Epoxy and/or -OH groups are then formed following oxygen transfer to the aromatic radicals.^{27, 56} Further oxidation includes two simultaneous and competing processes: (1) continued initiation of oxidation in the intrinsic graphene domains resulting in generation of more -OH and/or epoxy groups with a reaction rate of $v_{\text{generation}}$; and/or (2) further oxidation of the initially oxidized carbon atoms, ultimately leading to gasification of the carbon atoms (mostly CO or CO₂) and generation of small carbon residual species (which are separated during filtration), resulting in vacancies and holes throughout the graphene basal planes. This process is also called defect consumption or etching^{23, 57} with a reaction rate of $v_{\text{consumption}}$. It was consumption of the defects and generation of vacancies and holes

in the sidewalls of carbon nanotubes that led to rapid cutting of the CNTs into short pipes and cutting graphene sheets to small pieces.^{22, 23} The relative reaction rates of these two processes determine the overall speed of nanosheet fabrication and also the oxidation level of the nanosheets. The reaction speeds of these two processes can be described using Arrhenius equations as follows,

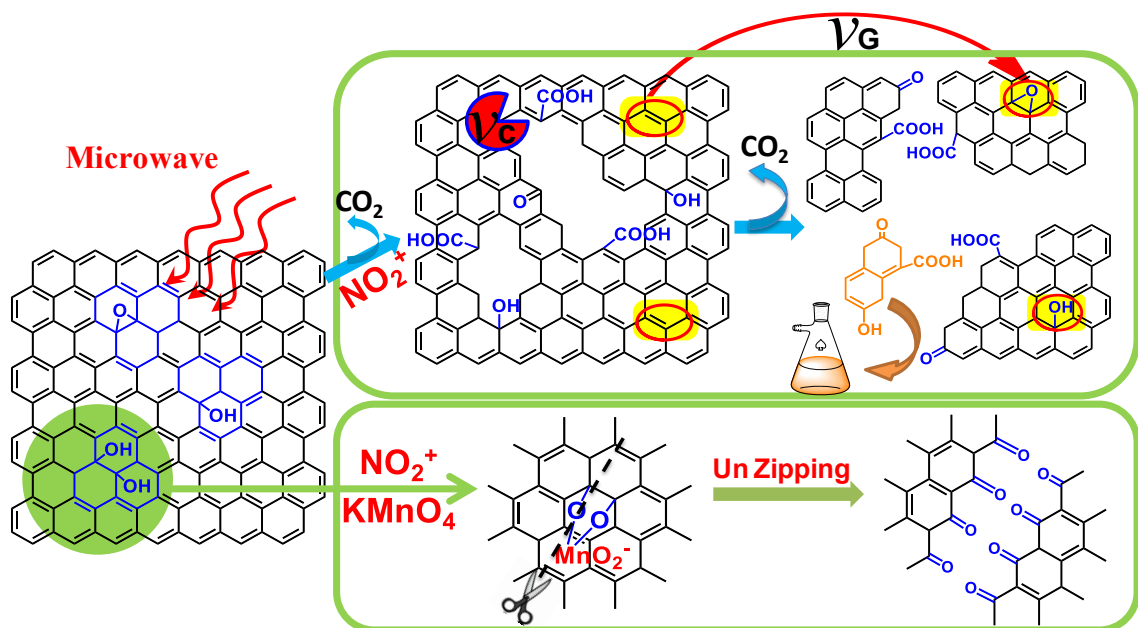
$$v_{Generation} = C_{Intrinsic-Gr} A e^{-Ea_{Generation} / RT}$$

$$v_{Consumption} = C_{Defects} A e^{-Ea_{Consumption} / RT}$$

In which, $C_{Intrinsic-Gr}$ and $C_{Defects}$ are the density of intrinsic graphene domains and the density of defects (such as oxygen containing groups) on a graphene sheets; $Ea_{Generation}$ is the activation energy of the initial oxidation of the intrinsic graphene domains and $Ea_{Consumption}$ is the activation energy of further oxidations of the already oxidized carbon atoms (defect consumption step).

When microwave heating is used to control the nitronium oxidation processes, the strong microwave absorption characteristic of graphite particles leads to the rapid achievement of high temperatures localized on/or near the graphite particles, which in turn dramatically increases the intercalation rate of nitronium ions into the graphite particles. This process is accompanied by the generation of a large amount of –OH and/or epoxy groups distributed over the entirety of the graphene sheets (high $C_{Defects}$). After this initial oxidation, in the subsequent competing reactions, it is possible that the defect consumption or etching speed ($v_{consumption}$) becomes faster than that of the continuing generation of

additional new defects ($v_{\text{generation}}$) on the intact graphene domains due to the high density of the -OH and/or epoxy groups generated in the first step (high C_{Defects}).⁵⁸ With the high temperatures obtained by microwave heating, the $v_{\text{consumption}}$ may be further increased compared to $v_{\text{generation}}$ due to the lower activation barrier of the defect consumption process compared to that generation of new defects.²¹ As a result, the graphene sheets are fractured into small pieces with the intrinsic structures of graphene within the pieces left largely intact. In contrast with traditional heating, much lower temperatures (bulk temperature of 85 °C was applied in most reports) can be utilized for the reaction without decomposing the nitronium ions. Consequently, a much lower density of -OH and/or epoxy groups can be generated in the first step. The subsequent competing reactions, in particular defect consumption vs. generation of new defects (low C_{Defects}), are also much slower compared to the case of microwave heating. Therefore a much longer reaction period was required to produce nanosized sheets. Furthermore, the low density of -OH and/or epoxy groups generated in the first oxidation step combined with the relative low reaction temperature may result in smaller differences in the two competing reaction rates. Therefore, even though graphene was fractured to small pieces with conventional heating, albeit with a much longer reaction time, the produced nanosheets are highly oxidized.



Scheme 2.1. Schematic of the possible cutting mechanisms by microwave assisted nitronium oxidation in the presence and absence of KMnO_4 . v_c and v_g are referred to $v_{\text{consumption}}$ (reaction rate of defect consumption) and $v_{\text{generation}}$ (reaction rate of defect generation), respectively.

When KMnO_4 is present, microwave heating also dramatically speeds up the overall oxidation processes, shortening the production times from days to tens of seconds compared to Hummer's method. However, the permanganate ions possibly bind some of the epoxy groups generated by the nitronium ions, which slows down further oxidation induced defect consumption events. As a consequence, KMnO_4 essentially slows down the overall speed in the production of nanosized sheets (**Figure 2.6A**). On the other hand, it may start oxidation processes following its own molecular cutting mechanism thereby generating smaller pieces of graphene oxide sheets with straight edges¹. Understanding these oxidative mechanisms with different oxidants allows us to controllably fabricate graphene sheets with different dimensions and electronic structures to accommodate a variety of applications.

Inspired by the strong near infrared (NIR) absorption, high photothermal conversion efficiency, and the exceptionally large surface area of graphene, graphene

nanosheets have emerged as a new high-potential nanomaterials for biological applications,^{59, 60} especially in the areas of photothermal therapy including photothermal enhanced drug and gene delivery systems.^{18, 60-63} It would be highly desirable to monitor the *in vivo* distribution of multifunctional drug delivery systems, evaluate their post-treatment therapeutic outcomes *in situ*, and most importantly, to track the long term fate of graphene sheets in the human body. These capabilities could largely facilitate their application in practical multifunctional nanomedicine regimes, fighting various diseases.

To study the *in vivo* behavior of PEGylated GO nanosheets, fluorescent- and radio-labeling have been used.⁶¹ However, the fluorescent quenching in liver and spleen has led to overestimated tumor targeting efficiency. The radio-labeling method has been considered to be more reliable and accurate than fluorescence imaging, but still suffers from long term stability problems.^{4, 64} To unambiguously determine their long term fate, graphene with different structures has been developed and rendered intrinsically fluorescent in the blue, green, and NIR regions for *in vitro* and *in vivo* imaging.^{37, 65} However, their practical applications will be limited by the low penetration depth of optical imaging methods in general.

Photoacoustic imaging (PAI), is a novel, hybrid, and non-invasive imaging modality that combines the merits of both optical and ultrasonic methods.⁶⁶ PAI, especially in the NIR region, where the attenuation of light by blood and soft tissue is relatively low, provides considerably greater spatial resolution than purely optical imaging in deep tissue while simultaneously overcoming the disadvantages of ultrasonic imaging regarding both biochemical contrast and speckle artifacts. This method could evaluate drug delivery

efficiency and therapeutic effects with a relatively high spatial resolution in biological tissue.

To generate PA signals with NIR light excitation, the following conditions should be satisfied: strong NIR absorption, non-radiative relaxation, heating, and acoustic wave generation. The ME-LOGr nanosheets exhibit strong and wavelength-independent absorption in the visible and NIR regions. Their absorption (with a coefficient of 22.7 L/g.cm at 808 nm) exceeds the best NIR fluorophores (for example, indocyanine green has an absorption coefficient of 13.9 L/g.cm at 808 nm) and the endogenous cellular background. The difference in NIR absorption between the graphene sheets and the background provides excellent optical confinement for PAI imaging applications.⁶⁷ Furthermore, graphene nanosheets are not luminescent, so that all the optical energy absorbed would transform to heat which can be used for acoustic wave generation. Therefore, it is reasonable to assume that a strong NIR PA signal could be generated from these graphene nanosheets upon NIR illumination. We should mention that no study has been reported to date on the PA properties of graphene, except for a recent work by Liu *et al.* which demonstrated that rGO nanosheets anchored with magnetic nanoparticles could be used for PA imaging.⁶⁸

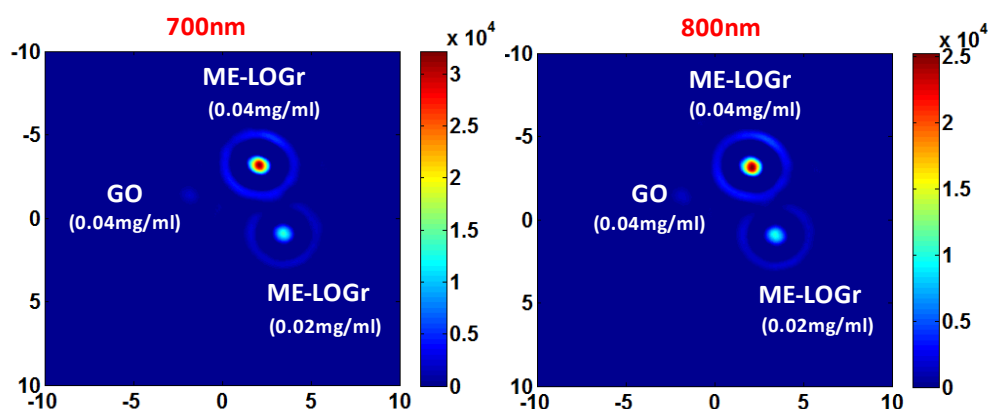


Figure 2.11. Photoacoustic (PA) signal of GO and graphene nanosheets of different concentrations, illuminated with 700nm and 800nm laser. The color coded vertical bar represents the strength of the photoacoustic signal generated. GO nanosheets were obtained *via* Control-A experiment.

Figure 2.11 shows that the ME-LOGr nanosheets exhibit remarkably strong PA signals under NIR laser illumination of 700 nm. In contrast, the GO nanosheets did not show any detectable PA signal at the same concentration and NIR illumination, possibly due to their low NIR absorption capability. Furthermore, the intensity of the PA signals depends on the concentration of the ME-LOGr nanosheets, suggesting the ME-LOGr nanosheets can be used as NIR contrast agent for in-situ NIR photoacoustic imaging. Since the strong NIR absorption of ME-LOGr nanosheets is almost independent of the wavelength in the NIR region, their NIR PA signal shows a similar trend of wavelength independence. **Figure 2.11** shows that PA signals generated under 800 nm illumination are similar to those illuminated at 700 nm. This “wavelength independent” characteristic is very different from other PA contrast agents, such as Au nanorods and Ag nanoplates which are highly wavelength dependent.⁶⁷

In addition to photoacoustic imaging, we have also explored the ME-LOGr nanosheets for multi-functional drug delivery applications for ovarian cancer treatment in collaboration with Dr. Taratula, at Oregon State University.⁶⁹ In this work, firstly, the graphene nanosheets were chemically modified with polypropylenimine dendrimers loaded with phthalocyanine (Pc), which is a photosensitizer molecule. After that, the graphene nanosheets were conjugated with poly (ethylene glycol), to improve biocompatibility, and with luteinizing hormone-releasing hormone (LHRH) peptide, for tumor-targeted delivery. Due to the strong NIR absorption and photothermal efficiency of ME-LOGr nanosheets, it performs a dual role, 1) heat generation for photothermal therapy

(PTT) and 2) production of reactive oxygen species (ROS)-production by activating Pc molecules for photodynamic therapy (PDT). This combinatorial phototherapy (PTT + PDT) resulted in an enhanced destruction of ovarian cancer cells, with a killing efficacy of 90%–95% at low Pc and low-oxygen graphene dosages as shown in figure xx, presumably conferring cytotoxicity to the synergistic effects of generated ROS and mild hyperthermia. This Pc loaded into the nanoplatform can be also employed as a NIR fluorescence agent for imaging-guided drug delivery. Hence, the newly developed Pc-graphene nanoplatform has the significant potential as an effective NIR theranostic probe for imaging and combinatorial phototherapy.⁶⁹

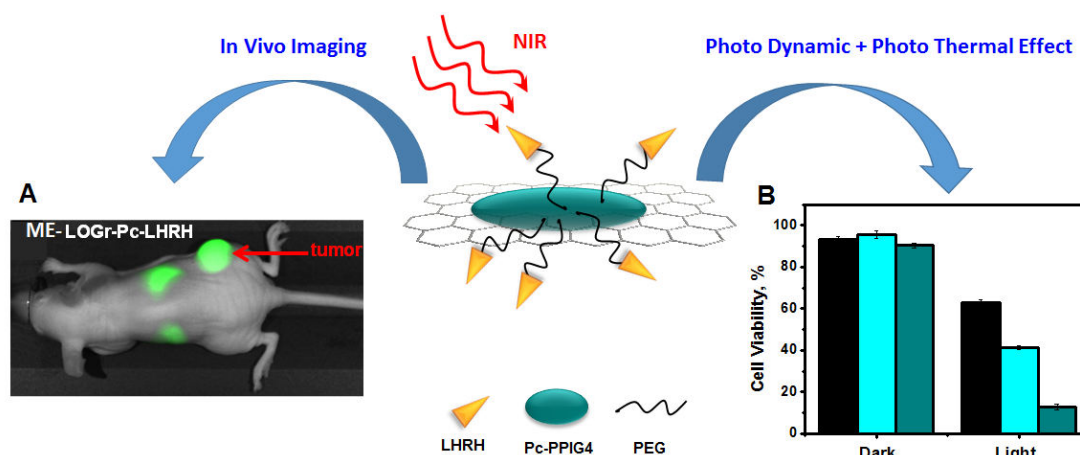


Figure 2.12. Schematic illustration of the multifunctional nanoplatform based on ME-LOGr nanosheets. A) In Vivo NIR fluorescence imaging of nude mice 12 hours after injection of saline ME-LOGr-Pc-LHRH. B) Combinatorial (PDT-PTT) therapeutic effects of ME-LOGr-Pc-LHRH (cyan color) on A2780/AD cell pellets (2,000,000) irradiated for 10 minutes using a 690 nm laser diode (0.95 W/cm^2), compared with controls- ME-LOGr-LHRH (black) and Pc-LHRH (sky blue).⁶⁹

2.3. Conclusions

In summary, for the first time, we demonstrated that graphene nanosheets can be directly fabricated from abundant and inexpensive graphite particles in a short one-pot nitronium oxidative reaction. The key is the utilization of microwave heating instead of traditional

convective heating, which selectively and rapidly increases the local temperature of graphite particles thus leading to a unique thermodynamic effect. As a result, several positive outcomes are produced which steer the graphite oxidation processes toward direct fabrication of graphene nanosheets instead of GO nanosheets: 1) The intercalation of nitronium ions into the inner parts of graphite particles is dramatically sped up. 2) A large amount of oxygen containing groups (defects) are generated simultaneously and they are randomly distributed across the entire graphene sheets. 3) Further oxidation of these defects or defect consumption reactions is more rapid than the pathways generating additional defects on the intact graphene domains. 4) Finally, graphene nanosheets are directly and rapidly fabricated with the intrinsic properties of graphene largely retained.

This fabrication process involved no toxic metal compounds or reducing agents during the fabrication, and the product can be easily cleaned and purified. It is noteworthy that this method of fabricating nanosheets is different from all the approaches relying on GO *via* Hummer's method or modified Hummer's methods, in which highly oxidative metallic compounds, such as KMnO_4 , were required for the oxidation and other chemicals for the reduction of the produced GO. Trace amounts of metal ions and other chemicals involved in the oxidation and subsequent reduction processes may participate in unwanted toxic reactions which could be detrimental to biological and other applications.^{70, 71} However, purification of GO is difficult due to its tendency to gel.⁵⁰ Therefore, extensive purification steps, which require large amount of solvents and long washing times, make the production of clean GO and rGO very time consuming.⁵⁰ Another merit of the produced ME-LOGr nanosheets is that they can be directly dispersed into aqueous and other polar organic solvents without surfactants or stabilizing agents, allowing for the production of solutions

of graphene nanosheets with “clean” surfaces. Most importantly, without the requirement for post-reduction processes, the fabricated graphene nanosheets exhibit strong NIR absorption, high photothermal, and photoacoustic conversion efficiencies. Therefore, they possess great potential as nanocarriers to develop multifunctional drug delivery systems with “on demand” release and *in vivo* photoacoustic imaging capabilities for *in-situ* evaluation of therapeutic effects and for tracking their long term fate.

2.4. Experimental Section

2.4.1. Materials

Synthetic graphite powder (20 μm) was purchased from Sigma Aldrich and used as received in all experiments. Concentrated sulfuric acid (98% H_2SO_4 , ACS grade) and concentrated nitric acid (70% HNO_3 , ACS grade) were purchased from Pharmco-AAPER and used as received. Deionized water (18.2 $\text{M}\Omega$) (Nanopure water, Barnstead) was used to prepare all solutions and to rinse and clean the samples.

2.4.2. Fabrication of ME-LOGr nanosheets

20mg of graphite are mixed with concentrated sulfuric acid and water in a round bottom flask. The mixture is then swirled and cooled in an ice bath for approximately 5 minutes. Concentrated nitric acid is then added (Different volume ratio of $\text{HNO}_3\text{:H}_2\text{SO}_4\text{:H}_2\text{O}$ is given in the **Table 2.2**). The entire mixture is swirled and mixed for another 30 seconds and placed into a microwave reactor chamber (CEM Discover). The flask is connected to a reflux condenser that passes through the roof of the microwave oven *via* a port. The reaction mixture is subject to microwave irradiation (300 watts) for 30 seconds. Subsequently, the reaction is quenched with 200ml of deionized followed by filtering through an alumina anodisc filter (0.02 μm pore size) and washing with 800ml deionized

water. The cake on the membrane is then redispersed into water with 30 minute bath sonication. The dispersion obtained is then left undisturbed for five days to let the unexfoliated graphite particles precipitate out. The supernatant is carefully decanted and this solution is stable for months in water without significant precipitation.

Table 2.2. Different volume ratio of $\text{HNO}_3\text{:H}_2\text{SO}_4\text{:H}_2\text{O}$.

No.	volume ratio ($\text{HNO}_3\text{:H}_2\text{SO}_4\text{:H}_2\text{O}$)	Total volume (ml)
(1)	1:1:0	10
(2)	1:42:7	10
(3)	1:2.5:0.07	10
(4)	1:17.5:1.5	10
(5)	1:4:0	10

2.4.3. Control experiments

Control-A experiment

100 mg of KMnO_4 is added to the ice cooled acid mixture, as described above. After 30 seconds of microwave irradiation, the mixture is transferred to 200ml of ice containing 5ml of 35% H_2O_2 to quench the reaction. The entire content is then filtered through an alumina anodisc filter (0.02 μm pore size) and washed with 3 times 100 ml of diluted hydrochloric acid (4%), followed by repeatedly (8 times) washing with 100ml DI water to remove all the acid and KMnO_4 residues, along with any byproducts. A colloidal graphene oxide (GO) solution is obtained by mild bath sonication (~30mins). Unexfoliated graphite powder can be removed by centrifugation at 4000 rpm for 20mins. The filtration and washing step in GO takes an entire day because of its paste-like character.

Control-B experiment

100 mg of KMnO_4 is added to the ice cooled 10ml concentrated sulfuric acid instead of acid mixture and other experimental procedure is similar as control-A experiment.

Control-C experiment

20mg graphite and acid mixture (No.3 in the **Table 2.2**) was heated at 85°C for 4 hours in water bath in a fume hood with the flask connected to a reflux condenser. After that washing procedure is followed similar as ME-LOGr nanosheets:-

2.4.4. Material Characterization

The morphology of the graphene and GO samples were studied using a Nanoscope IIIa Multimode scanning probe microscope system (Digital Instruments, Bruker) with a J scanner operated in the “Tapping Mode”. Micro Raman Spectroscopy (Kaiser Optical Systems Raman Microprobe) equipped with a 785 nm solid-state diode laser) was performed to measure the relative concentrations of nitronium ions formed *via* mixing concentrated HNO_3 and H_2SO_4 at different volume ratios. Spectra were obtained of these solutions held in a thin quartz cuvette. This instrument was also used to study the graphene and GO films deposited on an alumina filter membrane. XPS characterization was performed after depositing a layer of ME-LOGr nanosheets or GO onto a gold film (a 100 nm gold layer was sputter-coated on silicon with a 10 nm Ti adhesion layer). The thickness of the graphene or GO film on the gold substrates was roughly 30-50 nm. XPS spectra were acquired using a Thermo Scientific K-Alpha system with a monochromatic $\text{Al K}\alpha$ x-ray source ($h\nu = 1486.7 \text{ eV}$) and data were analyzed using Casa XPS 2.3.15 software. Absorption spectra were recorded on a Cary 5000 UV-vis-NIR spectrophotometer in the double beam mode using a 1cm quartz cuvette.

2.4.5. Photoacoustic characterization

A mechanically scanning photoacoustic system with a single acoustic transducer to collect the acoustic signals was employed, as described in detail previously.^{72, 73} A schematic of the system is shown in **Figure 2.13**. Briefly, pulsed light from an OPO laser (Continuum, pulse duration: 4–6 ns, repetition rate: 20Hz) was coupled into the phantom *via* an optical subsystem and generated acoustic signals. An acoustic transducer with 1 MHz nominal frequency (Valpey Fisher, Hopkinton, MA) was driven by a motorized rotator to receive acoustic signals over 360 °at an interval of 3°. Thus a total of 120 measurements were performed for one planar scanning. The acoustic transducer was immersed in the water tank while the phantoms were placed at the center of the tank and illuminated by the laser. The acoustic signal was amplified by a pulser/receiver (GE Panametrics, Waltham, MA) and was then acquired by a high-speed PCI data acquisition board.

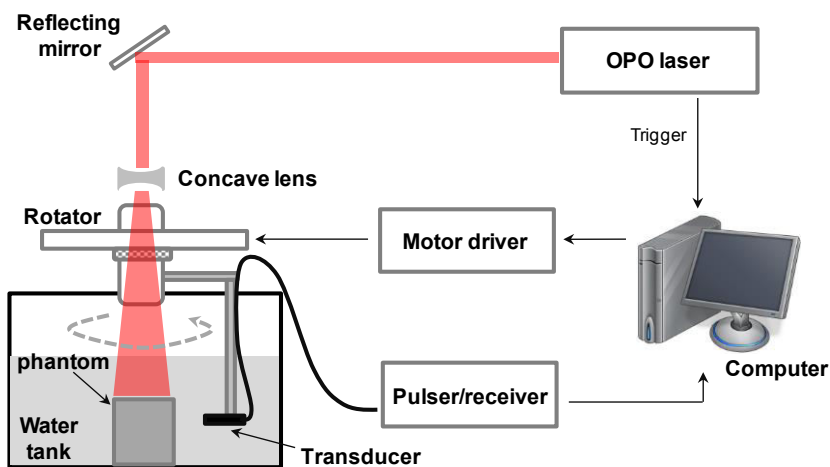


Figure 2.13. Schematic of the experimental setup for PA imaging

In these experiments, a solid cylindrical phantom with a diameter of 3 cm was prepared. The absorption and scattering coefficients were 0.01 mm^{-1} and 1.0 mm^{-1} at $\sim 700 \text{ nm}$ and 800 nm , respectively. $3 \mu\text{l}$ of ME-LOGr nanosheets or GO with different concentrations were then put into three holes of 1.4 mm in diameter that were located in

the center of the phantom. The phantom materials consisted of TiO₂ for scattering and India ink as an absorber with agar powder (1 – 2%) for solidifying the TiO₂ and India ink solution.

2.5. References

1. Kosynkin, D. V.; Higginbotham, A. L.; Sinitskii, A.; Lomeda, J. R.; Dimiev, A.; Price, B. K.; Tour, J. M. Longitudinal unzipping of carbon nanotubes to form graphene nanoribbons. *Nature* 2009, 458, 872-6.
2. Chen, X.; Zhou, X.; Han, T.; Wu, J.; Zhang, J.; Guo, S. Stabilization and induction of oligonucleotide i-motif structure via graphene quantum dots. *ACS Nano* 2013, 7, 531-7.
3. Ren, H.; Wang, C.; Zhang, J.; Zhou, X.; Xu, D.; Zheng, J.; Guo, S.; Zhang, J. DNA cleavage system of nanosized graphene oxide sheets and copper ions. *ACS Nano* 2010, 4, 7169-74.
4. Yang, K.; Wan, J.; Zhang, S.; Tian, B.; Zhang, Y.; Liu, Z. The influence of surface chemistry and size of nanoscale graphene oxide on photothermal therapy of cancer using ultra-low laser power. *Biomaterials* 2012, 33, 2206-14.
5. Radovic, L. R.; Bockrath, B. On the chemical nature of graphene edges: origin of stability and potential for magnetism in carbon materials. *J. Am. Chem. Soc.* 2005, 127, 5917-27.
6. Ohba, T.; Kanoh, H. Intensive Edge Effects of Nanographenes in Molecular Adsorptions. *J Phys Chem Lett* 2012, 3, 511-6.
7. Chou, S. S.; De, M.; Luo, J.; Rotello, V. M.; Huang, J.; Dravid, V. P. Nanoscale graphene oxide (nGO) as artificial receptors: implications for biomolecular interactions and sensing. *J. Am. Chem. Soc.* 2012, 134, 16725-33.
8. Pan, D.; Zhang, J.; Li, Z.; Wu, M. Hydrothermal route for cutting graphene sheets into blue-luminescent graphene quantum dots. *Adv. Mater.* 2010, 22, 734-8.
9. Li, Y.; Hu, Y.; Zhao, Y.; Shi, G.; Deng, L.; Hou, Y.; Qu, L. An electrochemical avenue to green-luminescent graphene quantum dots as potential electron-acceptors for photovoltaics. *Adv. Mater.* 2011, 23, 776-80.
10. Zhou, X.; Zhang, Y.; Wang, C.; Wu, X.; Yang, Y.; Zheng, B.; Wu, H.; Guo, S.; Zhang, J. Photo-Fenton reaction of graphene oxide: a new strategy to prepare graphene quantum dots for DNA cleavage. *ACS Nano* 2012, 6, 6592-9.
11. Hummers, W. S.; Offeman, R. E. Preparation of Graphitic Oxide. *J. Am. Chem. Soc.* 1958, 80, 1339.
12. Erickson, K.; Erni, R.; Lee, Z.; Alem, N.; Gannett, W.; Zettl, A. Determination of the local chemical structure of graphene oxide and reduced graphene oxide. *Adv. Mater.* 2010, 22, 4467-72.
13. Li, J. L.; Kudin, K. N.; McAllister, M. J.; Prud'homme, R. K.; Aksay, I. A.; Car, R. Oxygen-driven unzipping of graphitic materials. *Phys. Rev. Lett.* 2006, 96, 176101.
14. Zhang, L.; Liang, J. J.; Huang, Y.; Ma, Y. F.; Wang, Y.; Chen, Y. S. Size-controlled synthesis of graphene oxide sheets on a large scale using chemical exfoliation. *Carbon* 2009, 47, 3365-3368.

15. Wang, D.; Wang, L.; Dong, X. Y.; Shi, Z.; Jin, J. Chemically tailoring graphene oxides into fluorescent nanosheets for Fe³⁺ ion detection. *Carbon* 2012, 50, 2147-2154.
16. Luo, J.; Cote, L. J.; Tung, V. C.; Tan, A. T.; Goins, P. E.; Wu, J.; Huang, J. Graphene oxide nanocolloids. *J. Am. Chem. Soc.* 2010, 132, 17667-9.
17. Peng, J.; Gao, W.; Gupta, B. K.; Liu, Z.; Romero-Aburto, R.; Ge, L.; Song, L.; Alemany, L. B.; Zhan, X.; Gao, G.; Vithayathil, S. A.; Kaiparettu, B. A.; Marti, A. A.; Hayashi, T.; Zhu, J. J.; Ajayan, P. M. Graphene quantum dots derived from carbon fibers. *Nano Lett.* 2012, 12, 844-9.
18. Tian, B.; Wang, C.; Zhang, S.; Feng, L.; Liu, Z. Photothermally enhanced photodynamic therapy delivered by nano-graphene oxide. *ACS Nano* 2011, 5, 7000-9.
19. Robinson, J. T.; Tabakman, S. M.; Liang, Y.; Wang, H.; Casalongue, H. S.; Vinh, D.; Dai, H. Ultrasmall reduced graphene oxide with high near-infrared absorbance for photothermal therapy. *J. Am. Chem. Soc.* 2011, 133, 6825-31.
20. Zhang, M.; Bai, L. L.; Shang, W. H.; Xie, W. J.; Ma, H.; Fu, Y. Y.; Fang, D. C.; Sun, H.; Fan, L. Z.; Han, M.; Liu, C. M.; Yang, S. H. Facile synthesis of water-soluble, highly fluorescent graphene quantum dots as a robust biological label for stem cells. *J. Mater. Chem.* 2012, 22, 7461-7467.
21. Xu, S. C.; Irle, S.; Musaev, D. G.; Lin, M. C. Quantum chemical study of the dissociative adsorption of OH and H₂O on pristine and defective graphite (0001) surfaces: Reaction mechanisms and kinetics. *Journal of Physical Chemistry C* 2007, 111, 1355-1365.
22. Liu, J.; Rinzler, A. G.; Dai, H.; Hafner, J. H.; Bradley, R. K.; Boul, P. J.; Lu, A.; Iverson, T.; Shlimov, K.; Huffman, C. B.; Rodriguez-Macias, F.; Shon, Y. S.; Lee, T. R.; Colbert, D. T.; Smalley, R. E. Fullerene pipes. *Science* 1998, 280, 1253-6.
23. Ziegler, K. J.; Gu, Z.; Peng, H.; Flor, E. L.; Hauge, R. H.; Smalley, R. E. Controlled oxidative cutting of single-walled carbon nanotubes. *J. Am. Chem. Soc.* 2005, 127, 1541-7.
24. Kingston, H. M.; Haswell, S. J. *Microwave-Enhanced Chemistry: Fundamentals, Sample Preparation, and Applications*. American chemical society: Washington DC, 1997.
25. Kappe, C. O. Controlled microwave heating in modern organic synthesis. *Angew. Chem. Int. Ed. Engl.* 2004, 43, 6250-84.
26. Sun, T.; Fabris, S. Mechanisms for oxidative unzipping and cutting of graphene. *Nano Lett.* 2012, 12, 17-21.
27. Chiu, P. L.; Mastrogiovanni, D. D.; Wei, D.; Louis, C.; Jeong, M.; Yu, G.; Saad, P.; Flach, C. R.; Mendelsohn, R.; Garfunkel, E.; He, H. Microwave- and nitronium ion-enabled rapid and direct production of highly conductive low-oxygen graphene. *J. Am. Chem. Soc.* 2012, 134, 5850-6.
28. Patel, M. A.; Yang, H.; Chiu, P. L.; Mastrogiovanni, D. D. T.; Flach, C. R.; Savaram, K.; Gomez, L.; Hemnarine, A.; Mendelsohn, R.; Garfunkel, E.; Jiang, H.; He, H. Direct Production of Graphene Nanosheets for Near Infrared Photoacoustic Imaging. *ACS Nano* 2013, 7, 8147-8157.
29. Sun, X.; Luo, D.; Liu, J.; Evans, D. G. Monodisperse chemically modified graphene obtained by density gradient ultracentrifugal rate separation. *ACS Nano* 2010, 4, 3381-9.
30. Li, D.; Muller, M. B.; Gilje, S.; Kaner, R. B.; Wallace, G. G. Processable aqueous dispersions of graphene nanosheets. *Nat Nanotechnol* 2008, 3, 101-5.

31. Hernandez, Y.; Nicolosi, V.; Lotya, M.; Blighe, F. M.; Sun, Z.; De, S.; McGovern, I. T.; Holland, B.; Byrne, M.; Gun'Ko, Y. K.; Boland, J. J.; Niraj, P.; Duesberg, G.; Krishnamurthy, S.; Goodhue, R.; Hutchison, J.; Scardaci, V.; Ferrari, A. C.; Coleman, J. N. High-yield production of graphene by liquid-phase exfoliation of graphite. *Nat Nanotechnol* 2008, 3, 563-8.
32. Becerril, H. A.; Mao, J.; Liu, Z.; Stoltenberg, R. M.; Bao, Z.; Chen, Y. Evaluation of solution-processed reduced graphene oxide films as transparent conductors. *ACS Nano* 2008, 2, 463-470.
33. Bagri, A.; Mattevi, C.; Acik, M.; Chabal, Y. J.; Chhowalla, M.; Shenoy, V. B. Structural evolution during the reduction of chemically derived graphene oxide. *Nat Chem* 2010, 2, 581-7.
34. Eda, G.; Fanchini, G.; Chhowalla, M. Large-Area Ultrathin Films of Reduced Graphene Oxide as a Transparent and Flexible Electronic Materials. *Nature Nanotech.* 2008, 3, 270-274.
35. Loh, K. P.; Bao, Q.; Eda, G.; Chhowalla, M. Graphene oxide as a chemically tunable platform for optical applications. *Nat Chem* 2010, 2, 1015-24.
36. Park, S.; Ruoff, R. S. Chemical Methods for the Production of Graphene. *Nature Nanotech.* 2009, 4, 217-224.
37. Chien, C. T.; Li, S. S.; Lai, W. J.; Yeh, Y. C.; Chen, H. A.; Chen, I. S.; Chen, L. C.; Chen, K. H.; Nemoto, T.; Isoda, S.; Chen, M.; Fujita, T.; Eda, G.; Yamaguchi, H.; Chhowalla, M.; Chen, C. W. Tunable photoluminescence from graphene oxide. *Angew. Chem. Int. Ed. Engl.* 2012, 51, 6662-6.
38. Eda, G.; Chhowalla, M. Chemically derived graphene oxide: towards large-area thin-film electronics and optoelectronics. *Adv. Mater.* 2010, 22, 2392-415.
39. Eda, G.; Lin, Y. Y.; Mattevi, C.; Yamaguchi, H.; Chen, H. A.; Chen, I. S.; Chen, C. W.; Chhowalla, M. Blue photoluminescence from chemically derived graphene oxide. *Adv. Mater.* 2010, 22, 505-9.
40. Zhu, S.; Tang, S.; Zhang, J.; Yang, B. Control the size and surface chemistry of graphene for the rising fluorescent materials. *Chem Commun (Camb)* 2012, 48, 4527-39.
41. Moon, I. K.; Lee, J.; Ruoff, R. S.; Lee, H. Reduced graphene oxide by chemical graphitization. *Nat Commun* 2010, 1, 73.
42. Tung, V. C.; Allen, M. J.; Yang, Y.; Kaner, R. B. High-throughput solution processing of large-scale graphene. *Nat Nanotechnol* 2009, 4, 25-9.
43. Tuinstra, F.; Koenig, J. L. Raman spectrum of graphite. *J. Chem. Phys.* 1970, 53, 1126-1130.
44. Wang, H.; Robinson, J. T.; Li, X.; Dai, H. Solvothermal reduction of chemically exfoliated graphene sheets. *J. Am. Chem. Soc.* 2009, 131, 9910-1.
45. Niyogi, S.; Bekyarova, E.; Itkis, M. E.; Zhang, H.; Shepperd, K.; Hicks, J.; Sprinkle, M.; Berger, C.; Lau, C. N.; deHeer, W. A.; Conrad, E. H.; Haddon, R. C. Spectroscopy of covalently functionalized graphene. *Nano Lett.* 2010, 10, 4061-6.
46. Farmer, D. B.; Golizadeh-Mojarad, R.; Perebeinos, V.; Lin, Y. M.; Tulevski, G. S.; Tsang, J. C.; Avouris, P. Chemical doping and electron-hole conduction asymmetry in graphene devices. *Nano Lett.* 2009, 9, 388-92.
47. Lotya, M.; Hernandez, Y.; King, P. J.; Smith, R. J.; Nicolosi, V.; Karlsson, L. S.; Blighe, F. M.; De, S.; Wang, Z.; McGovern, I. T.; Duesberg, G. S.; Coleman, J. N. Liquid

- phase production of graphene by exfoliation of graphite in surfactant/water solutions. *J. Am. Chem. Soc.* 2009, 131, 3611-20.
48. Li, Z.; Zhang, W.; Luo, Y.; Yang, J.; Hou, J. G. How graphene is cut upon oxidation? *J. Am. Chem. Soc.* 2009, 131, 6320-1.
 49. Chen, Z.; Kobashi, K.; Rauwald, U.; Booker, R.; Fan, H.; Hwang, W. F.; Tour, J. M. Soluble ultra-short single-walled carbon nanotubes. *J. Am. Chem. Soc.* 2006, 128, 10568-71.
 50. Kim, F.; Luo, J. Y.; Cruz-Silva, R.; Cote, L. J.; Sohn, K.; Huang, J. X. Self-Propagating Domino-like Reactions in Oxidized Graphite. *Adv. Funct. Mater.* 2010, 20, 2867-2873.
 51. Marcano, D. C.; Kosynkin, D. V.; Berlin, J. M.; Sinitskii, A.; Sun, Z.; Slesarev, A.; Alemany, L. B.; Lu, W.; Tour, J. M. Improved synthesis of graphene oxide. *ACS Nano* 2010, 4, 4806-14.
 52. Edwards, H. G. M.; Fawcett, V. Quantitative Raman Spectroscopic Studies of Nitronium Ion Concentrations in Mixtures of Sulphuric and Nitric Acids. *J. Molecular Structure* 1994, 326, 131.
 53. Savaram, K.; Kalyanikar, M.; Patel, M.; Brukh, R.; Flach, C. R.; Huang, R.; Khoshi, M. R.; Mendelsohn, R.; Wang, A.; Garfunkel, E.; He, H. Synergy of oxygen and a piranha solution for eco-friendly production of highly conductive graphene dispersions. *Green Chemistry* 2015, 17, 869-881.
 54. Patel, M.; Feng, W.; Savaram, K.; Khoshi, M. R.; Huang, R.; Sun, J.; Rabie, E.; Flach, C.; Mendelsohn, R.; Garfunkel, E.; He, H. Microwave Enabled One-Pot, One-Step Fabrication and Nitrogen Doping of Holey Graphene Oxide for Catalytic Applications. *Small* 2015, 11, 3358-3368.
 55. Loughin, S.; Grayeski, R.; Fischer, J. E. Charge Transfer in Graphite Nitrate and the Ionic Salt Model. *J. Chem. Phys.* 1978, 69, 3740-3745.
 56. Esteves, P. M.; De, M. C. J. W.; Cardoso, S. P.; Barbosa, A. G.; Laali, K. K.; Rasul, G.; Prakash, G. K.; Olah, G. A. Unified mechanistic concept of electrophilic aromatic nitration: convergence of computational results and experimental data. *J. Am. Chem. Soc.* 2003, 125, 4836-49.
 57. Han, T. H.; Huang, Y. K.; Tan, A. T.; Dravid, V. P.; Huang, J. Steam etched porous graphene oxide network for chemical sensing. *J. Am. Chem. Soc.* 2011, 133, 15264-7.
 58. Bagri, A.; Mattevi, C.; Acik, M.; Chabal, Y. J.; Chhowalla, M.; Shenoy, V. B. Structural evolution during the reduction of chemically derived graphene oxide. *Nature Chemistry* 2010, 2, 581-587.
 59. Shen, H.; Liu, M.; He, H.; Zhang, L.; Huang, J.; Chong, Y.; Dai, J.; Zhang, Z. PEGylated graphene oxide-mediated protein delivery for cell function regulation. *ACS Appl Mater Interfaces* 2012, 4, 6317-23.
 60. Yang, K.; Feng, L.; Shi, X.; Liu, Z. Nano-graphene in biomedicine: theranostic applications. *Chem. Soc. Rev.* 2013, 42, 530-47.
 61. Yang, K.; Zhang, S.; Zhang, G.; Sun, X.; Lee, S. T.; Liu, Z. Graphene in mice: ultrahigh in vivo tumor uptake and efficient photothermal therapy. *Nano Lett.* 2010, 10, 3318-23.
 62. Yang, X. Y.; Zhang, X. Y.; Liu, Z. F.; Ma, Y. F.; Huang, Y.; Chen, Y. High-Efficiency Loading and Controlled Release of Doxorubicin Hydrochloride on Graphene Oxide. *Journal of Physical Chemistry C* 2008, 112, 17554-17558.

63. Zhang, L. M.; Wang, Z. L.; Lu, Z. X.; Shen, H.; Huang, J.; Zhao, Q. H.; Liu, M.; He, N. Y.; Zhang, Z. J. PEGylated reduced graphene oxide as a superior ssRNA delivery system. *Journal of Materials Chemistry B* 2013, 1, 749-755.
64. Zhang, Y.; Yang, K.; Hong, H.; Engle, J.; Feng, L.; Theuer, C.; Barnhart, T.; Liu, Z.; Cai, W. In Vivo Targeting and Imaging of Tumor Vasculature with Radiolabeled, Antibody-Conjugated Nano-Graphene. *Medical Physics* 2012, 39, 3950-3950.
65. Sun, X.; Liu, Z.; Welsher, K.; Robinson, J. T.; Goodwin, A.; Zaric, S.; Dai, H. Nano-Graphene Oxide for Cellular Imaging and Drug Delivery. *Nano Res* 2008, 1, 203-212.
66. Yang, X.; Skrabalak, S. E.; Li, Z. Y.; Xia, Y.; Wang, L. V. Photoacoustic tomography of a rat cerebral cortex in vivo with au nanocages as an optical contrast agent. *Nano Lett.* 2007, 7, 3798-802.
67. de la Zerda, A.; Kim, J. W.; Galanzha, E. I.; Gambhir, S. S.; Zharov, V. P. Advanced contrast nanoagents for photoacoustic molecular imaging, cytometry, blood test and photothermal theranostics. *Contrast Media Mol Imaging* 2011, 6, 346-69.
68. Yang, K.; Hu, L.; Ma, X.; Ye, S.; Cheng, L.; Shi, X.; Li, C.; Li, Y.; Liu, Z. Multimodal imaging guided photothermal therapy using functionalized graphene nanosheets anchored with magnetic nanoparticles. *Adv. Mater.* 2012, 24, 1868-72.
69. Taratula, O.; Patel, M.; Schumann, C.; Naleway, M. A.; Pang, A. J.; He, H.; Taratula, O. Phthalocyanine-loaded graphene nanoplateform for imaging-guided combinatorial phototherapy. *International journal of nanomedicine* 2015, 10, 2347.
70. Jachak, A. C.; Creighton, M.; Qiu, Y.; Kane, A. B.; Hurt, R. H. Biological interactions and safety of graphene materials. *MRS Bull.* 2012, 37, 1307-1313.
71. Sanchez, V. C.; Jachak, A.; Hurt, R. H.; Kane, A. B. Biological interactions of graphene-family nanomaterials: an interdisciplinary review. *Chem. Res. Toxicol.* 2012, 25, 15-34.
72. Yin, L.; Wang, Q.; Zhang, Q. Z.; Jiang, H. B. Tomographic imaging of absolute optical absorption coefficient in turbid media using combined photoacoustic and diffusing light measurements. *Opt. Lett.* 2007, 32, 2556-2558.
73. Zhang, Q.; Liu, Z.; Carney, P. R.; Yuan, Z.; Chen, H.; Roper, S. N.; Jiang, H. Non-invasive imaging of epileptic seizures in vivo using photoacoustic tomography. *Phys Med Biol* 2008, 53, 1921-31.

Chapter 3. Microwave Enabled One-Pot, One-Step Fabrication and Nitrogen Doping of Holey Graphene Oxide for Catalytic Applications

3.1 Introduction

The ever-increasing global depletion of fossil resources and their environmental impacts stimulate intense research activities in the development of alternative green and sustainable energy resources. Fuel cells and metal-air batteries are the most attractive clean and high-efficiency devices for power generation and energy storage.¹⁻³ However, their large-scale practical application will be difficult to realize if the expensive platinum-based electrocatalysts for oxygen reduction reaction (ORR) cannot be replaced by efficient, stable, low-cost, and sustainable catalysts in their electrodes. Recent efforts in reducing/replacing expensive platinum-based electrodes have led to the development of new ORR electrocatalysts.⁴⁻⁹ Among them, graphene, especially the heteroatom doped graphene, shows outstanding potential as a metal free catalyst. However, practical application of the graphene based metal free catalyst is hampered due to its remarkable impermeability.¹⁰ Hence, the reactants and products cannot access/leave the inner catalytic sites easily, which results in unsatisfactory performance and non-efficient mass transport. In contrast, holey graphene, referred to graphene sheets with nanoholes in its basal plane, not only provides “short cuts” for efficient mass transport, but also possess significantly more catalytic centers due to the increased edges associated with the existence of holes. Several approaches have been reported for the production of holey graphene sheets. Bottom-up approaches based on chemical vapor deposition methods,¹¹⁻¹³ and top-down

approaches via photo,¹⁴ electron,¹⁵ or plasma¹¹ etching utilize various templates, which provide good control over the sizes and shapes of the holes/pores. However, all these strategies suffer from difficulties in scaling up for large quantity production and high cost. On the other hand, chemical etching based processes, such as KOH etching,¹⁶ H₃PO₄ activation,¹⁷ HNO₃ oxidation,^{18, 19} hot steam etching,²⁰ and oxidative etching with catalytic nanoparticles like Fe₂O₃,²¹ Ag²² or other metal oxide nanoparticles²³ have advantages for large scale and cost effective synthesis. However, these chemical etching based approaches require graphene oxide (GO) or reduced graphene oxide (rGO) as a starting material, which takes hours to days for their fabrication, depending on the oxidation method applied. There is no approach that has been reported yet to rapidly fabricate holey graphene directly from graphite particles. Herein, we report our unexpected discovery that by replacing traditional heating with microwave heating, holey graphene oxide (HGO) sheets are directly and rapidly (40 seconds) fabricated from graphite particles via a one-step-one-pot reaction. Furthermore, by slightly shortening the microwave heating time, graphene oxide (GO) sheets without holes can be rapidly fabricated. This approach has the similar chemical recipe as the widely used Hummers method, but dramatically shortened the reaction time from days to tens of seconds with high production yield (120 wt% of graphite).

Heteroatom (N, P, B, and S) doping in graphene can effectively tailor its electronic properties and thus have a great impact on its wide range of applications in electronics, energy storage and metal free catalyst applications.²⁴⁻³⁵ There are quite a few methods available for nitrogen(N) doping.^{32, 36-43} However, all of these approaches require long time and/or high annealing temperature with various N containing molecules. Again, by taking advantage of the unique heating mechanism of microwave, we developed a fast and low

temperature approach to simultaneously reduce and dope graphene oxide sheets with nitrogen. The N doping type can be controlled simply by changing the microwave time. With 10 minutes of microwave irradiation, pyridinic and pyrrolic N reaches the highest percentage in holey graphene sheets, which shows the best catalytic activity toward electrochemical oxygen reduction reaction (ORR). These N-doped holey rGO (N-HrGO-10) sheets not only offer the lower over-potential and peak potential but also provides more than 4 times higher kinetic current density than non-porous N-doped rGO (N-rGO-10). It is likely due to the existence of nanoholes, which provides “short cuts” for efficient mass transport and also creates more catalytic centers due to the increased surface area and edges associated with the nanoholes in the N-HrGO-10. For the first time, we experimentally determined the effective diffusion coefficient constant of O_2 for the N-HrGO-10, which is indeed significantly higher than that of the N-rGO-10. Even though the onset potential is slightly higher than the Pt/C (0.09 V), the N-HrGO-10 shows much higher catalytic current, better stability and durability against methanol poisoning. The capability of rapid fabrication and N doping of HGO can lead us to develop efficient catalysts which can replace previous coin metals for energy generation and storage, such as fuel cells and metal–air batteries.

3.2 Results and Discussion

In the previous chapter, we have developed a fast, scalable, and low-energy approach to directly produce graphene nanosheets (GNs) from graphite powder.⁴⁴ These graphene nanosheets are highly uniform in size and largely retain their intrinsic graphitic structures without any post-reduction treatment. The key is to exclude $KMnO_4$ (as used in Hummers or Modified Hummers methods) and exploit pure nitronium ion oxidation and the unique

thermal and kinetic effects induced by microwave heating. Due to the unique effects of microwave heating, it is very likely that consumption/etching of defective carbons (already oxidized carbon or sp^3 carbon) was selectively enhanced more than that of the continuing oxidation of intact graphene domains (generation of more oxygen containing groups). As a result, the graphene sheets rapidly breakdown to small pieces with the intrinsic structures of graphene largely intact. In this work, we found that by including $KMnO_4$ in the reaction system, and by adjusting microwave irradiation time and amount of $KMnO_4$, the etching/consumption of the generated defective carbons can be controlled, so that graphene oxide sheets with controlled hole structures can be directly fabricated from graphite powder in one step.

In a typical experiment, the mixture of graphite powder, acids (concentrated H_2SO_4 , HNO_3 , 4:1) and $KMnO_4$ (500 wt% of graphite) was subjected to microwave irradiation at 300 watts for different times (30seconds for GO or 40seconds for HGO). The resulting products, after cleaning, are easy to disperse in water by simple bath sonication. Their dispersions in water have brown color (inset of **Figure 3.1E** and **F**), independent of microwave irradiation time. They all exhibit the typical $\sim 230nm$ peak in UV-visible spectrum (**Figure 3.1E** and **F**, respectively) due to $\pi \rightarrow \pi^*$ transition of $C=C$ with a shoulder around $300nm$ due to the $n \rightarrow \pi^*$ transition of carbonyl functional group. X-ray photoelectron spectroscopy (XPS) measurements were performed to carefully study their oxidation level and chemical functionalities. Interestingly, high resolution $C1s$ (**Figure 3.2C** and **D**) and $O1s$ peak (**Figure 3.2B**) analysis of GO and HGO shows that the C: O atomic ratio is ~ 2.38 , similar in both GO (**Table 3.1**), which indicates that both GOs have similar extent of oxidation in spite of different microwave time.

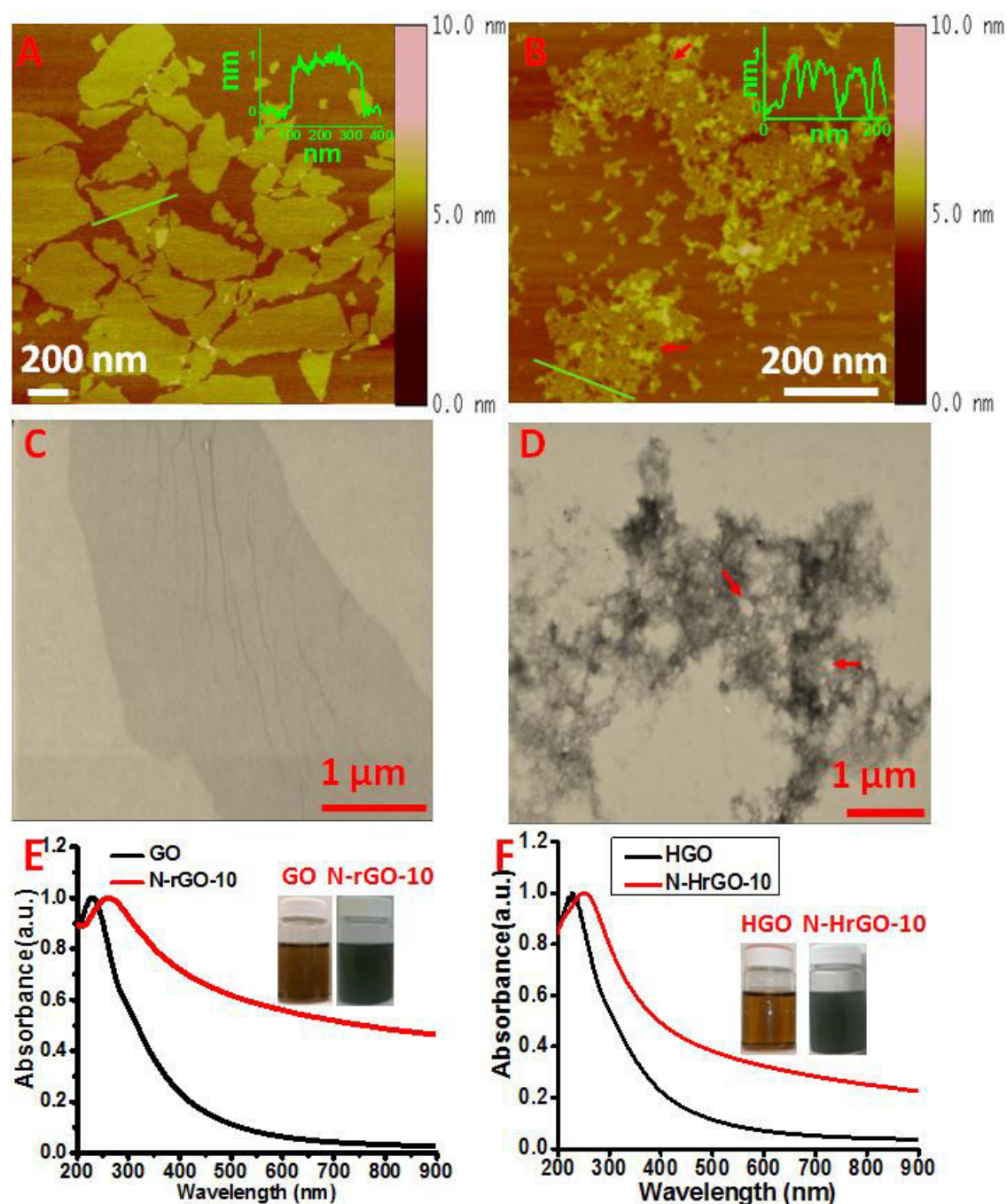


Figure 3.1. (A) AFM and (C) STEM of GO sheets obtained via 30seconds of microwave irradiation. (B) AFM and (D) STEM images of HGO sheets obtained via 40 seconds of microwave irradiation. (E) UV-Vis-NIR spectra of GO sheets (black line) and N-rGO-10 (red line). Inset (E) is a digital picture of an aqueous dispersion of GO (left) and N-rGO-10(right) shows different colors, indicating they are in different oxidation states. (F) UV-Vis-NIR spectra of HGO sheets (black line) and N-HrGO-10 (red line). Inset (F) is a digital picture of an aqueous dispersion of HGO (left), N-HrGO-10(right) shows different color,

indicating their different oxidation states. The red arrows in (B and D) shows hole on HGO sheet.

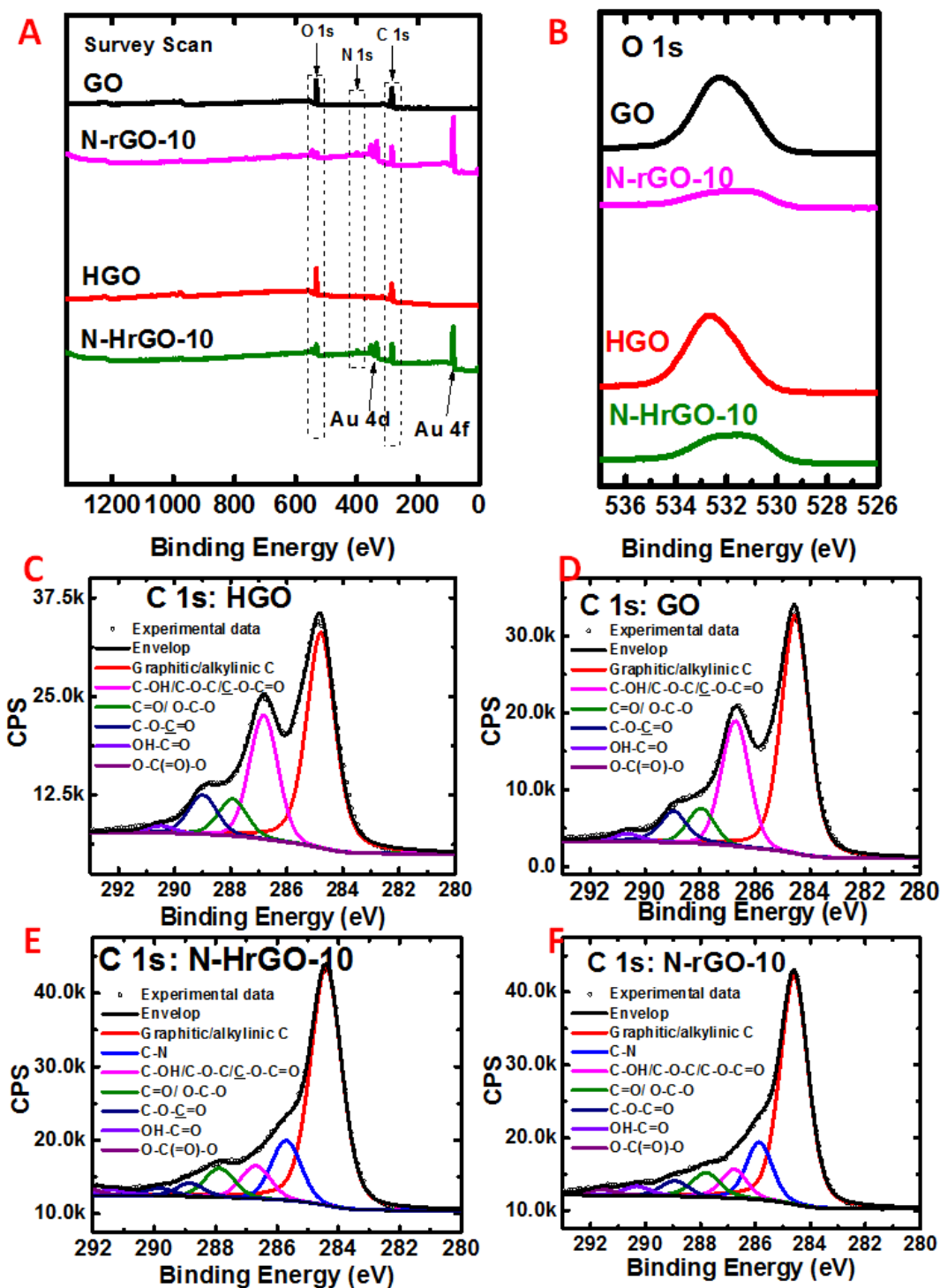


Figure 3.2. (A) XPS survey scan and (B) O 1s peak of GO, N-rGO-10, HGO and N-HrGO-10. XPS high resolution C 1s peak analysis of HGO (C), GO (D), N-HrGO-10 (E) and N-

rGO-10(F), where 10 denotes microwave treatment time (in minutes) of HGO/GO with NH_4OH at 120 °C.

Table 3.1 Atomic ratio of C, N and O calculated from high resolution C 1s, N 1s and O 1s XPS peak analysis of different catalysts.

Samples	un-oxidized C: oxidized C	N:C	C: O	% atomic N
GO	1.5	-	2.38	-
N-rGO-10	3.5	0.13	6.67	10.15%
HGO	1.5	-	2.38	-
N-HrGO-10	3.9	0.12	4.17	8.51%
N-HrGO-30	3.8	0.11	5.26	8.34%

However, we found that microwave irradiation times dramatically changed their geometric structures. For instance, 30 seconds of microwave irradiation resulted in GO sheets with nanoholes seldom being observed in the basal planes. The atomic force microscopy (AFM) and scanning transmission electron microscopy (STEM) (**Figure 3.1A** and C) images shows that most of the sheets are single layered and non-porous. Similar to the GO sheets produced via modified Hummer's method, these sheets have straight edges, indicating the dominant linear unzipping effect of KMnO_4 .⁴⁵ While, with 40 seconds of microwave irradiation, the lateral size of the GO sheets obtained is slightly decreased and their edges are not straight anymore from their AFM and STEM images (**Figure 3.1B** and D). More importantly, holes (from several nanometers to a few hundred nanometers) are randomly distributed across the entire sheets, demonstrating that holey GO (HGO) is directly fabricated from graphite powder via a fast, one step, one pot reaction. Further, the surface area of GO and HGO, after vacuum dry, was measured by methylene blue (MB)

dye adsorption approach (**Table 3.2**).⁴⁶ We found that the surface area of HGO (1424.16 m²/g) is ~1.5 times higher than that of GO (947.55 m²/g), possibly due to the existence of the holes in HGO. To our knowledge, this is the first report that solution phase GO with controlled hole structures can be rapidly fabricated directly from graphite powder (**Table 1.2.1**).

Table 3.2 The measured surface area of GO, HGO, N-rGO-10 and N-HrGO-10 via MB adsorption method.

Sample	Surface area(m ² /g)
GO	947.55
HGO	1424.16
N-rGO-10	560.71
N-HrGO-10	1194.97

Besides the difference in their edge morphology and hole structure of the GO and HGO, the color of the filtrate (waste), collected during cleaning via filtration, is also different. While the one obtained from GO cleaning is colorless, the one from HGO cleaning is light yellow (**Figure 3.3C-II**). The color of the filtrate (**Figure 3.3C-III**) becomes darker upon further increase in microwave irradiation time (45seconds) of the reaction mixture. We noticed that the resultant GO is still highly oxidized and porous from the Uv-Vis spectroscopy (**Figure 3.3B**) and AFM measurement (**Figure 3.3A**), but the product yield is dramatically decreased to ~50 wt%, in comparison to 120wt% product yield of HGO with 40 seconds of microwave irradiation. The yellow colored filtrates are fluorescent and the fluorescent intensity increases with the microwave time as shown in **Figure 3.3D**. In contrast, by excluding the KMnO₄ in reaction mixture, a similar dark

yellow filtrate was also obtained within 30 seconds of microwave irradiation (**Figure 3.3C-IV**), suggesting that KMnO_4 plays an important role in slowing down the carbon gasification/etching processes.⁴⁴ The large amount of carbon lost in the form of small organic compounds and/or gasification to CO_2/CO is related to the molecular mechanisms of graphite oxidation.⁴⁷

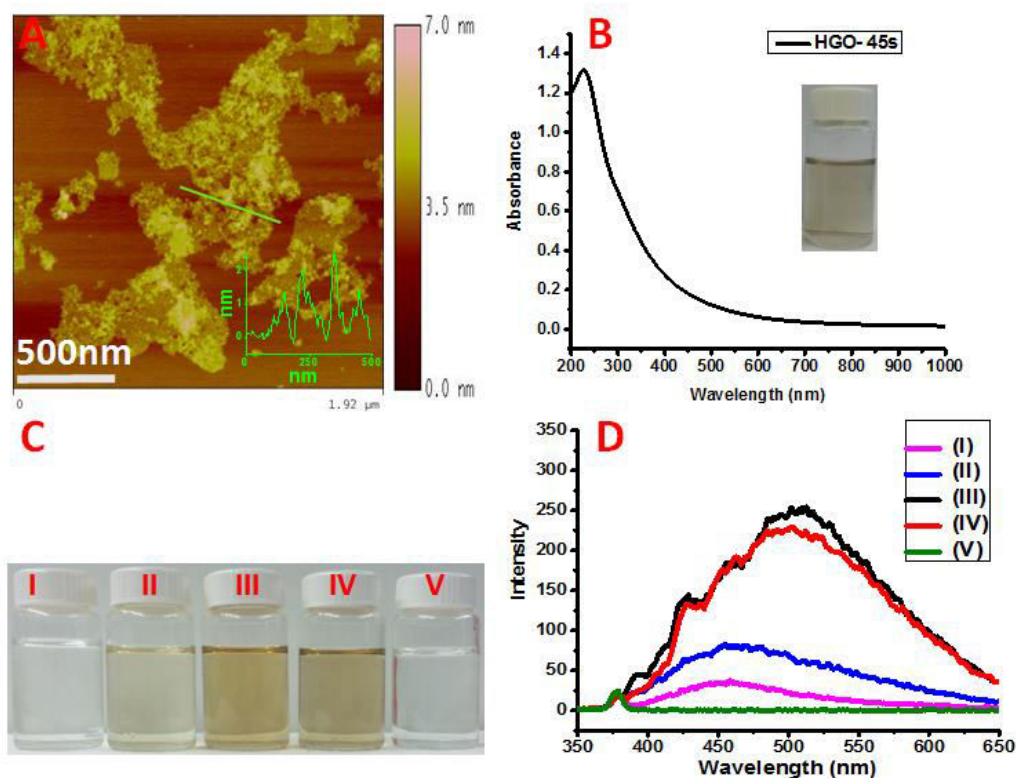


Figure 3.3. (A) AFM and (B) Uv-Vis-NIR spectrum of an aqueous dispersion of HGO sheets obtained via 45seconds of microwave heating. The inset of (B) shows its digital picture. (C) is the digital pictures and (D) is the fluorescence emission spectra ($\lambda_{\text{exc}} = 335\text{nm}$) of the filtrates, produced after graphite particles were oxidized with different microwave time: (I) 30seconds, (II) 40seconds, (III) 45seconds, respectively. (IV) is the filtrate obtained with the same experimental conditions as (I), except that KMnO_4 was excluded and (V) is the filtrate obtained with the same experiment condition as (II), except the graphite was excluded.

For an efficient approach to fabricate graphene sheets with controlled structures from graphite particles, the first requirement is to access the internal surfaces of graphite

particles by an oxidant. However, due to the strong interaction and close distance between the sheets, only the edges of graphite particles and the exposed graphene surface are readily accessible; the rest of the graphene is physically blocked from interaction with the oxidant molecules.⁴⁸ The oxidation of each layer of graphene includes several steps: Firstly, oxidation is initiated to create oxygen containing groups, such as -OH and/or epoxy groups, on the basal plane and edges of graphene sheets. Further oxidation includes two simultaneous and competing processes: (i) continuing initiation of oxidation in the intrinsic graphene domains resulting in generation of more -OH and/or epoxy groups, referred as defect generation; and/or (ii) further oxidation of the already oxidized carbon atoms, ultimately leading to gasification of the carbon atoms (mostly CO or CO₂) and generation of small organic carbon species (which are separated during filtration), resulting in vacancies and holes throughout the graphene basal planes. This process is also called defect consumption or etching.^{20, 49} Continuing etching eventually leads to fracture/cutting of graphene sheets to small pieces. The relative reaction rates of these processes determine the overall speed of the graphene fabrication as well as the oxidation level, the lateral size and holey structures of the fabricated graphene sheets.

We performed several control experiments to understand the role of the microwave heating, microwave irradiation time and KMnO₄ in controlling the oxidation level and the morphology/structure of the fabricated graphene oxide sheets. First we studied the effect of the amount of KMnO₄ on graphene's morphology, size and oxidation level. For this aim we performed experiments with different amount of KMnO₄ (0 and 125 wt% of graphite) and kept all the other reagents (H₂SO₄ and HNO₃) and microwave condition (300Watt, 30 seconds) the same. When the KMnO₄ is absent (0 wt% of graphite), we get uniform

graphene nanosheets (**Figure 3.4A**) with the intrinsic property of graphene largely remained, consistent with our previous chapter-2.⁴⁴ The lateral size of the graphene nanosheets is around 10 ± 4 nm from the AFM measurement (**Figure 3.4A**). The UV-Vis-NIR spectrum of the nanosheets solution (**Figure 3.4D**-black line) shows a peak at 264 nm along with strong NIR absorption. However, when the amount of KMnO_4 was increased to 125 wt% of graphite, the lateral sizes of the product slightly increased ranging from tens of nanometers to hundreds of nanometers, as shown in its AFM images (**Figure 3.4B**).

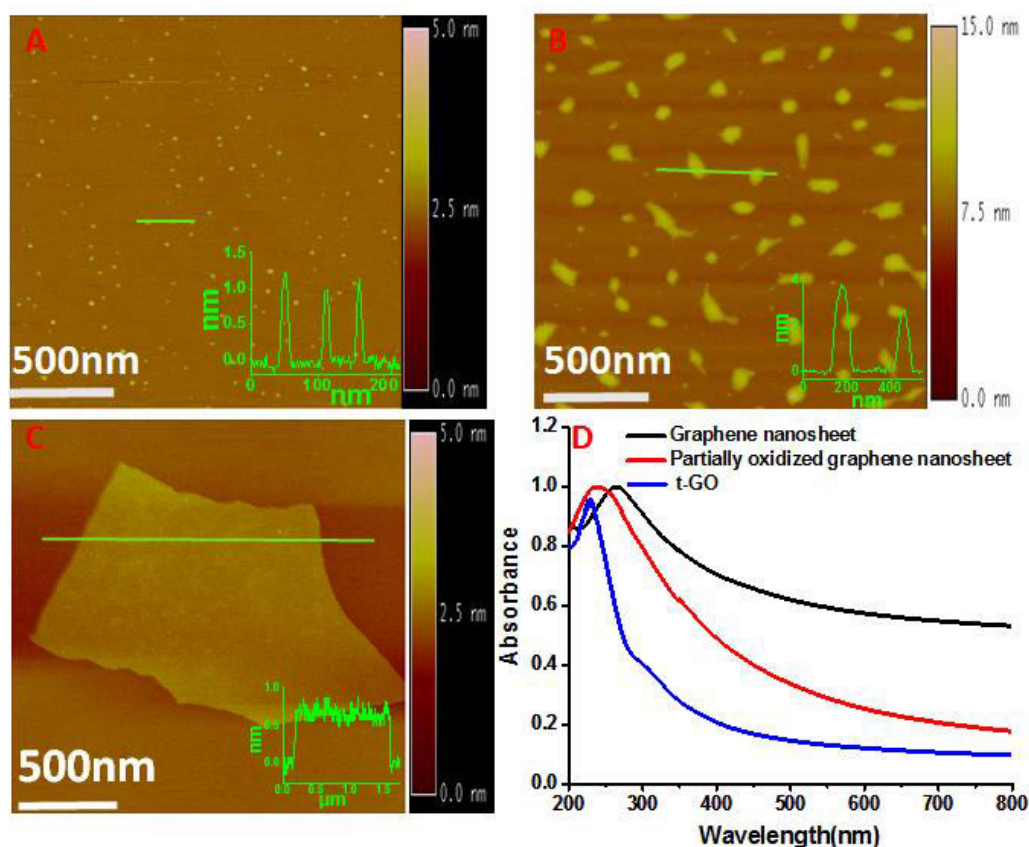


Figure 3.4. AFM images of the products obtained with different control experimental conditions. Microwave heating of the mixture of H_2SO_4 , HNO_3 and graphite (300W and 30 seconds) in the absence of KMnO_4 (A); in the presence of KMnO_4 (125wt% of graphite) (B); traditional heating of the mixture of H_2SO_4 , HNO_3 and graphite with KMnO_4 (500wt% of graphite) (C). (D) shows their corresponding UV-VIS-NIR spectrum: black curve for (A), red curve for (B) and blue curve for (C). The UV peak at 264 nm and the strong NIR absorption indicate the intrinsic properties of graphene are largely maintained in product

(A); the blue shift of the UV peak to 240 nm and the decrease in NIR absorption suggest that the product (B) is partially oxidized. The product (C) shows a typical UV-VIS-NIR spectrum of a highly oxidized graphene oxide.

Moreover, the UV-visible spectrum (**Figure 3.4D**-red line) of the product shows a peak position at 240 nm, which indicates the product are partially oxidized compared to those obtained without KMnO_4 . These results suggest that in absence of KMnO_4 , the defect consumption rate is much faster than the rate of new defect generation, resulting in uniform nanosized graphene with largely retained intrinsic properties. But in the presence of KMnO_4 , defect consumption speed is decreased possibly because the MnO_4^- ions anchor and /or bind to the defects (the oxygen containing functional groups generated in the first step of oxidation), which slows down the speed of defect consumption. Hence the lateral size and oxidation level of graphene is slightly increased.

We also performed another control experiment to study the importance of microwave heating over traditional heating in HGO synthesis. In this control experiment, instead of microwave heating, we heated the mixture of graphite, sulfuric acid, nitric acid and KMnO_4 (500 wt% of graphite) at 80 °C on oil bath for 12 hours. Similar to traditional Hummer's method, highly oxidized GO sheets (we referred as t-GO) were produced. The UV-Visible spectrum of the t-GO (**Figure 3.4D**-blue line) shows a typical absorption peak of GO at 230nm due to $\pi \rightarrow \pi^*$ transition of $\text{C}=\text{C}$ and a shoulder around 300 nm due to $n \rightarrow \pi^*$ transition of carbonyl functional groups (**Figure 3.4C**). The t-GO sheets are mainly single layered with their lateral sizes ranging from hundreds nanometers to a few micrometers. However, nanoholes in these sheets are seldom observed, suggesting that microwave heating is important to synthesis holey GO. This is possibly due to its ability to

generate much higher local temperatures on the graphene surface, which enhances the defect dramatically consumption compared to the case of traditional heating.

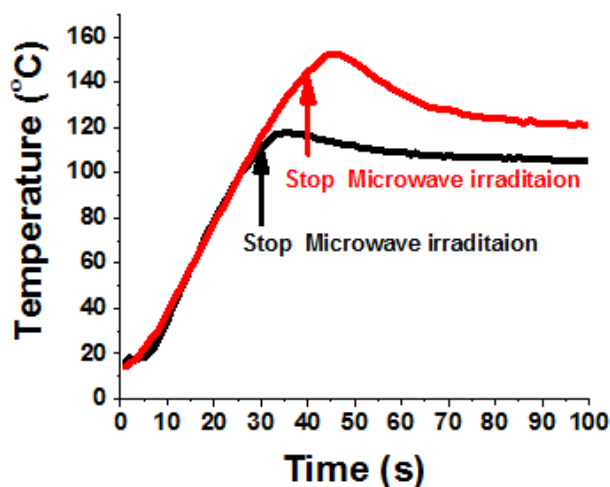
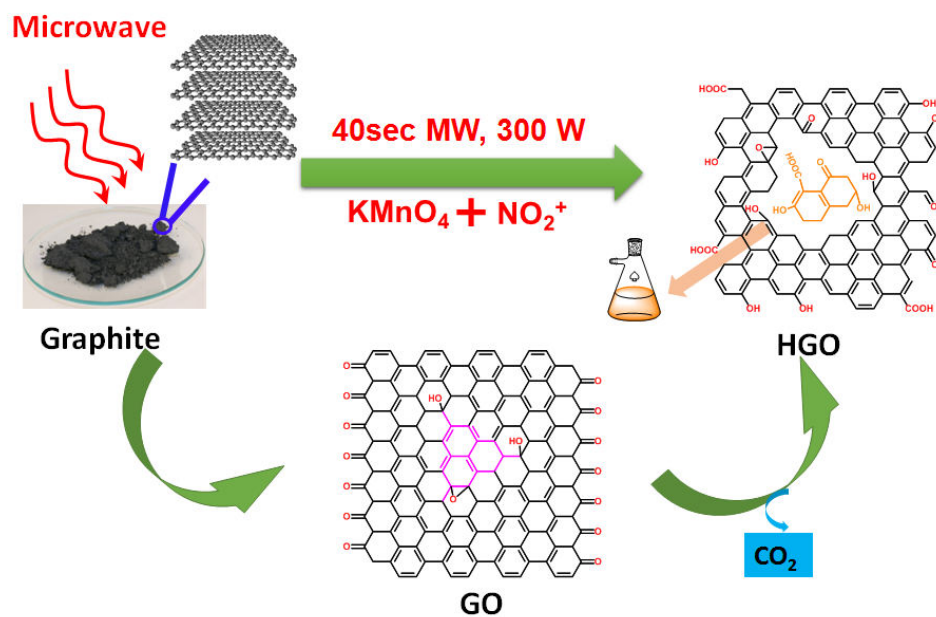


Figure 3.5. Microwave heating temperature (°C) profile with time during GO (black line) and HGO (red line) synthesis.

The exact mechanism of hole generation in the graphene oxide is not fully understood, which is worthy to further study. Based on our results, additional control experiments and combined with previous experimental and theoretical studies,^{45, 49-54} we hypothesize the following scenario might have occurred: It is known that KMnO_4 preferably oxidizes existing defects,⁴⁵ while nitronium ions have the power to oxidize both existing defects and intact graphene domains.^{45, 50, 51} It is very likely that the nitronium ions efficiently intercalate to the inner sites of graphite particles and initiate oxidation of graphene sheets and generates defects (functional groups such as $-\text{OH}$ and epoxy groups) across the entire sheets. In the following step, if KMnO_4 was not included, these defects were quickly etched away by losing small organic molecules and/or releasing CO_2/CO gases. As a result, holes are generated on the graphene sheets. However, this etching step is so fast that the generated holey graphene sheets were rapidly and uncontrollably

fractured to small pieces.⁴⁴ With KMnO_4 in the reaction system, MnO_4^- may bind to some of the epoxy/hydroxyl groups (defects), generated in the first step of oxidation by the nitronium ions, protects them from further oxidation and slows down the defect consumption/etching step. On the other hand, KMnO_4 starts its own unzipping like oxidative cutting mechanism.⁴⁵ At short microwave time (30 seconds), highly oxidized non-porous GO sheets were generated with straight edges and few holes/pores in their basal plane, similar to those fabricated with Hummers or modified Hummers methods. However with further slightly increasing the microwave time to 40 seconds, the temperature was significantly increased (**Figure 3.5**). Noted that the temperature was measured outside of the reaction vessel, the true temperature inside should be much higher than the measured ones. At the largely increased temperatures, the KMnO_4 could not protect the defects efficiently anymore, so etching occurs both in the basal plane and at the edges of GO, resulting in holey GO with irregular edges as shown in **Scheme 3.1**.



Scheme 3.1. Schematic drawing of proposed mechanism of HGO synthesis.

Heteroatom doping of graphene, especially N-doping, can effectively tailor and fine tune its electronic structures, thus has great impacts on its applications in electronics, energy storage and metal free catalysts.^{24, 28-31} There are quite a few strategies have been reported for N-doping of graphene, however all of them require high temperature (500 ~ 1000 °C) and/or long reaction time for N doping (**Table 1.3.1**). Recently, Tang *et al.* exploited microwave heating to reach high temperature and to shorten the doping time.⁵⁵ However, due to the low microwave absorption capability of GO, the microwave assisted N doping could be achieved only for pre-pyrolytic graphene oxide dry powder, which obtained by preheating of GO at ~250 °C before microwave treatment. Furthermore, the product is not easy for solution processible applications. Here in, again by taking an advantage of microwave heating, we report that solution processible N doped and concurrently reduced GO is achieved at low temperatures and with short reaction time. Specifically, a mixture of GO sheets and concentrated NH₄OH is heated in a closed glass vessel via microwave irradiation. In ~40 seconds, the apparent temperature reaches to 120 °C possibly due to dielectric and/or ionic heating mechanism. With a closed looped configuration of the microwave heating system, we held this temperature for 10 minutes. From Uv-vis spectroscopy, FT-IR, and XPS characterization, we found that this process results in simultaneous N-doping and reduction of GO/HGO. We refer the N-doped holey reduced GO as N-HrGO-10 and N-doped nonporous reduced GO as N-rGO-10, 10 denotes 10 minutes of microwave reaction time for N doping.

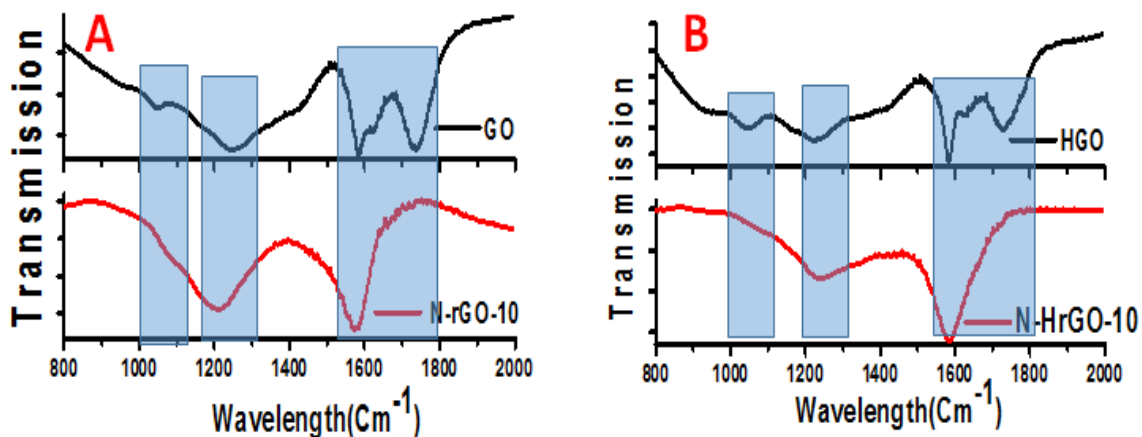


Figure 3.6. (A) FTIR spectrum of GO and N-rGO-10. (B) FTIR spectrum of HGO and N-HrGO-10.

Figure 3.1F and **E** shows that the UV absorption peak of N-HrGO-10 and N-rGO-10 red shifted to ~ 260 nm along with enhanced NIR absorption, indicating the aromatic conjugation of graphene was partially restored. The FT-IR spectrum analysis of GO, HGO, N-rGO-10 and N-HrGO-10 (**Figure 3.6**) also shows that the peaks at ~ 3400 cm^{-1} (O-H stretching), 1735 cm^{-1} (C=O stretching), 1625 cm^{-1} (adsorbed water bending) and 1048 cm^{-1} (C-O stretching vibrations), were initially present in the spectrum of GO and HGO, disappeared in N-rGO-10 and N-HrGO-10. This result soundly demonstrates the removal of oxygen containing functional groups from GO sheets and the GO sheets were reduced during the microwave reaction with NH_4OH . Meanwhile a new strong band near 1200 - 1240 cm^{-1} appears in N-rGO-10 and N-HrGO-10, which can be identified and assigned to C-N stretching vibrations, indicating N was successfully incorporated into the carbon matrix of the GO sheets. Furthermore, the successful N-doping is also proved by the appearance of strong N1s along with C1s and O1s peak in the XPS survey spectrum (**Figure 3.2A**) of N-rGO-10 and N-HrGO-10. Detailed quantitative study of the C1s and O1s peak (**Table 3.1**) shows an increased C:O atomic ratio and a decreased relative O1s

peak intensity in N-rGO-10 and N-HrGO-10 compared to that of GO and HGO, suggesting that the oxygen functional groups are extensively removed after the microwave reaction of GO with NH_4OH , consistent with the FTIR results (**Figure 3.6**). It was reported that NH_4OH can either serve as an epoxide ring opening agent and/or as a Lewis/Bronsted acid which reacts with epoxy/carboxyl groups of the GO, resulting in the introduction of N into graphitic structure along with the reduction of graphene oxide.⁴³ Indeed, the $-\text{OH}/\text{epoxy}$ and $-\text{COOH}$ peak intensity in the C 1s spectra of N-rGO-10 (**Figure 3.2F**) and N-HrGO-10 (**Figure 3.2E**) are greatly decreased as compared to GO and HGO (**Table 3.3**). However, the relative ratio of $\text{C}=\text{O}$ remained unaltered, showing that carbonyl moiety is not reactive in this reaction. Raman spectroscopy was also used to characterize the HGO sheets before and after N doping. As expected, the Raman spectra (**Figure 3.7**) of all the samples show D band (ca. 1315 cm^{-1}) and G band (ca. 1590 cm^{-1}) and the ratio intensities ($I_{\text{D}}/I_{\text{G}}$) of D and G band does not changed upon simultaneous N-doping and reduction. These results are consistent with previous reports that incorporation of heterogeneous N-dopants breaks the hexagonal symmetry of the graphene.⁵⁶ Therefore even the GO was reduced during N-doping, the $I_{\text{D}}/I_{\text{G}}$ ratio would not decrease, which is in contrast to the scenario of reduction of GO to rGO without introducing any heterogeneous dopants. The surface area of the N-HrGO-10 and N-rGO-10 was also measured via methylene blue absorption method. We found that the surface area of N-rGO-10 dramatically decreased from 947 to $560\text{ m}^2/\text{g}$ after simultaneous reduction and N-doping process (**Table 3.2**). In highly contrast, the high surface area of N-HrGO-10 is largely maintained (1424 to $1194\text{ m}^2/\text{g}$ for HGO and N-HrGO-10, respectively). From the SEM (scanning electron

microscopy) image of N-HrGO-10 (Figure 3.8), we can see that its holey structure is nicely preserved during the simultaneous reduction and N-doping process.

Table 3.3. The calculated relative % of different kind of carbon from XPS high resolution C1s deconvolution in different catalysts.

Catalysts	C=C	C-OH	C=O	COOH
GO	48.92	23.73	6.76	7.10
N-rGO-10	63.60	8.33	7.18	3.97
HGO	46.07	23.40	7.47	7.89
N-HrGO-10	65.43	7.89	7.00	3.19

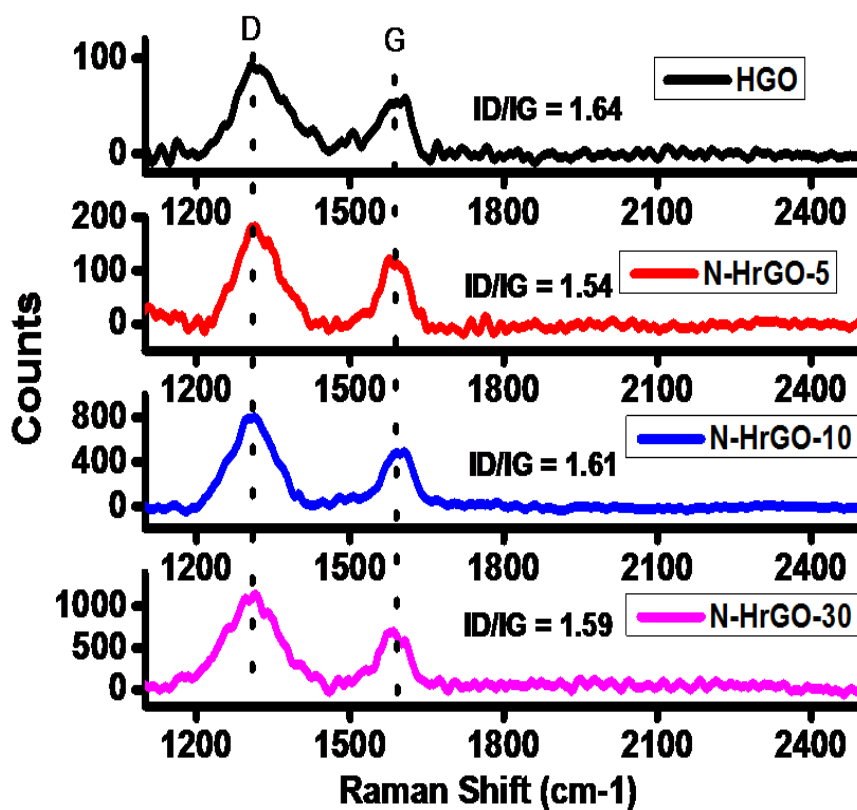


Figure 3.7. Raman spectra of HGO and N-HrGO-5, N-HrGO-10 and N-HrGO-30.

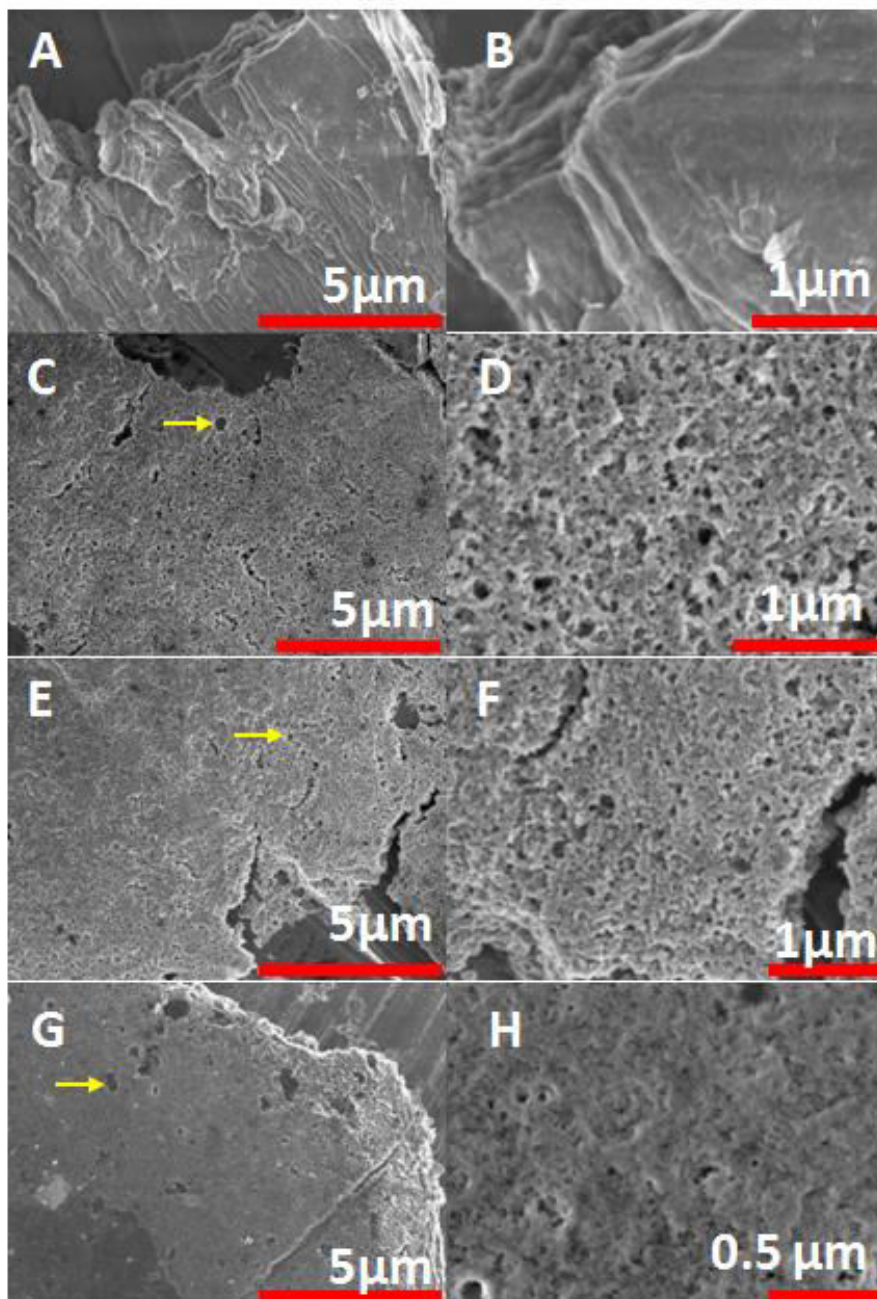


Figure 3.8. Scanning electron microscopic (SEM) images of N-rGO-10(A and B), N-HrGO-5(C and D), N-HrGO-10(E and F) and N-HrGO-30(G and H). The yellow arrow shows hole on N-HrGO's surface.

It is well documented that the incorporated N in graphene can be in different forms, which would influence the electronic structure and therefore the catalytic performance of the doped graphene.^{34, 57, 58} For example, pyridinic and pyrrolic N refers to N atoms bonded

to two carbon atoms and donates one and two p-electrons to the aromatic π -system, respectively. Quaternary-N atoms are incorporated into the graphene via substituting some carbon atoms within the graphene plane. The pyridinic and pyrrolic N are always located at the graphitic edge, whereas quaternary N can be both “edge-N” and “bulk-like-N”. To evaluate the type and level of N doping by this microwave approach, we deconvoluted high resolution XPS N1s peak (**Figure 3.9**) and summarize the relative ratio of each type of N species. The relative ratios of pyridinic-N (398.5 eV), amine-N (399.6 eV), pyrrolic-N (400.7 eV), quaternary-N (402.0 eV) and N-oxides (like NO at 403.4eV, NO₂ at 405.2eV and NO₃ at 406.6eV) are listed in **Table 3.4**. From this careful analysis, we found that the microwave approach results in similar N types as traditional heating approaches,^{24, 59} even though the total N content is slightly higher (8.5 atomic %). In addition, the relative ratio of each N type varies depending on the initial GO structures. With HGO, more pyridinic-N and pyrrolic-N were generated in comparison to the non-porous GO, possibly due to the difference in the amount of edges (**Table 3.4**).

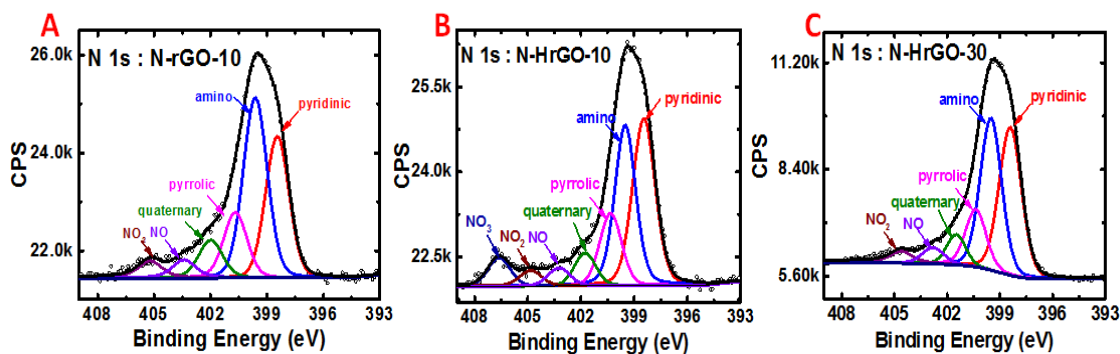


Figure 3.9. XPS high resolution N1s peak analysis of N-rGO-10 (A), N-HrGO-10 (c) and N-HrGO-30 (d), where 10 and 30 denotes microwave treatment time (in minutes) of GO/HGO with NH₄OH at 120 °C.

Table 3.4. Relative % ratio of different kind of N-dopant in N-HrGO-10, N-HrGO-30 and N-rGO-10.

N-Type (%)	Pyridinic-N	Amino-N	Pyrrolic-N	Quaternary-N	Other Oxidized N
N-HrGO-10	37.03	33.54	15.21	6.73	7.47
N-HrGO-30	35.97	35.61	13.91	6.47	8.04
N-rGO-10	29.36	38.72	14.19	8.47	9.25

N-doped carbon nanomaterials exhibited good catalytic activity for a wide range of catalytic reactions.^{6, 31, 35, 60, 61} Their performance depends on the level and type of N doping for the specific catalytic reaction of interest.^{60, 61} It has been already reported that N-doped graphene/CNT shows better electro catalytic activity for ORR,^{6, 62} however the detailed electro catalytic mechanisms of these N-doped carbon materials remains unclear. Several research groups have reported that enhanced ORR activity of N-doped carbon nanomaterials is due to the presence of pyridinic N at the edges^{63, 64} or a combined effect from pyrrolic and pyridinic N, which introduces an asymmetric spin density and atomic charge density in the graphene plane, making it possible for high ORR catalytic activity.⁶⁵

Table 3.5. Electrochemical parameters (onset potential, peak potential, current density at -0.4V and Tafel slopes- b1 and b2- calculated at low and high current density region, respectively) of different catalysts for ORR estimated from CV and RDE polarization curves in 0.1M KOH solution. All potential are measured using Ag/AgCl as a reference electrode.

Catalyst	Onset Potential	Peak Potential	Current density (mA cm ²) at -0.4V	Tafel slope (mV/decade)	
				b1	b2
Bare Electrode	-0.18V	-0.40V	0.74	57.28	143.93
EC-HrGO	-0.15V	-0.36V	2.08	58.58	107.11
N-rGO-10	-0.14V	-0.36V	1.04	87.46	152.57
N-HrGO-10	-0.11V	-0.28V	2.41	58.37	104.78
Pt/C	-0.02V	-0.21V	3.05	75.22	121.10

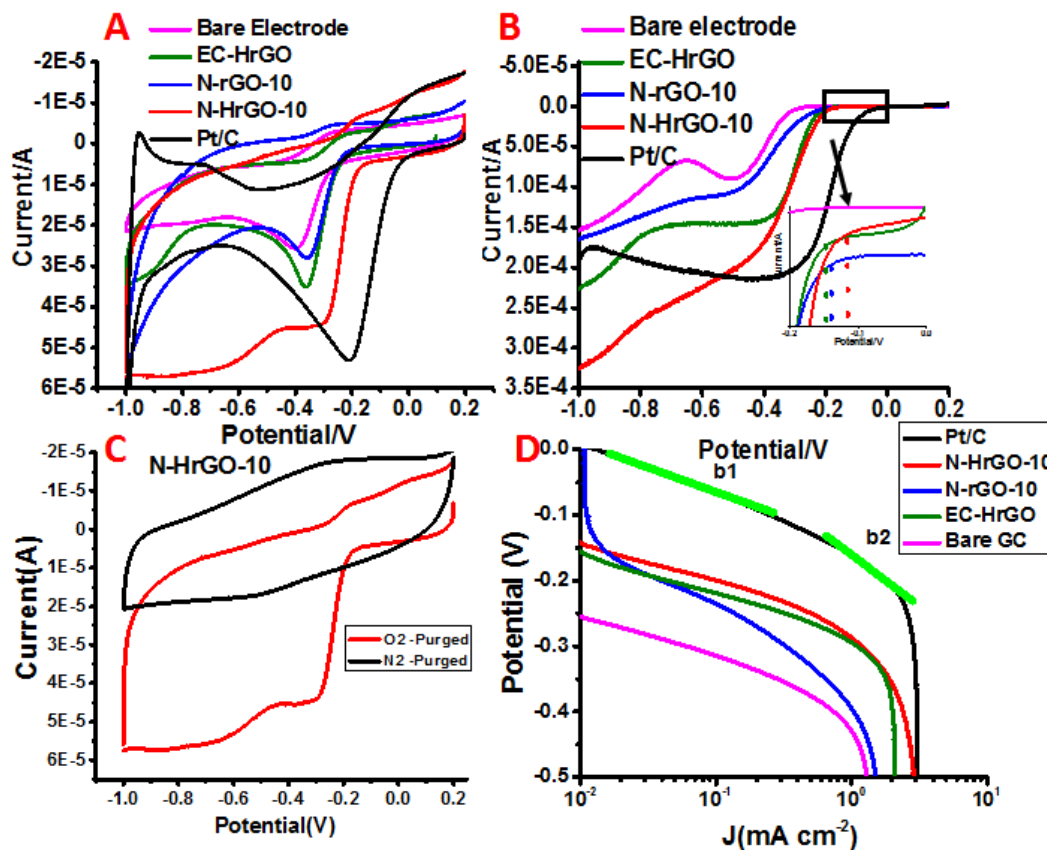


Figure 3.10. (A) and (B) is CV and LSV curves of Pt/C, EC-HrGO, N-HrGO-10, N-rGO-10 and bare electrode in O₂ saturated 0.1M KOH electrolyte at a scan rate of 50 mV/s and 10 mV/s, respectively. Inset (B) is zoomed in LSV curve of bare electrode, N-rGO-10 and N-HrGO-10. All potentials are measured using Ag/AgCl as a reference electrode. (C) CVs of N-HrGO-10 in N₂ and O₂ saturated 0.1M KOH electrolyte at a scan rate of 50 mV/s. (D) Tafel plots of Pt/C, N-HrGO-10, N-rGO-10, EC-HrGO and bare electrode derived by the mass-transport correction of corresponding RDE data (**Figure 3.10B**).

The electrocatalytic activity of N doped holey rGO (N-HrGO-10) was evaluated for ORR by cyclic voltammetry (CV) in a 0.1M KOH solution saturated with oxygen and nitrogen (**Figure 3.10C**). A large reduction peak was observed in the O₂ saturated electrolyte solution, but not in the N₂ saturated solution, suggesting that O₂ is electrocatalytically reduced on the N-HrGO-10 modified electrode. We compared the ORR capability of N-HrGO-10 with bare GC electrode, commercial Pt/C, N-rGO-10 and electrochemically reduced holey GO (EC-HrGO), which is obtained by electrochemical

reduction of HGO⁶⁶. From their CV and linear sweep voltammetry (LSV) curves obtained in O₂ saturated 0.1M KOH (**Figure 3.10A, B** and **Table 3.5**), we can see that the N-HrGO-10 shows much better ORR catalytic activity than the bare electrode, EC-HrGO and N-rGO-10 demonstrated by its more positive onset potential, peak potential and higher current density, which is similar or slight better than previously reported N-doped graphene, synthesized by traditional high temperature approaches.^{6, 57, 67, 68} However, N-HrGO-10 still shows slightly more negative potential and lower current density at lower potential region compared to the commercial Pt/C, indicates that the Pt/C catalyst still shows the best ORR performance. While it is noticed that at higher potentials (> -0.6 V), N-HrGO-10 shows higher current density, which indicates that it is possibly more kinetically facile toward ORR than the Pt/C at high over-potentials.

To understand the mechanism of oxygen adsorption on the electrocatalysts of the N-HrGO-10, we drew Tafel plots (**Figure 3.10D**) of N-HrGO-10 derived by the mass-transport correction of corresponding RDE data from **Figure 3.10B**. The same data treatment was also performed for Pt/C, N-rGO-10, EC-HrGO and bare electrode for comparison. The Tafel slopes from the plots were summarized in **Table 3.5**. The commercial Pt/C electrocatalyst shows two different Tafel slopes (75.22 mV/decade and 121.10 mV/decade at lower and higher current density region, respectively), which indicates a Langmuir adsorption and Temkin adsorption of oxygen.⁵⁶ Similar to Pt/C, the Tafel plots of N-HrGO-10 also shows two slopes (**Table 3.5**) but they are much lower from that of the Pt/C catalysts, indicates a possible different oxygen adsorption mechanism. Moreover, the N-HrGO-10 and EC-HrGO shows smaller Tafel slopes than the N-rGO-10, demonstrating that the existence of nanoholes and/or the large surface area could improve

the catalytic activities of carbon based catalysts. Furthermore, we also found that ORR activity of N-HrGO depends on the microwave reaction time of HGO with NH_4OH . At longer reaction time, the relative ratios of N types (**Table 3.4**) were changed, which largely influenced their ORR catalytic activity. From the CV curves (**Figure 3.11**), the onset potential and peak potential were negatively shifted and the kinetic current decreased on N-HrGO-30, which is obtained via 30 mins of microwave reaction time. Among all the graphene modified electrodes, N-HrGO-10 modified electrodes exhibit the lowest onset potential and peak potential, and highest ORR current.

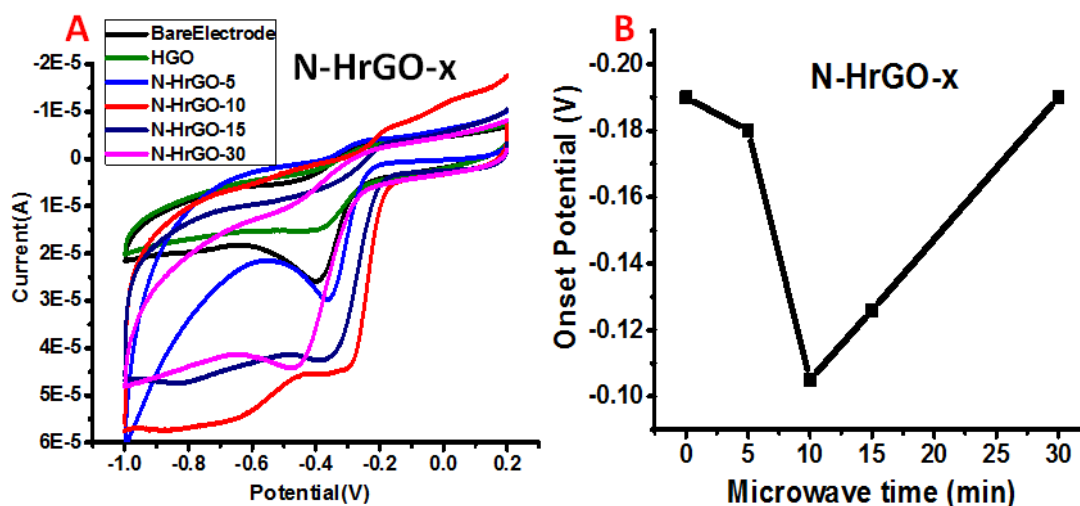


Figure 3.11. CV curves (A) and onset potential (B) of N-HrGO-x electrode in O_2 saturated 0.1M KOH electrolyte at a scan rate of 50mv/s, where “x” is different microwave time (0, 5, 10, 15, 30 minutes) used for synthesis of different N-HrGO. All potentials are measured using Ag/AgCl as a reference electrode.

ORR can occur either via a direct four electron reduction pathway or a two electron pathway. In the four electron pathway, oxygen is directly reduced to water, while in the two electron pathway, oxygen is reduced to peroxide. In fuel cells, the direct four electron pathway is preferred to achieve better energy conversion efficiency and prevent corrosion of cell components due to the hazardous peroxides. LSV of EC-HrGO (**Figure 3.10B**)

clearly shows a two-step reaction pathways for ORR (-0.2V to -0.4V and -0.7V to -1.0V), which indicates the two electron pathway mechanism while LSV of N-HrGO-10 shows almost one step reaction pathway, indicates 4 electron pathway for ORR. To carefully quantify the electron transfer numbers and the formation of peroxide species (HO_2^-) during the ORR process, we performed rotating ring disk electrode (RRDE) measurements. The % HO_2^- and the electron transfer number were determined by the following equations:

$$\% \text{HO}_2^- = \frac{(200 \times \frac{I_r}{N})}{(I_d + \frac{I_r}{N})} \quad (3.1)$$

$$n = \frac{(4 \times I_d)}{(I_d + \frac{I_r}{N})} \quad (3.2)$$

Where, I_d and I_r is the current measured from the disc and ring electrode, respectively, and N is current collection efficiency of the Pt ring electrode. N was determined to be 0.424 from the redox reaction of $\text{K}_3\text{Fe}(\text{CN})_6$. **Figure 3.12A** shows the disk and ring currents from N-HrGO-10, N-HrGO-30, EC-HrGO, N-rGO-10 and Pt/C modified electrodes, respectively. Notably, the N-HrGO-10 and Pt/C modified electrodes exhibited the lowest ring current among these graphene modified electrodes. The ring current increased on the N-HrGO-30 and EC-HrGO modified electrode shows the highest ring current. Based on the ring and disk currents, the electron transfer numbers (n) and % HO_2^- were calculated (**Figure 3.12B** and **C**). The EC-HrGO modified electrode demonstrated the lowest electron transfer number of 2.5 to 2.6, and it also generates the highest percentage of peroxide (75%). The electron transfer number for the N-HrGO-30 and N-rGO-10 are similar, slightly increased to about 3 and the amount of peroxide

generated decreased to 45-70% depending on the potentials applied during the ORR. In sharp contrast, the $n = 3.5$ to 3.8 for the N-HrGO-10 modified electrode over the whole potential range, emphasizing that the ORR proceeds mainly via a direct four-electron pathway. In consistent to the electron transfer number, the % of peroxide is as low as 12%. The much better performance of N-HrGO-10 over N-rGO-10 is possibly due to its relatively high concentration of pyridinic and pyrrolic N and the existence of holes and edges, which also provide higher surface area, largely facilitates the mass transport of O_2 and the electrolyte. On the other hand, EC-HrGO should have the same or similar amount edges, holes and surface area compared to the N-HrGO-10. Its poor performance is very likely due to the lack of N doped catalytic centers. Moreover, N-HrGO-30 also shows lower electron transfer number and higher % HO_2^- , possibly due to the change in N type upon prolonged microwave irradiation time. From XPS N1s peak analysis of N-HrGO-10 and N-HrGO-30 (**Figure 3.9B and C**), we summarized N type and relative ratio in **Table 3.1** and **Table 3.4**. Even though the atomic N% is not dramatically changed at different microwave reaction time, but the pyridinic N, pyrrolic N is decreased at longer microwave reaction time (30min), which can be the possible reason for decreased ORR catalysis.

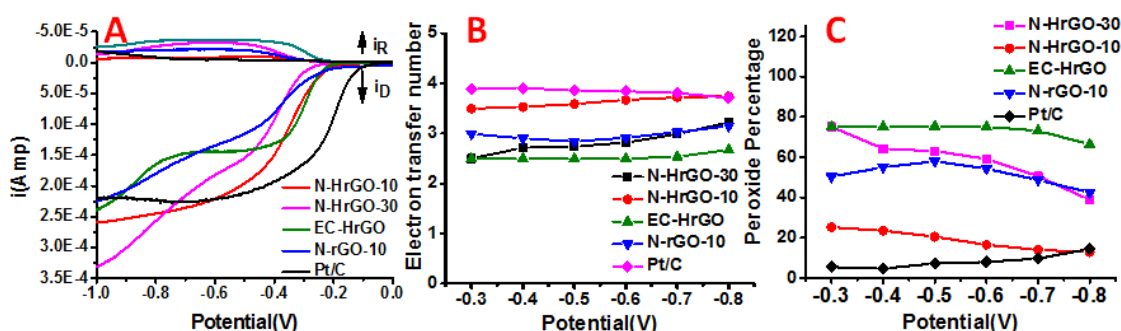


Figure 3.12. (a) RRDE voltammogram of N-HrGO-10, N-HrGO-30, EC-HrGO, N-rGO-10 and Pt/C modified electrode in oxygen saturated 0.1M KOH at a scan rate of 10mV/s and 1600rpm rotation speed. (b) and (c) is the number of electron transfer and relative

peroxide %, respectively, for all catalyst calculated from RRDE voltammogram. All potentials are measured using Ag/AgCl as a reference electrode.

To further study how the hole structures on the N-HrGO-10 influence their electron transfer kinetics involved in ORR, rotating disc electrode (RDE) measurements (**Figure 3.13**) were performed in O₂ saturated 0.1M KOH solutions under various electrode rotating rates. The same study also performed on the N-rGO-10 and Pt/C for comparison. As shown in **Figure 3.13**, the current density is increased with rotation speed from 250 to 2500 rpm due to the enhanced diffusion of the electrolytes and O₂. The kinetic parameters, such as kinetic current density (J_K), and the effective diffusion coefficient of O₂ (D₀) in ORR is then analyzed using the Koutecky-Levich (K-L) equation.⁶⁹

$$1/J = 1/J_L + 1/J_K = 1/B\omega^{0.5} + 1/J_K \quad (3.3)$$

Where $B = 0.62nFC_0(D_0)^{2/3}\nu^{-1/6}$ and $J_K = nFkC_0$

Here, J is the measured current density, J_L and J_K are the diffusion limiting and kinetic limiting current densities, ω is the angular rotation rate of the disc electrode (rad/s), B is Levich constant, n is the number of electrons transferred in the oxygen reduction reaction (mol⁻¹), F is the Faraday constant (F = 96485 C/mol), D₀ is the effective diffusion coefficient of O₂ (cm²/s), ν is the kinematic viscosity of the electrolyte (cm²/s), C₀ is the oxygen concentration (mol/cm³) and k is the electron transfer rate constant.

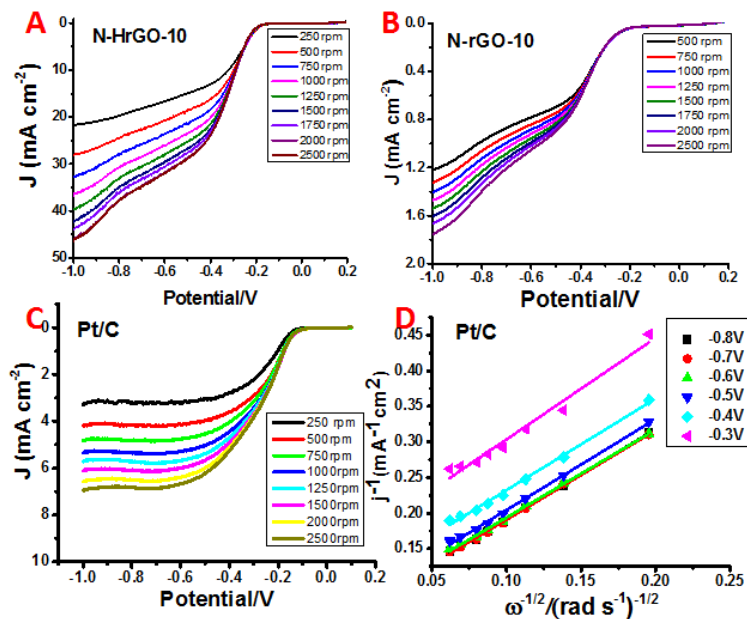


Figure 3.13. LSV curves of N-HrGO-10(a), N-rGO-10(b) and Pt/C(c) at different rotation speed in O₂ saturated 0.1M KOH solution at 10mV/s. (d) is K-L plot of Pt/C, obtained based on the LSV data(c). All potentials are measured using Ag/AgCl as a reference electrode.

We plotted the K-L plot (J^{-1} vs $\omega^{-1/2}$) for N-HrGO-10, N-rGO-10 and Pt/C at various electrode potentials (Figure 3.14A, 3.14B and 3.13D). From the linearity and parallelism of the plot at various electrode potentials, we consider that the ORR is a typical first order reaction kinetics with respect to the dissolved oxygen concentration. The slope and intercept of the K-L plot gives the Levich constant (B) and J_K , which then are used to calculate the effective diffusion coefficient constant of O₂ (D_0) and electrochemical rate constant k , respectively, by using electron transfer number n calculated from RRDE measurement. From Figure 3.14D, the N-HrGO-10 has more than 4 times higher k than the N-rGO-10. Here, for the first time, we found that the effective diffusion coefficient of O₂ is also much higher (Figure 3.14C) in N-HrGO-10, which quantitatively demonstrates that the holey structures on the basal plane of graphene indeed contributed to the enhanced diffusion of oxygen. The calculated kinetic current density (J_k) and rate constant (k) from

Equation 3.3 for N-HrGO-10 is found to be 462.38 mAcm^{-2} and 0.015 cm/s , respectively, which is much higher than other reported values for heteroatom doped graphene catalyst.⁷⁰

⁷¹ The relatively higher kinetic and diffusion current density, along with the $4e^-$ pathway of the N-HrGO-10 demonstrates its great potential to replace the commercial Pt/C catalyst for ORR.

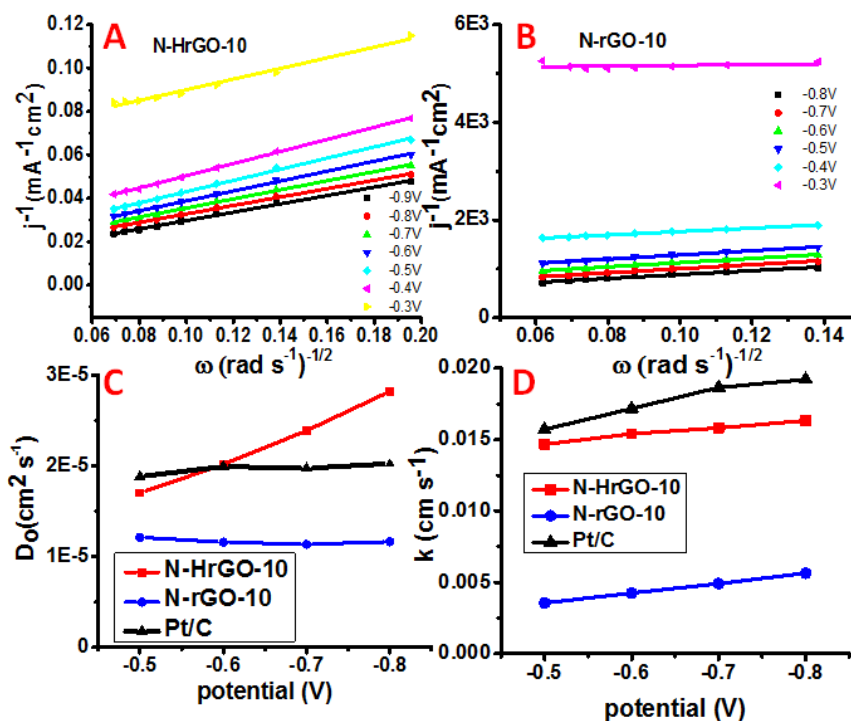


Figure 3.14. (A) and (B) are K-L plot of N-HrGO-10 and N-rGO-10, obtained based on the LSV curves at different rotating speeds (**Figure 3.13**), respectively. (C) is calculated oxygen diffusion coefficient and (D) is calculated rate constant for ORR, using slope and intercept from K-L plot of N-HrGO-10, N-rGO-10 and Pt/C. All potentials are measured using Ag/AgCl as a reference electrode.

Electrochemical impedance spectroscopy (EIS) studies were performed for N-HrGO-10, N-rGO-10, EC-HrGO and Pt/C modified electrodes respectively, to understand the underlying physics associated with their electroreduction catalytic activity. It is reported that the high frequency part in an EIS (**Figure 3.15A**), is attributed to the interfacial resistance at the surface of the active electrode, middle frequency part

corresponds to the charge transfer resistance, and the low frequency part is related to the impedance from the diffusion of electrolyte and O_2 through the catalysts.⁴³ The fitting of the EIS using a modified Randles equivalent circuit shows that N-HrGO-10 has a similar charge transfer resistance, interfacial resistance and oxygen/electrolyte diffusion resistance to the Pt/C electrodes. The nonporous N-rGO-10 shows much higher diffusion resistance, further demonstrating that the hole structures of graphene promotes better oxygen diffusion to the surface of electrode so that the redox reaction can be performed more efficiently. Based on these results we can conclude that the porous structure and N-doping in N-HrGO-10 attribute for better electro catalytic activity towards ORR.

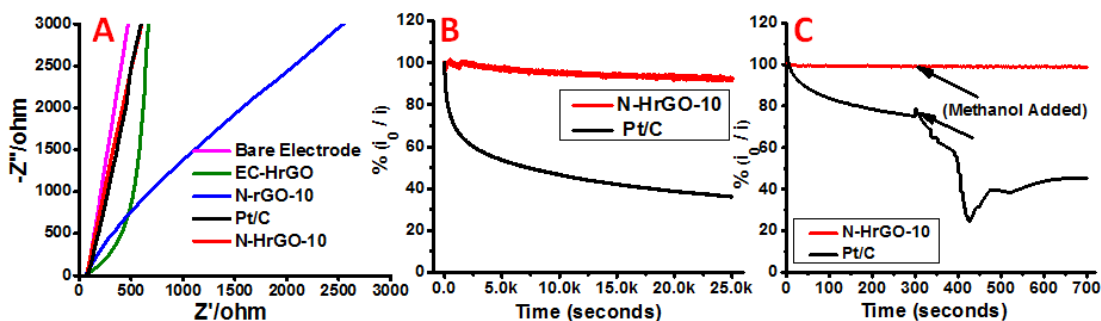


Figure 3.15. (A) is Nyquist plot of EIS for the oxygen reduction on the bare electrode, EC-HrGO, N-rGO-10, N-HrGO-10 and Pt/C. (B) is durability testing of the Pt/C and N-HrGO-10 electrode for ~7 hours at -0.38V and 1000rpm speed. (C) is chronoamperometric response of the N-HrGO-10 and Pt/C modified electrode for ORR upon addition of methanol after about ~300seconds at -0.38V. All potentials are measured using Ag/AgCl as a reference electrode.

For practical applications, the catalyst must have good catalytic activity along with good stability and durability. The durability of N-HrGO-10 with respect to commercial Pt/C was assessed through chronoamperometric measurements at -0.38 V (vs. Ag/AgCl) in a O_2 saturated 0.1M KOH at a rotation rate of 1600 rpm. From the **Figure 3.15B** we can see that, while more than 50% of the original activity of the Pt/C is lost within 4 hours, the

N-HrGO-10 loses only ~7% of its original activity after 7 hours, demonstrating that the N-HrGO-10 have far better durability. We also performed methanol cross over test to check stability of N-HrGO-10 and Pt/C against methanol. From **Figure 3.15C**, we can see that Pt/C loses its ~35% of its original activity in presence of methanol due to blockage of the active sites on Pt nanoparticle by methanol adsorption,⁷² while the introduction of methanol does not affect the ORR activity of N-HrGO-10, shows better stability against methanol cross over effect and great potential to replace Pt/C as a metal free catalysts.

3.3. Conclusions

In summary, by replacing traditional heating with microwave irradiation, holey graphene oxide sheets or graphene oxide sheets without holes can be controllably, directly and rapidly (tens of seconds) fabricated from graphite powder via a one-step-one-pot reaction with a production yield of 120 wt% of graphite. Again by taking advantage of the unique heating mechanism of microwave irradiation, a fast and low temperature approach to fabricate solution processable N doped graphene is developed. The N-doped holey graphene sheets (N-HrGO-10) demonstrated remarkable electro-catalytic capabilities for the electrochemical reduction of oxygen (ORR). The existence of the nanoholes not only provides a “short cut” for efficient mass transport, but also creates more catalytic centers due to the increased surface area and edges associated with the nanoholes. For the first time, we experimentally measure the effective diffusion constant of O₂ for N-HrGO-10 and N-rGO-10, which quantitatively demonstrates that the hole structures on the basal plane of graphene indeed contributed to the enhanced diffusion of oxygen in N-HrGO-10. Although the onset potential of N-HrGO-10 for ORR is slightly negative in comparison to that of commercial Pt/C catalysts, the N-HrGO-10 shows much better stability and durability

against methanol poisoning. The capability for rapid fabrication and N doping of holey GO can lead us to develop efficient catalysts which can replace precious coin metals for energy generation and storage, such as fuel cells and metal –air batteries.

3.4. Experimental Section

3.4.1. Synthesis of GO and HGO

Graphite powder (20mg, Sigma Aldrich, $\leq 20\ \mu\text{m}$ lateral size) was mixed with concentrated sulfuric acid (8mL, 98%, ACS grade) in a round bottom flask. The mixture is then swirled and cooled in an ice bath for approximately 5 minutes. Then concentrated nitric acid (2mL, 70%, ACS grade) was added and again cooled in ice bath for approximately 5 minutes. After that KMnO_4 (100mg, ACS grade) was added to the ice cooled acid mixture. The entire mixture was swirled and mixed for another 30 seconds and placed into a microwave reactor chamber (CEM Discover-SP). The reaction mixture was subjected to microwave irradiation (300 watts) for different time to produce GO and HGO. 30seconds of microwave results in GO, while 40seconds of microwave results in HGO. Subsequently, after microwave irradiation, the mixture is transferred to 200mL of ice containing 5mL of 35% H_2O_2 to quench the reaction and then filtered through polycarbonate filter paper (0.2 μm pore size) follow by washing with diluted hydrochloric acid ($\sim 4\%$) and deionized (DI) water. A colloidal graphene oxide (HGO and GO) solution is obtained by mild bath sonication (~ 30 minutes). The dispersion obtained is then left undisturbed for seven days to let the unexfoliated graphite particles precipitate out. The supernatant was carefully decanted and this solution is stable for months in water without significant precipitation.

3.4.2. N doping of GO and HGO

HGO or GO (3mL, 0.55 mg/mL) was mixed with concentrated ammonium hydroxide (3mL, 29.2%, ACS plus grade) in Pyrex tube and sealed with Teflon cap. This mixture is heated in microwave at 120°C for different time (5, 10, 15, 30 minutes) with the pressure limit set to 15 bars, which resulted into nitrogen doping and simultaneously reduction of GO and HGO to form N-rGO-x and N-HrGO-x, respectively, where x denotes microwave reaction time. After the reaction, the mixture is cooled down to 50°C and neutralized with sulfuric acid in order to precipitate out the product and then dialyzed with 12 kD membrane dialysis tube with DI water to remove any salt residues. Finally, the product was centrifuged and bath-sonicated to redisperse in water to achieve desired concentration.

3.4.3. Material Characterization

The morphology of the graphene samples were studied by using Tapping mode AFM Nanoscope-IIIa Multimode scanning probe microscope system (Digital Instruments, Bruker) with a J scanner and STEM/SEM (Hitachi S-4800). The sample for AFM and SEM was prepared by simple drop casting of sample on freshly cleaved mica surface and Cu tape, respectively and allowed it for air dry. The sample for STEM was also prepared by drop casting a sample (2 μ L) on carbon supported Cu grid (400 meshes, type or company) and allowed it to dry in air. X-ray Photoelectron Spectroscopy (XPS) characterization was performed after depositing a layer of all kinds of catalysts onto a gold film (a 100 nm gold layer was sputter-coated on silicon with a 10 nm Ti adhesion layer). The thickness of the film on the gold substrates was roughly 30-50 nm. XPS spectra were acquired using a Thermo Scientific K-Alpha system with a monochromatic Al K α x-ray source ($h\nu = 1486.7$ eV). For data analysis, Shirley background subtraction was performed, and the spectra were

fit with Gaussian/Lorentzian peaks using a minimum deviation curve fitting method (part of the Advantage software package). The surface composition of each species was determined by the integrated peak areas and the Scofield sensitivity factor provided by the Advantage software. Absorption spectra were recorded on a Cary 5000 UV-vis-NIR spectrophotometer in the double beam mode using a 1cm quartz cuvette. Raman spectra of the samples (deposited on anodisc membrane) were collected using Raman Microscope (Confocal) – Wi-Tec, Alpha 3000R with an excitation laser at 785 nm. FT-IR spectra of the samples (deposited on CaF₂ windows) were acquired with a Perkin Elmer Spotlight 300 system using the transmission mode. The surface area of GO, HGO, N-rGO-10 and N-HrGO-10 is measured by methylene blue (MB) adsorption method and described as below.

3.4.4. Surface area measurement of GO, HGO, N-rGO-10 and N-HrGO-10:

Methylene blue (MB) adsorption method is a common dye adsorption based approach used to determine the surface area of graphitic materials, with each mg of adsorbed methylene blue representing 2.54m² of surface area.⁷³ The surface area of graphene samples were calculated by adding a known mass of graphene sample into a standardized methylene blue solution (2mg/ml) in DI water. The solution was stirred for 24 hours to reach maximum adsorption of MB on the graphene samples. For each mg of graphene sample, 750μL of MB (2mg/ml) is added so that the total mass of MB will remain 1.5 times higher than each of the graphene samples to reach a full coverage of MB on the graphene samples. The mixture was then centrifuged at 5000 rpm for 5 minutes to separate the non-absorbed MB molecules, which are still the supernatant. Then the MB concentration in the supernatant was determined by UV-vis spectroscopy at wavelength of 664 nm and compared to the initial standard concentration of MB prior to interacting with the graphene sample.

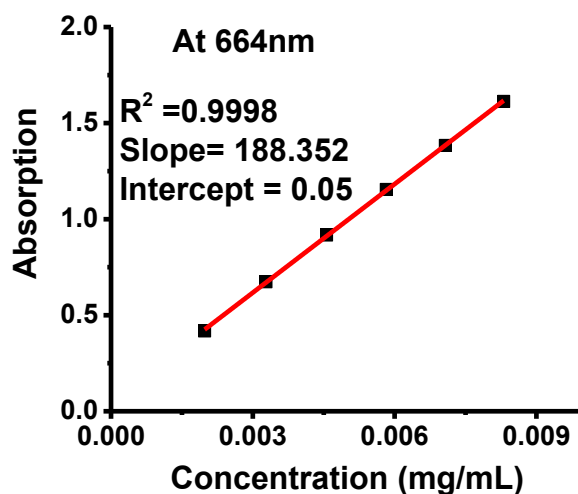


Figure 3.16. Linear relationships between the concentration of MB and its absorption at 664 nm.

3.4.5. Electrochemical Measurements

All the ORR experiments were conducted by using a computer-controlled potentiostat (CHI 760C, CH Instrument, USA) with a typical three-electrode cell. A platinum wire and saturated Ag/AgCl electrode is used as the counter-electrode and the reference electrode, respectively, in all measurement. A glassy carbon electrode was used as a working electrode and was polished each time prior to use with alumina slurry. All of the Catalyst (~2mg) were dispersed in 25% ethanol (1mL) containing Nafion (0.5 wt%) by bath sonication. Then 2 μ L of this dispersion was loaded on glassy carbon electrode and allowed to dry in vacuum. Before each testing, the electrolyte(0.1M KOH) was saturated with oxygen (O₂) by bubbling O₂ for 30 min. Cyclic voltammogram experiments were typically performed at the scan rate of 50mV/s in O₂ saturated 0.1M KOH. For control experiments in (nitrogen) N₂ saturated KOH, N₂ was bubbled in 0.1M KOH for 30min, while other conditions remain unchanged. RDE experiments were performed using glassy carbon disc electrode(3 mm diameter) in O₂ saturated 0.1M KOH with different rotation speed varying

from 250 to 2500rpm and 10mV/s scan rate. For a comparison, the commercially available Johnson Matthey (JM) Pt/C 40 wt% (Johnson Matthey Corp., Pt loading: 40 wt% Pt on carbon) electrode was also prepared similarly to other catalyst as above mentioned. For the RRDE measurement, catalyst and electrodes are prepared by the same method as RDE measurement, except using RRDE electrode (GC disc and Pt ring electrode). The chronoamperometry experiment was conducted by measuring current for 25,000 seconds at -0.38V potential and at 1000rpm rotation speed with continues maintaining oxygen flow to avoid any oxygen concentration effect. For methanol cross over effect, we conducted another amperometric experiment for 700seconds with same experiment condition as above, except 2mL of methanol was added at 300seconds during the experiment. The electrochemical impedance spectra (EIS) for ORR on the catalyst electrodes are measured in O₂-saturated 0.1M KOH solution at -0.31 V vs. Ag/AgCl.

3.5. References

1. Chen, H. S.; Cong, T. N.; Yang, W.; Tan, C. Q.; Li, Y. L.; Ding, Y. L. Progress in electrical energy storage system: A critical review. *Progress in Natural Science* 2009, 19, 291-312.
2. Chu, S.; Majumdar, A. Opportunities and challenges for a sustainable energy future. *Nature* 2012, 488, 294-303.
3. Linden, D. Handbook of batteries and fuel cells. *New York* 1984.
4. Yu, D. S.; Nagelli, E.; Du, F.; Dai, L. M. Metal-Free Carbon Nanomaterials Become More Active than Metal Catalysts and Last Longer. *Journal of Physical Chemistry Letters* 2010, 1, 2165-2173.
5. Liu, R. L.; Wu, D. Q.; Feng, X. L.; Mullen, K. Nitrogen-Doped Ordered Mesoporous Graphitic Arrays with High Electrocatalytic Activity for Oxygen Reduction. *Angew. Chem. Int. Ed.* 2010, 49, 2565-2569.
6. Qu, L. T.; Liu, Y.; Baek, J. B.; Dai, L. M. Nitrogen-Doped Graphene as Efficient Metal-Free Electrocatalyst for Oxygen Reduction in Fuel Cells. *Acs Nano* 2010, 4, 1321-1326.
7. Gong, K. P.; Du, F.; Xia, Z. H.; Durstock, M.; Dai, L. M. Nitrogen-Doped Carbon Nanotube Arrays with High Electrocatalytic Activity for Oxygen Reduction. *Science* 2009, 323, 760-764.

8. Jafri, R. I.; Rajalakshmi, N.; Ramaprabhu, S. Nitrogen-doped multi-walled carbon nanocoils as catalyst support for oxygen reduction reaction in proton exchange membrane fuel cell. *J. Power Sources* 2010, 195, 8080-8083.
9. Nagaiah, T. C.; Kundu, S.; Bron, M.; Muhler, M.; Schuhmann, W. Nitrogen-doped carbon nanotubes as a cathode catalyst for the oxygen reduction reaction in alkaline medium. *Electrochem. Commun.* 2010, 12, 338-341.
10. Joshi, R. K.; Carbone, P.; Wang, F. C.; Kravets, V. G.; Su, Y.; Grigorieva, I. V.; Wu, H. A.; Geim, A. K.; Nair, R. R. Precise and Ultrafast Molecular Sieving Through Graphene Oxide Membranes. *Science* 2014, 343, 752-754.
11. Bai, J.; Zhong, X.; Jiang, S.; Huang, Y.; Duan, X. Graphene nanomesh. *Nat Nanotechnol* 2010, 5, 190-4.
12. Kuhn, P.; Forget, A.; Su, D.; Thomas, A.; Antonietti, M. From microporous regular frameworks to mesoporous materials with ultrahigh surface area: dynamic reorganization of porous polymer networks. *J. Am. Chem. Soc.* 2008, 130, 13333-7.
13. Bieri, M.; Treier, M.; Cai, J.; Ait-Mansour, K.; Ruffieux, P.; Groning, O.; Groning, P.; Kastler, M.; Rieger, R.; Feng, X.; Mullen, K.; Fasel, R. Porous graphenes: two-dimensional polymer synthesis with atomic precision. *Chem Commun (Camb)* 2009, 6919-21.
14. Akhavan, O. Graphene nanomesh by ZnO nanorod photocatalysts. *ACS Nano* 2010, 4, 4174-80.
15. Fischbein, M. D.; Drndic, M. Electron beam nanosculpting of suspended graphene sheets. *Appl. Phys. Lett.* 2008, 93, 113107.
16. Zhu, Y.; Murali, S.; Stoller, M. D.; Ganesh, K. J.; Cai, W.; Ferreira, P. J.; Pirkle, A.; Wallace, R. M.; Cychosz, K. A.; Thommes, M.; Su, D.; Stach, E. A.; Ruoff, R. S. Carbon-based supercapacitors produced by activation of graphene. *Science* 2011, 332, 1537-41.
17. Wang, S.; Tristan, F.; Minami, D.; Fujimori, T.; Cruz-Silva, R.; Terrones, M.; Takeuchi, K.; Teshima, K.; Rodríguez-Reinoso, F.; Endo, M. Activation routes for high surface area graphene monoliths from graphene oxide colloids. *Carbon* 2014, 76, 220-231.
18. Zhao, X.; Hayner, C. M.; Kung, M. C.; Kung, H. H. Flexible holey graphene paper electrodes with enhanced rate capability for energy storage applications. *ACS Nano* 2011, 5, 8739-49.
19. Wang, X.; Jiao, L.; Sheng, K.; Li, C.; Dai, L.; Shi, G. Solution-processable graphene nanomeshes with controlled pore structures. *Scientific reports* 2013, 3.
20. Han, T. H.; Huang, Y. K.; Tan, A. T.; Dravid, V. P.; Huang, J. Steam etched porous graphene oxide network for chemical sensing. *J. Am. Chem. Soc.* 2011, 133, 15264-7.
21. Zhao, Y.; Hu, C.; Song, L.; Wang, L.; Shi, G.; Dai, L.; Qu, L. Functional graphene nanomesh foam. *Energy & Environmental Science* 2014, 7, 1913-1918.
22. Lin, Y.; Watson, K. A.; Kim, J.-W.; Baggett, D. W.; Working, D. C.; Connell, J. W. Bulk preparation of holey graphene via controlled catalytic oxidation. *Nanoscale* 2013, 5, 7814-7824.
23. Zhou, D.; Cui, Y.; Xiao, P.-W.; Jiang, M.-Y.; Han, B.-H. A general and scalable synthesis approach to porous graphene. *Nature communications* 2014, 5.
24. Li, X.; Wang, H.; Robinson, J. T.; Sanchez, H.; Diankov, G.; Dai, H. Simultaneous nitrogen doping and reduction of graphene oxide. *J. Am. Chem. Soc.* 2009, 131, 15939-44.

25. Xue, Y.; Yu, D.; Dai, L.; Wang, R.; Li, D.; Roy, A.; Lu, F.; Chen, H.; Liu, Y.; Qu, J. Three-dimensional B,N-doped graphene foam as a metal-free catalyst for oxygen reduction reaction. *Phys. Chem. Chem. Phys.* 2013, 15, 12220-6.
26. Zhang, C.; Mahmood, N.; Yin, H.; Liu, F.; Hou, Y. Synthesis of phosphorus-doped graphene and its multifunctional applications for oxygen reduction reaction and lithium ion batteries. *Adv. Mater.* 2013, 25, 4932-7.
27. Wang, H.; Zhou, Y.; Wu, D.; Liao, L.; Zhao, S.; Peng, H.; Liu, Z. Synthesis of boron-doped graphene monolayers using the sole solid feedstock by chemical vapor deposition. *Small* 2013, 9, 1316-20.
28. Wang, H. B.; Xie, M. S.; Thia, L.; Fisher, A.; Wang, X. Strategies on the Design of Nitrogen-Doped Graphene. *Journal of Physical Chemistry Letters* 2014, 5, 119-125.
29. Wang, H. B.; Maiyalagan, T.; Wang, X. Review on Recent Progress in Nitrogen-Doped Graphene: Synthesis, Characterization, and Its Potential Applications. *Acs Catalysis* 2012, 2, 781-794.
30. Hu, T.; Sun, X.; Sun, H.; Xin, G.; Shao, D.; Liu, C.; Lian, J. Rapid synthesis of nitrogen-doped graphene for a lithium ion battery anode with excellent rate performance and super-long cyclic stability. *Phys. Chem. Chem. Phys.* 2014, 16, 1060-6.
31. Chang, D. W.; Lee, E. K.; Park, E. Y.; Yu, H.; Choi, H. J.; Jeon, I. Y.; Sohn, G. J.; Shin, D.; Park, N.; Oh, J. H.; Dai, L.; Baek, J. B. Nitrogen-doped graphene nanoplatelets from simple solution edge-functionalization for n-type field-effect transistors. *J. Am. Chem. Soc.* 2013, 135, 8981-8.
32. Shao, Y. Y.; Zhang, S.; Engelhard, M. H.; Li, G. S.; Shao, G. C.; Wang, Y.; Liu, J.; Aksay, I. A.; Lin, Y. H. Nitrogen-doped graphene and its electrochemical applications. *J. Mater. Chem.* 2010, 20, 7491-7496.
33. Liu, Z.; Robinson, J. T.; Tabakman, S. M.; Yang, K.; Dai, H. Carbon materials for drug delivery & cancer therapy. *Mater. Today* 2011, 14, 316-323.
34. Zhang, B.; Wen, Z.; Ci, S.; Mao, S.; Chen, J.; He, Z. Synthesizing Nitrogen-doped Activated Carbon and Probing its Active Sites for Oxygen Reduction Reaction in Microbial Fuel Cells. *ACS applied materials & interfaces* 2014.
35. Chen, L.; Du, R.; Zhu, J.; Mao, Y.; Xue, C.; Zhang, N.; Hou, Y.; Zhang, J.; Yi, T. Three-Dimensional Nitrogen-Doped Graphene Nanoribbons Aerogel as a Highly Efficient Catalyst for the Oxygen Reduction Reaction. *Small* 2014.
36. Wu, Z. S.; Ren, W. C.; Xu, L.; Li, F.; Cheng, H. M. Doped Graphene Sheets As Anode Materials with Superhigh Rate and Large Capacity for Lithium Ion Batteries. *Acs Nano* 2011, 5, 5463-5471.
37. Panchakarla, L.; Subrahmanyam, K.; Saha, S.; Govindaraj, A.; Krishnamurthy, H.; Waghmare, U.; Rao, C. Synthesis, structure, and properties of boron-and nitrogen-doped graphene. *Adv. Mater.* 2009, 21, 4726.
38. Reddy, A. L.; Srivastava, A.; Gowda, S. R.; Gullapalli, H.; Dubey, M.; Ajayan, P. M. Synthesis of nitrogen-doped graphene films for lithium battery application. *ACS Nano* 2010, 4, 6337-42.
39. Deng, D. H.; Pan, X. L.; Yu, L. A.; Cui, Y.; Jiang, Y. P.; Qi, J.; Li, W. X.; Fu, Q. A.; Ma, X. C.; Xue, Q. K.; Sun, G. Q.; Bao, X. H. Toward N-Doped Graphene via Solvothermal Synthesis. *Chem. Mater.* 2011, 23, 1188-1193.

40. Wang, X. R.; Li, X. L.; Zhang, L.; Yoon, Y.; Weber, P. K.; Wang, H. L.; Guo, J.; Dai, H. J. N-Doping of Graphene Through Electrothermal Reactions with Ammonia. *Science* 2009, 324, 768-771.
41. Guo, H. L.; Su, P.; Kang, X. F.; Ning, S. K. Synthesis and characterization of nitrogen-doped graphene hydrogels by hydrothermal route with urea as reducing-doping agents. *Journal of Materials Chemistry A* 2013, 1, 2248-2255.
42. Sheng, Z. H.; Shao, L.; Chen, J. J.; Bao, W. J.; Wang, F. B.; Xia, X. H. Catalyst-free synthesis of nitrogen-doped graphene via thermal annealing graphite oxide with melamine and its excellent electrocatalysis. *ACS Nano* 2011, 5, 4350-8.
43. Jiang, Z. Q.; Jiang, Z. J.; Tian, X. N.; Chen, W. H. Amine-functionalized holey graphene as a highly active metal-free catalyst for the oxygen reduction reaction. *Journal of Materials Chemistry A* 2014, 2, 441-450.
44. Patel, M. A.; Yang, H.; Chiu, P. L.; Mastrogiovanni, D. D.; Flach, C. R.; Savaram, K.; Gomez, L.; Hemnarine, A.; Mendelsohn, R.; Garfunkel, E.; Jiang, H.; He, H. Direct production of graphene nanosheets for near infrared photoacoustic imaging. *ACS Nano* 2013, 7, 8147-57.
45. Kosynkin, D. V.; Higginbotham, A. L.; Sinitskii, A.; Lomeda, J. R.; Dimiev, A.; Price, B. K.; Tour, J. M. Longitudinal unzipping of carbon nanotubes to form graphene nanoribbons. *Nature* 2009, 458, 872-U5.
46. Aboutalebi, S. H.; Jalili, R.; Esrafilzadeh, D.; Salari, M.; Gholamvand, Z.; Aminorroaya Yamini, S.; Konstantinov, K.; Shepherd, R. L.; Chen, J.; Moulton, S. E. High-Performance Multifunctional Graphene Yarns: Toward Wearable All-Carbon Energy Storage Textiles. *ACS nano* 2014, 8, 2456-2466.
47. Bagri, A.; Mattevi, C.; Acik, M.; Chabal, Y. J.; Chhowalla, M.; Shenoy, V. B. Structural evolution during the reduction of chemically derived graphene oxide. *Nat Chem* 2010, 2, 581-7.
48. Dimiev, A. M.; Tour, J. M. Mechanism of Graphene Oxide Formation. *Acs Nano* 2014, 8, 3060-3068.
49. Ziegler, K. J.; Gu, Z.; Peng, H.; Flor, E. L.; Hauge, R. H.; Smalley, R. E. Controlled oxidative cutting of single-walled carbon nanotubes. *J. Am. Chem. Soc.* 2005, 127, 1541-7.
50. Liu, J.; Rinzler, A. G.; Dai, H. J.; Hafner, J. H.; Bradley, R. K.; Boul, P. J.; Lu, A.; Iverson, T.; Shelimov, K.; Huffman, C. B.; Rodriguez-Macias, F.; Shon, Y. S.; Lee, T. R.; Colbert, D. T.; Smalley, R. E. Fullerene pipes. *Science* 1998, 280, 1253-1256.
51. Chen, Z. Y.; Kobashi, K.; Rauwald, U.; Booker, R.; Fan, H.; Hwang, W. F.; Tour, J. M. Soluble ultra-short single-walled carbon nanotubes. *J. Am. Chem. Soc.* 2006, 128, 10568-10571.
52. Li, J.-L.; Kudin, K. N.; McAllister, M. J.; Prud'homme, R. K.; Aksay, I. A.; Car, R. Oxygen-Driven Unzipping of Graphitic Materials *Phys. Rev. Lett.* 2006, 96, 176101.
53. Sun, T.; Fabris, S. Mechanisms for Oxidative Unzipping and Cutting of Graphene. *Nano Lett.* 2012, 12, 17-21.
54. Li, Z. Y.; Zhang, W. H.; Luo, Y.; Yang, J. L.; Hou, J. G. How Graphene Is Cut upon Oxidation? *J. Am. Chem. Soc.* 2009, 131, 6320-+.
55. Tang, P.; Hu, G.; Gao, Y.; Li, W.; Yao, S.; Liu, Z.; Ma, D. The microwave adsorption behavior and microwave-assisted heteroatoms doping of graphene-based nano-carbon materials. *Scientific reports* 2014, 4.

56. Zhang, Y.; Fugane, K.; Mori, T.; Niu, L.; Ye, J. Wet chemical synthesis of nitrogen-doped graphene towards oxygen reduction electrocatalysts without high-temperature pyrolysis. *J. Mater. Chem.* 2012, 22, 6575-6580.
57. Lai, L. F.; Potts, J. R.; Zhan, D.; Wang, L.; Poh, C. K.; Tang, C. H.; Gong, H.; Shen, Z. X.; Jianyi, L. Y.; Ruoff, R. S. Exploration of the active center structure of nitrogen-doped graphene-based catalysts for oxygen reduction reaction. *Energy & Environmental Science* 2012, 5, 7936-7942.
58. Jiao, Y.; Zheng, Y.; Jaroniec, M.; Qiao, S. Z. Origin of the electrocatalytic oxygen reduction activity of graphene-based catalysts: a roadmap to achieve the best performance. *J. Am. Chem. Soc.* 2014, 136, 4394-403.
59. Sun, Y.; Li, C.; Shi, G. Nanoporous nitrogen doped carbon modified graphene as electrocatalyst for oxygen reduction reaction. *J. Mater. Chem.* 2012, 22, 12810-12816.
60. Kong, X.-K.; Chen, C.-L.; Chen, Q.-W. Doped graphene for metal-free catalysis. *Chem. Soc. Rev.* 2014, 43, 2841-2857.
61. Navalon, S.; Dhakshinamoorthy, A.; Alvaro, M.; Garcia, H. Carbocatalysis by Graphene-Based Materials. *Chem. Rev.* 2014.
62. Gong, K.; Du, F.; Xia, Z.; Durstock, M.; Dai, L. Nitrogen-doped carbon nanotube arrays with high electrocatalytic activity for oxygen reduction. *Science* 2009, 323, 760-4.
63. Kurak, K. A.; Anderson, A. B. Nitrogen-Treated Graphite and Oxygen Electroreduction on Pyridinic Edge Sites. *Journal of Physical Chemistry C* 2009, 113, 6730-6734.
64. Rao, C. V.; Cabrera, C. R.; Ishikawa, Y. In Search of the Active Site in Nitrogen-Doped Carbon Nanotube Electrodes for the Oxygen Reduction Reaction. *Journal of Physical Chemistry Letters* 2010, 1, 2622-2627.
65. Zhang, L. P.; Xia, Z. H. Mechanisms of Oxygen Reduction Reaction on Nitrogen-Doped Graphene for Fuel Cells. *Journal of Physical Chemistry C* 2011, 115, 11170-11176.
66. Peng, X. Y.; Liu, X. X.; Diamond, D.; Lau, K. T. Synthesis of electrochemically-reduced graphene oxide film with controllable size and thickness and its use in supercapacitor. *Carbon* 2011, 49, 3488-3496.
67. Wang, S. Y.; Yu, D. S.; Dai, L. M.; Chang, D. W.; Baek, J. B. Polyelectrolyte-Functionalized Graphene as Metal-Free Electrocatalysts for Oxygen Reduction. *Acs Nano* 2011, 5, 6202-6209.
68. Lin, Z.; Waller, G.; Liu, Y.; Liu, M.; Wong, C. P. Facile Synthesis of Nitrogen-Doped Graphene via Pyrolysis of Graphene Oxide and Urea, and its Electrocatalytic Activity toward the Oxygen-Reduction Reaction. *Advanced Energy Materials* 2012, 2, 884-888.
69. Liu, R.; Wu, D.; Feng, X.; Mullen, K. Nitrogen-doped ordered mesoporous graphitic arrays with high electrocatalytic activity for oxygen reduction. *Angew. Chem. Int. Ed. Engl.* 2010, 49, 2565-9.
70. Moses, K.; Kiran, V.; Sampath, S.; Rao, C. N. Few-layer borocarbonitride nanosheets: platinum-free catalyst for the oxygen reduction reaction. *Chem Asian J* 2014, 9, 838-43.
71. Zheng, Y.; Jiao, Y.; Ge, L.; Jaroniec, M.; Qiao, S. Z. Two-step boron and nitrogen doping in graphene for enhanced synergistic catalysis. *Angew. Chem. Int. Ed. Engl.* 2013, 52, 3110-6.

72. Zhang, Y.; Huang, Q. H.; Zou, Z. Q.; Yang, J. F.; Vogel, W.; Yang, H. Enhanced Durability of Au Cluster Decorated Pt Nanoparticles for the Oxygen Reduction Reaction. *Journal of Physical Chemistry C* 2010, 114, 6860-6868.
73. McAllister, M. J.; Li, J.-L.; Adamson, D. H.; Schniepp, H. C.; Abdala, A. A.; Liu, J.; Herrera-Alonso, M.; Milius, D. L.; Car, R.; Prud'homme, R. K. Single sheet functionalized graphene by oxidation and thermal expansion of graphite. *Chem. Mater.* 2007, 19, 4396-4404.

Chapter 4. P-Doped Porous Carbon as Metal Free Catalysts for Selective Aerobic Oxidation with an Unexpected Mechanism

4.1. Introduction

Catalytic oxidation of inexpensive and widely available chemicals to produce high value-added chemicals remains a significant task in many important current industrial and fine-chemical processes. Ideal catalytic oxidation processes would use non-toxic sustainable catalysts and the most environmentally benign and abundant oxidants, such as molecular oxygen (O_2), with good conversion and selectivity. A wide range of homogeneous and heterogeneous transition metal-based catalysts have been developed for these reactions. Unfortunately, many metals are not widely available and/or are toxic, which presents sustainability and environmental challenges. For these reasons, there is ever increasing interest in developing sustainable and eco-friendly metal-free, “carbon based catalysts”, including graphene and other nanocarbon based catalysts.¹⁻⁵

Compared to traditional metal based catalysts, carbon based materials provide additional advantages because the existence of giant π structures promotes strong interactions with various reactants. More importantly, its physicochemical and electronic properties, which in principle determine the catalytic properties of a material, can be tailored and fine-tuned by molecular engineering and/or heteroatomic doping.⁶ A plethora of reports have demonstrated that doping of heteroatoms into graphene and other carbon based materials gives rise to enhanced performance in electrocatalytic oxygen reduction reaction (ORR), when compared to their undoped analogues.⁷⁻¹⁰ Compared to ORR, studies

that use doped and/or co-doped carbon materials as catalysts for selective organic synthesis are in their early stages of development, although a great potential has already been demonstrated.¹¹ Importantly, these carbocatalysts merge the benefits of green synthesis with heterogeneous reaction conditions, which greatly simplifies work-up conditions and is particularly attractive from an industrial standpoint. However, there are few reports demonstrating that carbon based materials match the efficiency and recyclability of transition metal catalysts.¹¹ On the other hand, limited “types” of graphene and carbon materials have been explored so far.^{2, 12-15} The majority of the research has been focused on graphene oxide (GO) possibly due to its large availability.¹⁶⁻¹⁸ Carbon materials doped with nitrogen (N) and N-codoped with other heteroatoms have been explored for C-H activation and aerobic alcohol oxidation.^{12, 15, 19, 20} Among three types of nitrogen species doped into the graphene lattice, pyridinic N, pyrrolic N, and graphitic N, the graphitic sp^2 N species were established to be catalytically active centers. However, the requirement of high temperature to fabricate the graphitic sp^2 N violates the original idea for energy saving and sustainability.²¹ Furthermore, the planar structure of graphitic sp^2 N brings difficulties in overcoming substrate steric hindrance effects, which causes limited catalytic reaction scope of N-doped carbon materials.^{20, 22}

Recently, growing interest has emerged in phosphorus (P) doped carbon materials.²³⁻²⁶ P has the same number of valence electrons as N, making P-doped carbon materials also electron rich.²⁴ While, the polarity of the C–P bond is opposite to that of the C–N bond due to lower electronegativity of P atoms (2.19) than C (2.55), making P partially positively charged and possibly the catalytic sites,^{27, 28} instead of the neighboring C atoms as in the N-doped carbon materials.^{12, 15, 19} Furthermore, as the diameter of P is much larger

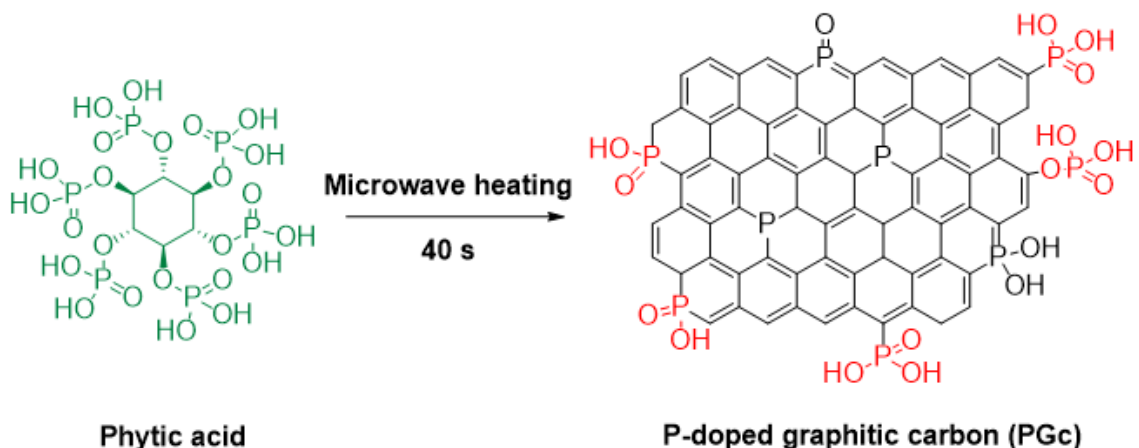
than C, P-doping results in more local structural distortion of the hexagonal carbon framework and in such a configuration, P protrudes out of the graphene plane.^{27, 28} Finally, when compared with N-doping, distinct effects by P-doping may also arise from the additional vacant 3d orbitals and the valence electrons in the third shell. All these characteristics empower P-doped carbon materials to overcome the steric hindrance effects encountered in N-doped carbon materials.^{12, 20} However, experimentally, most of the approaches for P-doping necessitate accompanying O doping, forming various P and O containing functional groups.^{25, 26, 29} How these functional groups, and the bonding configuration of P in a carbon matrix, influence the electronic property and therefore its catalytic performance remains unknown. Furthermore, most of the P-doped materials were fabricated *via* high temperature annealing for long periods of time in an inert environment, which also violates the original idea for energy saving and sustainability.

Herein we report an extremely simple and rapid (seconds) approach to directly synthesize gram quantities of P-doped porous carbon materials from abundant biomass molecules. The work function of P-doped carbon materials and its connectivity to the P bond configuration in the carbon matrix have been studied *via* PeakForce Kelvin probe force microscopy (PF KPFM). Most significantly, the capability of the P-doped carbon materials as metal free catalysts for aerobic oxidation reactions have been demonstrated for the first time. As expected, unlike N-doped carbon material, the steric problem does not exist for P-doped carbon materials. The P-doped materials can efficiently catalyze aerobic oxidation of both primary and secondary benzyl alcohols to the corresponding aldehydes or ketones. A kinetic study shows that the P-doped carbon material have an activation energy of $\sim 49.6 \text{ kJ.mol}^{-1}$ for benzyl alcohol oxidation, which is lower than N-doped carbon

($\sim 56.1 \text{ kJ.mol}^{-1}$)²⁰ catalyst and similar to Ru based catalysts ($\sim 48 \text{ kJ.mol}^{-1}$).^{30, 31} Further, to our surprise, the P-doped carbon materials with higher work functions shows higher capability in catalyzing aerobic oxidation reactions, which is opposite to the trend when N-doped carbon materials are used as metal free catalysts for aerobic oxidation reactions^{20, 32} and electrochemical catalysts for ORR.³³ The P-doped materials also exhibit a different selectivity rule for electron rich and electron deficient molecules compared to other heteroatom doped carbon materials.^{20, 34} The reaction pathway was studied to understand these questions. We found that molecular oxygen is not involved in the first step of aerobic oxidation of benzyl alcohol, however, it is required to regenerate the catalytic sites on the P-doped carbon materials. The unique and unexpected catalytic pathway endows the P-doped carbon materials with not only good catalytic efficiency but also recyclability, which is a major challenge in GO based catalysis.^{18, 35} This, combined with rapid and energy saving approach to be able to fabricate the material in a large scale, suggests that the P-doped porous carbon is promising material for “green catalysis” due to their higher theoretical surface area, sustainability, environmental friendliness and low cost.

4.2. Results and Discussion

Scheme 4.1. Schematic drawing of PGc synthesis from Phytic acid by microwave heating.



In this approach, a novel sustainable biomass molecule, phytic acid, a well-known anti-nutrient molecule in food was chosen as our starting material. Phytic acid is a snowflake-like molecule, containing 6 phosphorous acid “arms” (**Scheme 4.1**). The existence of both high levels of C and P in one molecule ensures uniform P doping in the fabricated carbon materials. Most importantly, phytic acid strongly absorbs microwave energy. Therefore the as-purchased phytic acid solution can be directly used for the fabrication of P doped graphitic carbon product (PGC) with microwave energy without the requirements of preheating and drying treatment or adding an additional microwave absorber.^{36, 37} This is very different from most biomass molecules and organic materials that are typically transparent to microwave energy, thus prohibiting their direct use for microwave carbonization. Using microwave heating instead of traditional heating ensures that the approach is both sustainable and low energy cost. Furthermore, the fabrication can be performed in air, under ambient conditions without the requirement of inert environment, which makes this approach even more cost effective and convenient.

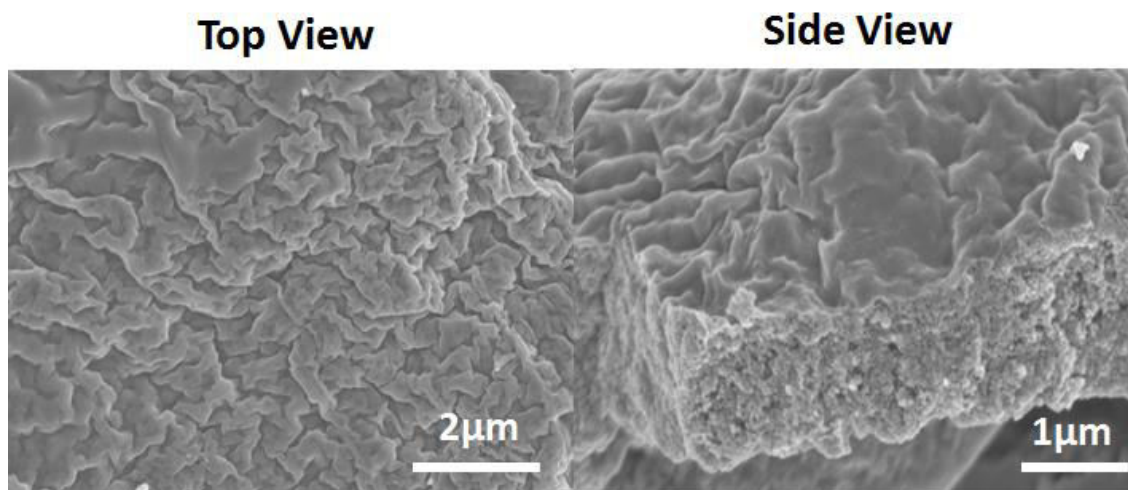


Figure 4.1. Scanning electron microscope (SEM) images of the as-fabricated PGC catalyst.

Figure 4.1 shows a scanning electron microscope (SEM) image of the as-fabricated PGc which is obtained by subjecting the as-purchased phytic acid solution (50 wt% in water) to short (40 seconds) microwave irradiation. PGc has a very unique structure in which a porous carbon monolith sandwiched by two highly wrinkled graphene-like sheets (**Figure 4.1**). The wrinkled structure is possibly the result of P doping and the larger diameter of P atoms compared to C atoms which induce local geometrical distortion in the carbon network. Indeed, the Energy-dispersive X-ray spectroscopy (**Figure 4.2B**) and X-ray photoelectron spectroscopy (XPS) measurements (**Figure 4.2A** and **Table 4.1**) shows that PGc incorporates 4.9 atomic % P, demonstrating that P is doped in the carbon matrix. Raman spectroscopy was also used to characterize the PGc material. As shown in **Figure 4.2C**, the Raman spectrum of the PGc shows G band ($\sim 1594\text{ cm}^{-1}$) and D band ($\sim 1312\text{ cm}^{-1}$). The presence of G band (1594 cm^{-1}) confirms the presence of graphitic sp^2 carbon in its structure. The intensity of D band (1312 cm^{-1}) and the intensity ratio (I_D/I_G) of D and G band are very similar to that of GO and reduced GO (rGO). These results are consistent with the previous reports that incorporation of heterogeneous dopants, such as P and N, breaks the hexagonal symmetry of the graphene plane, which leads to the high intensity of D band in their Raman spectra.^{9, 10, 34} Furthermore the material has a large surface area ($\sim 1200\text{ m}^2/\text{g}$), measured *via* Brunauer-Emmett-Teller (BET) (**Figure 4.2D**) and it has high thermal stability as demonstrated by thermo gravimetric analysis (**Figure 4.3**). All these features combined with the ease of large scale production should lead to a wide range of applications of this material, including as metal free catalysts.

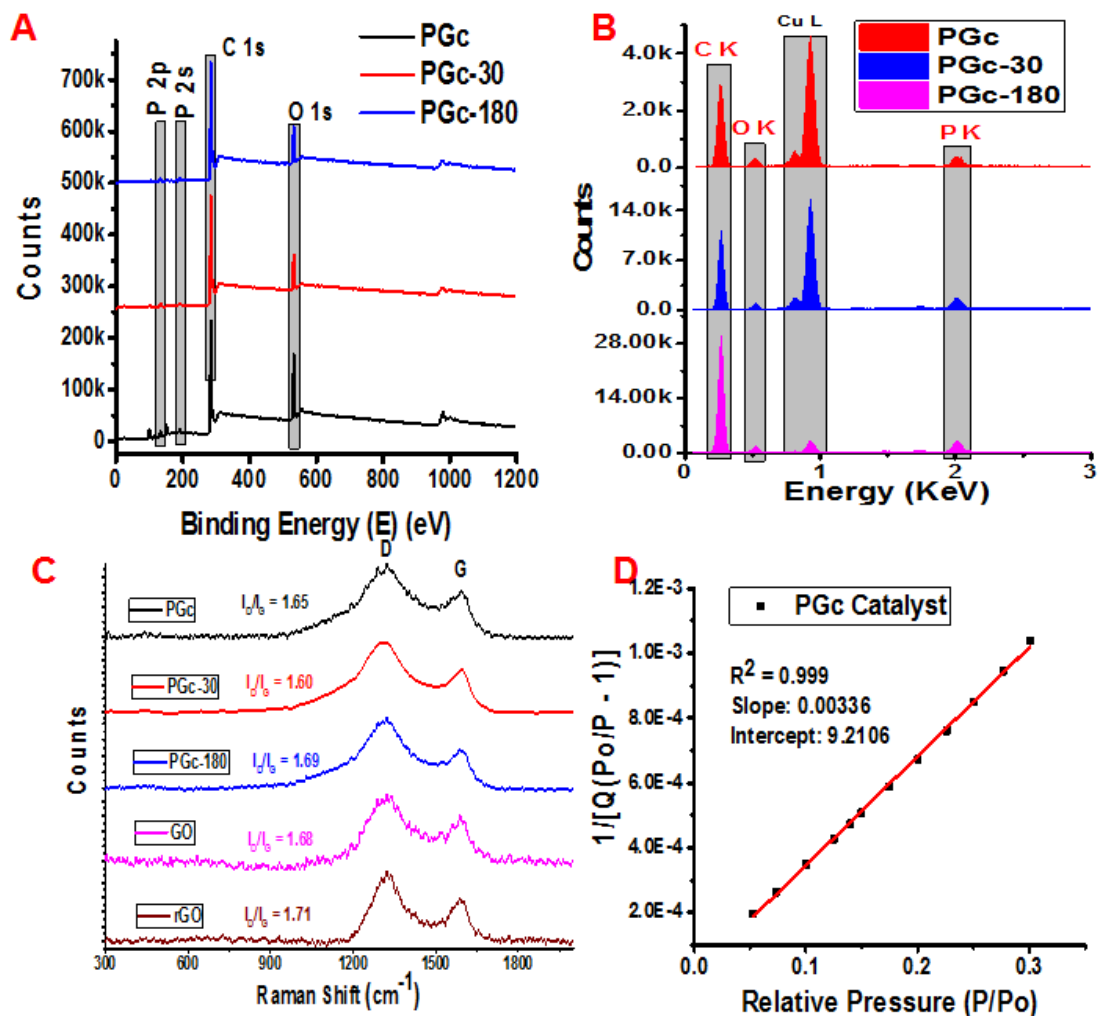


Figure 4.2. (A) XPS and (B) EDS spectra of PGc, PGc-30 and PGc-180 catalysts. (C) The Raman spectra of different catalysts. (D) 12-point BET plot of PGc catalyst.

Table 4.1. Calculated atomic % of C, P and O for PGc, PGc-30 and PGc-180 catalysts.

Catalyst	% C	% O	% P
PGc	73.94	21.17	4.89
PGc-30	83.26	13.52	3.21
PGc-180	83.56	13.60	2.84

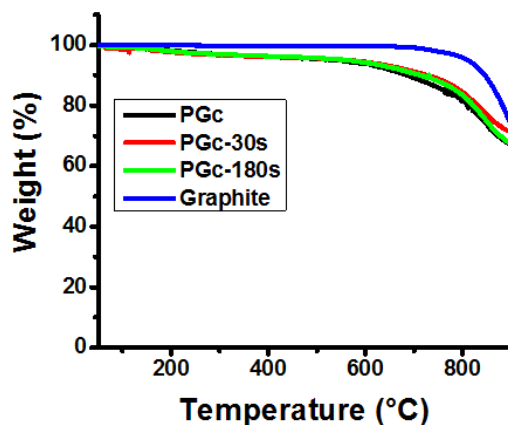
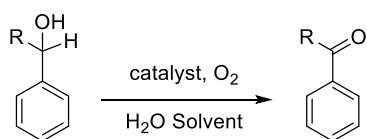


Figure 4.3. TGA (Thermo Gravimetric Analysis) spectra of different phosphorus doped carbon catalyst and graphite.

Table 4.2. Benzyl alcohol oxidation catalyzed by PGc in water^a.



Entry	Catalyst	R	Temp(°C)	Conversion (%)	Selectivity (%)
1	PGc	H	40	17.5	>99.0
2	PGc	H	60	24.1	>99.0
3	PGc	H	80	37.7	>99.0
4	PGc	H	100	48.4	>98.5
5 ^b	PGc	H	100	41.9	>99.0
6	no catalyst	H	60	1.5	>99.0
7	rGO	H	60	7.4	>99.0
8	PGc-30	H	60	17.6	>99.0
9	PGc-180	H	60	14.4	>99.0
10	PGc	CH ₃	80	46.5	>99.0
11 ^c	PGc	H	60	33.4	>99.0
12 ^c	N-doped Graphene ²⁰	H	70	12.8 ²⁰	100

Reaction conditions: ^a2.0 mg alcohol, 3.0 mg catalyst, 5 mL water, oxygen balloon, 14 hours reaction time. ^b20mg alcohol (0.2mmol), 30mg catalyst, 50 mL water, 1 atm O₂, 7 hours reaction time. ^c0.1mmol alcohol, 30mg catalyst, 80 mL water, 1 atm O₂, 10 hours reaction time. % conversion to the alcohol and % selectivity with respect to benzaldehyde calculated using high performance liquid chromatography (HPLC).²⁰ is refers to numbered reference in the text.

We first studied the catalytic efficiency of PGc for selective oxidation of benzyl alcohol to benzaldehyde in aqueous solution at different temperatures (**Table 4.2**). The conversion increased with the reaction temperatures and it reached 48% at 100 °C without losing the selectivity to aldehyde (>99%) (Entry 1-4). In a control experiment without PGc (entry 6) or with reduced GO (rGO) as the catalyst (entry 7), negligible conversion of benzyl alcohol is achieved, demonstrating the critical role of PGc in this reaction. It is worthy to mention that the conversion is 33.4% at 60°C with >99% selectivity to benzaldehyde (entry 11), which is approximately three times higher than the conversion (entry 12) when N-doped graphene was used as the catalyst under almost identical reaction conditions (catalyst loading 300 wt%, and reaction time 10 hours, except the reaction was performed at slightly higher temperature 70 °C for N-doped graphene).²⁰ A detailed kinetic study of the selective oxidation of benzyl alcohol to benzaldehyde in aqueous solution by PGc catalyst was also performed. **Figure 4.4A** shows the molarity of benzaldehyde formed as a function of the reaction time at different temperatures (40 to 100 °C). From these linear plots, we calculated the reaction rates (*k*) for benzyl alcohol oxidation. Then, the apparent activation energy (*E_a*) is calculated from the slope of the linear plot of ln *k* versus 1/*T* (**Figure 4.4B**). According to the Arrhenius equation of $\ln k = \ln A - E_a/RT$, the activation energy was calculated to be 49.6 kJ.mol⁻¹, which is lower than that of reported for N-doped carbon catalysts (56.1 kJ.mol⁻¹)²⁰ and similar to Ru metal-based catalysts (47.8 kJ.mol⁻¹).^{30,31} Moreover, unlike the N-doped carbon catalysts,²⁰ the PGc catalyst is able to catalyze

the oxidation of secondary benzylic alcohols (1-phenethyl alcohol) with even better conversion (**Table 4.2**, entry 10). This is probably due to the unique "protruding out" structure of phosphorus atom in the graphene matrix, which is different than that of nitrogen.

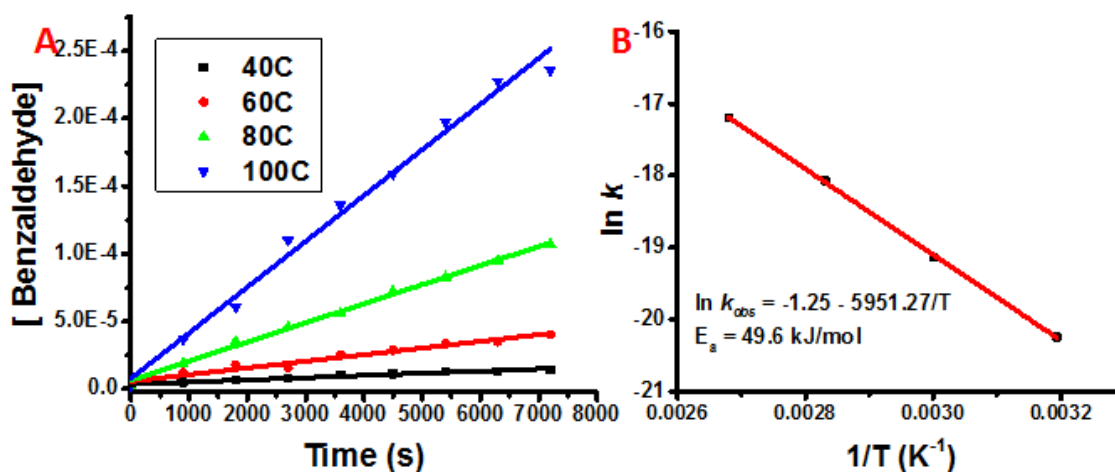


Figure 4.4. (A) Molarity of benzaldehyde vs reaction time plot at different reaction temperatures to study the rate of oxidation of benzyl alcohol. Reaction conditions: 7 mg benzyl alcohol, 10.5 mg PGc catalyst, 10 ml water, 1 atm O₂. (B) Arrhenius plot for the benzyl alcohol oxidation. The rate constant (k) values at different temperature were regarded as the pseudo-zero-order rate constants (k_{obs}) because the plot of the molarity of benzaldehyde produced versus time is linear.

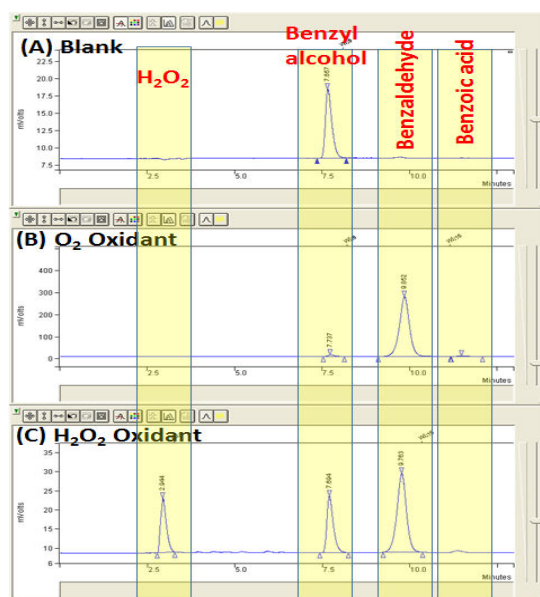


Figure 4.5. HPLC chromatogram of blank (No catalyst), PGc catalyst with an oxygen oxidant (B) and PGc catalyst with an H₂O₂ oxidant (C). Reaction condition for (A) and (B)

can be found in Table 4.3- entry no. 1 and 4. Reaction condition for (C) can be found in Table 4.8 entry no. 4.

Table 4.3. Optimization experiments for solvent free alcohol oxidation catalyzed by PGc^a

Entry	catalyst	Conversion (%)	Selectivity (%)	TON (X 10 ⁻²)
1	No catalyst	<0.1	100	NA
2	2.5wt% PGc	2.7	>99	1.10
3	5 wt% PGc	5.1	>99	1.03
4	50wt% PGc	21.7	98	0.44
5 ^b	20wt% PGc	27.5	96.4	1.40
6 ^b	50wt% PGc	56.1	95.7	1.14
7 ^b	200wt% PGc	90.2	96.3	0.46
8	5wt% GO	3.7	>99	0.75
9	50wt% GO	13.0	95	0.26
10	50wt% re-GO ^c	4.2	95	0.09
11	50wt% PGc-30	14.9	97	0.30
12	50wt% PGc-180	8.4	94	0.17
13 ^b	20 wt% recycled PGc ^d	22.5	96.1	1.14

Reaction conditions: ^a 50mg catalyst, different weight of benzyl alcohol to make different wt% of catalyst, 1atm O₂, 80°C, 48 hours. ^b Reaction was performed at 100°C for 24 hours. ^c re-GO is the catalyst, recovered from entry # 9. ^d PGc catalyst is recovered from entry #5. % conversion to the alcohol and % selectivity with respect to benzaldehyde calculated using ¹H NMR. The turnover number (TON) was calculated as a ratio of the (mol of oxidized product) / (mass of catalyst).

It was reported that the formation of a large amount of H₂O₂ byproduct seems to be unavoidable when using noble metal based catalysts for selective oxidation of alcohols to aldehydes by molecular oxygen.³⁸ The generated H₂O₂ not only can possibly further react with the aldehyde product, thus leading to selectivity loss, but it could also etch the reaction

equipment. Therefore, it is worth mentioning that there is no detectable H₂O₂ byproduct generated in the present reaction (**Figure 4.5**), which is another advantage compared to transition metal catalysis.³⁸⁻⁴⁰

For industrial applications, solvent free catalytic reactions are preferred to avoid extra cost related to the use of and handling of solvents. Previously, Bielawski reported that GO is capable of catalyzing oxidation and hydration reactions in solvent free conditions.¹⁸ To test whether PGc can also catalyze benzyl alcohol oxidation without any solvent, neat benzyl alcohol was heated to 80 °C for 48 hours in the presence of different wt% of PGc, under 1 atm of oxygen (**Table 4.3**). The %conversion with PGc catalyst increases from 2.7% to 22% with the increase of the amount of catalyst loading (entries 2-4). If the reaction is performed under the same conditions, the catalytic efficiency of PGc is similar or slightly better compared to GO reported by Bielawski *et al.*¹⁸ (entries 5-7). For example, the alcohol conversion increases to 56% and 90% with 50 and 200 wt% catalyst loading, respectively, at 100°C for 24 hours (entries 5-7). The high aldehyde selectivity is largely maintained ($\geq 96\%$). It was reported that at 20 wt% GO catalyst loading, a dramatic decrease in conversion efficiency from 24% to 5% was reported, indicating that majority of the catalytic sites have been lost during the catalytic cycle.¹⁸ It has also been reported that the graphitic N in N-doped graphene suffered from serious stability issues.³² To test the recyclability of the PGc, we recovered the PGc catalyst by filtration at the end of the reaction and recycled the catalyst for eight runs. Significantly, with 50 wt% PGc catalyst loading, the decrease in alcohol conversion and selectivity was not obvious (**Figure 4.6A**), which is in sharp contrast to GO catalysts (**Table 4.3**, entry 9 and 10). With 20 wt% loading, the decrease in % conversion is much less compared to that of GO (**Table 4.3**,

entry 5 and 13). We further compared the initial reaction rates for the fresh and the recycled PGc catalysts. As shown in **Figure 4.6B**, only a trivial decrease in the reaction rate for the recycled PGc catalyst was observed. All these results suggest that the PGc catalyst has much better recyclability compared to GO.

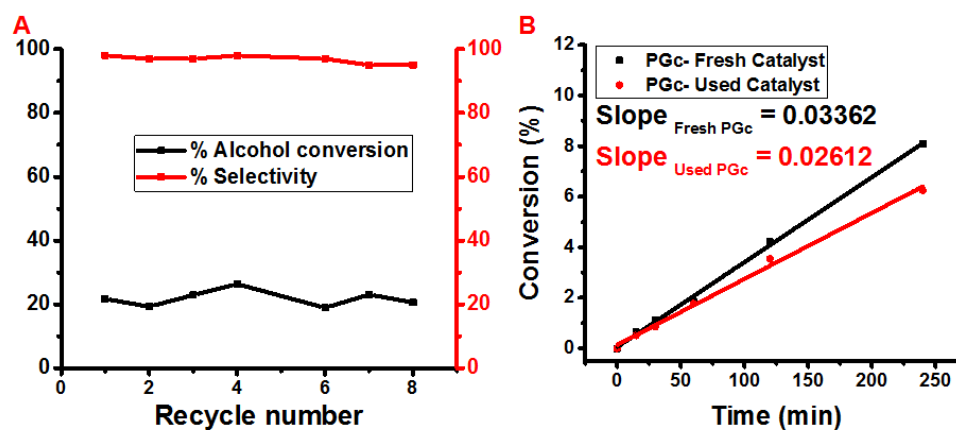


Figure 4.6. (A) Recycling the PGc catalyst for benzyl alcohol oxidation. Reaction condition: 50mg catalyst, 100mg benzyl alcohol, 1atm O₂, 80°C, 48hours. (B) Time conversion plot of a fresh and used PGc catalyst. Reaction condition: 10 mg catalyst, 50 mg benzyl alcohol, 1 atm O₂, 100°C. The used catalyst is recycled twice (at reaction conditions specified in Figure 4.6A before the time conversion measurement).

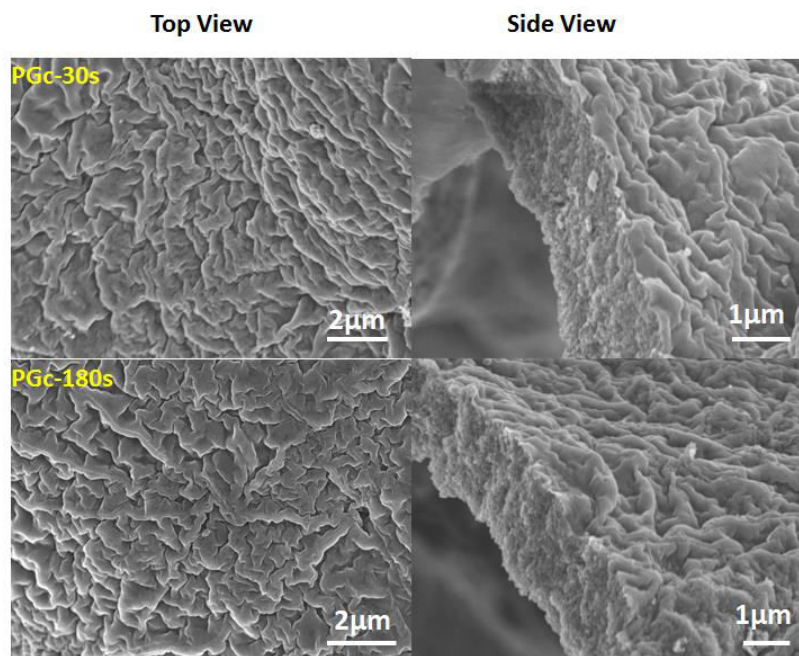


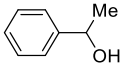
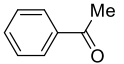
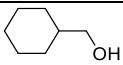
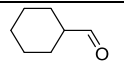
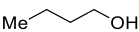
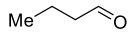
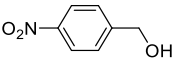
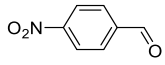
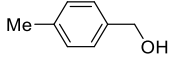
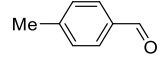
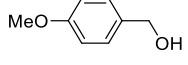
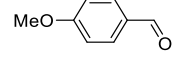
Figure 4.7. Scanning electron microscope image of the fabricated PGc-30 and PGc-180 catalysts.

To further shed light on the role of PGc in the oxidation of benzyl alcohols, we fabricated different PGc materials. In brief, by treating the dried PGc powder with microwave irradiation for additional 30s and 180s, we obtained different PGc materials, which we named as PGc-30 and PGc-180, respectively. The wrinkle and porous structures of these PGc materials are similar to the original PGc as shown in **Figure 4.7**. Detailed treatment procedures is described in experimental section and characterization can be found in the **Figure 4.2** and **4.3**. Next, we compared the catalytic ability of these new catalysts with the original PGc in the alcohol oxidation reaction in both aqueous and solvent free conditions. As shown in **Tables 4.2** and **4.3**, the original PGc shows the highest alcohol conversion. The PGc-180, which was fabricated with the longest microwave irradiation time, shows the lowest conversion, followed by PGc-30 (**Table 4.2**, entry 8, 9 and **Table 4.3**, entry 11, 12) (vide infra).

The reactivity of the P-doped carbon materials for different types of alcohols was further explored using a variety of primary, secondary benzylic (1-phenethyl alcohol), alicyclic (cyclohexylmethanol) and linear (1-butanol) alcohols in solvent free conditions and the results are summarized in **Table 4.4**. We found that the PGc catalyst can catalyze secondary benzylic alcohol oxidation (23.3% conversion, entry 1) but not of aliphatic alcohols (entry 2 and 3), which is consistent with the higher reactivity of the former substrates. Very interestingly, we found that the electron donating and withdrawing properties of the functional groups attached to the aromatic ring of benzylic alcohols dramatically influenced the oxidation efficiency. 4-CH₃O-substituted benzylic alcohol reached > 98% conversion and > 98% selectivity to benzyl aldehyde. In contrast, the -NO₂ substituted benzyl alcohol resulted in negligible conversion (< 2.5%) at the same reaction

conditions. This selectivity trend has been often observed in metal-catalyzed oxidation of alcohols, but rarely in the metal free catalysis. For example, N-doped material shows no selectivity as the catalyst in the oxidation of benzylic alcohols with regard to the properties of the substituents, with electron withdrawing and donating groups showing almost the same reactivity.²⁰ Interestingly, the N, S, O tri-doped porous carbon materials show the opposite selectivity trend.³⁴

Table 4.4. The catalytic activity of PGc in the oxidation of different alcohols^a

Entry	Substrate	Product	Conversion (%)	Selectivity (%)
1 ^b			23.3	95.0
2			ND	ND
3			ND	ND
4			2.2	64.1
5			52.5	94.2
6			98.9	99.9

Reaction conditions: ^a 50mg PGc catalyst, 100mg alcohol, 1atm O₂, 80 °C, 48 hours. ^b reaction was run for 24 hours due to acetal formation. % conversion and %selectivity calculated using ¹H NMR. ND = not determined (conversion <2.0%).

We performed several control experiments to get insight into the PGc catalyzed alcohol oxidation reaction. It was proposed that doping with nitrogen in graphene matrix changes the electronic structure of the adjacent carbon atoms, which then react with oxygen to give peroxo-like species, which initiates the oxidation reactions.^{7, 15} P has the same number of valence electrons as N, and both theoretical and experimental studies have demonstrated that P-doped graphene and other graphitic carbon materials is also capable

of activating molecular oxygen, which facilitates electrochemical oxygen reduction reaction (ORR).^{9, 23, 25, 41} Thus, it is reasonable to expect that the oxygen activation is the initial step in the catalytic PGc oxidation reactions, similar to N-doped graphene. If this is true, the work function of the PGc, which is closely related to its electronegativity and ionization energy, should correlate with the catalytic activity.⁴² Very recently, Cheon *et al.* demonstrated that the enhanced ORR activity in doped nanocarbon is closely correlated with the variation in their nanoscale work function.³³ It was reported that among three types of nitrogen species doped into the graphene lattice, namely pyridinic N, pyrrolic N, and graphitic N, only the graphitic sp² N species contribute to decreasing the work function of N doped graphene.⁴³ Accordingly, only the graphitic sp² N species were established to be catalytically active centers for the aerobic oxidation reactions.^{15, 20} We hypothesized that PGc with lower work function should have better catalytic activity. We used PeakForce Kelvin probe force microscopy (PF-KPFM) to study the work function of the PGc fabricated with different microwave irradiation conditions (See details in experimental section). Unexpectedly, the PGc, which exhibited the highest activity in the oxidation of benzyl alcohol, has the highest work function (**Figure 4.8A, B** and **Figure 4.15A, B**). PGc-180, which showed the lowest reactivity, has the lowest work function (**Figure 4.8C, D** and **Figure 4.15C, D**). These unexpected results prompted us to reconsider whether O₂ is involved in the initiation step of the reaction.

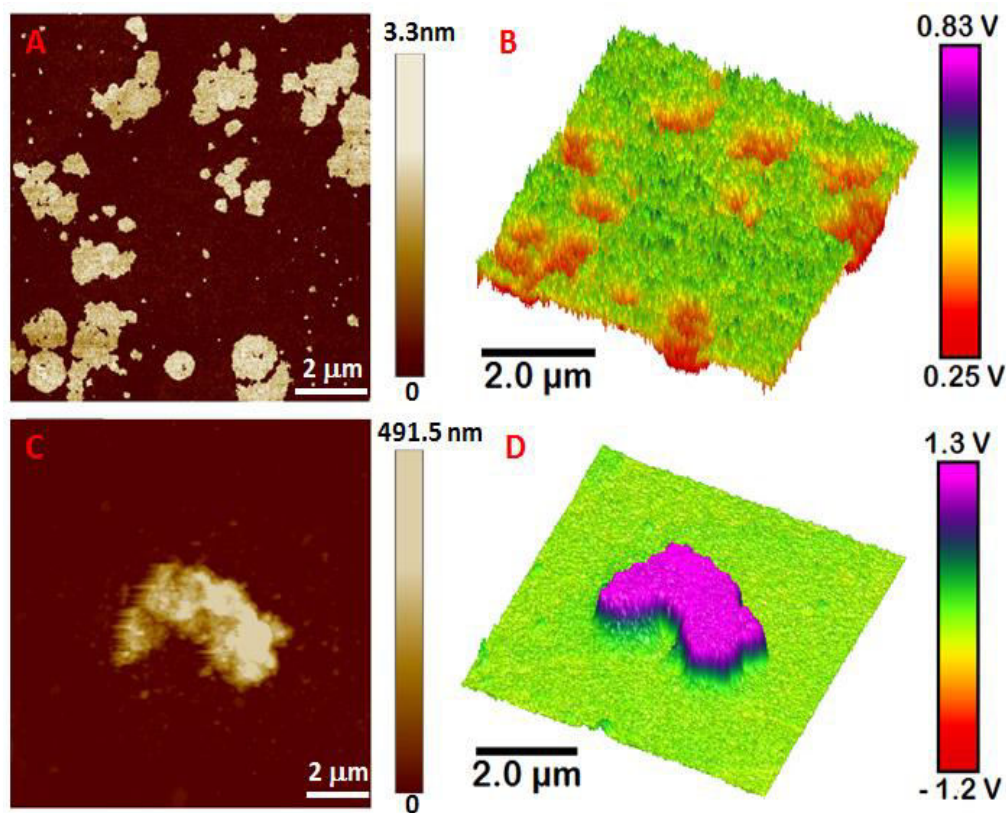


Figure 4.8. (A, C) topography and (B, D) PF-KPFM images of PGc and PGc-180 catalysts, respectively.

For previously reported catalytic aerobic oxidation reactions, which involve oxygen activation in the first step of the reaction, the conversion decreased dramatically when the reaction was performed in an O_2 free environment.^{20, 32, 44} To determine whether the first step of oxidation using PGc catalyst involves activation of O_2 to form peroxo like species as with N-doped graphene and other graphitic carbon materials, the oxidation reaction was performed under an atmosphere of N_2 , instead of O_2 (**Table 4.5**). After 48 hours of reaction at $80^\circ C$, 18% alcohol conversion was found, which is just slightly lower than that under 1 atm O_2 (23% conversion), indicating that some functional groups on PGc are directly involved in the alcohol oxidation reaction without the requirement for external O_2 . Very interestingly, we found that the alcohol conversion decreased significantly (3%) after the

same PGc catalyst was cleaned under N₂ environment, and reused for the catalytic reaction under N₂ environment. However, % alcohol conversion recovered back to 23% when the PGc catalyst was recycled for the third time, but the reaction was performed in the presence of 1 atm O₂. Altogether, these results suggest that O₂ does not directly react with the substrate, yet it is needed to regenerate the functional groups/active sites on PGc for the catalytic oxidation. This is very different from GO, N-doped, and N, B-codoped carbon catalysts.^{12, 15, 18, 20}

Table 4.5. Recycling the PGc catalyst in benzyl alcohol oxidation in presence of different environment.

Entry	Catalyst	Oxidant	Conversion (%)	Selectivity (%)
1	PGc	N ₂	17.6	99.8
2	PGc-2 nd cycle	N ₂	3.2	99.9
3	PGc-3 rd cycle	O ₂	22.7	94.0

Reaction conditions: 50mg PGc catalyst, 100mg of alcohol, 1atm oxidant, 80 °C, 48 hours. % conversion to the alcohol and % selectivity with respect to benzaldehyde calculated using ¹H NMR.

Table 4.6. The benzyl alcohol oxidation in presence of radical quencher.

Entry	Catalyst	Radical Inhibitor	Conversion (%)	Selectivity (%)
1	50wt% PGc	---	21.2	>99
2	50wt% PGc	BHT	22.2	98.6

Reaction conditions: 50mg PGc catalyst, 100mg of alcohol, 0.3mLacetonitrile, 1atm O₂, 80°C, 24 hours. 0.1mmol of butylated hydroxytoluene (BHT) is added in entry 2 for controlled reaction. % conversion for alcohols and % selectivity to benzaldehyde is calculated using ¹HNMR.

To understand if free radical intermediates are involved during the PGc catalyzed oxidation, we performed the benzyl alcohol oxidation reaction (PGc catalyst, 1 atm O₂) in the presence of butylated hydroxytoluene (BHT, 20 wt %), a known free radical quencher

(**Table 4.6**). After 24 hours, analysis of the reaction mixture revealed that the same conversion and selectivity were reached, suggesting that the presence of BHT did not inhibit the reaction. This result is also very different from GO catalyzed aerobic oxidation of alcohols in which a dramatic decrease of the conversion efficiency was observed upon addition of BHT, from 24 to 5%.¹⁸ This result is also different from those of N and N, B-codoped graphene-like materials in aerobic oxidation of benzylic compounds.¹² In these cases, it was found that including BHT in the reaction mixture completely blocked the benzylic oxidation.

To find out the possible active sites on PGc catalysts, the detailed chemical composition and the bonding configuration of phosphorus atoms in the P-doped carbon materials were studied by X-ray photoelectron spectroscopy (XPS) and Fourier transform infrared spectroscopy (FT-IR). The XPS spectrum showed that the PGc contains mainly three elements C, O and P with atomic % to be 74.0%, 21.2%, and 4.9%, respectively (**Figure 4.2A**, **Table 4.1**). The PGc material was also analyzed by X-ray fluorescence spectroscopy (XRF) to calculate % P in the bulk material and found to be ~3 atomic % or ~9 wt% (see detail in experimental section). To determine the chemical bond configuration of P present in the PGc, both the high resolution P 2p peak and O 1s peak were deconvoluted (**Figure 4.9**). It is worth mentioning that the peak deconvolution and assignment are discussed in many papers.⁴⁵ It is widely accepted that the P 2p peaks at higher binding energy (>132 eV) are P-containing functional groups associated with -C-O-C, -OH, or =O, and the peak position shifts to higher binding energy as the oxidation state of P becomes higher.⁴⁵ For the sake of simplicity, in this work the P 2p peak was deconvoluted into two components. According to the most comprehensively explained

results in the literature, the peak centered at 132.5 eV was assigned to P-C (28.4%), which suggested that P atoms are indeed incorporated into the carbon lattice. The peak at 134.7 eV was assigned to P-O (~71.6%) bonds, which represents all the P-containing functional groups associated with O.

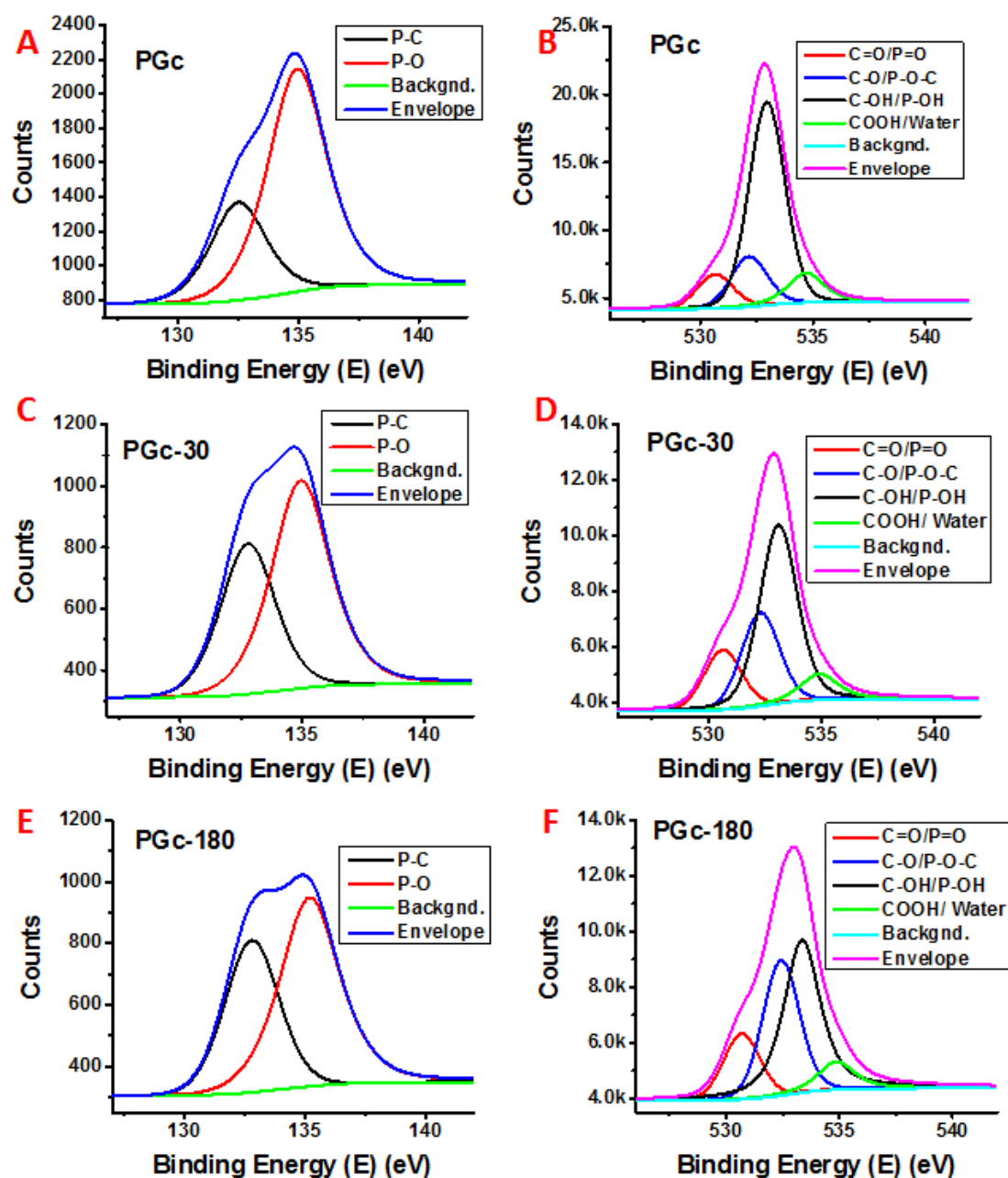


Figure 4.9. P 2p (A, C, E) and O 1s (B, D, F) Peak deconvolution of different PGc catalysts, PGc, PGc-30 and PGc-180, respectively.

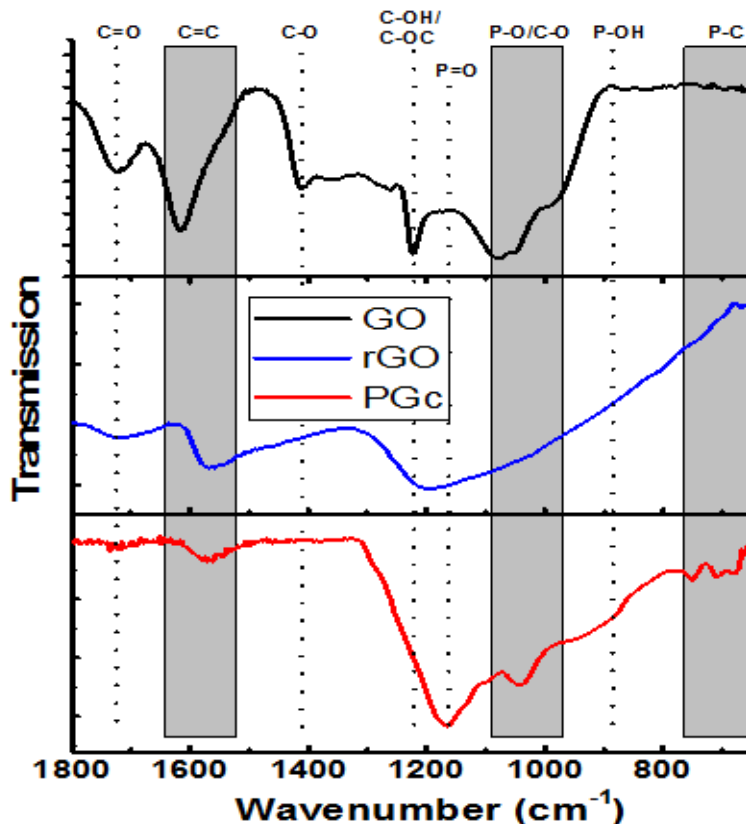


Figure 4.10. The FT-IR spectrum comparison of PGc with GO and rGO catalysts.

Table 4.7. Calculated % of different type of oxygen present in PGc, PGc-30 and PGc-180 catalysts.

Catalysts	Absolute %					Relative %				
	C=O/ P=O	C-O/ P-O-C	C-OH/ P-OH	COOH/ Water	Total	C=O/ P=O	C-O/ P-O-C	C-OH/ P-OH	COOH/ Water	Total
PGc	2.22	3.38	13.25	2.32	21.17	10.49	15.97	62.57	10.96	99.99
PGc-30	2.17	3.42	6.78	1.15	13.52	16.05	25.30	50.15	8.51	100.01
PGc-180	2.14	4.45	5.88	1.13	13.60	15.74	32.72	43.24	8.31	100.01

Absolute % is calculated based on presence of all the elements (C, P and O) in the material. Relative % is calculated based on total amount of P present.

Table 4.8. Calculated % of P-C and P-O present in PGc, PGc-30 and PGc-180 catalysts.

Catalyst	Absolute %			Relative %		
	% P-C	% P-O	Total	% P-C	% P-O	Total
PGc-0	1.39	3.50	4.89	28.43	71.57	100
PGc-30	1.27	1.94	3.21	39.56	60.44	100
PGc-180	1.15	1.69	2.84	40.49	59.51	100

Absolute % is calculated based on all the elements (C, P and O) in the material.

Relative % is calculated based on total amount of P present.

The deconvolution of O1s peak demonstrated that 62.6% of the total oxygen is in the form of C-OH/P-OH, 16.0% C-O-P/C-O-C, 10.5% C=O/P=O and 11.0% in the form of adsorbed water/COOH functionality. It is difficult to differentiate between C=O and P=O, C-O-P and C-O-C, and P-OH and C-OH due to their very close binding energy. To solve these problems, the PGc was further characterized with FT-IR spectroscopy (**Figure 4.10**). The spectrum of GO and rGO is also displayed for comparison. Unlike GO, PGc does not show the strong peaks at 1719 cm^{-1} (C=O stretching), 1410 cm^{-1} (C-O stretching in carboxylic acid or carboxylate) and 1230 cm^{-1} (C-OH/C-O-C stretching).^{46, 47} However, the spectrum clearly shows several peaks at 1166 cm^{-1} , 1131 cm^{-1} (shoulder), 1035 cm^{-1} , 900 cm^{-1} (shoulder), and several weaker peaks (750 cm^{-1} to 663 cm^{-1}), which can be assigned to P=O stretching, P-C of P-aromatic stretching, P-O-C, P-OH, and P-C.^{48, 49} These results demonstrate that mainly P=O, instead of C=O exists in the PGc, C-O-C groups are below the detection limit, and the majority of -OH present in PGc is directly bonded to P with abundant P-OH functionalities. Moreover, since the atomic O/P ratio is ~ 4 from XPS studies, some P atoms possibly connect with two or more oxygen containing functionalities, such as OH groups as schematically proposed in **Scheme 4.1**.

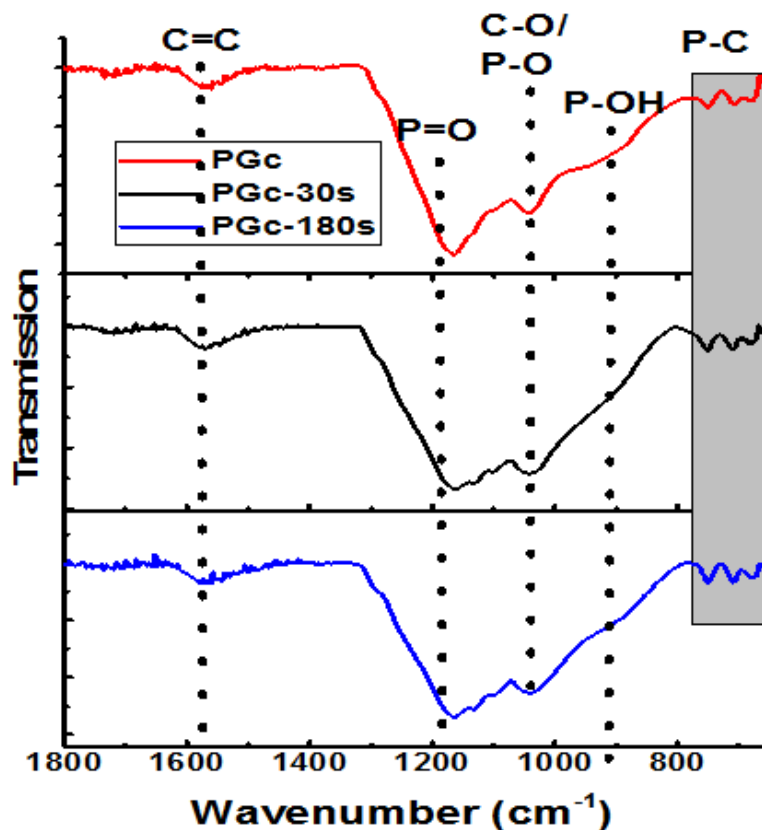


Figure 4.11. The FT-IR spectrum of PGc, PGc-30 and PGc-180 catalysts.

To study which functionality is important for the observed catalytic activities of PGc, we carefully studied the functional groups of PGc-30 and PGc-180 materials. The XPS spectrum showed that both catalysts PGc-30 and PGc-180, have similar amount of % O (13.52, 13.60% respectively), which is lower than PGc (21.17% O) (**Table 4.1**). Furthermore, XPS and FT-IR analysis showed that they (PGc-30 and PGc-180) contain similar amounts of C-O-P and P=O groups, while PGc-180 has the lowest content of P-OH functionalities as per O1s XPS peak analysis of PGc-180 catalyst (**Figure 4.9** and **Figure 4.11** and **Table 4.7**). Note that PGc-180 also exhibited the lowest alcohol conversion, followed by PGc-30 and PGc, respectively, suggesting that the P-OH functional groups on PGc are likely to play an important role in the oxidation. On the other hand, we have also

performed benzyl alcohol oxidation reaction in the presence of molecules containing P=O and P-OH functional groups, such as phytic acid and phosphorous acid. The reaction does not proceed, which indicates the importance of the graphitic regions on the PGc material for aromatic substrate interaction.

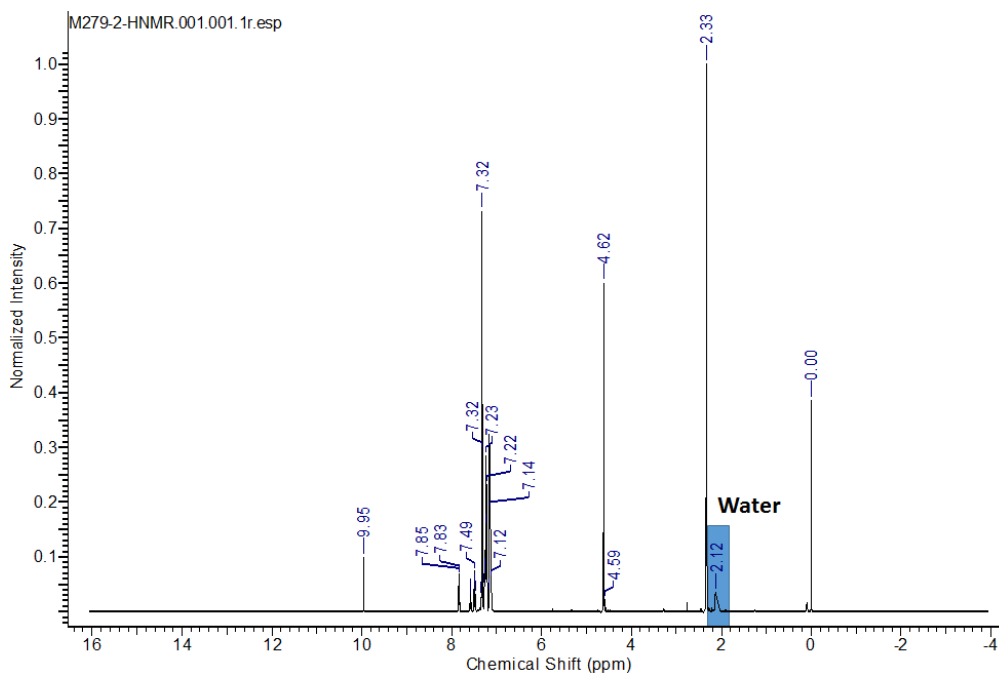


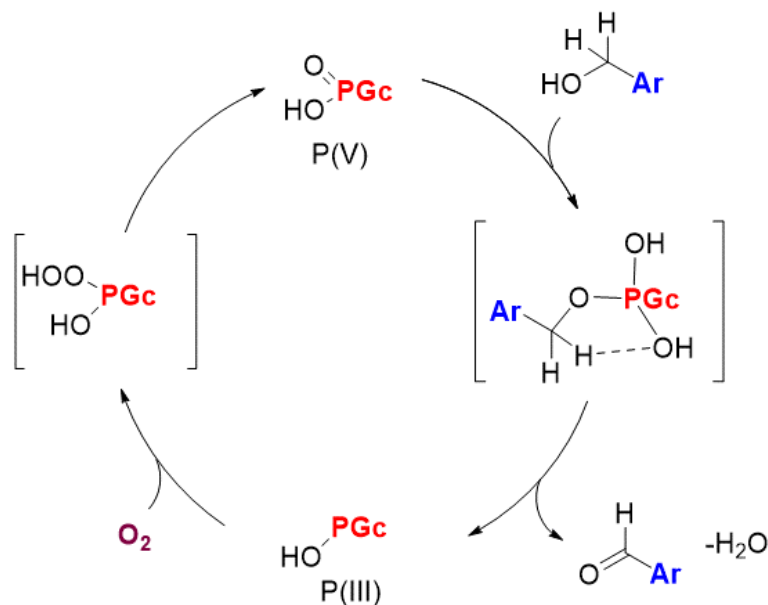
Figure 4.12. H-NMR spectrum of reaction mixture (**Table 2-** entry no. 4) containing benzyl alcohol (2H, 4.62 ppm), Benzaldehyde (1H, 9.95 ppm) and trace amount of water (2.12 ppm).

Based on all the experimental results described above, we have concluded the following important points regarding the catalytic mechanism of alcohol oxidation by PGc.

- (1) The PGc with higher work function shows higher catalytic activity, which is opposite to that of N-doped graphene and other graphitic carbon materials.
- (2) Molecular oxygen is not involved in the first step of the reaction, which is also different from N-doped graphene. However the presence of oxygen is critical for regenerating the active sites on the PGc catalysts.
- (3) The co-existence of P=O, P-OH functionalities along with the graphitic regions on PGc play a pivotal role in the catalytic alcohol oxidation reaction.
- (4) A radical

inhibitor, BHT, does not inhibit the oxidation reaction. (5) There are no detectable H_2O_2 as byproduct generated during the reaction (**Figure 4.5**). (6) In addition, the reaction is associated with loss of water when reaction was performed under oxygen as demonstrated by the presence of water peak in ^1H NMR spectroscopy of the final product mixture (**Figure 4.12**).

Scheme 4.2. Proposed mechanism of benzyl alcohol oxidation catalyzed by PGc in presence of oxygen as an oxidant.



Based on these findings and previous reports using P_2O_5 to accelerate the oxidation of alcohols⁵⁰ and carbohydrates,⁵¹ and especially, a recent finding suggested the importance of ketonic O in catalysis of benzylic alcohol oxidation,⁵² we propose the following mechanism as shown in **Scheme 4.2** where primary benzyl alcohol is used as an example. In the first step of catalysis, condensation between the alcohol and $\text{P}=\text{O}$ moieties on PGc takes place, and an alcoholate intermediate is formed. The condensation is likely facilitated by the interaction of the alcohol with the PGc surface by π - π interactions with the graphitic domains and hydrogen bonding with the polar groups (such as $\text{P}-\text{OH}$). In the second step

of the reaction, a rate determining H transfer takes place, possibly through a cyclic transition state. This step is supported by the linear Hammett correlation in the oxidation of 4-substituted benzylic alcohols by PGc (**Figure 4.13**, plot of $\log k$ vs σ gives a ρ value of -1.50, $R^2 = 0.98$, independent rates), indicating build-up of a positive charge in the transition state. The proton transfer step is facilitated by P-OH moieties on PGc surface. Notably, the observed Hammett rho value is in the range reported for oxidation of benzylic alcohols using pyridinium chlorochromate (-1.4 to -1.7)⁵³⁻⁵⁵ and much higher than that reported for oxidation of benzylic alcohols *via* the radical mechanism (-0.4).⁵⁶⁻⁵⁸ It is likely that the presence of hydrogen bonding between the substrate and the PGc polar groups stabilizes the transition state, enabling the alcohol oxidation in the close proximity to the material surface. The aldehyde product and a water molecule are released simultaneously. Next, the generated P (III) groups on PGc react with molecular oxygen to regenerate the P (V) centers for further reactions, thus completing the catalytic cycle (**Scheme 4.2**). The PGc catalyst after the reaction was characterized *via* FT-IR. The peaks at 1166 cm^{-1} (P=O), 1035 cm^{-1} (P-O/C-O), 900 cm^{-1} (shoulder, P-OH) have similar intensities as the fresh PGc catalyst (**Figure 4.14**), indicating that the catalytic sites are largely being regenerated during the reaction. Moreover, recently, Hasegawa *et al.* demonstrated that the reduced form of P functionalities, which were initially introduced into the carbon matrix of graphene, were unstable and gradually oxidized and/or hydrolyzed by O₂ and humidity at ambient conditions and room temperature, leading to the formation of oxidized P-containing functional groups.⁴⁵ This study also soundly supports the hypothesis that P-OH/P=O functionalities of PGc, can be readily regenerated.

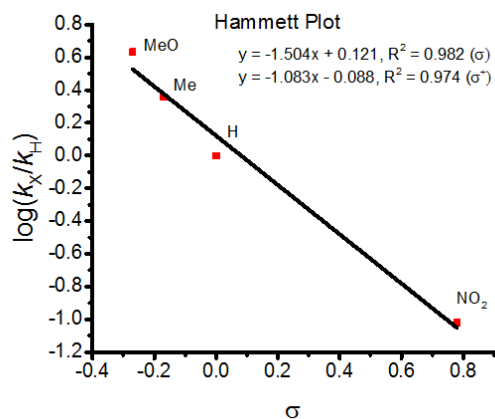


Figure 4.13. Hammett plot of Plot of $\log k$ vs. σ for the oxidation of 4-substituted benzyl alcohols with PGc catalyst.

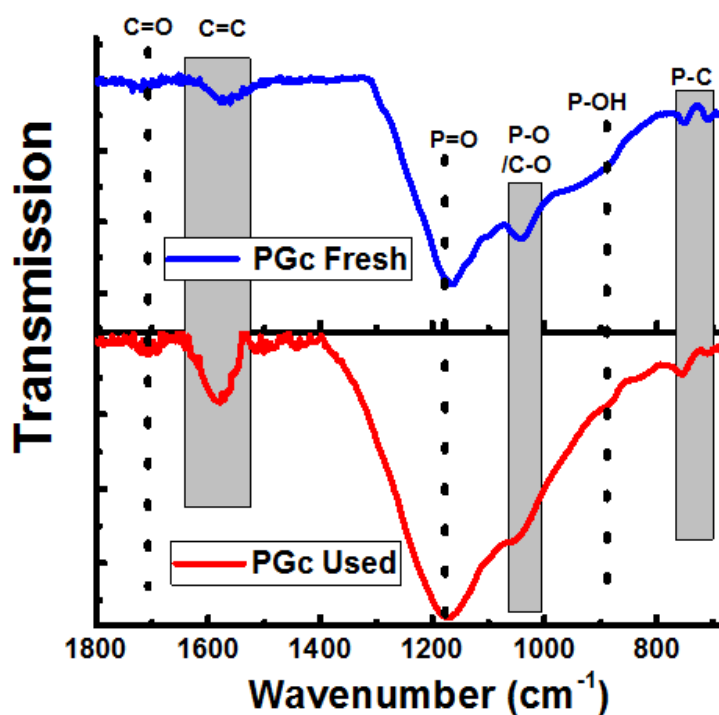
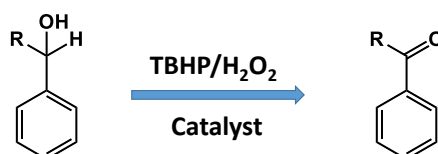


Figure 4.14. The FT-IR spectrum of the fresh and used PGc catalyst. The used catalyst was recycled twice (the reaction conditions were specified in Figure 4.6A caption) before this FT-IR measurement.

The excellent recyclability is one of the key advantages of PGc compared to the GO based catalysts. Boukhvalov *et al.* applied density functional theory (DFT) calculations on GO to reveal that the partially reduced catalyst, which is different from the inert graphite

or pristine graphene, can be recharged by molecular oxygen, allowing for catalyst turnover.³⁵ However, experimentally, it was reported that after the reaction, the GO catalyst was transformed to rGO, especially at relatively low catalyst loading such as 20 wt%. The recovered rGO has similar electronic properties as rGO intentionally prepared by other methods, indicating that regeneration of the active sites under the reaction conditions did not occur fast enough.¹⁸

Table 4.9. The benzyl alcohol oxidation catalyzed by PGc in the presence of H₂O₂ and TBHP oxidants ^a



Entry	Catalyst, Oxidant	R	(%) Conversion	(%) Selectivity	TON (x 10 ⁻²)
1	No catalyst, TBHP	H	13.92	96.0	-
2	PGc, TBHP	H	98.78	0.01%- Benzaldehyde 99.99% Benzoic acid	5.02
3	PGc, TBHP	CH ₃	95.73	>99	4.36
4	PGc, H ₂ O ₂	H	27.74	68.7	1.41
5	PGc, H ₂ O ₂	CH ₃	27.25	92.1	1.24

Reaction conditions- 10 mg catalyst, 50 mg alcohol (0.5 mmol), oxidant-TBHP/H₂O₂ (1.5 mmol), 80°C, 24 hours. Acetonitrile added as a solvent to make final reaction volume 0.3ml in all reactions. % conversion for alcohols and % selectivity to benzaldehyde calculated using ¹H NMR. The turnover number (TON) was calculated as a ratio of the (mol of oxidized product) / (mass of catalyst).

Furthermore, we have also explored the effect of different oxidants, such as H₂O₂ and TBHP, on benzylic alcohol oxidation (**Table 4.9**). With H₂O₂, the oxidation of primary alcohol results in 28 % conversion with moderate selectivity (69%, 20 wt% catalyst

loading). Which also suggests that presence of H_2O_2 is affecting the selectivity of aldehyde products. Interestingly, when the oxidant is switched to TBHP, even at relatively low catalyst loading (20 wt %), the conversion of both primary and secondary benzylic alcohol reaches $\geq 95\%$. However, the product for the oxidation of the primary benzylic alcohol is benzoic acid instead of benzaldehyde (100% selectivity) possibly due to the faster oxidation of aldehyde to acid in the presence of a strong oxidant (TBHP).

4.3. Conclusions

In summary, we have reported an extremely simple, energy effective, and scalable approach to rapidly fabricate P-doped carbon materials with controlled P bond configuration. For the first time, we demonstrated that the P-doped carbon materials can be used as a selective metal free catalyst for aerobic oxidation of benzylic alcohols with $>98\%$ selectivity to benzaldehydes. The P bond configuration influences the work function of P-doped carbon materials. However, in sharp contrast to N-doped graphene and other graphitic carbon materials, the PGc material with higher work function shows high activity in catalytic aerobic oxidation. Based on our extensive experimental studies, a unique catalytic mechanism seem to be operating when PGc catalysts are used, which is different from both GO and N-doped graphene obtained by high temperature nitrification. While the apparent conversion is similar to GO, the key advantage compared to GO is that this catalyst, even with low catalyst loading, can be reused multiple times with simple filtration without losing its catalytic activity. Compared to the N-doped graphene, not only the conversion increased 3 times without losing selectivity, this catalyst also shows no steric effect as both primary and secondary alcohol can be converted with similar conversion efficiency. Finally, while our study focused on alcohol oxidation, it is also worthy to

mentioning that phosphate functionalized carbon materials have been used for acidic catalytic reactions,⁵⁹ to increase the selectivity of the oxidative dehydration reactions,⁶⁰ and widen the electrochemical potential window in high capacitance applications.⁶¹ All these are due to the different P bond configuration in these carbon materials, which in turn demonstrated the rich P chemistry can be tailored to fit different applications. Importantly, we have already demonstrated that P carbon materials co-doped with other heteroatoms, such as N, B, S, and Si can also be fabricated by this microwave assisted approach by simply adding a suitable dopant precursor into the reactor.⁶² Altogether, these facts combined with the capability of co-doping with other heteroatoms *via* this simple microwave assisted approach, it is reasonable to predict that tailored carbon materials can be designed and quickly fabricated to develop more efficient and metal free carbon based catalysts for wide range of reactions and other sustainable applications.

4.4. Experimental Section

4.4.1. PGc (Phosphorus doped graphitic carbon) fabrication

The phytic acid (Sigma Aldrich, 50 w/w% in water, 1 mL) was placed in 35 mL Pyrex glass vessel (CEM, #909036) and then closed with Teflon lined cap (CEM, #909235). This closed glass vessel was kept in 500 mL beaker and then the whole assembly was covered with watch glass before transferring to a domestic microwave oven (1100 W, Sanyo-EM-S9515W, 2.45 GHz). A microwave irradiation was applied for 40 seconds which results into black carbonized material. After microwave treatment, the glass tube was left in a fume hood for a few minutes to remove any gas generated during microwave reaction and then dispersed in ethanol by bath sonication (5 minutes). The resulting dispersion is filtered by 0.8 μ m polycarbonate filter paper (Millipore, ATTP 04700) and washed with water

(~800 mL) and ethanol (~400 mL). After filtration, the product was dried in vacuum oven at ~110°C overnight before further use. The yield of product (PGc) was calculated to be ~12% by the weight of pure phytic acid or ~90% by weight of carbon present in phytic acid. Note: The above fabrication reaction can be also carried out in single mode cavity using commercial CEM microwave (CEM Discover SP, 300 Watts). This microwave unit provides much higher energy density than domestic microwave and so PGc can be synthesized in shorter time (30 seconds at 300 watts) than domestic microwave. It is also worthy to mention that the bulk price of phytic acid is \$0.03 per gram, which is much cheaper compared to GO (~\$200 per gram) and it is also sustainable for synthesis of P doped carbon materials.

4.4.2. Fabrication of PGc-30 and PGc-180

The PGc powder was further heated in the same microwave oven with additional microwave irradiation of total 30s and 180s, respectively. In detail, ~100 mg of PGc powder weighed into small porcelain dish and covered with a piece of watch glass before transferring into the domestic microwave chamber. The microwave radiation was applied in pulse of 10 seconds for different times with a 10-15 minute interval between two microwave pulses to avoid over heating or burning of the carbon material. For example, to synthesize PGc-180, 10 seconds of microwave radiation was repeated for 18 times with 10-15 minutes interval in between each microwave pulse.

4.4.3. Synthesis of GO and rGO for catalysis

GO is synthesized according to Hummer's method with slight modification.⁶³ In brief, the graphite powder (2 g, Sigma Aldrich, <20 μm) is mixed with 55 mL sulfuric acid (PHARMCO-AAPER, ACS grade 95-98%) and stirred in ice bath for 15min. After that we

added 12 mL nitric acid (BDH, ACS grade 69-70%) and again stirred in ice bath for additional 15 minute to cool down the mixture. Then we added 10 g of KMnO_4 (10 g, Sigma Aldrich, ACS grade) in a small portions while stirring the mixture in ice bath. After 2 hours of stirring in ice bath, the mixture was stirred in water bath at 45 °C for 6 hours to complete the oxidation of graphite. After Reaction was completed, it was quenched in 500 mL ice containing 10 mL of H_2O_2 (BDH, 35 w/w %) and filtered using what man filter paper (grade 5, 47 mm). Then the brown solid powder was resuspended in ~4% HCl and washed with it for 5 times by centrifugation at 8000 rpm * 30 minutes. After that it was washed with acetone for 10 times at 10000 rpm* 45 minutes of centrifugation and then dried in vacuum oven for 3 days before further use.

To synthesize rGO, 500 mg of GO was taken in the round bottom flask and then heated with microwave of 300 Watt (CEM discover SP) for 40secs. The brown colored GO powder was converted to black colored reduced graphene oxide (rGO) which was used as a control in catalytic reaction of benzyl alcohol oxidation to benzaldehyde in water solvent.

4.4.4. Catalytic oxidation of primary and secondary alcohol Reaction.

All the chemicals were used as received for catalytic reaction. Benzyl Alcohol (Millipore, $\geq 99\%$) and DL-sec-phenyl ethyl alcohol (Acros Organics, $\geq 97\%$), Cyclohexane methanol (Alfa Aesar, 99%), n butanol (anhydrous, Sigma Aldrich, 99.8%), 4-methoxybenzyl alcohol (TCI, $>98\%$), 4-methylbenzyl alcohol (Sigma Aldrich, 98%), 4-nitrobenzyl alcohol (Alfa Aesar, 99%), Toluene (anhydrous, Sigma Aldrich, 99.8%) Ethyl benzene (Alfa Aesar, 99%), tert-butyl hydroperoxide (TBHP) (Alfa Aesar, 70%), H_2O_2 (BDH, 35% w/w).

Alcohol oxidation in water: The aerobic oxidation reactions were carried out in a round bottom flask or 35ml reaction tube (depending on the size of the reaction) by stirring water,

alcohol and catalyst under 1 atm oxygen environment (using oxygen balloon). The detailed experimental condition and the amount of reagent and catalyst are specified in **Table 4.2** footnote. After the reaction is completed, reaction mixture is filtered *via* 0.02 μm syringe filter and analyzed by HPLC (Varian Pro-Star and Phenomenex C18 column, mobile phase 50:50 ratio of Methanol: 0.44% Acetic acid). For kinetic studies, the experiment was carried out at different temperatures. During each of the experiments, ~ 0.3 mL of aliquot was withdrawn at a regular interval of 15 minutes, filtered *via* 0.02 μm syringe filter and analyzed by HPLC.

Solvent free alcohol oxidation: In a typical reaction, benzyl alcohol was purged with oxygen for 10 minutes prior to mixing with a specified amount of catalyst (as mentioned in **Table 4.3**) in a microwave reaction vial (VWR, 10-20 mL, #89079-402) and sealed with PTFE faced aluminum cap. The reaction vial was heated in oil bath at specified temperature and time. For controlled experiment, nitrogen gas was used instead of oxygen. For control experiment with a radical inhibitor, BHT (Butylated hydroxytoluene), specified amount of BHT and acetonitrile (for maintaining uniform dispersion of BHT) was added to the above described mixture in the beginning of the reaction. For alcohol oxidation using TBHP or H_2O_2 as oxidant, TBHP or H_2O_2 was mixed with the specific alcohol and catalysts and then sealed in ambient environment. The experimental condition and the amount of the reactant and catalysts are specified in the table footnote. For control experiment using P-OH functional containing molecules (such as phytic acid or phosphoric acid) as a catalyst, we have mixed 1 mmol of benzyl alcohol and catalyst such that mmols of P-OH functional group comes to 1.2 mmols and heated under 80 $^{\circ}\text{C}$ for 48 hours under 1 atm O_2 . After completion of the reaction, ~ 0.7 mL of CDCl_3 was mixed with the reaction mixture and

filtered *via* 0.02 μm syringe filter and analyzed by ^1H NMR spectroscopy (Bruker Avalanche 500 MHz).

4.4.5. Material Characterization

PF-KPFM measurements of the PGc and PGc-180 catalysts were conducted using a Dimension ICON AFM setup inside a nitrogen-filled glove box where both H_2O and O_2 level were below 0.1 ppm. The tips used were PFQNE-AL (Bruker AFM Probes), composed of a silicon nitride cantilever with a sharp silicon tip. The morphology of graphene samples were studied using the scanning electron microscopy (SEM, Hitachi S-4800). The sample for SEM was prepared by directly adding the powder sample on a conductive carbon tape. X-ray photoelectron spectroscopy (XPS) characterization was performed after depositing a layer of the catalyst to be studied onto a Si substrate. The thickness of the film on the substrates was roughly 30–50 nm. XPS spectra were acquired using a Thermo Scientific K-Alpha system with a monochromatic Al $\text{K}\alpha$ x-ray source ($h\nu = 1486.7$ eV). For data analysis, Smart background subtraction was performed, and the spectra were fit with Gaussian/Lorentzian peaks using a minimum deviation curve fitting method (part of the Advantage software package). The surface composition of each species was determined by the integrated peak areas and the Scofield sensitivity factor provided by the Advantage software. The FT-IR spectra of the samples (thin films deposited on ZnSe windows) were acquired with a Thermo-Nicolet 6700 spectrometer (Thermo-Electron Corp., Madison, WI), using a sample shuttle and a mercury-cadmium-telluride (MCT) detector. Four blocks of 128 scans each were co-added with 4 cm^{-1} spectral resolution and two levels of zero-filling so that data was encoded every 1 cm^{-1} . Thermogravimetric analyses (TGA) of the PGc samples were performed on a TGA instrument (TA

instruments, Discovery TGA) under N₂ atmosphere. ~5 mg sample was loaded on to TGA platinum HT pan and kept at 40 °C for 5 minutes before each analysis. After 5 minutes, the temperature is increased from 40 °C to 900 °C at 5 °C/min under N₂ flow (20 ml/min). The Raman spectra of the PGc and other samples (deposited on Anodisc membrane) were collected using Raman Microscope (Confocal) – Wi-Tec, Alpha 3000R with an excitation laser at 785 nm. The X-ray fluorescence spectroscopic (XRF) measurement was carried out using Horiba XGT-1000WR with high purity Si detector.

The Surface area measurement by Brunauer-Emmett-Teller (BET) method:

The surface areas of the PGc catalyst was determined using a 12-point BET method (Micromeritics, ASAP 2020) and nitrogen as the adsorbate using.⁶⁴ After the BET measurements, the isotherms of these measurement are converted into BET plots as shown in **Figure 4.2D** and then the specific surface area of the catalyst was calculated using the value of the slope and intercept of the linear best fit line and below BET equation.⁶⁴

$$\frac{1}{Q[(P_0/P) - 1]} = \frac{c - 1}{Q_{mc}} \left(\frac{P}{P_0} \right) + \frac{1}{W_{mc}}$$

Here, Q is adsorbed gas quantity, Q_{mc} is monolayer quantity of adsorbed gas, c is the BET constant, P and P_0 are the equilibrium and the saturation pressure of adsorbates at the temperature of adsorption, respectively. The Calculated surface area of the PGc catalyst is 1260 m²/g.

PF-KPFM measurement of PGc catalysts:

To understand the mechanism of the alcohol oxidation reaction catalyzed by PGc materials, we have conducted a PeakForce Kelvin probe force microscopy (PF-KPFMTM). PF-KPFMTM, the combination of PeakForce Tapping mode and frequency modulated KPFM

(FM-KPFM), integrates the benefits and capabilities of PeakForce Tapping and the superior spatial resolution and accuracy of FM-KPFM. PF-KPFM has the best performance of KPFM working in a dual-pass fashion.⁶⁵ By using KPFM, one can measure the local surface potential of nanoscale materials, concurrently imaging their topography. Since KPFM measures the voltage required to nullify the work function (ϕ) difference between the conductive tip and the sample ($\phi_{\text{tip}} - \phi_{\text{sample}}$) or vice versa (depending on whether the potential was applied to the sample or the probe), the contrast in the contact potential difference (CPD) is equivalent to the local work function variation of the sample on a supporting substrate. So the local surface potential can be used to calculate the work function of the materials, if the work function of the tip is known. KPFM has been widely used to investigate the influence of dopants or atomic scale defects on the variation of work function. It has also been used to study the work function of graphene as a function of number of layers and heteroatomic doping.⁶⁶⁻⁶⁸

PF-KPFM measurements on the PGc materials were conducted with a Dimension ICON AFM setup inside an Argon-filled glove box where both H₂O and O₂ levels were below 0.1 ppm. The probes used were PFQNE-AL (Bruker AFM Probes), composed of a silicon nitride cantilever with a sharp silicon tip. The inert environment helped us to obtain more accurate measurements, since the dipole moment of any absorbed species can directly induce a difference in contact potential and, subsequently, a phase shift of our samples.⁶⁹ To ascertain the accuracy of our surface potential measurements, the CPD measurement was first conducted for a piece of freshly cleaved highly ordered pyrolytic graphite (HOPG) in the glove box. The average CPD value of 0.60 V (with the standard deviation of 0.02 V) was obtained from the measurements at four different spots on the same HOPG. Knowing

the work function of the probe tip from previous experiments (4.08 eV), the average work function ϕ of HOPG was calculated to be 4.68 eV. This value is in agreement with the literatures.⁷⁰ To measure the work function of PGc and PGc-180 with PF-KPFM, we first break the monolith of PGc and PGc-180 to small particles and disperse them into water or ethanol using bath sonication for 3 minutes. Then the samples for CPD measurements were prepared by drop casting the PGc and PGc-180 particles onto a doped silicon (Si) substrate with 50 nm SiO₂ layer. Because the PGc or PGc-180 particles only partially covers the Si substrate, the measured CPD value of Si substrate can be used as the reference value to calculate the work functions of PGc or PGc-180.

Figure 4.15 shows the topographical and CPD images simultaneously taken on the PGc and PGc-180, respectively. From the AFM images, we found that upon sonication treatment, the unique sandwich structure of PGc and PGc-180 was separated to graphene sheet like structures and irregular particles, which possibly from the porous monolith sandwiched between the sheets. The CPD for the sheets of PGc and PGc-180 is -287.71 mV and -173.03 mV, respectively, from which we calculate the work function of PGc is 4.87 eV, which is 0.120 eV higher than that of PGc-180 (4.75 eV). Noted that the dark contrast observed in the CPD image indicates their work function is higher than the Si substrate used in this work. We also calculated the work function of the Si substrate is 4.58 eV, which is consistent with the values (4.60–4.85 eV) reported in literatures, further demonstrating the accuracy of the measurements. By conducting PF-KPFM with several samples, which have particles of different sizes we found that the work function of PGc particles barely changes with their height. The average work function is 4.78 eV, slightly lower than that of the corresponding sheets. However, for the PGc-180, the work function

dramatically changes with the height of the particles. The higher ones have lower work functions. The lowest work function measured is 3.3 eV with an average particle height of 400 nm, which is dramatically lower than that of PGc. Even though we still have difficulty to explain these results, they unambiguously demonstrated that the PGc-180 has much lower work functions.

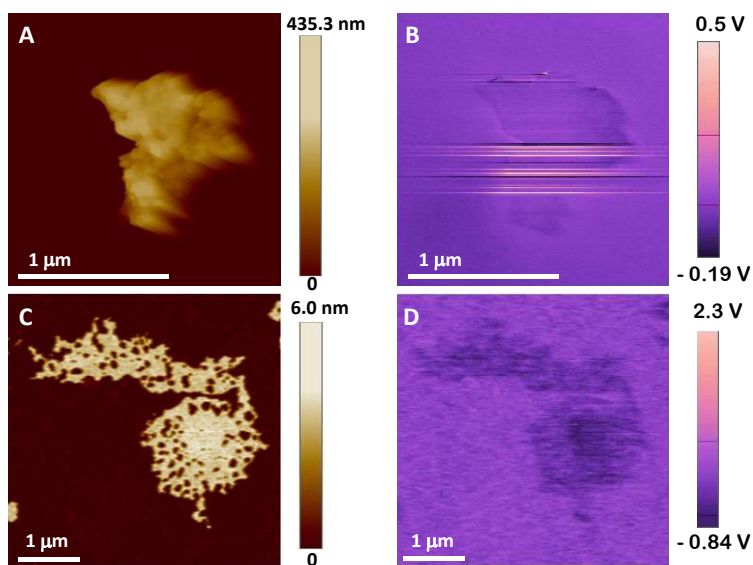


Figure 4.15. (A, C) AFM Topography and (B, D) PF-KPFM images for the PGc and the PGc-180 catalysts.

X-ray fluorescence spectroscopic (XRF) measurement of PGc (fresh and used):

To calculate % P in PGc, XRF measurement was carried out using Horiba XGT-1000WR instrument with a high purity Si detector. The x-ray tube and current parameters were set to 50 kV and 1 mA. The standard samples were prepared by mixing known weight of ammonium phosphate with rGO and analyzed using XRF. The intensity versus % P plotted to get linear calibration curve (**Figure 4.16**). After that, using the slope and intercept, we can calculate % P presence in unknown samples (PGc fresh and used). The calculated % P

in fresh PGc and used PGc catalyst is to be 2.3 atomic % (or 7.9 wt %) and 2.6 atomic % (or 9.5 wt %).

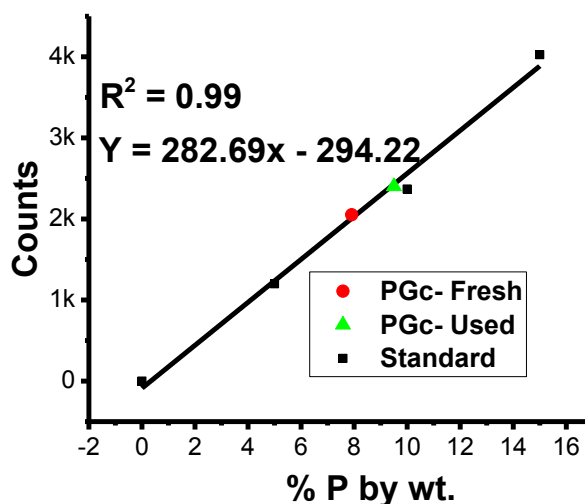


Figure 4.16. X-ray fluorescence spectroscopic (XRF) analysis of standard mixture (rGO with different % P). The used catalyst is recycled twice (at reaction conditions specified in the caption of Figure 4.6) before XRF measurement.

4.5. References

1. Navalon, S.; Dhakshinamoorthy, A.; Alvaro, M.; Garcia, H. Carbocatalysis by Graphene-Based Materials. *Chem. Rev.* 2014, 114, 6179-6212.
2. Su, C.; Loh, K. P. Carbocatalysts: graphene oxide and its derivatives. *Acc. Chem. Res.* 2012, 46, 2275-2285.
3. Fan, X.; Zhang, G.; Zhang, F. Multiple roles of graphene in heterogeneous catalysis. *Chem. Soc. Rev.* 2015, 44, 3023-35.
4. Hu, H. W.; Xin, J. H.; Hu, H.; Wang, X. W.; Kong, Y. Y. Metal-free graphene-based catalyst-Insight into the catalytic activity: A short review. *Applied Catalysis a-General* 2015, 492, 1-9.
5. Su, D. S.; Perathoner, S.; Centi, G. Nanocarbons for the development of advanced catalysts. *Chem. Rev.* 2013, 113, 5782-816.
6. Kong, X. K.; Chen, C. L.; Chen, Q. W. Doped graphene for metal-free catalysis. *Chem. Soc. Rev.* 2014, 43, 2841-57.
7. Gong, K.; Du, F.; Xia, Z.; Durstock, M.; Dai, L. Nitrogen-doped carbon nanotube arrays with high electrocatalytic activity for oxygen reduction. *Science* 2009, 323, 760-4.
8. Jiao, Y.; Zheng, Y.; Jaroniec, M.; Qiao, S. Z. Origin of the electrocatalytic oxygen reduction activity of graphene-based catalysts: a roadmap to achieve the best performance. *J. Am. Chem. Soc.* 2014, 136, 4394-403.

9. Zhang, C.; Mahmood, N.; Yin, H.; Liu, F.; Hou, Y. Synthesis of phosphorus-doped graphene and its multifunctional applications for oxygen reduction reaction and lithium ion batteries. *Adv. Mater.* 2013, 25, 4932-7.
10. Patel, M.; Feng, W.; Savaram, K.; Khoshi, M. R.; Huang, R.; Sun, J.; Rabie, E.; Flach, C.; Mendelsohn, R.; Garfunkel, E.; He, H. Microwave Enabled One-Pot, One-Step Fabrication and Nitrogen Doping of Holey Graphene Oxide for Catalytic Applications. *Small* 2015, 11, 3358-68.
11. Su, C.; Acik, M.; Takai, K.; Lu, J.; Hao, S. J.; Zheng, Y.; Wu, P.; Bao, Q.; Enoki, T.; Chabal, Y. J.; Loh, K. P. Probing the catalytic activity of porous graphene oxide and the origin of this behaviour. *Nat Commun* 2012, 3, 1298.
12. Dhakshinamoorthy, A.; Primo, A.; Concepcion, P.; Alvaro, M.; Garcia, H. Doped Graphene as a Metal-Free Carbocatalyst for the Selective Aerobic Oxidation of Benzylic Hydrocarbons, Cyclooctane and Styrene. *Chemistry-a European Journal* 2013, 19, 7547-7554.
13. Li, X. H.; Chen, J. S.; Wang, X.; Sun, J.; Antonietti, M. Metal-free activation of dioxygen by graphene/g-C₃N₄ nanocomposites: functional dyads for selective oxidation of saturated hydrocarbons. *J. Am. Chem. Soc.* 2011, 133, 8074-7.
14. Li, X. H.; Antonietti, M. Polycondensation of boron- and nitrogen-codoped holey graphene monoliths from molecules: carbocatalysts for selective oxidation. *Angew. Chem. Int. Ed. Engl.* 2013, 52, 4572-6.
15. Gao, Y.; Hu, G.; Zhong, J.; Shi, Z.; Zhu, Y.; Su, D. S.; Wang, J.; Bao, X.; Ma, D. Nitrogen-Doped sp²-Hybridized Carbon as a Superior Catalyst for Selective Oxidation. *Angew. Chem. Int. Ed.* 2013, 52, 2109-2113.
16. Jia, H. P.; Dreyer, D. R.; Bielawski, C. W. Graphite Oxide as an Auto-Tandem Oxidation-Hydration-Aldol Coupling Catalyst. *Adv. Synth. Catal.* 2011, 353, 528-532.
17. Jia, H. P.; Dreyer, D. R.; Bielawski, C. W. C-H oxidation using graphite oxide. *Tetrahedron* 2011, 67, 4431-4434.
18. Dreyer, D. R.; Jia, H. P.; Bielawski, C. W. Graphene oxide: a convenient carbocatalyst for facilitating oxidation and hydration reactions. *Angew. Chem. Int. Ed. Engl.* 2010, 49, 6813-6.
19. Li, W. J.; Gao, Y. J.; Chen, W. L.; Tang, P.; Li, W. Z.; Shi, Z. J.; Su, D. S.; Wang, J. G.; Ma, D. Catalytic Epoxidation Reaction over N-Containing sp⁽²⁾ Carbon Catalysts. *Acs Catalysis* 2014, 4, 1261-1266.
20. Long, J. L.; Xie, X. Q.; Xu, J.; Gu, Q.; Chen, L. M.; Wang, X. X. Nitrogen-Doped Graphene Nanosheets as Metal-Free Catalysts for Aerobic Selective Oxidation of Benzylic Alcohols. *Acs Catalysis* 2012, 2, 622-631.
21. Khai, T. V.; Na, H. G.; Kwak, D. S.; Kwon, Y. J.; Ham, H.; Shim, K. B.; Kim, H. W. Significant enhancement of blue emission and electrical conductivity of N-doped graphene. *J. Mater. Chem.* 2012, 22, 17992-18003.
22. Wang, X.; Sun, G.; Routh, P.; Kim, D.-H.; Huang, W.; Chen, P. Heteroatom-doped graphene materials: syntheses, properties and applications. *Chem. Soc. Rev.* 2014, 43, 7067-7098.
23. Yang, D. S.; Bhattacharjya, D.; Inamdar, S.; Park, J.; Yu, J. S. Phosphorus-Doped Ordered Mesoporous Carbons with Different Lengths as Efficient Metal-Free Electrocatalysts for Oxygen Reduction Reaction in Alkaline Media. *J. Am. Chem. Soc.* 2012, 134, 16127-16130.

24. Some, S.; Kim, J.; Lee, K.; Kulkarni, A.; Yoon, Y.; Lee, S.; Kim, T.; Lee, H. Highly air-stable phosphorus-doped n-type graphene field-effect transistors. *Adv. Mater.* 2012, 24, 5481-6.
25. Liu, Z. W.; Peng, F.; Wang, H. J.; Yu, H.; Zheng, W. X.; Yang, J. Phosphorus-doped graphite layers with high electrocatalytic activity for the O₂ reduction in an alkaline medium. *Angew. Chem. Int. Ed. Engl.* 2011, 50, 3257-61.
26. Latorre-Sanchez, M.; Primo, A.; Garcia, H. P-doped graphene obtained by pyrolysis of modified alginate as a photocatalyst for hydrogen generation from water-methanol mixtures. *Angew. Chem. Int. Ed. Engl.* 2013, 52, 11813-6.
27. Zhang, X. L.; Lu, Z. S.; Fu, Z. M.; Tang, Y. A.; Ma, D. W.; Yang, Z. X. The mechanisms of oxygen reduction reaction on phosphorus doped graphene: A first-principles study. *J. Power Sources* 2015, 276, 222-229.
28. Wang, H. M.; Wang, H. X.; Chen, Y.; Liu, Y. J.; Zhao, J. X.; Cai, Q. H.; Wang, X. Z. Phosphorus-doped graphene and (8,0) carbon nanotube: Structural, electronic, magnetic properties, and chemical reactivity. *Appl. Surf. Sci.* 2013, 273, 302-309.
29. Liu, Z. W.; Peng, F.; Wang, H. J.; Yu, H.; Zheng, W. X.; Wei, X. Y. Preparation of phosphorus-doped carbon nanospheres and their electrocatalytic performance for O₂ reduction. *Journal of Natural Gas Chemistry* 2012, 21, 257-264.
30. Yamaguchi, K.; Mizuno, N. Scope, kinetics, and mechanistic aspects of aerobic oxidations catalyzed by ruthenium supported on alumina. *Chemistry-A European Journal* 2003, 9, 4353-4361.
31. Dijkman, A.; Marino-Gonzalez, A.; Payeras, A. M. I.; Arends, I. W. C. E.; Sheldon, R. A. Efficient and selective aerobic oxidation of alcohols into aldehydes and ketones using ruthenium/TEMPO as the catalytic system. *J. Am. Chem. Soc.* 2001, 123, 6826-6833.
32. Watanabe, H.; Asano, S.; Fujita, S.; Yoshida, H.; Arai, M. Nitrogen-Doped, Metal-Free Activated Carbon Catalysts for Aerobic Oxidation of Alcohols. *Acs Catalysis* 2015, 5, 2886-2894.
33. Cheon, J. Y.; Kim, J. H.; Kim, J. H.; Goddeti, K. C.; Park, J. Y.; Joo, S. H. Intrinsic relationship between enhanced oxygen reduction reaction activity and nanoscale work function of doped carbons. *J. Am. Chem. Soc.* 2014, 136, 8875-8.
34. Meng, Y. Y.; Voiry, D.; Goswami, A.; Zou, X. X.; Huang, X. X.; Chhowalla, M.; Liu, Z. W.; Asefa, T. N-, O-, and S-Tridoped Nanoporous Carbons as Selective Catalysts for Oxygen Reduction and Alcohol Oxidation Reactions. *J. Am. Chem. Soc.* 2014, 136, 13554-13557.
35. Boukhvalov, D. W.; Dreyer, D. R.; Bielawski, C. W.; Son, Y. W. A Computational Investigation of the Catalytic Properties of Graphene Oxide: Exploring Mechanisms by using DFT Methods. *Chemcatchem* 2012, 4, 1844-1849.
36. Ramasahayam, S. K.; Nasini, U. B.; Bairi, V.; Shaikh, A. U.; Viswanathan, T. Microwave assisted synthesis and characterization of silicon and phosphorous co-doped carbon as an electrocatalyst for oxygen reduction reaction. *Rsc Advances* 2014, 4, 6306-6313.
37. Ramasahayam, S. K.; Nasini, U. B.; Shaikh, A. U.; Viswanathan, T. Novel tannin-based Si, P co-doped carbon for supercapacitor applications. *J. Power Sources* 2015, 275, 835-844.

38. Enache, D. I.; Edwards, J. K.; Landon, P.; Solsona-Espriu, B.; Carley, A. F.; Herzing, A. A.; Watanabe, M.; Kiely, C. J.; Knight, D. W.; Hutchings, G. J. Solvent-free oxidation of primary alcohols to aldehydes using Au-Pd/TiO₂ catalysts. *Science* 2006, 311, 362-5.
39. Liu, H. L.; Liu, Y. L.; Li, Y. W.; Tang, Z. Y.; Jiang, H. F. Metal-Organic Framework Supported Gold Nanoparticles as a Highly Active Heterogeneous Catalyst for Aerobic Oxidation of Alcohols. *Journal of Physical Chemistry C* 2010, 114, 13362-13369.
40. Zhu, J.; Wang, P. C.; Lu, M. Selective oxidation of benzyl alcohol under solvent-free condition with gold nanoparticles encapsulated in metal-organic framework. *Applied Catalysis a-General* 2014, 477, 125-131.
41. Liu, Z. W.; Peng, F.; Wang, H. J.; Yu, H.; Tan, J.; Zhu, L. L. Novel phosphorus-doped multiwalled nanotubes with high electrocatalytic activity for O₂ reduction in alkaline medium. *Catal. Commun.* 2011, 16, 35-38.
42. Gholizadeh, R.; Yu, Y. X. Work Functions of Pristine and Heteroatom-Doped Graphenes under Different External Electric Fields: An ab Initio DFT Study. *Journal of Physical Chemistry C* 2014, 118, 28274-28282.
43. Schiros, T.; Nordlund, D.; Palova, L.; Prezzi, D.; Zhao, L.; Kim, K. S.; Wurstbauer, U.; Gutierrez, C.; Delongchamp, D.; Jaye, C.; Fischer, D.; Ogasawara, H.; Pettersson, L. G.; Reichman, D. R.; Kim, P.; Hybertsen, M. S.; Pasupathy, A. N. Connecting dopant bond type with electronic structure in N-doped graphene. *Nano Lett.* 2012, 12, 4025-31.
44. Dreyer, D. R.; Jia, H. P.; Bielawski, C. W. Graphene oxide: a convenient carbocatalyst for facilitating oxidation and hydration reactions. *Angewandte Chemie* 2010, 122, 6965-6968.
45. Hasegawa, G.; Deguchi, T.; Kanamori, K.; Kobayashi, Y.; Kageyama, H.; Abe, T.; Nakanishi, K. High-Level Doping of Nitrogen, Phosphorus, and Sulfur into Activated Carbon Monoliths and Their Electrochemical Capacitances. *Chem. Mater.* 2015, 27, 4703-4712.
46. Patel, M.; Feng, W.; Savaram, K.; Khoshi, M. R.; Huang, R.; Sun, J.; Rabie, E.; Flach, C.; Mendelsohn, R.; Garfunkel, E. Microwave Enabled One-Pot, One-Step Fabrication and Nitrogen Doping of Holey Graphene Oxide for Catalytic Applications. *Small* 2015.
47. Marcano, D. C.; Kosynkin, D. V.; Berlin, J. M.; Sinitskii, A.; Sun, Z.; Slesarev, A.; Alemany, L. B.; Lu, W.; Tour, J. M. Improved synthesis of graphene oxide. *ACS Nano* 2010, 4, 4806-14.
48. Puziy, A. M.; Poddubnaya, O. I.; Martinez-Alonso, A.; Suarez-Garcia, F.; Tascon, J. M. D. Surface chemistry of phosphorus-containing carbons of lignocellulosic origin. *Carbon* 2005, 43, 2857-2868.
49. Puziy, A. M.; Poddubnaya, O. I.; Ziatdinov, A. M. On the chemical structure of phosphorus compounds in phosphoric acid-activated carbon. *Appl. Surf. Sci.* 2006, 252, 8036-8038.
50. Khazaei, A.; Rad, M. N. S.; Borazjani, M. K.; Saednia, S.; Borazjani, M. K.; Golbaghi, M.; Behrouz, S. Highly Efficient Etherification and Oxidation of Aromatic Alcohols Using Supported and Unsupported Phosphorus Pentoxide as a Heterogeneous Reagent. *Synth. Commun.* 2011, 41, 1544-1553.
51. Onodera, K.; Hirano, S.; Kashimura, N. Oxidation of carbohydrates with dimethyl sulfoxide containing phosphorus pentoxide. *J. Am. Chem. Soc.* 1965, 87, 4651-4652.

52. Jeyaraj, V. S.; Kamaraj, M.; Subramanian, V. Generalized Reaction Mechanism for the Selective Aerobic Oxidation of Aryl and Alkyl Alcohols over Nitrogen-Doped Graphene. *Journal of Physical Chemistry C* 2015, 119, 26438-26450.
53. Banerji, K. K. Oxidation of Substituted Benzyl Alcohols by Pyridinium Fluorochromate - a Kinetic-Study. *J. Org. Chem.* 1988, 53, 2154-2159.
54. Stewart, R.; Lee, D. G. THE CHROMIC ACID OXIDATION OF ARYL TRIFLUOROMETHYL ALCOHOLS: ISOTOPE AND SUBSTITUENT EFFECTS. *Can. J. Chem.* 1964, 42, 439-446.
55. Banerji, K. K. Kinetics and mechanism of the oxidation of substituted benzyl alcohols by pyridinium chlorochromate. *Journal of the Chemical Society, Perkin Transactions 2* 1978, 639-641.
56. De Nooy, A. E.; Besemer, A. C.; van Bekkum, H. On the use of stable organic nitroxyl radicals for the oxidation of primary and secondary alcohols. *Synthesis* 1996, 1153-1174.
57. Minisci, F.; Recupero, F.; Cecchetto, A.; Gambarotti, C.; Punta, C.; Faletti, R.; Paganelli, R.; Pedulli, G. F. Mechanisms of the Aerobic Oxidation of Alcohols to Aldehydes and Ketones, Catalysed under Mild Conditions by Persistent and Non-Persistent Nitroxyl Radicals and Transition Metal Salts– Polar, Enthalpic, and Captodative Effects. *Eur. J. Org. Chem.* 2004, 2004, 109-119.
58. Koshino, N.; Saha, B.; Espenson, J. H. Kinetic study of the phthalimide N-oxyl radical in acetic acid. Hydrogen abstraction from substituted toluenes, benzaldehydes, and benzyl alcohols. *J. Org. Chem.* 2003, 68, 9364-70.
59. Villa, A.; Schiavoni, M.; Fulvio, P. F.; Mahurin, S. M.; Dai, S.; Mayes, R. T.; Veith, G. M.; Prati, L. Phosphorylated mesoporous carbon as effective catalyst for the selective fructose dehydration to HMF. *Journal of Energy Chemistry* 2013, 22, 305-311.
60. Zhang, J.; Liu, X.; Blume, R.; Zhang, A.; Schlogl, R.; Su, D. S. Surface-modified carbon nanotubes catalyze oxidative dehydrogenation of n-butane. *Science* 2008, 322, 73-7.
61. Hulicova-Jurcakova, D.; Puziy, A. M.; Poddubnaya, O. I.; Suarez-Garcia, F.; Tascon, J. M.; Lu, G. Q. Highly stable performance of supercapacitors from phosphorus-enriched carbons. *J. Am. Chem. Soc.* 2009, 131, 5026-7.
62. Patel, M.; Savaram, K.; Keating, K.; He, H. Rapid Transformation of Biomass Compounds to Metal Free Catalysts via Short Microwave Irradiation. *Journal of Natural Products Research Updates* 2015, 1, 18-28.
63. Hu, F.; Patel, M.; Luo, F.; Flach, C.; Mendelsohn, R.; Garfunkel, E.; He, H.; Szostak, M. Graphene-Catalyzed Direct Friedel-Crafts Alkylation Reactions: Mechanism, Selectivity, and Synthetic Utility. *J. Am. Chem. Soc.* 2015, 137, 14473-80.
64. Brunauer, S.; Emmett, P. H.; Teller, E. Adsorption of gases in multimolecular layers. *J. Am. Chem. Soc.* 1938, 60, 309-319.
65. Chunzeng Li, S. M., Yan Hu, Ji Ma, Jianli He, Henry Mittel, Vinson Kelly, Natalia Erina, Senli Guo, Thomas Mueller. *PeakForce Kelvin Probe Force Microscopy, Application Note #140*; Bruker Corporation: 2013.
66. Baumgart, C.; Helm, M.; Schmidt, H. Quantitative dopant profiling in semiconductors: A Kelvin probe force microscopy model. *Physical Review B* 2009, 80, 085305.

67. Koren, E.; Berkovitch, N.; Rosenwaks, Y. Measurement of active dopant distribution and diffusion in individual silicon nanowires. *Nano Lett.* 2010, 10, 1163-1167.
68. Ziegler, D.; Gava, P.; Güttinger, J.; Molitor, F.; Wirtz, L.; Lazzeri, M.; Saitta, A.; Stemmer, A.; Mauri, F.; Stampfer, C. Variations in the work function of doped single-and few-layer graphene assessed by Kelvin probe force microscopy and density functional theory. *Physical Review B* 2011, 83, 235434.
69. Lagel, B.; Baikie, I. D.; Petermann, U. A novel detection system for defects and chemical contamination in semiconductors based upon the Scanning Kelvin Probe. *Surf. Sci.* 1999, 433, 622-626.
70. Beerbom, M. M.; Lagel, B.; Cascio, A. J.; Doran, B. V.; Schlaf, R. Direct comparison of photoemission spectroscopy and in situ Kelvin probe work function measurements on indium tin oxide films. *J. Electron. Spectrosc. Relat. Phenom.* 2006, 152, 12-17.

Chapter 5. Rapid Transformation of Biomass Compounds to Metal Free Catalysts via Short Microwave Irradiation

5.1. Introduction

The pivotal role of catalytic materials in various industries is unambiguously demonstrated by the fact that up to 90% of commercially available chemical products involve the use of catalysts at some production stage.¹ However, most catalytic materials were developed based on toxic and/or precious metals, which are unsustainable and possess environmental risks. In the drive towards green and sustainable chemistry, there is an increasing interest in developing new carbon-based materials that are benign, abundant, readily available, and metal free to act as catalysts for chemical synthesis. A plethora of reports have demonstrated that doping graphene matrices with heteroatoms modifies its physicochemical and electronic properties towards enhanced electrocatalytic oxygen reduction reaction (ORR) performance, when compared to undoped analogs.²⁻⁸ In addition, co-doping with several different heteroatoms shows further improvements in ORR performances.^{3, 4, 9-16} Compared to ORR studies, the use of doped and/or co-doped carbon materials as catalysts for selective organic synthesis are in their early stages of development, although a great potential has been demonstrated. Importantly, these carbocatalysts merge the benefits of green synthesis with heterogeneous reaction conditions, which greatly simplifies work-up conditions and is particularly attractive from an industrial standpoint. To convert this great potential to practical industrial reality, methods for the large-scale fabrication, that is both cost and energy efficient, of these novel heteroatom-doped graphene-based materials, is required.

Various approaches have been developed for the fabrication of heteroatom-doped graphene. Most of the reported doping procedures are long and require high temperature annealing of graphene oxide (GO) with doping precursors in an inert environment.¹⁷⁻²⁰ Furthermore, although single layer graphene has the largest surface area (2600 m²/g), the effective surface area, especially in some solvents or reactants, is much lower due to aggregation. The aggregated structures dramatically influence mass transport of reactants to the active sites and inhibit the products from leaving the active centers. On the other hand, porous carbon materials can be beneficial for mass transport due to their large surface area and the existence of large amount of pores so that the active sites are easily accessible. Furthermore, these materials can be made from cheap abundant biomass compounds, ensuring sustainability of resources.²¹⁻²⁴ However, all the porous carbon materials, including the heteroatom doped ones, have been also fabricated via long period (hours) of high temperature reaction or annealing procedures in inert environments to afford stable materials with the desired performance, which deviates the concept of energy saving and sustainability.

The use of microwave heating instead of traditional high temperature annealing is attractive due to its energy savings and rapid fabrication advantages. However, the challenge with using microwave energy is that most of the biomass and organic compounds are transparent to microwave energy, prohibiting their direct use for microwave irradiation to undergo carbonization. This problem has been partially solved by pre-heating with traditional heating or by adding some microwave absorbing materials, such as mineral oxides, and some type of carbon.²⁵⁻²⁷ However, these microwave-absorbing materials may introduce unintentional contaminations to the obtained carbon materials, which is not

desirable for catalytic applications in organic synthesis. Therefore, choosing the right microwave-adsorbing materials is important to avoid this problem.

In chapter-4, it was discovered that phytic acid, a sustainable biomass compound, can be used directly for P doped carbon material fabrication with microwave irradiation.²⁸ Phytic acid is the principal storage form of phosphorus in many plant tissues, especially in the bran of grains and other seeds, and it is well known as an anti-nutrient substance in food. Phytic acid is a snowflake-like compound, containing six phosphorous acid “arms” (**Scheme 5.1**). The existence of both high levels of C and P in one molecule ensures uniform P doping in the fabricated carbon materials. Most importantly, phytic acid strongly absorbs microwave energy, so that the as-purchased phytic acid solution can be directly subjected to short (40 seconds) microwave irradiation for the fabrication of P doped graphene like carbon product (PGc). By simply changing the microwave irradiation time, PGc with different P bond configurations were fabricated, as determined by combined FTIR and X-ray photoelectron spectroscopy (XPS).²⁸ Using microwave heating instead of traditional heating ensures that this approach is both sustainable and energy efficient. Furthermore, the fabrication can be performed under ambient conditions without the requirements of an inert environment, which makes this approach even more cost effective and convenient.

Furthermore, the capability of the P doped carbon materials as metal free catalysts for aerobic oxidation reactions has been demonstrated for the first time.²⁸ It was found that P doped carbon materials efficiently catalyzed aerobic oxidation of both primary and secondary benzyl alcohols to the corresponding aldehydes or ketones. To our surprise, the PGc with higher work functions showed higher capacity in catalyzing aerobic oxidation

reactions, which is opposite to the trend when N doped carbon materials were used as metal free catalysts for aerobic oxidation reactions and electrochemical catalysts for ORR. Since both ORR and aerobic oxidation reactions involve activation of molecular oxygen at certain stages of the reactions, it was hypothesized that a strong correlation should exist between these two processes. However, it is not certain if the best catalysts for aerobic reaction are also good electrocatalysts for ORR. The main focus of this work is to study the ORR performance as a function of P bond configuration and reveal any correlations between the catalytic behavior for ORR and aerobic oxidation.

It was well accepted that different heteroatomic doping confers graphene with distinct properties due to their different electronic structures and atomic diameters.^{10, 29, 30} Furthermore, it is reported that co-doping with different heteroatoms generates new properties and/or creates synergistic effects, which results in largely improved electrocatalytic ORR performances. These synergistic effects could also be beneficial for other catalytic applications.³⁰⁻³² Interestingly, a recent study by Garcia *et al.* demonstrated that graphene like carbon materials without any heteroatom doping gave excellent catalytic performance for selective acetylene hydrogenation and alkene hydrogenation in the absence of metal catalysts.³³ The fabrication of this material was achieved by carbonization of alginate at high temperatures (900 °C for 6 hours). Therefore it provides a scope for this simple and energy effective approach to be extended to fabricate carbon materials with or without heteroatom doping, and P co-doping with other heteroatoms to accommodate a large range of catalytic applications. In this work, it was demonstrated that, the microwave-assisted carbonization approach can be extended to fabricate co-doped carbon catalysts such as P-N, P-S, P-Si, and P-B co-doped carbon materials, labeled as PN-Gc, PS-Gc, PSi-

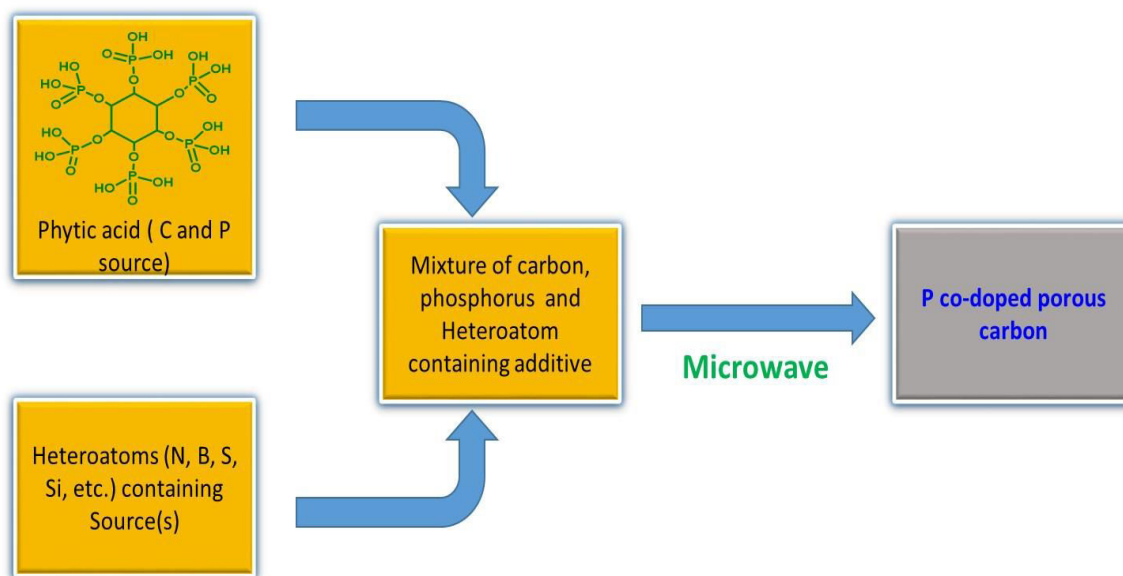
Gc, PB-Gc, respectively, by simply adding a suitable dopant precursor into phytic acid solution prior to microwave irradiation. The fabrication of carbon materials without heteroatom doping or sole heteroatom doping with S, Si, B and N is not straightforward by this microwave assisted carbonization technique. This is because the available precursors for these materials are transparent to microwave irradiation. By changing the carbon resource to inositol (a biomass compound similar to phytic acid but without the phosphate arms), and using H_2SO_4 as a microwave absorber and dehydrating agent, carbon materials without doping or sole doping with one type of heteroatom were successfully fabricated. The ORR performance of the phosphorus doped carbon material was carefully studied. The correlation among their ORR performance, aerobic catalytic performance, and the P bond configuration in their carbon matrix was revealed. We found that the PGc catalyst with prominent P-C bonding, which exhibits inferior aerobic oxidation, is more facile to kinetically catalyze the ORR via four-electron pathway. Whereas on the other hand, the PGc with more P-O bonding exhibits the reverse trend (2e^- pathway in ORR and superior oxidation). In addition, we also analyzed the ORR characteristic of these co-doped catalysts (PN-Gc, PB-Gc, PS-Gc, and PSi-Gc) and found that PN co-doped carbon materials (PN-Gc) is the most beneficial for ORR catalysis toward 4e^- electron pathway among all co-doped carbon catalysts.

5.2. Results and Discussion

The fabrication of phosphorus (P) co-doped carbon material with other heteroatoms (N, B, S, Si) was carried out by simply adding a suitable heteroatom dopant precursor into a phytic acid solution before subjecting the mixture to microwave radiation as shown in **Scheme 5.1**. For example, microwave heating of a mixture of phytic acid (P and C source)

with ammonium hydroxide or urea, amorphous sulfur, tetraethyl orthosilicate (TES), or boric acid, PN-Gc, PS-Gc, PSi-Gc, PB-Gc were fabricated, respectively (**Figure 5.1A-D**). By adding p-amino phenyl boronic acid to phytic acid prior to microwave heating, N-B-P triple-doped carbon material (PBN-Gc, **Figure 5.1E**) was obtained. It is worth mentioning that the irradiation time for the fabrication of these co-doped or triple-doped carbon materials, is different depending on the respective precursors. As for an example, the fabrication of N-P co-doped carbon material (PN-Gc) required 90 seconds of microwave heating, which is 50 seconds longer than that for only P doped carbon material. This is because the precursors for N, S, Si, and B are microwave transparent. Adding these materials to the original phytic acid increased the volume and/or amount of the materials that needs to be heated up.

Scheme 5.1. The General Scheme of P and other heteroatom co-doped carbon fabrication.



The Energy Dispersive X-ray Spectroscopy (EDS) measurements (**Figure 5.1**) of these co-doped materials demonstrate the co-existence of the P atoms and other corresponding heteroatoms, suggesting that this simple, rapid and energy efficient

approach successfully fabricated the co-doped and triple-doped carbon materials. A summary of the atomic composition of all the co-doped and triple doped carbon materials is given in **Table 5.1**. Moreover, similar to the P-doped carbon materials, the co-doped materials also showed sandwich-like structures as observed in the corresponding scanning electron microscopic (SEM) images (**Figure 5.1**), where a porous carbon network is covered by a wavy or wrinkled graphene like structure on both sides (top and bottom). However, the intensity of the wrinkles on the surface was different for all P co-doped catalysts and tri-doped catalysts. The wrinkles on the surface of co-doped catalysts become less intense for the materials containing B as a co-dopant (such as in PB-Gc and PBN-Gc).

Table 5.1. Atomic composition of different atoms in all co-doped carbon materials as determined from EDS measurements.

Catalysts	C atomic %	O atomic %	P atomic %	Heteroatom atomic %
PS-Gc	88.6	7.2	1.6	S: 2.6
PN-Gc	87.4	5.9	1.4	N: 5.3
PB-Gc	49.4	27.7	14.4	B: 8.3
PSi-Gc	83.2	13.5	1.4	Si: 2.0
PBN-Gc	35.0	42.7	9.5	B: 8.2 N: 3.3

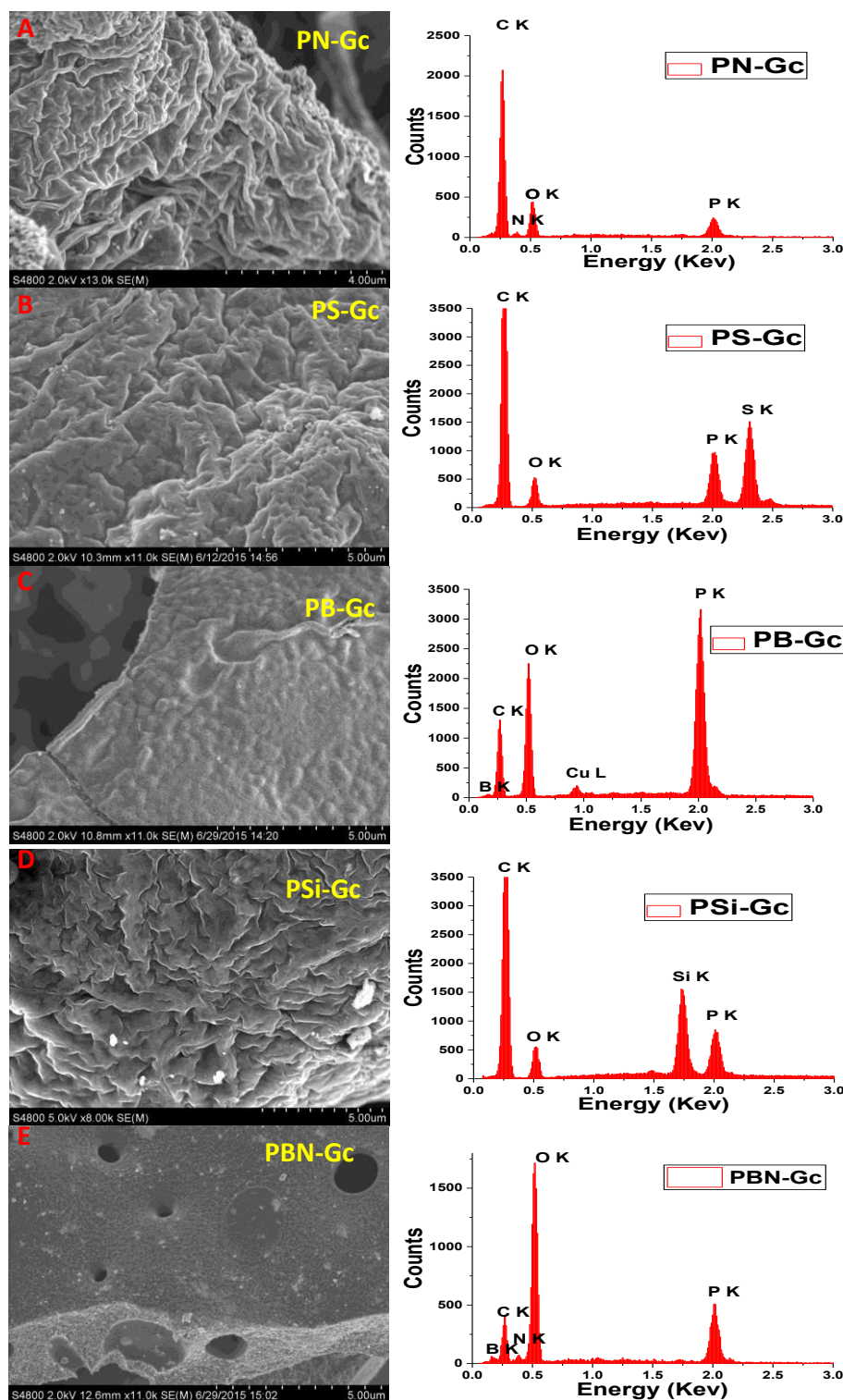


Figure 5.1. The SEM images and EDS spectra of (A) PN-Gc, (B) PS-Gc, (C)PB-Gc, (D)PSi-Gc, (E)PBN-Gc. The EDS spectra were taken by drop casting each of the co-doping carbon materials on a Cu tape.

The fabrication of carbon materials without heteroatom doping (non-doped carbon materials) or sole-doped with N, B, S, or Si using this microwave assisted rapid carbonization approach poses a challenge. This is because phytic acid, the microwave absorber cannot be included in the fabrication processes to intentionally exclude co-doping with P. It was reported that phytic acid can be synthesized with inositol and phosphoric acid.³⁴⁻³⁶ We wondered if inositol alone can be used as the carbon source for the microwave fabrication of non-doped and sole doped materials. However, inositol is microwave transparent, and hence carbonization via microwave heating does not occur even after 6 minutes of microwave irradiation. Since phosphoric acid is a strong microwave absorbent and a dehydrating agent, consequently, we tested if using inositol and phosphoric acid as C and P resources with similar microwave irradiation can lead to P doped carbon materials (P-Gc). Indeed, similar porous carbon monolith sandwiched between two pieces of wrinkled graphene like structures were obtained with a slightly longer microwave time (~50s) required for the fabrication. The existence of P atoms was confirmed by EDS analysis (**Figure 5.2A**). When the phosphoric acid was replaced with H₂SO₄, a carbonized porous material sandwiched with flat graphene-like structure was obtained instead of wrinkled structures, possibly due to the absence of P in the resulting material (**Figure 5.2B**). There was no detectable sulfur (S) in the material, therefore, a pure porous carbon material (called as Non doped-Gc) without heteroatom doping (except with a small amount of O) was successfully fabricated via microwave irradiation. To produce N-, B-, S- and Si-sole-doped porous carbon materials, we applied microwave irradiation to inositol and H₂SO₄ with a suitable dopant precursor, where inositol was the C resource, and H₂SO₄ as the dehydration agent and microwave absorber. With this strategy, we successfully

fabricated S doped carbon materials (S-Gc) using amorphous sulfur as a S dopant source. The EDS confirmed the presence of S (2.5% atomic) in the S-Gc materials. We also successfully fabricated sole-B doped carbon materials (B-Gc), indicated by the existence of B and non-detectable S signal in its EDS spectrum. This approach was extended to fabricate sole-N (N-Gc) and Si (Si-Gc) doped carbon materials even though a small amount of S impurity was found. A EDX characterization demonstrated there was $\sim 0.7\%$ atomic of S co-existed with N (3.93% atomic) and $\sim 1.78\%$ atomic of S co-existed with Si (15.6% atomic). Further optimization is needed to exclude S impurity to get sole-N or sole-Si doped carbon materials. Nevertheless, this rapid, simple and energy effective approach provides a powerful tool for the fabrication of various porous carbon materials with tailored electronic and geometric structures allowing us to explore wide variety of applications.

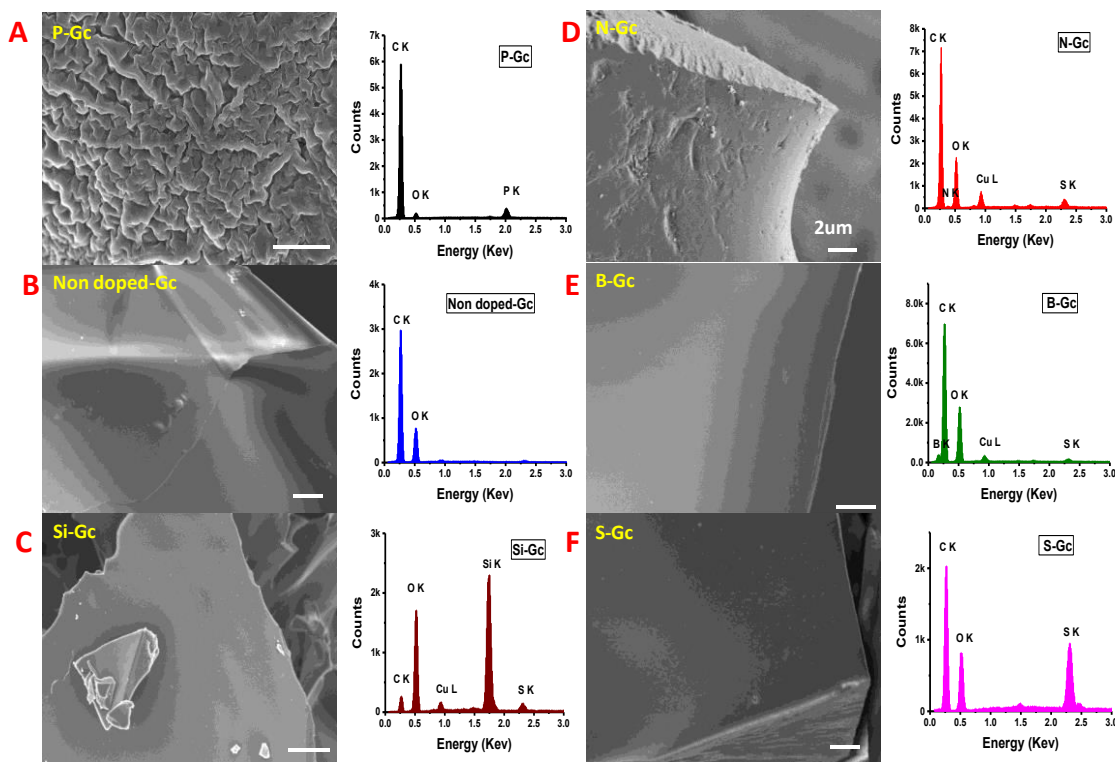


Figure 5.2. The SEM image and EDS spectrum of the PGc (A), Non doped-Gc (B), Si-Gc (C), N-Gc (D), B-Gc (E), S-Gc (F), which were fabricated by heating the mixture of inositol and phosphoric acid, inositol and sulfuric acid, inositol + sulfuric acid + tetraethyl

orthosilicate (TES), inositol + sulfuric acid + NH_4OH , inositol + sulfuric acid + boric acid, and inositol + sulfuric acid + amorphous sulfur in microwave, respectively. The scale bar shown in all SEM images is 2 μm .

To study the effect of P bond configuration (P-O and P-C bond type) in PGc catalysts on the reaction kinetics and pathways in oxygen reduction reaction (ORR), PGc, PGc-30 and PGc-180 were fabricated with the same procedures as described in previous chapter.²⁸ As we go from PGc, to PGc-30 and then PGc-180, the % P-O type of P decreased from 71.6% to 59.5%, while relatively, the % P-C type of P becomes prominent (from 28.4% to 40.5%), as confirmed from XPS and FTIR analysis.²⁸ In brief, as-purchased phytic acid solution (50 wt% in water) is directly subjected to a domestic microwave (Sanyo-EM-S9515W, 1100W, 2.45GHz) for 40s under ambient conditions. Due to the unique structure of phytic acid, where one phosphate group is attached to each carbon atom in the cyclohexane ring, it acts as both source of carbon and heteroatom (P) dopant without adding any external phosphorus source containing substance or material. During microwave treatment, the yellow/orange-brown phytic acid solution was first converted to a thick paste due to loss of water and then carbonized to a black solid mass. Moreover, sparks were observed in the microwave cavity in the last 15-20 seconds of microwave heating, which indicates that high temperatures for carbonization was achieved within the initial 20-25 seconds in microwave heating due to the strong microwave absorption capability of phytic acid. After microwave treatment, the product (PGc) was cleaned and dried before further characterization. To fabricate PGc-30 and PGc-180, the dried PGc powder in a porcelain dish was further treated with microwave irradiation for 10s with the full power of 1100 W for multiple times with a 15-minute of interval. In detail, to obtain PGc-30 and PGc-180, microwave treatment of PGc for 10s * 3 times and 10s * 18times was applied, respectively.

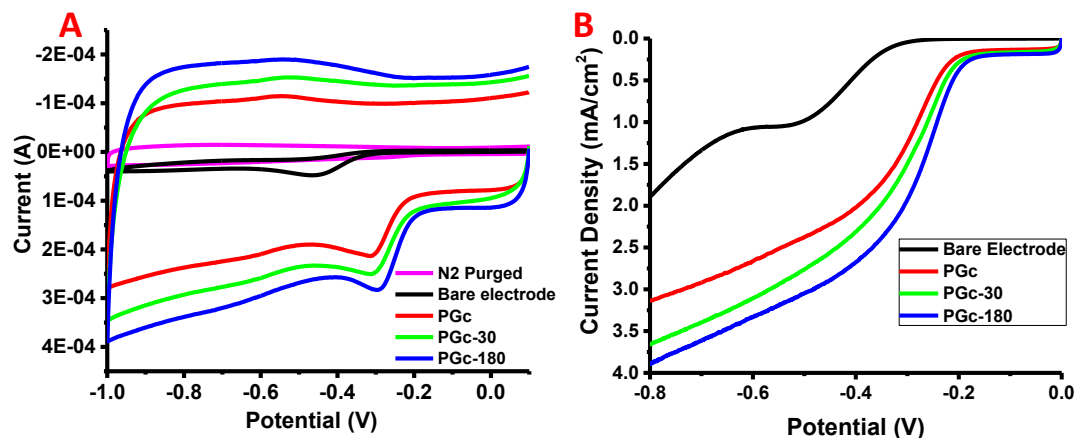


Figure 5.3. (A) is Cyclic voltammetry (CV) and (B) is Linear sweep voltammetry (LSV) curves of different phosphorus doped carbon catalyst in O₂ saturated 0.1M KOH. LSV measurements were performed using rotating ring disc (RRDE) electrode at 2000 rpm.

The ORR performance of PGc, PGc-30 and PGc-180 catalysts were evaluated by cyclic voltammetry (CV) and linear sweep voltammetry (LSV) in a 0.1M KOH solution saturated with oxygen and nitrogen gas. The same amount of materials for each catalysts was deposited onto a glassy carbon electrode for easy comparison. A bare glassy carbon electrode without any catalyst was used as a control. As shown in **Figure 5.3A**, a large reduction peak was observed in all the CV curves, while only in the O₂ saturated electrolyte but not the N₂, which suggests that O₂ is electro-catalytically reduced on the modified and bare electrodes. However, the PGc, PGc-30 and PGc-180 modified electrodes show much lower onset and peak potentials compared to the bare electrode (**Figure 5.3** and **Table 5.2**). Among all the PGc catalysts, the PGc-180 modified electrode shows the lowest peak potential (-0.292 V) and the highest current density (3.33 mA. cm⁻² at -0.60 V) in LSV. These result demonstrates that the PGc-180 catalyst shows the best catalytic ORR performance and is more kinetically facile toward ORR than the PGc-30 and PGc catalysts.

Table 5.2. Electrochemical parameters (onset potential, peak potential, current density, no of electrons, % HO₂⁻, rate constant k and Tafel slopes-b1 and -b2 of different catalysts for ORR estimated from CV and RRDE polarization curves in 0.1 m KOH solution. b1 and b2

are calculated at low and high current density region, respectively. All potentials were measured using Ag/AgCl as the reference electrode.

Catalyst	Calculated from CV		Calculated from RRDE		Calculated from LSV			
	Onset Potential (V)	Peak Potential (V)	n at -0.60 V	% HO_2^- at -0.60 V	J_k (Current density) mA. Cm^{-2}	k(rate constant) cm/s	Tafel Slope-b1	Tafel Slope-b2
Pt/C	-0.02	-0.227	3.90	4.21	5.69	0.0126	75.22	121.10
Bare electrode	-0.17	-0.466	2.84	58	1.07	0.0032	79.68	133.95
PGc	-0.11	-0.315	3.03	48.82	2.67	0.0076	103.09	158.85
PGc-30	-0.11	-0.313	3.25	37.69	3.11	0.0083	103.53	154.24
PGc-180	-0.08	-0.292	3.55	22.25	3.33	0.0081	96.78	160.89
PB-Gc	-0.16	-0.316	2.98	50.98	1.33	0.0039	68.44	125.99
PSi-Gc	-0.15	-0.307	3.09	45.33	0.739	0.0021	87.74	148.01
PS-Gc	-0.16	-0.314	3.27	37.30	1.46	0.0038	69.89	120.52
PN-Gc	-0.13	-0.294	3.58	21.1	2.19	0.0053	105.24	188.28

It is possible that the observed large current density in CV and LSV curves of PGc-180 is due to its higher effective surface area compared to the PGc and PGc 30. This is because prolonged microwave irradiating during PGc-180 fabrication may induce more carbon lost so that more porous structures may be formed. Brunauer-Emmett-Teller (BET) measurements and N_2 adsorption/desorption isotherm measurement of the PGc, PGc-30 and PGc-180 were performed to study their surface area and pore sizes. As shown in **Figure 5.4** and **Table 5.3**, it was observed that the surface area and the pore size of the PGc, PGc-30 and PGc-180 are very similar; suggesting that the additional microwave irradiation to synthesize PGc-30 and PGc-180 did not affect their morphologies. The similar surface area

and pore structures nullified the possibility of mass transport and diffusion effects of the electrolyte and O_2 from the observed high current density in its CV and LSV curves.

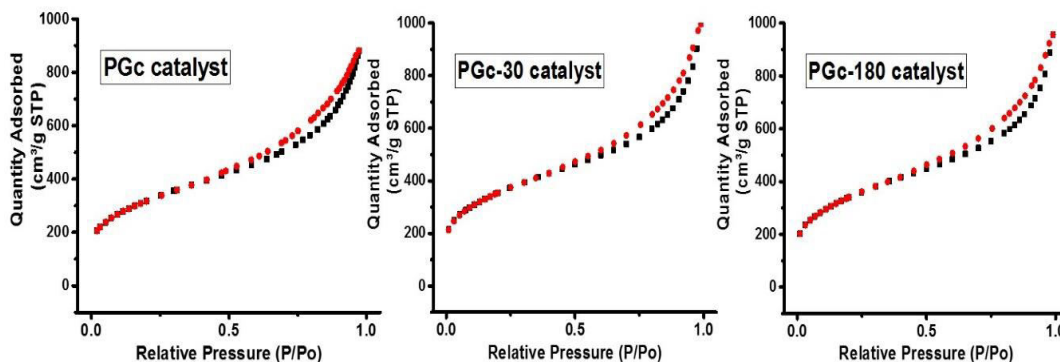


Figure 5.4. N_2 adsorption/desorption isotherms for different phosphorus doped carbon catalysts.

In ORR, oxygen can be reduced via a direct four-electron reduction pathway or a two-step, two-electron pathway. To understand the ORR pathway, a rotating ring disk electrode (RRDE) voltammetry was used to quantify the electron transfer number (n) and the formation of peroxide species (HO_2^-) during the ORR process on the PGc, PGc-30 and PGc-180 catalyst modified electrodes (**Figure 5.5D**). The electron transfer numbers (n) and % HO_2^- were calculated at -0.60 V based on the ring and disk currents of their respective RRDE voltammograms (see material characterization for details) and summarized in **Table 5.2**. The PGc modified electrode showed the lowest electron transfer number (3.0 at -0.60 V) and generated the highest percentage of peroxide (48.8 % at -0.60 V), suggesting that oxygen is being reduced via a combination of the two and four electron pathways. In contrast, the electron transfer number increased to 3.3 and 3.6 at -0.60 V for PGc-30 and PGc-180, respectively. At the same time, the % peroxide generated on PGc-30 and PGc-180 modified electrodes also decreased to 37.7 and 22.3 at -0.60 V, respectively. These

results suggest that the PGc-180 modified electrode catalyzes the oxygen reduction more toward four-electron pathway and generates the least amount of peroxide species.

Table 5.3. BET analysis summary of different phosphorus doped carbon catalysts.

Analysis	PGc	PGc-30	PGc-180
Single point surface area at P/Po = 0.3	1078.73 m ² /g	1052.11 m ² /g	994.19 m ² /g
BJH Adsorption cumulative volume of pores	1.021 cm ³ /g	1.387 cm ³ /g	1.336 cm ³ /g
BJH Desorption cumulative volume of pores	1.263 cm ³ /g	1.395 cm ³ /g	1.349 cm ³ /g
BJH Adsorption average pore diameter	7.03 nm	6.11 nm	5.89 nm
BJH Desorption average pore diameter	5.64 nm	5.94 nm	5.69 nm

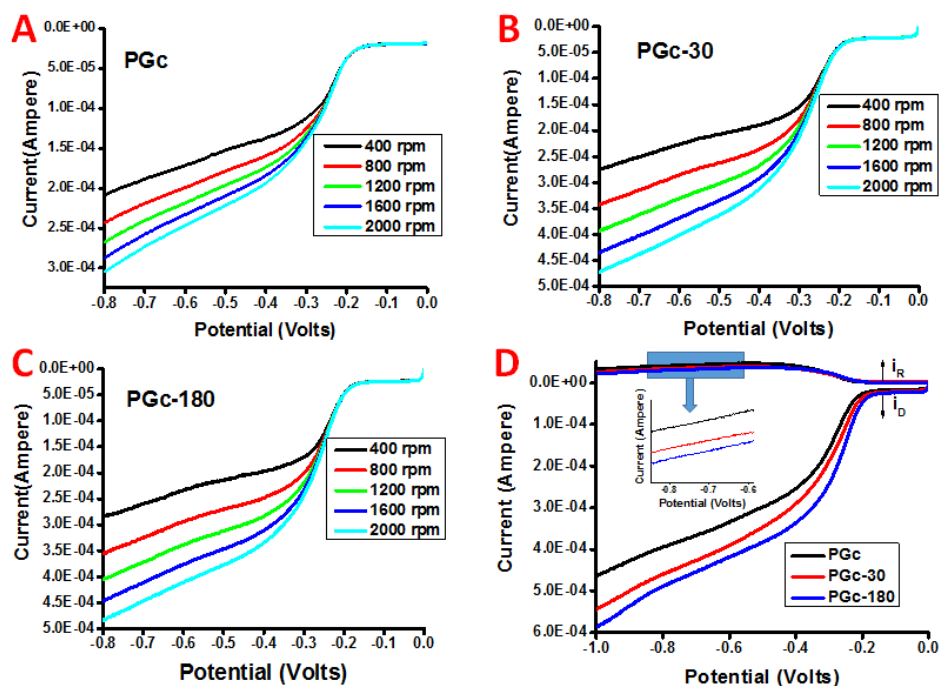


Figure 5.5. (A, B and C) are Linear sweep voltammetry (LSV) curves for PGc, PGc-30 and PGc-180 carbon catalysts, respectively, at different rotating speed in O₂ saturated 0.1M KOH solution at 10mV/s. (D) is RRDE curve comparison of PGc, PGc-30 and PGc-180 modified electrode at 2000 rpm in O₂ saturated 0.1M KOH solution at 10mV/s. Inset (D) is zoom out of ring current comparison of PGc, PGc-30 and PGc-180 catalysts.

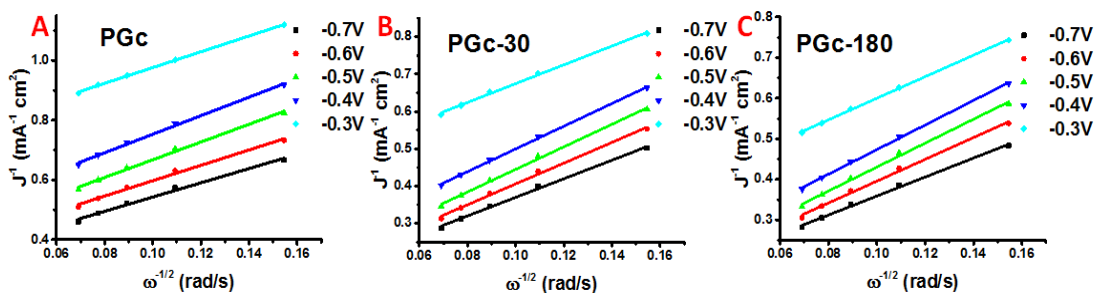


Figure 5.6. Koutecky-Levich (K-L) plots of PGc, PGc-30 and PGc-180 catalysts at different potentials, calculated from their respective LSV curves at different rotating speed (rpm).

To further study how the P bond type influences the electron transfer kinetics of the PGc catalysts involved in ORR, rotating disc electrode (RDE) measurements were performed in O₂ saturated 0.1M KOH solutions under various electrode rotating rates. As shown in **Figure 5.5** A-C, the current density increased with the rotation speed from 400 rpm to 2000 rpm due to the improved diffusion of the electrolyte and O₂. The kinetic current density (J_k) in ORR is then analyzed using the Koutecky-Levich (K-L) equation.³⁷ We plotted the Koutecky–Levich (K-L) plot (J^{-1} vs. $\omega^{-1/2}$) for PGc, PGc-30 and PGc-180 at various electrode potentials (**Figure 5.6**) to quantitatively analyze the kinetic current density (J_k) and ORR rate constant (k).³⁷ All the catalysts show linear and parallel K-L plots at all electrode potentials, suggesting that ORR followed a typical first order reaction kinetics with respect to the dissolved oxygen concentration. We calculated the rate constant k using the J_k from the slope of the K-L plot and then calculated the electron transfer number n from the RRDE measurement.⁸ From **Table 5.2**, we can see that all the PGc catalysts have similar rate constant (k) at potential -0.60V. We also plotted the Tafel plot (**Figure 5.7**) for all three catalysts, PGc, PGc-30 and PGc-180, from their LSV curves and the calculated slope summarized in **Table 5.2**. We found that all three catalysts have similar

Tafel slopes and thus the oxygen adsorption mechanism on the surface of these catalysts should be similar. When compared with the commercial Pt/C modified electrode, the slopes are different suggesting that the P doped carbon catalysts have a different oxygen adsorption mechanism on their surface.

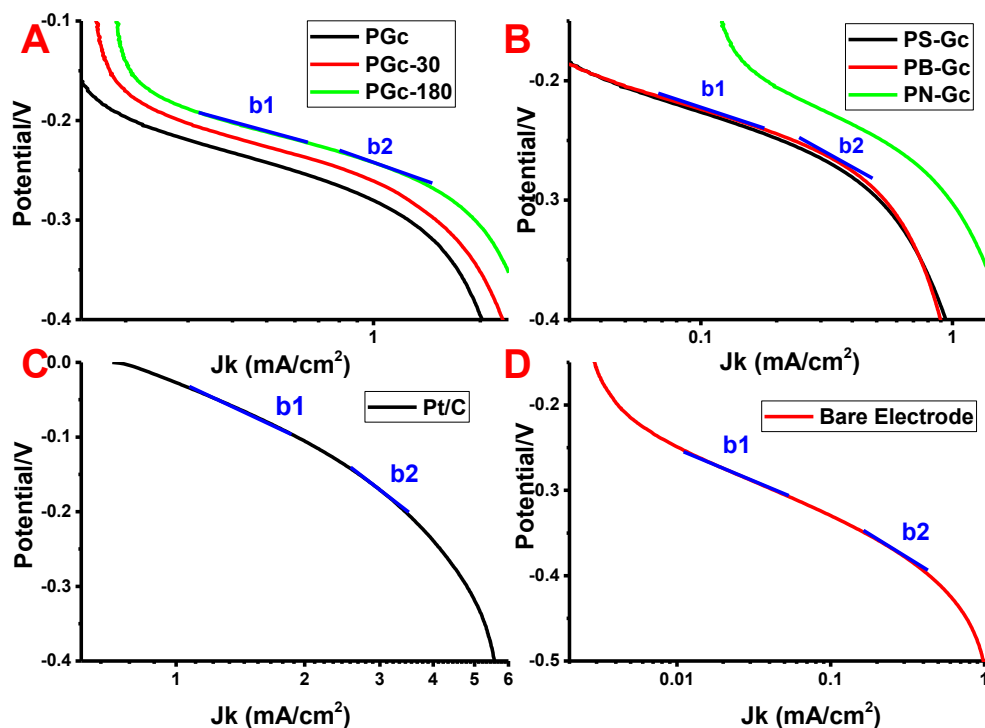


Figure 5.7. The Tafel plot and respective Tafel slopes (b1 and b2) of different P doped carbon catalysts (A), P and other heteroatoms co-doped carbon catalysts (B), Pt/C catalyst (C) and Bare electrode (D).

All these results demonstrated that phosphorus bond configuration in the PGc catalysts does not influence the oxygen adsorption mechanism and electrochemical ORR rate constant, but largely affects the ORR pathways. Our previous study in chapter-4 clearly demonstrated that the P bond configuration dramatically affected their catalytic aerobic oxidation performance.²⁸ However the effects are on the opposite trends: with higher concentration of P-C bonds, the PGc catalysts are more facile for ORR with 4e⁻ pathway, which are more desirable for fuel cell applications since the only product is water without

forming any hazardous peroxides. However, these catalysts show inferior catalytic performance for aerobic oxidation reactions. On the other hand, the PGc catalysts with higher concentration of P-O bonds facilitate the two-step, two-electron pathway of ORR where oxygen is reduced to peroxide as intermediates. These catalysts demonstrated excellent catalytic capability in aerobic oxidation of both primary and secondary alcohols. Based on these results, we conclude that catalysts with ORR of $2e^-$ pathway may be preferred for catalytic aerobic reactions. In these systems, the peroxide intermediates may have enough lifetime to oxidize the substrates.

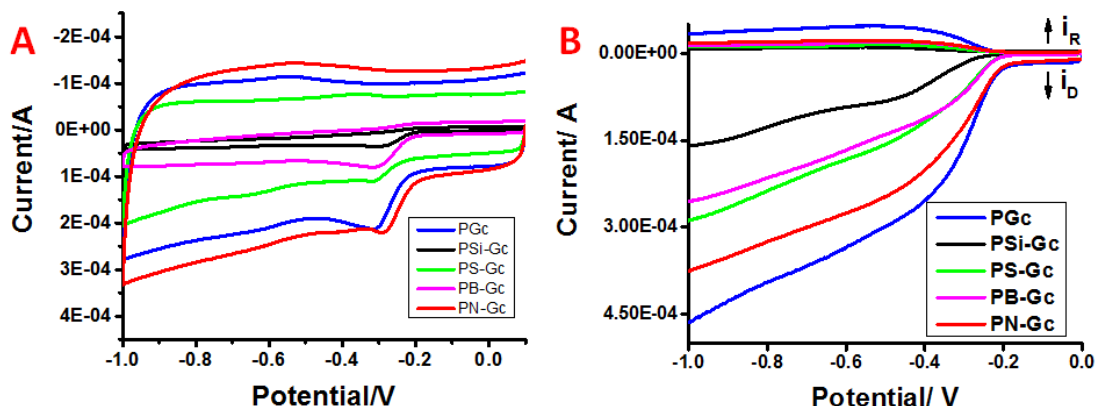


Figure 5.8. (A) Cyclic voltammetry (CV) and (B) is RRDE curves of different phosphorus (P) and other heteroatoms (B, N, S) co-doped carbon catalysts in O_2 saturated 0.1M KOH electrolyte. The RRDE experiment was performed at 2000 rpm using rotating ring disc (RRDE) electrode in O_2 saturated 0.1M KOH solution at 10 mV/s.

The ORR performance of co-doped carbon materials was also studied to determine if synergistic actions between the different heteroatoms exist to alter the ORR behavior. The results are shown in **Figure 5.8** and the measured electron transfer number, relative % HO_2^- and rate constants are summarized in **Table 5.2**. Among all the co-doped catalysts, PN-Gc catalyst shows the lowest onset potential (-0.128 V) and the highest electron transfer number (3.6). This performance is similar to that of PGc-180. It is worth mentioning that the extra 180 seconds of microwave treatment, which was required for the

fabrication of PGc-180, was not applied during the fabrication of PN-Gc catalyst. Therefore certain synergistic interactions between N and P exists, which leads the ORR performance more toward $4e^-$ pathway compared to P dopant alone as in PGc. While other co-doped materials, such as PB-Gc, PSi-Gc, and PS-Gc catalyze ORR more toward $2e^-$ electron pathway, which are opposite to those reported in literatures.^{18, 26} While more experiments will be performed to understand these interesting results, the preferable $2e^-$ ORR pathway indicates that these co-doped materials can be used as excellent metal free catalytic materials for aerobic oxidation reactions.

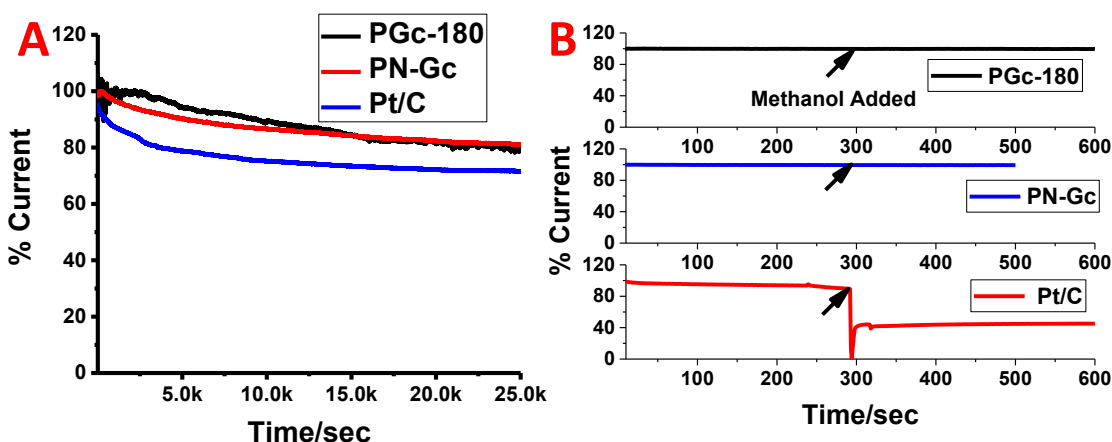


Figure 5.9. (A) is Durability testing of the Pt/C, PGc-180 and PN-Gc catalyst modified electrode for ~ 7 hours at -0.35V and 2000 rpm rotating speed. (B) is Methanol tolerance test of the Pt/C, PN-Gc and PGc-180 catalysts, where methanol was added at about 300 seconds of amperometric analysis at -0.35 V. All potentials were measured using Ag/AgCl as the reference electrode.

The relatively better ORR performance (such as lower onset and peak potentials, higher diffusion current density along with the preferable $4e^-$ pathway) of PGc-180 and PN-Gc catalysts make them promising cost effective metal free ORR catalysts for fuel cell applications. For practical applications, the catalysts require stability and durability along with good catalytic activity. To test the stability of PGc-180 and PN-Gc catalysts, we performed amperometric measurements of PGc-180 and PN-Gc catalysts, where the

amperometric current was being continuously measured for hours at constant potential of -0.35 V in 0.1M KOH. From **Figure 5.9**, we can see that after 7 hours, the amperometric current decreased by only 20% demonstrating the stability of PGc-180 and PN-Gc catalysts. Moreover, we have also performed the methanol cross over test for PGc-180 and PN-Gc catalysts to check its stability against methanol poisoning. In the presence of methanol, they were much more stable than that of the commercial Pt/C catalyst, where the catalytic activity was dramatically decreased in presence of methanol possibly due to the blockage of active sites on Pt nanoparticles by methanol adsorption.³⁸

5.3. Conclusions

In summary, it has been shown that a simple and scalable microwave assisted approach to synthesize P doped carbon materials can be easily extended for the synthesis of non-doped porous carbon materials, P and other heteroatoms (B, N, S and Si), dual-doped porous carbon material, and even triple-doped carbon material (such as B, N, and P doped). Extensive study on the ORR performance of these carbon materials as a function of P bond configuration and co-doping type reveals that P doped carbon material with higher P-C bond type shows better ORR performance. Out of all the co-doped carbon materials, PN co-doped carbon materials (PN-Gc) shows the best ORR performance among the others, prone more towards $4e^-$ pathway and less % HO_2^- generation. P doped carbon materials with higher P-O bond type and P co-doped with B, Si and S exhibit $2e^-$ ORR pathway. In the previous chapter-4, we clearly demonstrated the P doped carbon materials with higher P-O bond type has excellent catalytic performance in aerobic oxidation of benzyl alcohol to benzyl aldehyde.²⁸ We hypothesize that these B-, Si-, and S- co-doped P

carbon materials are possibly good catalytic materials as metal free catalytic materials for aerobic oxidation reactions, which are still under study.

5.4. Experimental Section

5.4.1. Synthesis of the PGc (Phosphorus doped graphitic carbon), PGc-30 and PGc-180:

The PGc, PGc-30 and PGc-180 was synthesized as per our previous work.²⁸ In brief, to synthesize PGc, 1.0 ml of Phytic acid (Sigma Aldrich, 50 w/w% in water) is placed in 35ml Pyrex glass vessel (CEM, #909036) and closed with Teflon lined cap (CEM, #909235). Then this assembly is placed in 500 mL beaker, covered with watch glass and heated in Domestic microwave (1100W, Sanyo-EM-S9515W, 2.45GHz) chamber by apply microwave irradiation for 40seconds. This procedure results into black carbonized material, which is left in fume hoods for few minutes to remove any gas that generated during microwave reaction. After that product is sonicated in ethanol solvent for 5 minute and filtered via 0.8uM polycarbonate filter paper (Millipore, ATTP 04700). The Product is washed and clean with water and ethanol (first wash with 250ml ethanol, then subsequent wash with 500ml water and final wash with 250ml ethanol). Dry this product in vacuum oven at ~110- 120C overnight before further use.

To synthesize PGc-30 and PGc-180, ~60mg of PGc powder was placed in small porcelain dish and cover with a piece of watch glass. Then this assembly is heated into domestic microwave chamber by applying microwave radiation for 10seconds for multiple times. For example in order to synthesize PGc-30 and PGc-180, 10sec microwave radiation was applied for 3 and 18 times, respectively. During each interval of applying microwave radiation, wait for 15 minutes to cool down the material.

5.4.2. Synthesis of P and other heteroatoms (N, B, S and Si) co-doped catalysts:

A 1.0 ml of phytic acid (w/w% in water) is mixed with other heteroatom source such that moles/atomic ratio of all heteroatom dopants stays 1:1 or in other words the mole ratio between phytic acid and heteroatom dopant molecules is 1:6, because each mole of phytic acid contains 6 moles of phosphate group. Here, we have shown the examples of P co-doped with B, N, S and Si. We can also synthesize P, B and N triple-doped carbon material.

P, N co-doped graphitic carbon (PN-Gc) material synthesis:

0.45 ml of ammonia solution was mixed with 1.0 ml of phytic acid in 35 ml Pyrex glass vessel. This vessel is closed with Teflon lined cap and the resultant mixture is heated in the domestic microwave for 90 sec. After that, the resultant product mixture is left in fume hood to cool down. Finally the product is filtered, washed and dried as described for PGc product.

P, S co-doped graphitic carbon (PS-Gc) material synthesis:

A 67.0 mg of amorphous sulfur powder was mixed with 1.0 ml of phytic acid in 35 ml Pyrex glass vessel by 5 to 10 minute of bath sonication. This vessel is closed with Teflon lined cap and the resultant mixture is heated in the domestic microwave for 42 sec. After that, the resultant product mixture is left in fume hood to cool down. Finally the product is filtered, washed and dried as described for PGc product.

P, B co-doped graphitic carbon (PB-Gc) material synthesis:

Aqueous solution of boric acid is prepared via dissolving 230.0 mg of boric acid into 5.0 ml deionized water in 35 ml Pyrex glass vessel. The boric acid solubility in water at room

temperature is very low, hence the sample is heated until the boric acid dissolves completely (around 10mins to reduce the total water volume approx. 2ml). After that, add 1.0 ml of phytic acid and closed with Teflon lined cap. The resultant mixture is heated in the domestic microwave for 150 sec. The resultant product mixture is left in fume hood to cool down. Finally the product is filtered, washed and dried as described for the PGc product.

P, B, N doped carbon (PBN-Gc) material synthesis:

Aqueous dispersion of 4-amino phenyl boric acid is prepared via dispersing it (~ 430 mg) into 1.0 ml deionized water in 35ml Pyrex glass vessel. This vessel is closed with Teflon lined cap, followed by short period of sonication to get a uniform suspension. After that, add 1.0 ml of phytic acid and the resultant mixture is heated in the domestic microwave for 150 sec. The resultant product mixture is left in fume hood to cool down. Finally the product is filtered, washed and dried as described for the PGc product.

P, Si doped carbon (PSi-Gc) material synthesis:

A 1.0 ml of Phytic acid and 0.125 ml of n-propyl triethoxysilane or tetraethyl orthosilicate is mixed in 35 ml Pyrex glass vessel. This vessel is closed with Teflon lined cap and then sonicated to get a uniform suspension. The resulting suspension is heated in the domestic microwave for 120 sec. The resulting product mixture is left in fume hood to cool down. Finally the product is filtered, washed and dried as described for the PGc product.

5.4.3. Synthesis of P-doped and Non-carbon catalysts using Inositol and phosphoric acid/sulfuric acid for control experiment.

In this experiment, 200.0 mg of inositol is mixed with concentrated phosphoric acid such that Inositol to phosphoric acid mole ratio become 1:6 on in other ward , carbon to phosphorus mole ratio become 1:1. This reaction mixture is heated in microwave chamber for 50 sec. After that, the resultant product mixture is left in fume hood to cool down. Finally the product is filtered, washed and dried as described for PGc product. A similar reaction was performed by replacing the concentrated phosphoric acid with sulfuric acid.

5.4.4. Synthesis of sole heteroatoms (B, N, S, or Si) doped carbon materials using Inositol as carbon (C) source.

To Synthesize different sole heteroatoms (-B, -N, -S, and -Si) doped carbon material, mixture of ~250 mg of myo-Inositol (act as C source), ~0.6 mL of concentrated sulfuric acid (act as strong dehydrating agent and microwave absorbing agent) and heteroatom dopant source is heated in the domestic microwave chamber for specific time. To synthesize B doped carbon, 500 mg of boric acid is used as B source and heated for 100s in microwave chamber. To synthesize N-doped carbon, 0.5 ml of concentrated NH_4OH added to above mixture and heated for 60 seconds. To synthesize S-doped carbon, ~67mg amorphous sulfur was added to above mixture and heated for 60 seconds. To synthesize Si-doped carbon, 0.25ml of tetraethyl orthosilicate was added to above mixture and heated for 150 seconds. The resultant product is left in fume hood to cool down and then filtered, washed and dried as described for PGc product.

5.4.5. Electrochemical Characterization:

The electrochemical characterization for all catalysts were conducted through a computer-controlled CHI 760C potentiostat with a three electrode cell, where a platinum wire and saturated Ag/AgCl electrode were used as the counter-electrode and the reference electrode, respectively. A glassy carbon (GC) electrode was used as a working electrode and was polished each time prior to use with alumina slurry. A catalyst slurry (2mg/ml) was prepared by sonicating (Bath sonicator, 60minutes) preweighed catalysts in DI water containing Nafion (0.5 wt %). A 20 μL of this dispersion was drop casted on glassy carbon electrode and allowed to dry under vacuum. The electrolyte (0.1 M KOH) was saturated with oxygen (O_2) by bubbling O_2 for 30 min prior to all experiments. Cyclic voltammetry experiments were typically performed at the scan rate of 50 mV s^{-1} in O_2 saturated 0.1 M KOH. For control experiment in oxygen reduction reaction, N_2 saturated 0.1 M KOH was used as an electrolyte while other conditions remain unchanged. A RDE experiments were performed using RRDE electrode (GC disc- 4mm diameter and Pt ring electrode) in O_2 saturated 0.1 M KOH with different rotation speed varying from 250 to 2500 rpm and 10 mV s^{-1} scan rate. The RRDE measurements were carried by RRDE electrode (GC disc and Pt ring electrode) in O_2 saturated 0.1 M KOH at 2000 rpm and 10 mV s^{-1} scan rate. The durability of catalysts were tested using the Chrono-amperometry experiment, where the current continuously measured for 25 000 s at -0.35 V potential. The rotation speed was set at 2000 rpm with continues maintaining oxygen flow to avoid any oxygen concentration effect. The methanol cross over effect for catalysts was also tested via amperometric experiment. Here in, the current was continuously measured for 700 s with same experiment condition as for durability testing, but 1 mL of methanol was added at around

300 s during the experiment. For standard comparison with Pt/C catalyst, the commercially available Pt/C (40 wt% Pt on Carbon, Johnson Matthey Corp.) electrode was also used and prepared similarly to other catalyst as mentioned above.

RDE and RRDE calculations:

The electron transfer number (n) and percentage of peroxide species (% HO_2^-) involved in the oxygen reduction reaction (ORR) was calculated by RRDE method. The n and percentage (%) of peroxide species (% HO_2^-) was determined based on ring and disc current, measured during RRDE experiment from the following equations.

$$n = \frac{(4 \times I_d)}{(I_d + \frac{I_r}{N})}$$

$$\% \text{HO}_2^- = \frac{(200 \times \frac{I_r}{N})}{(I_d + \frac{I_r}{N})}$$

Where I_d is the disc current I_r is the ring current in the RRDE, and N is the collection efficiency of the Pt ring electrode. N was determined to be 0.40 from measurement of reduction of $\text{K}_3\text{Fe}[\text{CN}]_6$.

In RDE method, the Koutecky-Levich (K-L) plot was obtained from LSV curves of a catalyst at different rotating speed. The kinetic parameters, such as kinetic current density (J_K), and rate constant (k) (D_0) in ORR performance is calculated using the Koutecky-Levich (K-L) equation.³⁷

$$\frac{1}{J} = \frac{1}{J_L} + \frac{1}{J_K} = \frac{1}{B\omega^{0.5}} + \frac{1}{J_K}$$

Where $B = 0.62nFC_0(D_0)^{2/3}\nu^{-1/6}$ and $J_K = nFkC_0$

Here, J is the measured current density, J_L and J_K are the diffusion limiting and kinetic limiting current densities, ω is the angular rotation rate of the disc electrode (rad/s), B is Levich constant, n is the number of electrons transferred in the oxygen reduction reaction, F is the Faraday constant ($F = 96485$ C/mol), D_0 is the diffusion coefficient (cm^2/s), ν is the viscosity of the electrolyte (cm^2/s), C_0 is the oxygen concentration (mol/cm^3) and k is the electron transfer rate constant. The values of k and J_K were obtained from the slope and y-intercept, respectively, of the K-L plots (or J^{-1} vs. $\omega^{-1/2}$) and using $C_0 = 1.2 \times 10^{-6}$ mol/cm^3 , $D_0 = 1.9 \times 10^{-5}$ cm^2/s and $\nu = 0.01$ cm^2/s in the equation.

5.4.6. Material Characterization:

The morphology of porous carbon materials were studied using the scanning electron microscopy (SEM, Hitachi S-4800). The sample for SEM imaging was prepared by simple drop casting of the sample on to carbon tape and allowed it for air dry. The heteroatom doping and atomic % of all elements in the porous carbon was analyzed by Energy Dispersive X-ray Spectroscopy (EDS) characterization. The sample for EDS imaging was prepared by simple drop casting of the slurry of a sample on to copper tape and allowed it for air dry. The surface area of catalysts was measured by Brunauer–Emmett–Teller (BET) and the pore size was measured using Nitrogen adsorption-desorption isotherm.

Surface Area and pore size measurements by BET and N_2 adsorption- desorption method:

The surface area and porosity of phosphorus doped carbon catalysts (PGc, PGc-30 and PGc-180) were analyzed nitrogen Brunauer–Emmett–Teller (BET) and nitrogen adsorption-desorption isotherms, respectively. The measurements are carried out at 77K using Micromeritics ASAP 2020. Each sample was dried by first at room temperature and then at 100C for overnight under vacuum, prior to measurement. The specific surface area was calculated using BET method and pore size was calculated using BJH adsorption-desorption analysis.

5.5. References

1. Hu, H. W.; Xin, J. H.; Hu, H.; Wang, X. W.; Kong, Y. Y. Metal-free graphene-based catalyst-Insight into the catalytic activity: A short review. *Applied Catalysis a-General* 2015, 492, 1-9.
2. Cheon, J. Y.; Kim, J. H.; Kim, J. H.; Goddeti, K. C.; Park, J. Y.; Joo, S. H. Intrinsic relationship between enhanced oxygen reduction reaction activity and nanoscale work function of doped carbons. *J. Am. Chem. Soc.* 2014, 136, 8875-8.
3. Wang, H.; Zhou, Y.; Wu, D.; Liao, L.; Zhao, S.; Peng, H.; Liu, Z. Synthesis of boron-doped graphene monolayers using the sole solid feedstock by chemical vapor deposition. *Small* 2013, 9, 1316-20.
4. Meng, Y. Y.; Voiry, D.; Goswami, A.; Zou, X. X.; Huang, X. X.; Chhowalla, M.; Liu, Z. W.; Asefa, T. N-, O-, and S-Tridoped Nanoporous Carbons as Selective Catalysts for Oxygen Reduction and Alcohol Oxidation Reactions. *J. Am. Chem. Soc.* 2014, 136, 13554-13557.
5. Yang, D. S.; Bhattacharjya, D.; Inamdar, S.; Park, J.; Yu, J. S. Phosphorus-Doped Ordered Mesoporous Carbons with Different Lengths as Efficient Metal-Free Electrocatalysts for Oxygen Reduction Reaction in Alkaline Media. *J. Am. Chem. Soc.* 2012, 134, 16127-16130.
6. Zhang, C.; Mahmood, N.; Yin, H.; Liu, F.; Hou, Y. Synthesis of phosphorus-doped graphene and its multifunctional applications for oxygen reduction reaction and lithium ion batteries. *Adv. Mater.* 2013, 25, 4932-7.
7. Zhang, X. L.; Lu, Z. S.; Fu, Z. M.; Tang, Y. A.; Ma, D. W.; Yang, Z. X. The mechanisms of oxygen reduction reaction on phosphorus doped graphene: A first-principles study. *J. Power Sources* 2015, 276, 222-229.
8. Patel, M.; Feng, W.; Savaram, K.; Khoshi, M. R.; Huang, R.; Sun, J.; Rabie, E.; Flach, C.; Mendelsohn, R.; Garfunkel, E.; He, H. Microwave Enabled One-Pot, One-Step Fabrication and Nitrogen Doping of Holey Graphene Oxide for Catalytic Applications. *Small* 2015, 11, 3358-68.

9. Li, R.; Wei, Z. D.; Gou, X. L. Nitrogen and Phosphorus Dual-Doped Graphene/Carbon Nanosheets as Bifunctional Electrocatalysts for Oxygen Reduction and Evolution. *Acs Catalysis* 2015, 5, 4133-4142.
10. Liu, J.; Song, P.; Ning, Z. G.; Xu, W. L. Recent Advances in Heteroatom-Doped Metal-Free Electrocatalysts for Highly Efficient Oxygen Reduction Reaction. *Electrocatalysis* 2015, 6, 132-147.
11. Liu, Z. W.; Fu, X.; Li, M.; Wang, F.; Wang, Q. D.; Kang, G. J.; Peng, F. Novel silicon-doped, silicon and nitrogen-codoped carbon nanomaterials with high activity for the oxygen reduction reaction in alkaline medium. *Journal of Materials Chemistry A* 2015, 3, 3289-3293.
12. Qiao, X. C.; Liao, S. J.; You, C. H.; Chen, R. Phosphorus and Nitrogen Dual Doped and Simultaneously Reduced Graphene Oxide with High Surface Area as Efficient Metal-Free Electrocatalyst for Oxygen Reduction. *Catalysts* 2015, 5, 981-991.
13. Shi, Q. Q.; Peng, F.; Liao, S. X.; Wang, H. J.; Yu, H.; Liu, Z. W.; Zhang, B. S.; Su, D. S. Sulfur and nitrogen co-doped carbon nanotubes for enhancing electrochemical oxygen reduction activity in acidic and alkaline media. *Journal of Materials Chemistry A* 2013, 1, 14853-14857.
14. Sun, X.; Xu, J.; Ding, Y.; Zhang, B.; Feng, Z.; Su, D. S. The Effect of Different Phosphorus Chemical States on an Onion-like Carbon Surface for the Oxygen Reduction Reaction. *ChemSusChem* 2015, 8, 2872-6.
15. Tian, G. L.; Zhang, Q.; Zhang, B. S.; Jin, Y. G.; Huang, J. Q.; Su, D. S.; Wei, F. Toward Full Exposure of "Active Sites": Nanocarbon Electrocatalyst with Surface Enriched Nitrogen for Superior Oxygen Reduction and Evolution Reactivity. *Adv. Funct. Mater.* 2014, 24, 5956-5961.
16. Wang, D. W.; Su, D. S. Heterogeneous nanocarbon materials for oxygen reduction reaction. *Energy & Environmental Science* 2014, 7, 576-591.
17. Shin, H. J.; Choi, W. M.; Choi, D.; Han, G. H.; Yoon, S. M.; Park, H. K.; Kim, S. W.; Jin, Y. W.; Lee, S. Y.; Kim, J. M.; Choi, J. Y.; Lee, Y. H. Control of electronic structure of graphene by various dopants and their effects on a nanogenerator. *J. Am. Chem. Soc.* 2010, 132, 15603-9.
18. Choi, C. H.; Park, S. H.; Woo, S. I. Binary and ternary doping of nitrogen, boron, and phosphorus into carbon for enhancing electrochemical oxygen reduction activity. *ACS Nano* 2012, 6, 7084-91.
19. Choi, C. H.; Park, S. H.; Woo, S. I. Phosphorus-nitrogen dual doped carbon as an effective catalyst for oxygen reduction reaction in acidic media: effects of the amount of P-doping on the physical and electrochemical properties of carbon. *J. Mater. Chem.* 2012, 22, 12107-12115.
20. Kong, X. K.; Chen, C. L.; Chen, Q. W. Doped graphene for metal-free catalysis. *Chem. Soc. Rev.* 2014, 43, 2841-57.
21. Latorre-Sanchez, M.; Primo, A.; Garcia, H. P-doped graphene obtained by pyrolysis of modified alginate as a photocatalyst for hydrogen generation from water-methanol mixtures. *Angew. Chem. Int. Ed. Engl.* 2013, 52, 11813-6.
22. Hulicova-Jurcakova, D.; Puziy, A. M.; Poddubnaya, O. I.; Suarez-Garcia, F.; Tascon, J. M.; Lu, G. Q. Highly stable performance of supercapacitors from phosphorus-enriched carbons. *J. Am. Chem. Soc.* 2009, 131, 5026-7.

23. Puziy, A. M.; Poddubnaya, O. I.; Socha, R. P.; Gurgul, J.; Wisniewski, M. XPS and NMR studies of phosphoric acid activated carbons. *Carbon* 2008, 46, 2113-2123.
24. Zhao, X. C.; Wang, A. Q.; Yan, J. W.; Sun, G. Q.; Sun, L. X.; Zhang, T. Synthesis and Electrochemical Performance of Heteroatom-Incorporated Ordered Mesoporous Carbons. *Chem. Mater.* 2010, 22, 5463-5473.
25. Nasini, U. B.; Bairi, V. G.; Ramasahayam, S. K.; Bourdo, S. E.; Viswanathan, T.; Shaikh, A. U. Oxygen Reduction Reaction Studies of Phosphorus and Nitrogen Co-Doped Mesoporous Carbon Synthesized via Microwave Technique. *Chemelectrochem* 2014, 1, 573-579.
26. Ramasahayam, S. K.; Nasini, U. B.; Bairi, V.; Shaikh, A. U.; Viswanathan, T. Microwave assisted synthesis and characterization of silicon and phosphorous co-doped carbon as an electrocatalyst for oxygen reduction reaction. *Rsc Advances* 2014, 4, 6306-6313.
27. Guiotoku, M.; Rambo, C. R.; Hotza, D. Charcoal produced from cellulosic raw materials by microwave-assisted hydrothermal carbonization. *J. Therm. Anal. Calorim.* 2014, 117, 269-275.
28. Patel, M.; Luo, F.; Khoshi, M. R.; Rabie, E.; Zhang, Q.; Flach, C.; Mendelsohn, R.; Garfunkel, E.; Szostak, M.; He, H. P-Doped Porous Carbon as Metal Free Catalysts for Selective Aerobic Oxidation with an Unexpected Mechanism. *ACS Nano* 2015, 10, 2305-2315.
29. Duan, J. J.; Chen, S.; Jaroniec, M.; Qiao, S. Z. Heteroatom-Doped Graphene-Based Materials for Energy-Relevant Electrocatalytic Processes. *Acs Catalysis* 2015, 5, 5207-5234.
30. Joshi, R. K.; Carbone, P.; Wang, F. C.; Kravets, V. G.; Su, Y.; Grigorieva, I. V.; Wu, H. A.; Geim, A. K.; Nair, R. R. Precise and Ultrafast Molecular Sieving Through Graphene Oxide Membranes. *Science* 2014, 343, 752-754.
31. Nasini, U. B.; Bairi, V. G.; Ramasahayam, S. K.; Bourdo, S. E.; Viswanathan, T.; Shaikh, A. U. Phosphorous and nitrogen dual heteroatom doped mesoporous carbon synthesized via microwave method for supercapacitor application. *J. Power Sources* 2014, 250, 257-265.
32. Zhang, J.; Zhao, Z.; Xia, Z.; Dai, L. A metal-free bifunctional electrocatalyst for oxygen reduction and oxygen evolution reactions. *Nat Nanotechnol* 2015, 10, 444-52.
33. Primo, A.; Neatu, F.; Florea, M.; Parvulescu, V.; Garcia, H. Graphenes in the absence of metals as carbocatalysts for selective acetylene hydrogenation and alkene hydrogenation. *Nat Commun* 2014, 5, 5291.
34. Mitsuhashi, N.; Ohnishi, M.; Sekiguchi, Y.; Kwon, Y. U.; Chang, Y. T.; Chung, S. K.; Inoue, Y.; Reid, R. J.; Yagisawa, H.; Mimura, T. Phytic acid synthesis and vacuolar accumulation in suspension-cultured cells of *Catharanthus roseus* induced by high concentration of inorganic phosphate and cations. *Plant Physiol* 2005, 138, 1607-14.
35. Raboy, V. The ABCs of low-phytate crops. *Nat. Biotechnol.* 2007, 25, 874-5.
36. Anderson, R. Synthesis of phytic acid. *J. Biol. Chem.* 1920, 43, 117-128.
37. Liu, R.; Wu, D.; Feng, X.; Mullen, K. Nitrogen-doped ordered mesoporous graphitic arrays with high electrocatalytic activity for oxygen reduction. *Angew. Chem. Int. Ed. Engl.* 2010, 49, 2565-9.

38. Zhang, Y.; Huang, Q. H.; Zou, Z. Q.; Yang, J. F.; Vogel, W.; Yang, H. Enhanced Durability of Au Cluster Decorated Pt Nanoparticles for the Oxygen Reduction Reaction. *Journal of Physical Chemistry C* 2010, 114, 6860-6868.

Chapter 6. Phosphorus and Sulfur Dual-Doped Graphitic Porous Carbon Metal-Free Catalysts for Aerobic Oxidation Reactions: Enhanced Catalytic Activity and Active Sites.

6.1. Introduction

In the drive towards green and sustainable chemistry, using molecule oxygen as the sole oxidant and metal free carbon-based materials as eco-friendly, abundant, and readily available heterogeneous catalysts are attractive for chemical synthesis.¹⁻⁹ Among these, carbon-based materials such as graphene and porous graphitic materials are actively being pursued recently due to their large surface area, tunable electronic and surface properties, and most importantly, the easy accessibility of a large amount of materials without metal contamination. Since the pioneering work by Bielawski's group using graphene oxide (GO, oxygen doped graphene) as a catalyst for chemoselective oxidation of alcohols under mild conditions,¹⁰ other heteroatoms, such as N-doped, B-doped and N,B-codoped graphitic carbon materials have been exploited to oxidize petroleum molecules to value-added compounds.^{6, 7, 9, 11} Recently, we have also exploited P-doped graphitic porous carbon materials as metal-free catalysts for aerobic oxidation of benzyl alcohol.¹² It can selectively oxidize both primary and secondary benzyl alcohols to the corresponding aldehydes or ketones. This is different from N-doped graphitic materials, which can only oxidize primary benzyl alcohol to an aldehyde.¹¹ We attributed this difference to the "protruding out" structure of P, compared to the planar structure of N in the carbon matrix, which minimized the steric hindrance for secondary alcohol to access the catalytic centers. Further, to our surprise, the P-doped carbon materials with higher work functions shows

higher capability in catalyzing aerobic oxidation reactions, which is opposite to the trend when N-doped carbon materials were used as metal-free catalysts for aerobic oxidation reactions^{11, 13} and electrochemical catalysts for ORR.¹⁴ The P-doped materials also exhibit a different selectivity rule for electron rich and electron deficient molecules compared to other heteroatom-doped carbon materials.^{11, 15} The mechanistic study demonstrated that even though molecular oxygen is not involved in the first step of aerobic oxidation of benzyl alcohol, it is required to regenerate the catalytic sites on the P-doped carbon materials. The unique and unexpected catalytic pathway endows the P-doped carbon materials with not only good catalytic efficiency but also recyclability, which is a major challenge in GO-based catalysis.^{16, 17} However, we found that high catalysts loading is still required to reach the desired high conversion and yield.¹⁸ This is possible due to the limited catalytic centers, and with the currently available method, it is difficult to further increase the loading of P doping.

It has been widely accepted and experimentally demonstrated that co-doping multiple heteroatoms could further improve the catalytic performance of carbon catalyst in ORR due to the synergistic effects from multiple doping heteroatoms.^{15, 19-21} Since both ORR and aerobic oxidation require activation of inert molecule O₂, it has been assumed that the efficient catalyst for ORR might be good catalysts for aerobic oxidation reactions. Compared to ORR, studies that use doped and/or co-doped carbon materials as catalysts for selective organic synthesis are very limited.²² This is possibly due to the lack of generic access for large scale synthesis of the novel multiple heteroatom-doped graphene-based materials, which have fine-tuned molecular, electronic and geometric structures for a carbon catalyst with high performance. In our previous reports^{12, 23}, we have demonstrated

that by combining the unique heating properties of microwave with the strong microwave absorption power of phytic acid, a biomass molecule present in plant tissue such as brans of grain and seed, P-doped porous carbon can be directly synthesized from the phytic acid by very short microwave irradiation (40 seconds). In addition to that, it has been also demonstrated that by simply mixing the other heteroatom (N, S, B) sources (such as ammonium hydroxide -N source, amorphous sulfur -S source, boric acid -B source) with phytic acid prior to microwave heating, we can also synthesize various P-coped porous carbon materials. This as synthesized co-doped porous carbon materials such as P-N, P-S, and P-B co-doped porous carbon materials, denoted as PN-Gc, PS-Gc, and PB-Gc, respectively.

By taking the advantage of this simple technique to synthesize these co-doped carbon materials, in this chapter, we have compared the catalytic performance of these co-doped carbon catalysts (PN-Gc, PS-Gc and PB-Gc) for benzylic alcohol oxidation and found that PS-Gc catalyst shows the most improved catalytic performance compared to single doped (S-Gc and P-Gc) and co-doped carbon catalysts (PB-Gc and PN-Gc). The detailed characterization and control experiments were performed to gain understanding about the catalytic centers in the PS-Gc catalyst and their mechanism to catalyze the benzylic alcohol oxidation reaction.

6.2. Results and Discussion

For large scale synthesis of valuable chemicals in industry, solvent free reactions are highly preferred to eliminate additional cost related to the use and handling of reaction solvents. Therefore, our catalytic studies of these P-codoped carbon materials were performed in solvent-free reaction conditions. Firstly, we have compared the catalytic

efficiency of the various as synthesized P co-doped porous carbon catalysts for selective oxidation of benzyl alcohol to benzaldehyde at 80°C for 48 hours. As we can see from the **Table 6.1**, benzyl alcohol oxidation cannot proceed efficiently in the absence of a catalyst (entry 1), in the presence of carbon-based catalysts without heteroatom doping (rGO or non-doped carbon), and or with heteroatom S source (amorphous sulfur for PS-Gc synthesis). The PS-Gc and PN-Gc show much improved catalytic efficiency (~54% and ~35% conversion, respectively) than P-Gc (~21% conversion). Surprisingly, codoping of B with P (PB-Gc) deteriorates the catalytic activity of P-Gc to ~4% conversion for benzyl alcohol oxidation. This may be due to the formation of P-B type functionalities during B doping, which destroys the catalytic sites similar the scenario in N, B-codoped carbon catalysts²⁴. It is also possible that the electron deficient nature of B makes the catalyst less electron rich and deactivates the catalytic activity of catalytic centers in P-Gc. Based on the above results it was concluded that PS-Gc shows the most improved catalytic performance toward benzyl alcohol oxidation among all the P co-doped carbon catalysts (PS-Gc, PN-Gc, and PB-Gc). To know whether the improved catalytic performance of PS-Gc is due to a synergistic effect or an additive effect of two different heteroatoms (P and S), we have synthesized the P-doped carbon (P-Gc) and S-doped carbon (S-Gc) and tested their catalytic performance toward benzyl alcohol oxidation. From the results listed in **Table 6.1**, it is clear that PS-Gc codoped carbon catalysts shows higher conversion (~54%) than the addition of the conversion from P and S only doped carbon catalysis (P-Gc (~21%) and S-Gc (18%)), which suggests that the P and S heteroatom doping in PS-Gc imparts addition as well as synergistic effects. Because of the unique and enhanced catalytic effect of PS-Gc catalyst, in this chapter we will focus on the studies of the unique structure of

PS-Gc and its catalytic performance in various alcohol oxidation. Especially, most efforts were devoted to understanding its catalytic mechanism and finally to identify the catalyst sites of this catalyst.

Table 6.1. Comparison of various heteroatom-doped porous carbon for its catalytic efficiency towards selective benzylic alcohol oxidation^a

entry	Catalysts	% Conversion	% Yield	% Selectivity	TON ($\times 10^{-2}$)
1	--	ND	ND	--	0
2	Non doped carbon	4.17	--	97.0	0.08
3	rGO	3.70	--	96.0	0.08
4	Amorphous sulfur ^b	3.45	3.29	51.4	0.07
5	P-Gc ¹²	21.2	20.8	95.6	0.43
6	S-Gc	18.3	14.5	86.8	0.37
7	PS-Gc	53.8	47.6	87.7	1.09
8	PN-Gc	35.4	35.5	97.2	0.72
9	PB-Gc	3.8	3.9	94.7	0.08

Reaction conditions: ^a0.1 mL benzyl alcohol (~1 mmol), 50 mg catalyst, 1 atm O₂, 80 °C, 48 hours. ^b8 mg of amorphous sulfur was used. % conversion to the alcohol, % yield to the products (benzaldehyde and benzoic acid) and % selectivity on benzaldehyde calculated using ¹H NMR. ¹² is referred to numbered reference in the text. “ND” = not detectable (conversion < 1%). The turnover number (TON) was calculated as a ratio of the (mol of the oxidized substrate) / (mass of catalyst).

First, the physical and chemical properties of PS-Gc were characterized by scanning electron microscope (SEM), Energy Dispersive X-ray Spectroscopy (EDS), X-ray photoelectron spectroscopy (XPS), FT-IR and Raman spectroscopy. A SEM image of PS-Gc (**Figure 6.1A**) shows similar geometric structure as the P-Gc materials. Two highly wrinkled graphene-like sheets sandwiched a porous carbon monolith (**Figure 6.1A**). The wrinkled structures possibly result from the large atomic size of both P and S heteroatoms compared to C atom which induces local geometrical distortion in the carbon network.

Furthermore, XPS and EDS analysis (**Figure 6.1B**, 6.2A, 6.3A and **Table 6.2**) of PS-Gc confirms that PS-Gc contains ~2.5 atomic % P and ~6 atomic% S doping in its carbon matrix.

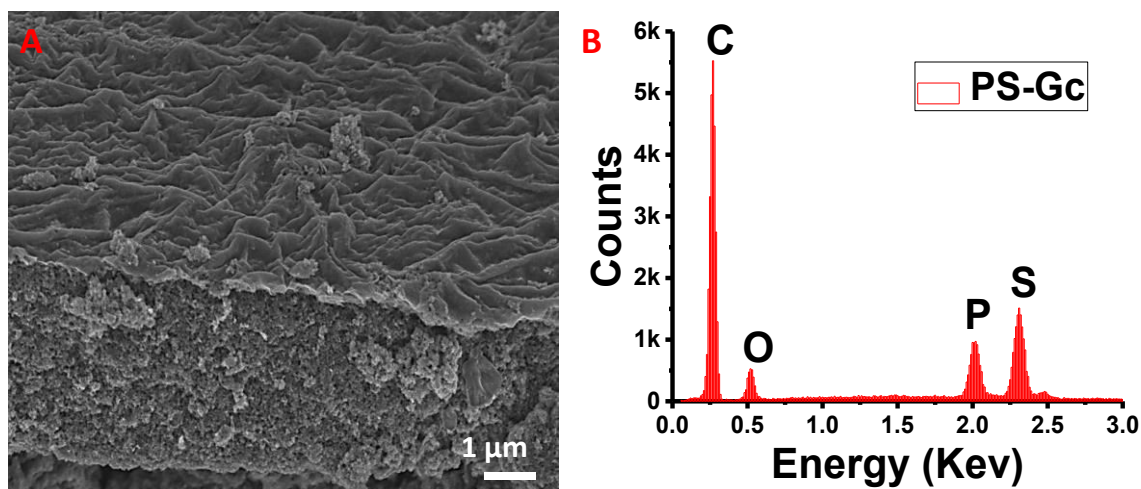


Figure 6.1. (A) is scanning electron microscopic (SEM) of PS-Gc and (B) Energy Dispersive X-ray Spectra (EDS) of PS-Gc.

Table 6.2. Calculated atomic % of C, O, P and S from EDS and XPS analysis.

Catalyst	C (atomic %)		O (atomic %)		P (atomic %)		S (atomic %)	
	EDS	XPS	EDS	XPS	EDS	XPS	EDS	XPS
PS-Gc	78.00	74.27	12.72	18.14	2.20	2.76	6.97	4.85
PS-Gc-used	84.33	82.96	10.40	11.42	1.97	1.74	3.31	3.86
PS-Gc-TA	86.51	81.21	6.30	11.01	1.39	1.82	5.81	5.97
PS-Gc-TA-used	85.68	85.68	7.57	10.03	1.41	1.50	5.35	6.19

Table 6.3. Calculated atomic % different type of O present in catalyst by XPS analysis.

Catalysts	O atomic %			
	C/P/S=O (~530.9 eV)	C/P/S-O-C (~532.5 eV)	C/P/S-O-H (~533.2 eV)	COOH/water (~535.1 eV)
PS-Gc	3.83	7.09	5.61	1.48
PS-Gc-used	2.59	3.72	4.23	0.82
PS-Gc-TA	2.86	1.95	5.42	0.72
PS-Gc-TA-used	2.88	1.25	5.03	0.85

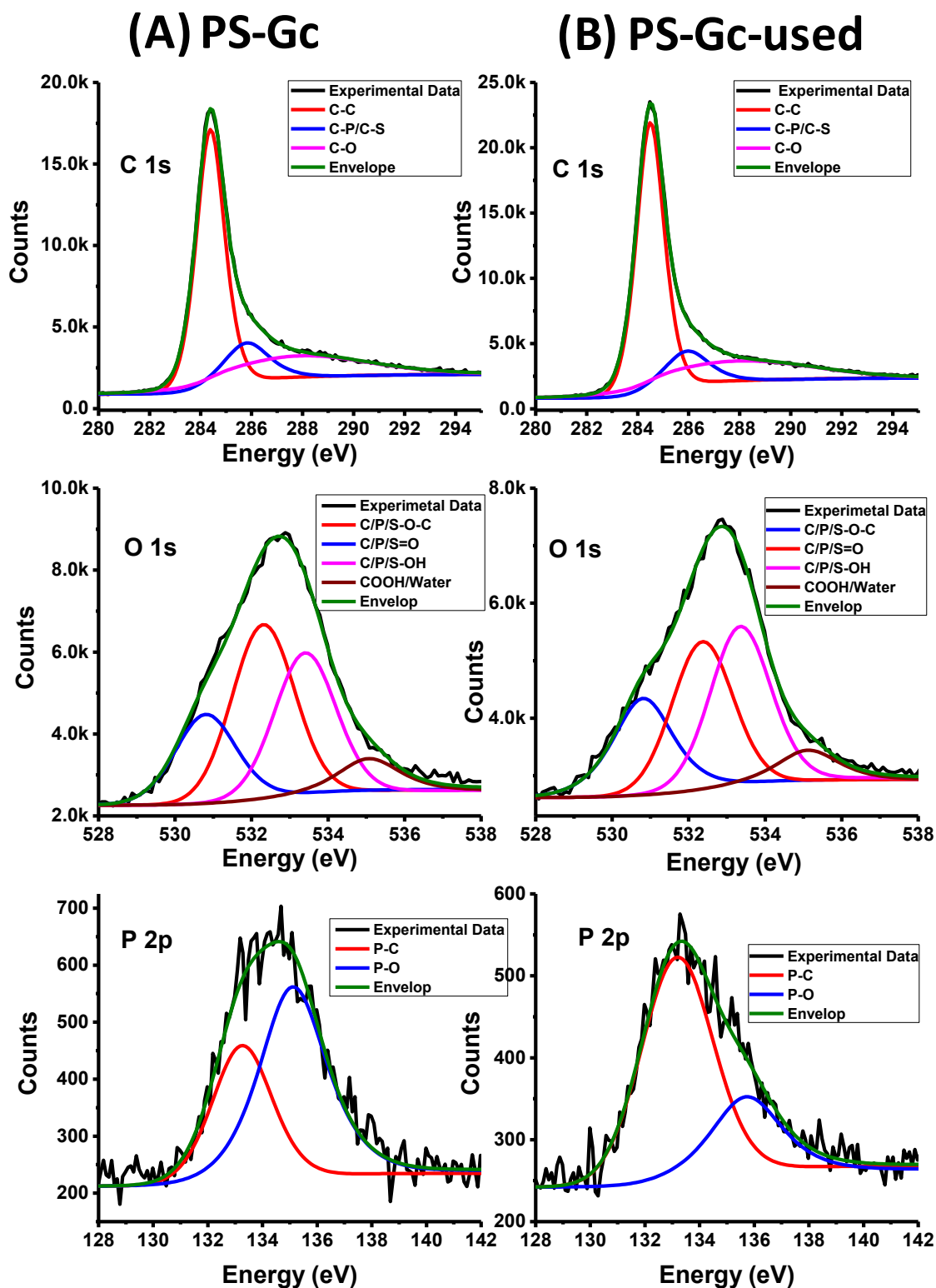


Figure 6.2. C1s, O 1s and P2p XPS peak deconvolution of PS-Gc catalyst (A) and PS-Gc-used catalyst (B).

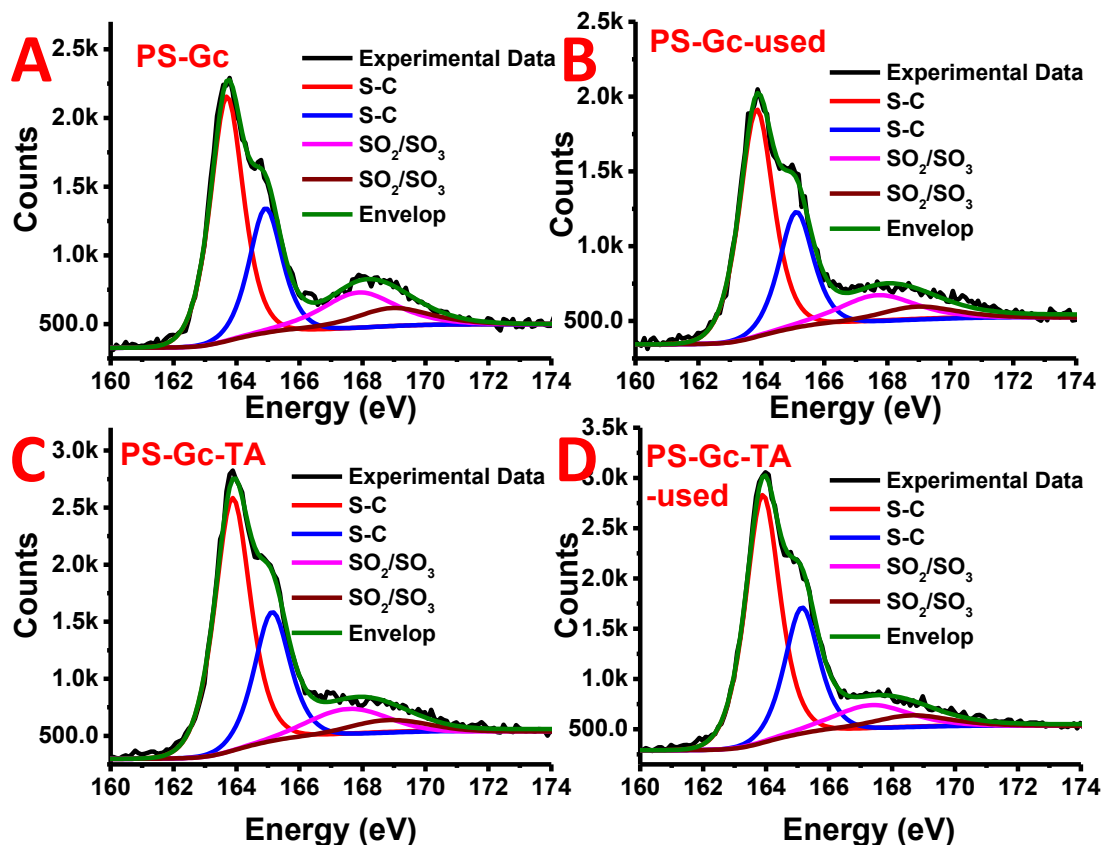


Figure 6.3. S 2p XPS peak deconvolution of PS-Gc catalyst (A), PS-Gc-used catalyst (B), PS-Gc-TA catalyst (C) and PS-Gc-TA-used (D).

Table 6.4. Calculated atomic % different type of P and S present in catalyst by XPS analysis.

Catalysts	P atomic %		S atomic %	
	P-C (133.5 eV)	P-O (~135.5 eV)	S-C (~163.7 eV)	S-O (~167.9 eV)
PS-Gc	1.02	1.72	4.09	1.32
PS-Gc-used	1.29	0.45	3.43	0.91
PS-Gc-TA	1.09	0.71	5.30	1.09
PS-Gc-TA-used	0.76	0.73	5.38	1.13

To study the bond configurations of P and S in PS-Gc, the P2p, and S2p XPS peaks were carefully deconvoluted as shown in **Figure 6.2A** and **6.3** and the results are summarized in **Table 6.4**. Bases on the P2p peak deconvolution, it was found that PS-Gc

contains more P-O (~ 135.11 eV, 1.72%) type of P doping, compare to P-C (~ 133.25 eV, 1.02%) type of P doping. This may be beneficial for the catalytic activity of the PS-Gc as it was already demonstrated that P-O functionality plays a crucial role in the catalytic oxidation of benzyl alcohols.¹² For S doping, the S2p peak deconvolution analysis shows that the PS-Gc contains mainly -C-S-C (~ 163.7 eV, 4.09%) type of S (such as exocyclic epoxide like S or heterocyclic thiophenic S) with a small amount of oxidized S (-SO_x , $x=2-3$, ~ 167.9 eV, 1.32%). The O 1s peak deconvolution of PS-Gc demonstrates that it contains carbonyl (~ 530.9 eV, 3.83%), epoxide/ether (~ 532.5 eV, 7.09%), hydroxyl (~ 533.2 eV, 5.61%) and carboxyl/adsorbed water (~ 535.1 eV, 1.48%) peaks. However, it is not clear if this oxygen functionalities are directly attached with heteroatoms (P and S) or carbon atom.

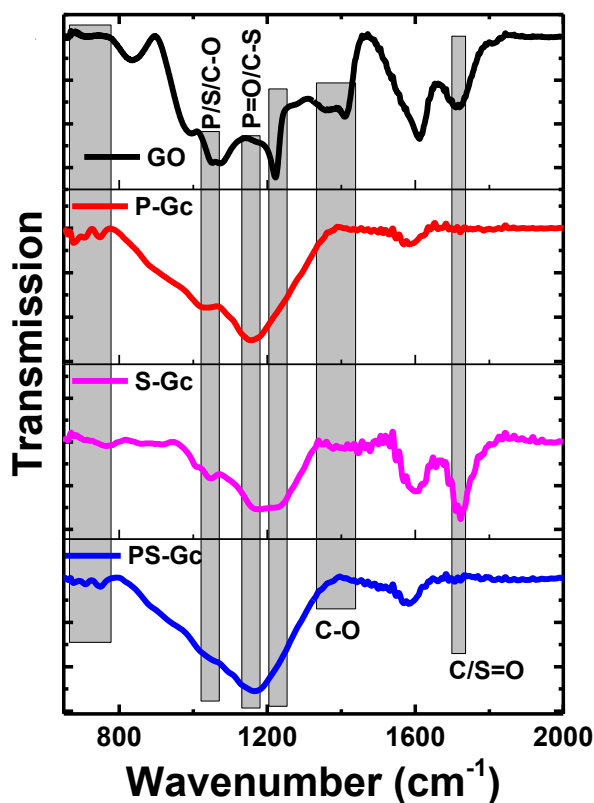


Figure 6.4. The FT-IR spectra of GO, P-Gc, S-Gc and PS-Gc.

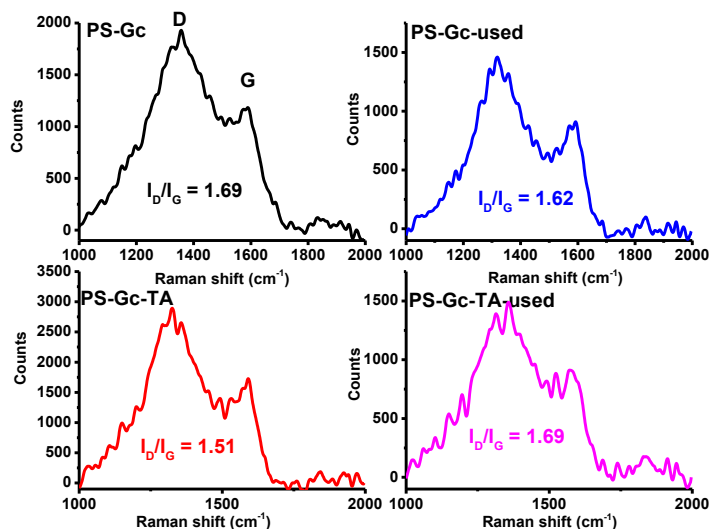


Figure 6.5. The Raman spectra of PS-Gc, PS-Gc-used, PS-Gc-TA and PS-Gc-TA-used.

To get a better understanding of these various oxygen functional groups present in the PS-Gc catalyst, the Fourier Transform Infrared spectroscopic (FT-IR) measurement of PS-Gc catalyst along with other catalysts such as P-Gc, S-Gc, and GO (also known as O doped graphene) was performed (**Figure 6.4**). All four samples show several common peaks at $1040 - 1050 \text{ cm}^{-1}$ (C-O alkoxy or P-O stretching vibration or -SO_3), 1589 cm^{-1} (C=C), 1236 cm^{-1} (C-O/P-O of C-OH/C-O-C/P-O-C/P-OH as a small shoulder in P-Gc and PS-Gc, while these peaks becomes stronger peak in GO and S-Gc). On the other hand, unlike P-Gc and PS-Gc, GO shows strong peak at 1354 cm^{-1} (-OH or C-O stretching vibrations), 1412 cm^{-1} (C-O of COOH), 1712 cm^{-1} (C=O/S=O as it also present in S-Gc), 1816 cm^{-1} (-CO-O-CO-) and 833 cm^{-1} (C-H/C-O). P-Gc, S-Gc, and PS-Gc show a stronger peak at 1155 cm^{-1} , which is due to the presence of P=O and/or C-S-C/C-S. These results further confirms that S is successfully doped in the PS-Gc and S-Gc materials however the majority of the oxygen containing functional groups are anchored on heteroatoms rather than on C atom, which is similar to previous results of P-doped carbon materials.¹² Furthermore, to confirm the presence of graphite or sp^2 carbon domains in the chemical

structure of PS-Gc, Raman measurement of PS-Gc was performed using 785 nm laser. As shown in **Figure 6.5**, the presence of G band ($\sim 1594\text{ cm}^{-1}$) and D band ($\sim 1312\text{ cm}^{-1}$) in the Raman spectra of PS-Gc confirms the presence of graphitic sp^2 carbon in its structure. The presence of strong D band also indicates a large amount of defects exist in the PS-Gc, which may be due to the presence of non-graphitic C in its structure and also due to the chemical doping (P and S) along with its unique porous morphology. The surface area of the porous PS-Gc material was measured by the methyl blue dye adsorption method, which is calculated to be $\sim 900\text{ m}^2/\text{g}$. A high surface area of the catalyst is important for effective mass transfer as well as for facile access to the catalytic centers by reactants. Combining all these unique features of PS-Gc material such as the very high surface area, unique morphology, chemical doping and the ease of large-scale production of PS-Gc, it can be an excellent metal-free catalyst for many reactions.

The selective oxidation of benzyl alcohol to benzaldehyde in solvent free condition with the PS-Gc catalyst was further optimized. First, the reactions at the various reaction temperatures (40 to $100\text{ }^\circ\text{C}$), times (4 to 48 hours) and catalyst loadings (10 to 100 wt %) were performed to optimize the reaction condition (**Table 6.5**). As we can see from the **Table 6.5** (entries 1 to 4) that as the reaction time is increased from 4 to 48 hours (at 50 wt% catalyst and $80\text{ }^\circ\text{C}$), the conversion of benzyl alcohol increases from 6 to 50%. But the selectivity to benzaldehyde drops below 90% if the reactions run for more than 24 hours, suggesting that the longer reaction time affects the reaction selectivity to an aldehyde. The conversion of benzyl alcohol increases from 2 to 68 % (**Table 6.5**, entry 3, 5 to 7) as the reaction temperature is raised from 40 to $100\text{ }^\circ\text{C}$ (50 wt% catalyst, 24 hours) with good aldehyde selectivity ($> 90\%$). Furthermore, the conversion of benzyl alcohol

also increases from 17 to >90 % (**Table 6.5**, entry 3, 8 to 10) as the catalyst loading increases from 10 to 100 wt% (100 °C, 24 hours) with good aldehyde selectivity (> 90%). In comparison to GO-based catalyst (24% conversion)¹⁶, the PS-Gc catalyst also shows better catalytic performance (34.5% conversion) at similar reaction conditions (**Table 6.5**, entry 9 and 12). Furthermore, the calculated turnover number (TON; expressed as a ratio of mol of oxidized substrate/mass of catalyst because of the non-Berthollide nature of the PS-Gc) of PS-Gc is also higher (1.75) compared to that of GO catalysts (1.1)¹⁶ and other heteroatom-doped/co-doped catalysts (**Table 6.1** - all entries, **Table 6.5**- entry 9 and 12). Based on the above results, it was concluded that the PS-Gc is a much better catalyst for benzylic alcohol oxidations than GO and other heteroatom-doped/co-doped catalyst at similar reaction conditions (**Table 6.1**).

Table 6.5. Optimization experiments for solvent free alcohol oxidation catalyzed by PS-Gc at 1atm O₂^a

Entry	Catalyst (mg)	Benzyl alcohol (μL)	Temperature (°C)	Time (hours)	% Conversion	% Yield	%Selectivity	TON (× 10 ⁻²)
1	50	100	80	4	5.8	4.1	96.8	0.12
2	50	100	80	8	10.1	7.8	94.9	0.21
3	50	100	80	24	25.5	25.7	91.7	0.46
4	50	100	80	48	50.4	42.8	87.3	1.03
5	50	100	40	24	2.2	2.2	98.5	0.04
6	50	100	60	24	10.7	9.7	96.5	0.22
7	50	100	100	24	67.6	53.6	91.0	1.38
8	10	100	100	24	17.2	16.6	93.5	1.75
9	20	100	100	24	34.5	30.7	92.0	1.75

10	75	100	100	24	85.5	54.0	87.2	1.16
11	100	100	100	24	93.3	70.8	96.5	0.95
12 ¹⁶	GO (20)	100	100	24	24.0	--	100	1.1

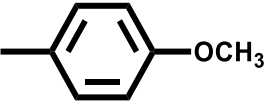
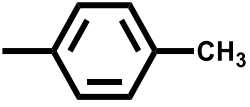

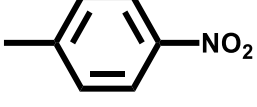
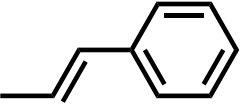
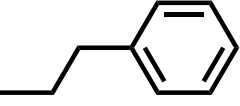
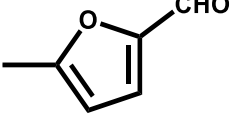
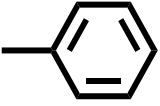
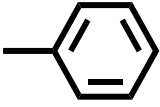
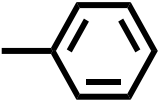
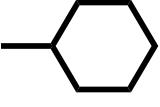

% conversion to the alcohol, % Yield to the products (benzaldehyde and benzoic acid) and % selectivity with respect to benzaldehyde calculated using ¹H NMR. ¹⁶ is referred to numbered reference in the text. The turnover number (TON) was calculated as a ratio of the (mol of the oxidized substrate) / (mass of catalyst).

Next, to enlarge the possible application of the PS-Gc catalyst, the scope of the PS-Gc materials for different types of alcohols was explored (primary and secondary benzylic alcohols, non-benzylic aromatic alcohols and other aliphatic alcohols such as alicyclic (cyclohexyl methanol, cyclohexanol) and linear (1-butanol) alcohols) in solvent free conditions and the results are summarized in **Table 6.6**. From the results it was found that the PS-Gc catalyst shows excellent catalytic performance for wide range of aromatic benzylic alcohol such as secondary benzylic alcohols (diphenylmethanol- 88 %conversion and 1-phenethyl alcohol- 67 %conversion), cinnamyl alcohols (79 %conversion), 5-(hydroxymethyl)-2-furaldehyde (51 %conversion) with very good selectivity (>90%) towards their respective aldehyde/ketone products. These results indicate that the PS-Gc catalyst can selectively oxidize aromatic primary benzylic alcohols and also the secondary benzylic alcohols without any steric hindrance problem, which is a unique advantage than N-doped carbon catalyst¹¹. We have also tested the catalytic ability of PS-Gc for aliphatic alcohols (**Table 6.6**, entry 10 to 12) such as cyclohexyl methanol, 1-butanol, and cyclohexanol. But, in contrast to aromatic benzylic alcohol, PS-Gc catalyst found to be inactive (< 5% conversion) for aliphatic alcohol oxidation reaction. This may be because of higher reactivity of aromatic substrate than that of the aliphatic substrate. In addition to that, the presence of conjugated system in aromatic benzylic alcohol may be necessary to

activate adjacent carbon bonding to the hydroxyl group as well as it also promotes the better substrate interaction of aromatic alcohols on the aromatic surface of PS-Gc catalyst. Furthermore, the presence of polar groups such as hydroxyl group on the benzylic activated carbon also facilitates substrate/catalyst interaction by hydrogen bonding to catalytic sites on the catalyst. This result was also supported by the inability of PS-Gc to oxidize the aromatic non-benzylic alcohol such as 3-phenyl-1-propanol (**Table 6.6**, entry 6). Moreover, the results also show that the electron donating and withdrawing properties of the functional group attached to the para position of benzyl alcohol greatly affects the oxidation efficiency, where electron donating groups favor the oxidation of benzylic alcohol to aldehyde selectively. For example, 4-methoxy substituted benzyl alcohol reached >90% conversion with very high selectivity (>99%) to respective benzaldehyde. In contrast, 4-nitro substituted benzyl alcohol shows poor conversion (~10%) with moderate selectivity (~51%) towards respective aldehydes. These substituent effect for benzyl alcohol oxidation by PS-Gc catalyst is very similar to P-Gc catalyst¹² and other metal based catalysts^{25, 26}, but it was not observed in N-doped graphene catalyst¹¹. Finally, it is also worth mentioning that the catalytic performance for the substituted benzyl alcohols is also much higher than that of P-Gc, which further demonstrates the superior catalytic ability of PS-Gc compared to that of P-Gc. For example, 4-methyl substituted benzyl alcohol shows ~90% conversion by PS-Gc versus ~53% conversion by P-Gc under similar condition (50 wt% catalyst, 100 °C, 24 hours).

Table 6.6. The scope of PS-Gc in the oxidation of different alcohols^a

Entry	R ₁	R ₂	% Conversion	% Selectivity
-------	----------------	----------------	--------------	---------------

1 ^b	-H		92.3	100
2	-H		89.9	100
3	-H		69.2	91.6
4	-H		9.9	51
5	-H		79.0	90.5
6	-H		< 1	100
7 ^c	-H		50.8	100
8	-CH ₃		67.2	100
9 ^d			88.4	97.2
10	-H		< 1	100
11	-H		< 1	41

12		4.1	100
----	---	-----	-----

Reaction conditions: ^a25mg PS-Gc catalyst, 0.5mmol alcohol, 1atm O₂, 100°C, 24 hours. ^b20mg catalyst was used. ^c50mg PS-Gc catalyst, 0.5mmol alcohol, 1atm O₂, 80°C, 24 hours. ^c and ^d reaction were performed at 80 °C temperature to avoid decomposition of substrate alcohol.

In general, a catalyst facilitates a reaction by lowering the activation energy (E_a), the energy needed for a reaction to proceed form an intermediate and/or the desired product. For P-doped carbon (P-Gc) catalyst¹², the calculated activation energy is 49.6 kJ.mol⁻¹, which is similar to Ru metal-based catalysts (51.4 kJ.mol⁻¹ for Ru/Al₂O₃ catalyst²⁷ and 47.8 for Ru/TEMPO catalyst²⁸) but lower than that of reported for N-doped carbon catalysts¹¹ (56.1 kJ.mol⁻¹). To know whether the presence of two heteroatom dopants (P and S) in PS-Gc are responsible for further lowering the activation energy for alcohol oxidation reaction and thus enhancing the catalytic efficiency of the catalyst, the kinetic studies of PS-Gc was performed. For that, a kinetic study of the selective oxidation of benzyl alcohol to benzaldehyde by PS-Gc catalyst was performed in aqueous solution at the different reaction temperatures. The sample was collected from the reaction mixture at 15 minutes time intervals for each different reaction temperature experiment and analyzed by High-Performance Liquid Chromatography (HPLC). A plot (**Figure 6.6**) of the concentration of benzaldehyde as a function of the reaction time at different temperatures (40 to 100 °C) was drawn and from these linear plots and the apparent reaction rates (k_{obs}) for different reaction temperature was calculated. After that, the apparent activation energy (E_a) for PS-Gc is calculated from the slope of the linear plot ($\ln k_{obs}$ versus $1/T$, **Figure 6.6**) and using the Arrhenius equation of $\ln k = \ln A - E_a/RT$. The E_a value (32.02 kJ.mol⁻¹) of PS-Gc for benzyl alcohol oxidation is found to be much lower than P-Gc, N-doped carbon

catalysts, and Ru metal based catalysts, suggesting that P and S heteroatom co-doping lower the activation energy and so showing very good catalytic performance than P-doped carbon catalyst.

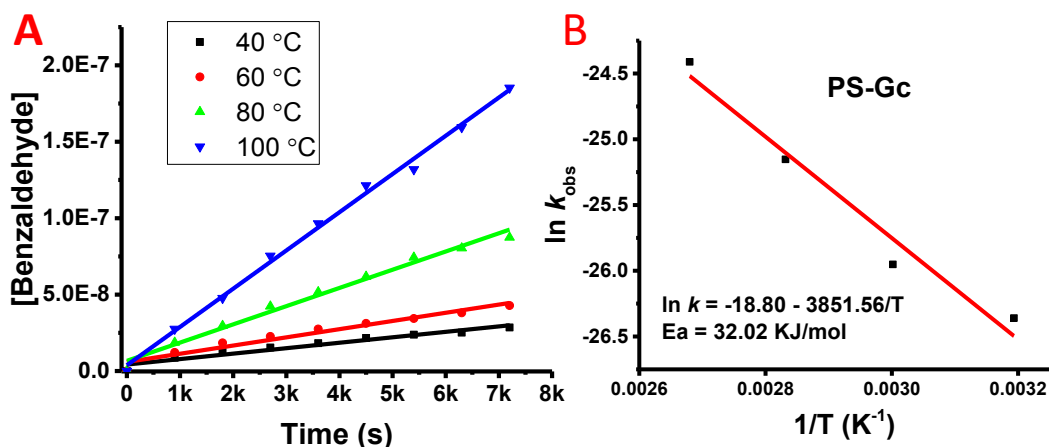


Figure 6.6. (A) The plot of different reaction temperatures versus benzaldehyde concentration in molarity. Reaction conditions: 10 mg benzyl alcohol, 5 mg PS-Gc catalyst, 10 ml water, 1 atm O₂. (B) Arrhenius plot for the Benzyl alcohol oxidation. The rate constant (*k*) values at different temperature were regarded as the pseudo-zero-order rate constants (*k*_{obs}) because the plot of the molarity of benzaldehyde versus reaction time is linear.

To understand the mechanism of catalytic oxidation of benzylic alcohols with the PS-Gc catalyst, several control experiments were performed to get insight into the above-mentioned catalytic reactions. In a first control experiment, we have performed the benzyl alcohol oxidation reaction in the presence of 1 atm O₂, air, and inert environment to see if the activation of oxygen is the primary step as N-doped graphene^{11, 13}. As shown in **Table 6.7**, we found that the conversion of benzyl alcohol decreased from ~71% to 31% if the reaction was run in the presence of air instead of pure O₂. It further decreases to 14% if the same reaction was run in the presence of N₂. But if the catalyst is recovered from the reaction, which runs under 1 atm N₂, and reuse in the presence of 1 atm O₂, the alcohol conversion increases to ~54%. These results clearly indicate that the activation of oxygen

is important in the first step of the catalysis. The moderate conversion (14%) achieved in N₂ environment is possibly due to the active sites from P doping (especially P-O type functionalities) in PS-Gc. In our previous report¹², we have shown that P-Gc can initiate the oxidation of benzylic alcohol in the absence of oxygen because oxygen containing functionalities on P-Gc (P-OH and P=O) directly involved in the oxidation of benzyl alcohol in the first step of catalysis. To further support this conclusion, we have tested the catalytic performance of S-Gc in the presence of 1 atm N₂ and O₂ environment, respectively. As shown in **Table 6.7** (entry 5 and 6), S-Gc can catalyze the benzyl alcohol oxidation in the presence of O₂ (18 %conversion) but not in the presence of N₂ (< 4 %conversion). These results suggest that the S-Gc is very different from P-Gc, the first step of catalysis for the active sites from S doping is oxygen activation. Altogether these results suggest that PS-Gc might have two different kinds of active centers, one comes from S doping, and the other one results from P doping. These two resources of catalytic centers additively/synergistically facilitate the oxidation of benzylic alcohol.

Table 6.7. The catalytic performance of the PS-Gc and S-Gc in benzyl alcohol oxidation in presence of different environments^a

Entry	Catalyst (~50 wt %)	Oxidant	%Conv	% Yield	%Selectivity
1	PS-Gc	1atm O ₂	71.11	52.87	90.73
2	PS-Gc	1atm air	31.65	30.62	97.4
3	PS-Gc	1atm N ₂	14.04	11.82	99.08
4 ^b	PS-Gc	N ₂ to O ₂	53.80	46.26	93.6
5	S-Gc	1atm O ₂	18.28	14.51	86.75
6	S-Gc	1atm N ₂	3.62	---	94.3

Reaction conditions: ^a25mg catalyst, 0.5 mmol of benzyl alcohol, 1atm oxidant, 100°C, 24 hours. ^bPS-Gc catalyst was recovered from entry 3. % conversion to the alcohol, % yield to the product and % selectivity with respect to benzaldehyde calculated using ¹H NMR.

To understand whether free radical intermediates are involved in the PS-Gc catalyzed the reaction, we have performed the benzyl alcohol oxidation (100 °C, 24 Hr, 1atm O₂) in the presence of butylated hydroxytoluene (BHT, 50 wt %), a known free radical quencher in acetonitrile solvent (to dissolve BHT). As shown in **Table 6.8**, the conversion of benzyl alcohol is barely influenced by the addition of BHT in the reaction system. This result suggests that there is no radical intermediate involved in the catalytic pathway. A similar result was observed previously in only P-doped graphitic carbon material (P-Gc)¹² but not in GO¹⁶ and N-doped carbon catalyst^{11, 13}. These results also suggest that P and S doping creates unique catalytic centers in the carbon material which are completely different from those in GO or N-doped carbon catalysts.

Table 6.8. The benzyl alcohol oxidation in presence of BHT (radical quencher)^a

Entry	Catalyst (~50 wt %)	% conversion	% yield	% selectivity
1	PS-Gc + BHT	28.01	26.54	97.24
2	PS-Gc	34.23	32.59	96.59

Reaction conditions: ^a25mg catalyst, 0.5 mmol of benzyl alcohol, 0.3mLacetonitrile, 1atm O₂, 100°C, 24 hours. 0.125 mmol (or 50 wt% of benzyl alcohol) of butylated hydroxytoluene (BHT) is added in entry 1 for controlled reaction. % conversion to the alcohol, % yield to the product and % selectivity with respect to benzaldehyde calculated using ¹H NMR.

No doubt that it is economically beneficial if the catalyst can be synthesized in a cost effective manner, in very short time, without using toxic chemicals, with minimal waste and using a simple protocol to avoid any cost associated with the operation. It is also helpful if the catalyst can be easily recovered at the end of the reaction and recycle/reuse

for many subsequent reactions to save cost associated with chemical production. In this report, we have shown that the PS-Gc catalyst not only can be synthesized quickly but also, its fabrication uses cheap and widely available biomass molecules and hence avoids toxic chemicals. To find out whether the PS-Gc catalyst (100 wt %) can recycle for multiple times or not, we have recovered the PS-Gc catalyst at the end of reaction via simple filtration and recycled it in solvent free optimized reaction condition at 100 °C for 24 hours under 1atm O₂. As shown in Table 6 (entry 1 to 3), the % conversion of alcohol is decreased from 93.3% to 74.7% upon the first recycle and further decreased to 57.5 % upon second recycle. The same result was obtained even if we tried to recycle the catalyst at lower catalyst loading to 50 wt % as well as lower reaction temperatures to 80 and 60 °C (Table 6, entry 4 to 12). The inability to reuse the PS-Gc catalyst, even at a lower temperature (60 °C), indicates that either the active site is not stable in the catalyst or it may undergo some chemical transformation during the catalytic reaction.

Table 6.9. Recycling the catalyst at different reaction conditions.^a

Entry	Catalyst	Catalyst loading	Temp °C	% conversion	% yield	% selectivity
1	1 st use PS-Gc	100 wt%	100	93.32	70.79	96.54
2	2 nd use PS-Gc	100 wt%	100	74.68	58.98	95.28
3	3 rd use PS-Gc	100 wt%	100	57.47	39.93	99.93
4	1 st use PS-Gc	50 wt%	100	67.6	53.55	91.03
5	2 nd use PS-Gc	50 wt%	100	50.75	42.07	94.03
6	3 rd use PS-Gc	50 wt%	100	33.42	29.78	95.40
7	1 st use PS-Gc	50 wt%	80	25.48	25.68	91.7
8	2 nd use PS-Gc	50 wt%	80	16.28	14.65	96.70
9	3 rd use PS-Gc	50 wt%	80	13.52	12.09	96.97
10	1 st use PS-Gc	50 wt%	60	10.70	9.66	96.48

11	2 nd use PS-Gc	50 wt%	60	6.61	6.12	97.79
12	3 rd use PS-Gc	50 wt%	60	6.36	5.96	97.92
13	1 st use PS-Gc-TA	50 wt%	100	62.98	47.27	90.80
14	2 nd use PS-Gc-TA	50 wt%	100	42.98	37.27	91.28
15	3 rd use PS-Gc-TA	50 wt%	100	28.54	21.76	92.62

Reaction conditions: ^a 0.5 mmol of benzyl alcohol and 1atm O₂, 24 hours. % conversion to the alcohol, % yield to the product and % selectivity with respect to benzaldehyde calculated using ¹H NMR.

To know the exact reason behind these results, we have performed EDS and XPS measurement of used PS-Gc catalyst (labeled as PS-Gc-used) to determine the % P and % S in the PS-Gc after the reaction. As shown in **Table 6.2**, it was found that both % P and % S are decreased in the PS-Gc-used catalyst from 2.76% and 4.85% to 1.74% and 3.86%, respectively, as per XPS analysis. So first, we tried to solve the stability problem of P and S dopant in PS-Gc by thermal annealing of the as-synthesized PS-Gc catalyst in a thermal furnace at 450 °C for 60 minutes under constant nitrogen flow and the new product is named as PS-Gc-TA. The PS-Gc-TA have a similar amount of S (~ 6 atomic %), but P amount is slightly decreased to ~ 1.8 atomic % than the original PS-Gc catalyst. This PS-Gc-TA catalyst gives ~63 % conversion for benzyl alcohol oxidation when the reaction is performed at 50 wt% catalyst and 100 °C for 24 hours (**Table 6.9**, entry 13), which is similar or slight decreased from PS-Gc catalyst (67.8% conversion). Moreover, after recycling the PS-Gc-TA for a second and third time, the conversion is still decreased to ~43 and 28.5%, respectively, even though the atomic% of P and S did not decrease in the PS-Gc-TA-used compared to the fresh PS-Gc-TA catalyst as confirmed from EDS and XPS analysis (**Table 6.2**). From the P2p and S2p deconvolution results (**Figure 6.3B**, **6.4A** and **Table 6.4**), we can see that P in both used and fresh PS-Gc-TA catalyst. Moreover, In

our previous report,¹² it has been reported that P-doped carbon (P-Gc) can be recycled at least 8 times without losing its catalytic performance in benzyl alcohol oxidation. However, It has been reported that XPS was not able to clearly differentiate the doped S with different oxidation (-2 to +8) due to the resolution problem²⁹. We have also compared the FT-IR spectra of fresh and used, PS-Gc and PS-Gc-TA catalysts, as shown in **Figure 6.7**. From the results, we can see that the peak at $\sim 1720\text{ cm}^{-1}$, which was not detectable in both fresh PS-Gc and PS-Gc-TA catalyst, becomes slightly stronger in the used PS-Gc and PS-Gc-TA catalyst suggesting that carbonyl oxygen (S=O / C=O) were possibly generated in the used catalyst. As the majority of the oxygen functionalities are connected with S, we suspect that the reduced S type is converted to S=O type of functionalities during the catalytic reaction. Nevertheless, due to overlapping of different peaks at a similar frequency in FT-IR measurements and poor resolution of XPS to separate S species with different oxidation states, we were not able to get any detailed information about changes in S functionalities in fresh and used PS-Gc catalyst.

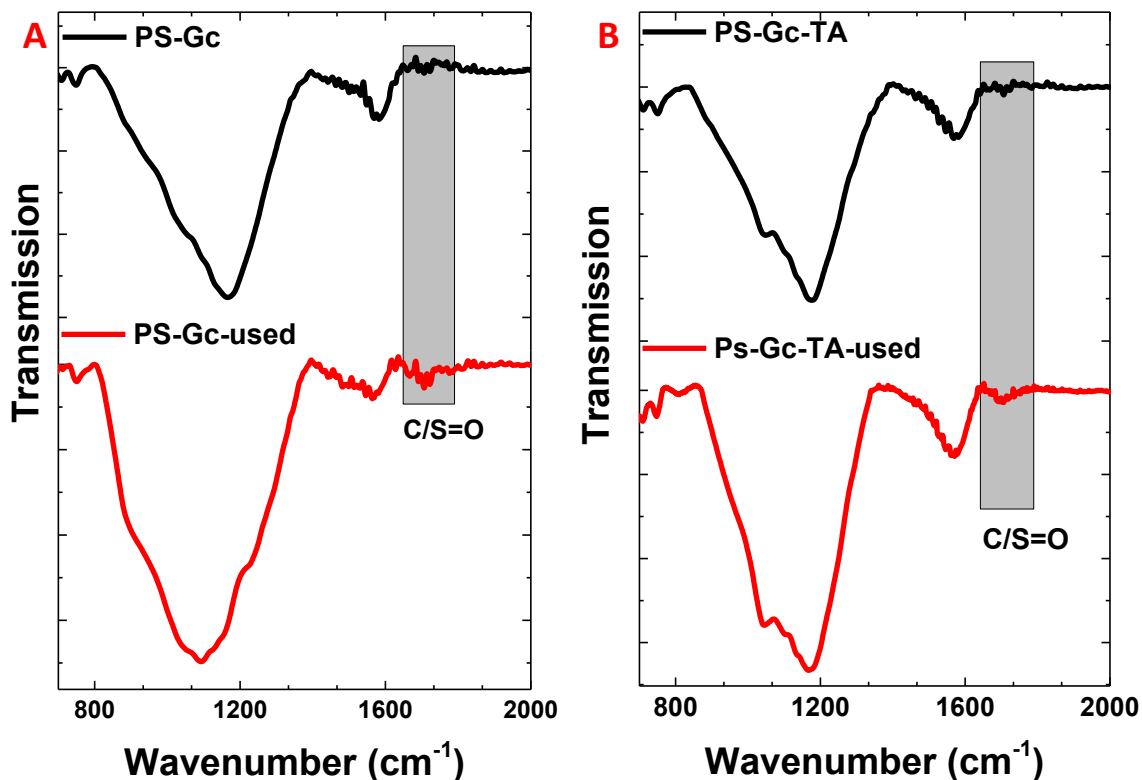


Figure 6.7. The FT-IR spectra of fresh and used PS-Gc catalysts (A) and PS-GC-TA catalysts (B).

To study the electronic structure or nature of S doping in PS-Gc catalyst, we have performed X-ray absorption near edge spectroscopy (XANES) to study sulfur K-edge spectra, which is widely used analytical technique to study sulfur bond configuration in different S containing materials.²⁹⁻³¹ As we can see that S K-edge spectra (**Figure 6.8**) of the fresh PS-Gc catalyst shows two separate and broad peaks, the one at higher energy is for oxidized S species (~ 2483 eV) and the other one is at lower energy for reduced S species (~ 2473 eV). Based on the literature assigned energy values²⁹, the peak in oxidized S region at ~ 2483 eV can be deconvoluted into two peaks at ~ 2481.5 and 2483.2 eV, assigned to sulfonate and sulfate type of S species, respectively. While the reduced S region in fresh PS-Gc catalysts can be deconvoluted into four different peaks at 2470.4 , 2472.7 ,

2474.3 and 2476.2 eV, which can be assigned to inorganic sulfide, exocyclic sulfur, heterocyclic sulfur and sulfoxide, respectively. The results were summarized in **Table 6.10**

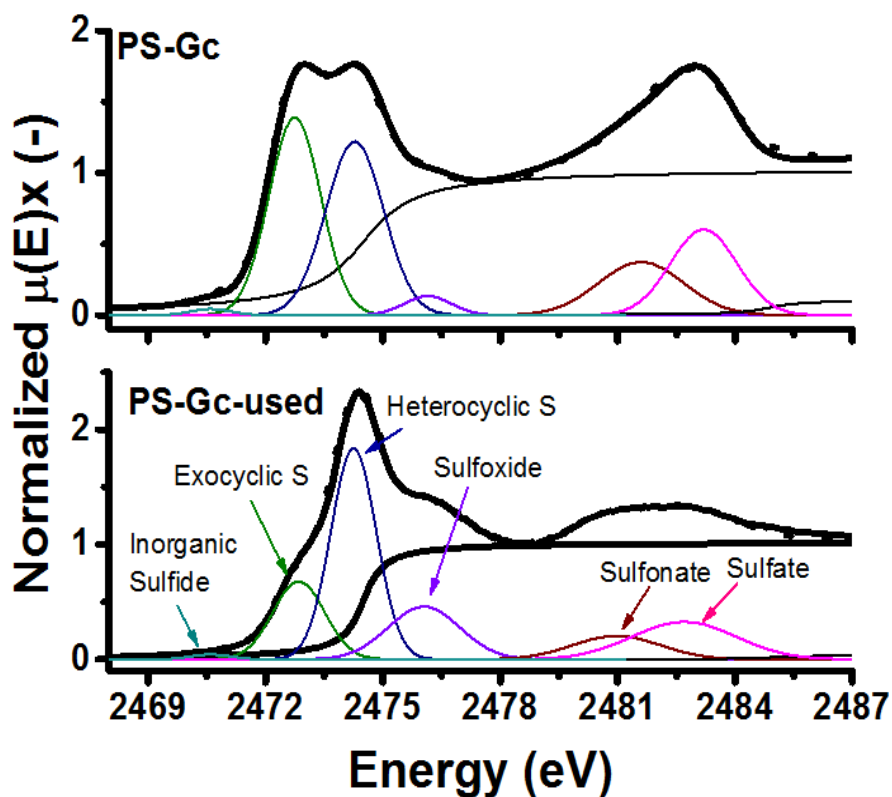


Figure 6.8. The deconvolution of normalized S K-edge XANES spectra of fresh and used PS-Gc catalysts.

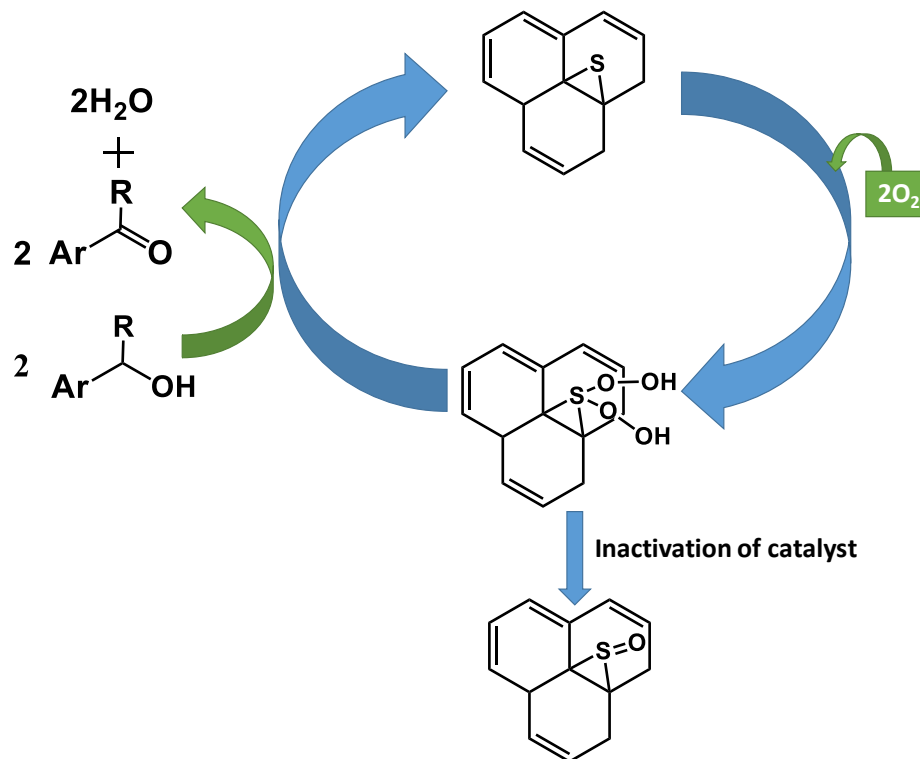
Table 6.10. Calculated atomic % of the different type of S functionalities from S K-edge XANES peak deconvolution analysis.

Catalysts	Atomic %S						Total
	Inorganic Sulfide	Exocyclic S	Heterocyclic S	Sulfoxide	Sulfonate	Sulfate	
PS-Gc	0.04	1.54	1.51	0.13	0.68	0.86	4.85
PS-Gc-used	0.03	0.68	1.62	0.64	0.2	0.66	3.86

From a comparison of the fresh PS-Gc catalyst with the PS-Gc-used catalyst, we found that the exocyclic sulfur (C-S-C) peak drastically decreased and at the same time sulfoxide (C-S(O)-C) peak becomes stronger in used PS-Gc-used catalyst. These results in facts are in line with the FT-IR characterization results where a new peak for S=O type functional groups appeared at $\sim 1720\text{cm}^{-1}$ in the PS-Gc-used catalyst. All these results clearly demonstrate that the exocyclic S species (which is more like epoxides in GO, who are playing a major role in catalysis¹⁷) plays the crucial role in activating the oxygen and catalyzing the benzyl alcohol oxidation reaction. During the catalytic reactions, exocyclic S is oxidized to sulfoxide type of S and thus catalytic centers were diminished.

The proposed mechanism of P-doped active sites was already reported in our previous report¹² where it has been demonstrated that the alcohol molecule interacts with P-O (P-OH and P=O) functionalities to produce aldehyde/ketone without needing any oxidant (such as oxygen). But in the following step, in the presence of oxygen, these functional groups on the catalytic site (P) are regenerated and will continue the reaction cycle. Here in this report, we found that S and P co-doping shows catalytic synergistic effects. Based on the above control experiments and detailed characterization by FT-IR, XANES, and XPS, we have proposed that exocyclic S species play a major role in the observed synergistic catalytic effect, and the catalytic mechanism was proposed for alcohol oxidation reaction in **Scheme 6.1**.

Scheme 6.1. The proposed mechanism for benzylic alcohol oxidation by exocyclic S active center.



From control experiments, it was concluded that oxygen activation is the first step in the catalytic oxidation of benzyl alcohol for S-doped active sites. Even though a mechanism of oxygen activation has been studied exclusively for N atom dopant, but it is in the early stage for sulfur doped graphene/carbon. Recently, a theoretical study on the oxygen reduction reaction (ORR) mechanism for S-doped graphene reported that exocyclic sulfur doping cannot introduce any extra unpaired electrons in the carbon matrix, and so it will not affect the spin and charge densities of the carbon atoms in graphene.³² It was also reported that the mechanism of oxygen reduction (two electron pathway or four-electron pathway) in S-doped carbon depends on the catalytically active centers. If S species in the graphene matrix are the catalytic centers, ORR would have a two-step, two-electron pathway. While if the catalytic centers are on the C atoms, which have high charge/spin

density due to S doping, the ORR will have a four-electron pathway.³² In our PS-Gc catalyst, due to the presence of an exclusive amount of exocyclic S, no additional charge/spin density was introduced in the catalyst. So, we suspect that oxygen is being reduced on the S atom (active site) to reactive oxygen species (ROS) via two electron pathway. The oxygen reduction via two-electron pathway could result in different types of ROS, such as hydroxyl radical ($\cdot\text{OH}$), peroxide like species OOH, hydrogen peroxide (H_2O_2), superoxide radical ($\cdot\text{O}_2^-$). Based on our control experiments in the presence of a radical quencher (BHT), it was clearly demonstrated that there are no radicals generated during the catalytic oxidation of alcohols. These results suggest that activation of oxygen resulted in non-radical ROS such as peroxides like species OOH and hydrogen peroxide (H_2O_2). It has also been reported that producing the excess amount of H_2O_2 via oxygen reduction is the key parameter to affect the selectivity of aldehyde/ketone products in metal catalyzed reactions. But our experimental results suggested that the benzyl alcohol is selectively oxidized to aldehyde/ketone without producing the carboxylic acid, and moreover, we could not detect any peroxide species by HPLC, suggesting that either the generated peroxide amount is too small that there are no detectable detrimental effects on the product selectivity was not observed or a transient peroxo like species (OOH) were generated, which directly oxidized the benzyl alcohol before it converted to peroxide. N-doped graphene has already been reported for the generation of peroxo like species in previous reports, where graphitic N is playing a catalytic role.^{33, 34} The same graphitic N is also responsible for reducing the oxygen via two electron pathway^{35, 36}, which indirectly supports our conclusion that S-doped active site may be responsible for reducing oxygen via two electron pathway to peroxo like species. Now in the next step of oxidation, the

produced OOH type of ROS oxidized the alcohol to the respective aldehydes or ketones. During this oxidation, the exocyclic S active sites in PS-GC may be converted to C–S(O)–C type of functionalities which cannot further act as catalytic centers to activate molecule oxygen. As a consequence, the catalytic activity of the PS-Gc catalyst was decreased largely upon recycling. Currently, we are working on methods to regenerate the active sites in the used PS-Gc catalyst, so we can able to reuse them multiple times.

6.3. Conclusions

In this chapter, it has been shown that the S and P codoped porous carbon (PS-Gc) material shows better catalytic performance than single doped (S-Gc and P-Gc) and other P codoped carbon catalysts (PB-Gc and PN-Gc) for benzylic alcohol oxidations. Moreover, the PS-Gc catalyst can selectively oxidize a variety of primary and secondary benzylic alcohols to the respective aldehydes/ketone without steric hindrance. The calculated activation energy for benzyl alcohol oxidation is ~ 32 kJ/mol for the PS-Gc, which is lower than P-doped, N-doped carbon catalyst as well as Ru metal based catalysts. From the various control experiments and the detailed characterization of the fresh and used PS-Gc catalysts we have concluded the following points. 1) PS-Gc catalyst probably contains two distinct types of catalyst centers from P and S-doping. 2) PS-Gc catalyst requires oxygen activation as the first step of oxidation, which is different than P-doped Carbon. 3) S is doped with multiple S species while only the exocyclic sulfur (C-S-C) species play the important role in activating the oxygen molecule as well as selectively oxidizing the benzylic alcohols. 4) The S containing active sites (exocyclic S) were not stable during the catalytic reaction and converted to sulfoxide type of S species which cannot be reduced back into the reaction conditions. Thus, the reusability of the PS-Gc catalyst is limited.

6.4. Experimental Section

6.4.1. Synthesis of catalysts

Synthesis of P and other heteroatoms (N, B, S and Si) co-doped catalysts: The P and another heteroatom co-doped porous carbon catalyst were synthesized according to previously published protocol.²³ In brief, 1.0 ml of phytic acid (Sigma-Aldrich 50 w/w% in water) is mixed with pre-weighed amount of other heteroatom source (such as amorphous sulfur or ammonium hydroxide or boric acid as S, N and B source, respectively) in 35 mL Pyrex glass vessel (CEM, #909036) and closed with Teflon-lined cap (CEM, #909235). The amount of heteroatom source is calculated such that the moles ratio of P and other heteroatom dopants stays 1:1. The uniformed dispersion or suspension of the phytic acid and heteroatom source is obtained by the aid of bath sonicating the mixture for 15 minutes. After that, the resultant mixture is heated in the domestic microwave (Sanyo-EM-S9515W, 1100 W, 2.45 GHz) chamber for a different time to obtain co-doped carbon material. The microwave heating time is depending on the microwave absorption capacity of heteroatom precursor and the resultant mixture. For example, the microwave heating time is 42s, 90s and 150s for the synthesis of PS-Gc, PN-Gc and PB-Gc, respectively. The microwave heating time is also varied based on the type of domestic microwave, size or physical dimensions of microwave cavity and microwave output power. After heating the mixture in microwave, the resultant product is left in fume hood to cool down and then filtered, washed and dried as described in the previous report.²³

To prevent the loss of % atomic S and P heteroatom dopant in PS-Gc catalyst during the catalytic oxidation of benzyl alcohol oxidation, the as-synthesized PS-Gc material was further heated at 450 °C for 60 minutes under constant N₂ flow in a thermal furnace. After

treatment, the new material is again filtered with water and ethanol solvent to remove any impurities and labeled as a PS-Gc-TA.

Synthesis of S-doped carbon material (S-Gc): The S-doped porous carbon catalyst was also synthesized according to previously published protocol.²³ In brief, ~250 mg of myo-Inositol (act as C source), ~0.6 mL of concentrated sulfuric acid (act as strong dehydrating agent and microwave absorbing agent) and heteroatom dopant source, which is ~67 mg amorphous sulfur, was mixed by bath sonication for 15 minutes and then heated in microwave for 60 seconds. The resultant product is left in fume hood to cool down and then filtered, washed and dried as described in the previous report.²³

6.4.2. Catalytic oxidation of primary and secondary alcohol Reaction.

Materials: Benzyl Alcohol (Millipore, $\geq 99\%$), DL-sec-phenyl ethyl alcohol (Acros Organics, $\geq 97\%$), Cyclohexane methanol (Alfa Aesar, 99%), n-butanol (anhydrous, Sigma-Aldrich, 99.8%), 4-methoxybenzyl alcohol (TCI, $>98\%$), 4-methylbenzyl alcohol (Sigma-Aldrich, 98%), 4-nitrobenzyl alcohol (Alfa Aesar, 99%), 4-fluorobenzyl alcohol (Sigma-Aldrich, $\geq 97\%$), cinnamyl alcohol (Sigma-Aldrich, $\geq 98\%$), diphenylmethanol (Sigma-Aldrich, 99%), 5-(hydroxymethyl)-2-furaldehyde (Sigma-Aldrich, 99%), Cyclohexanol (Sigma-Aldrich, 99%), Toluene (anhydrous, Sigma-Aldrich, 99.8%).

Solvent free alcohol oxidation: A catalytic reaction for benzylic alcohol oxidation was carried out by mixing the pre-determined amount of catalyst and benzylic alcohol in a 10 mL microwave reaction vial (VWR 89079-402) and then sealed with PTFE-faced aluminum cap. After that, the air inside of the reaction vessel is removed using traditional vacuum system and replaced with the desired atmosphere before heating the reaction vial in an oil bath for specified time and at a specified temperature. For control experiment with

a radical inhibitor, BHT (Butylated hydroxytoluene), specified amount of BHT and acetonitrile (for maintaining uniform dispersion of BHT) was added to the above-described mixture at the beginning of the reaction. The detailed experimental condition, the amount of the reactant and catalysts were specified in the footnote of each table. After completion of each reaction, ~0.7 mL of CDCl_3 and 100 μL of anhydrous toluene (internal standard) was mixed with the reaction mixture and filtered *via* 0.02 μm syringe filter and analyzed by ^1H NMR spectroscopy (Bruker Avalanche 500 MHz).

Kinetic study of an alcohol oxidation in water: The kinetic studies for aerobic oxidation reactions at different reaction temperatures were carried out in 20 ml microwave reaction vial sealed with PTFE-faced aluminum cap. Here, 5mg of PS-Gc and 10 μL of benzyl alcohol is added to 10 mL of oxygen saturated deionized water solvent in reaction vial and the reaction is carried out at 1atm O_2 environment. during the experiments, ~0.3 mL of the aliquot was withdrawn at a regular interval of 15 minutes, filtered *via* 0.02 μm syringe filter and analyzed by HPLC (Varian Pro-Star and Phenomenex C18 column, mobile phase 50:50 ratio of Methanol: 0.44% Acetic acid) to monitor the amount of benzaldehyde produced.

6.4.3. Material characterization

The morphology of PS-Gc materials was studied using the scanning electron microscopy (SEM, Hitachi S-4800). The sample for SEM was prepared by sprinkling the dried PS-Gc powder on the carbon tape. The heteroatom doping and atomic % of all elements in the porous carbon were analyzed by Energy Dispersive X-ray Spectroscopy (EDS) characterization. The sample for EDS imaging was prepared by simple drop casting of the slurry of a sample on to copper tape and allowed it for air dry. The X-ray photoelectron

spectroscopy (XPS) characterization was performed after drop casting the catalyst onto a Si substrate. The thickness of the catalyst film on the Si substrates was roughly 30–50 nm. XPS spectra were acquired using a Thermo Scientific K-Alpha system with a monochromatic Al K α X-ray source ($h\nu = 1486.7$ eV). For data analysis, Smart Background subtraction was performed, and the spectra were fit with Gaussian/Lorentzian peaks using a minimum deviation curve fitting method (part of the Advantage software package). The surface composition of each species was determined by the integrated peak areas and the Scofield sensitivity factor provided by the Advantage software. The Fourier transform infrared spectroscopy (FT-IR) spectra of PS-Gc samples (thin films deposited on ZnSe windows) were acquired with a Thermo-Nicolet 6700 spectrometer (Thermo-Electron Corp., Madison, WI), using a sample shuttle and a mercury-cadmium-telluride (MCT) detector. Four blocks of 128 scans each was co-added with 4 cm^{-1} spectral resolution and two levels of zero-filling so that data was encoded every 1 cm^{-1} . Raman spectra of the PS-Gc material (deposited on Anodisc membrane) was collected using Raman Microscope (Confocal) – Wi-Tec, Alpha 3000R with an excitation laser at 785 nm. The Surface area of PS-Gc material was measured using Methylene blue(MB) adsorption method as described in the previous report.³⁷ The S K-edge (2472.02 eV) XANES spectra were recorded at APS at 9-BM beamline in fluorescence mode at room temperature using a Lytle detector. The Si (111) monochromator was calibrated relative to the 3% sodium thiosulfate standard. Three scans were collected in order to confirm absence of X-ray damage, processed and averaged in Athena program.³⁸ All the spectra were deconvoluted using Gaussians and 2 arctangent functions using Athena.³⁸

6.5. References

1. Zhang, J.; Liu, X.; Blume, R.; Zhang, A. H.; Schlogl, R.; Su, D. S. Surface-modified carbon nanotubes catalyze oxidative dehydrogenation of n-butane. *Science* 2008, 322, 73-77.
2. Su, D. S.; Zhang, J.; Frank, B.; Thomas, A.; Wang, X. C.; Paraknowitsch, J.; Schlogl, R. Metal-Free Heterogeneous Catalysis for Sustainable Chemistry. *ChemSuschem* 2010, 3, 169-180.
3. Su, D. S.; Perathoner, S.; Centi, G. Nanocarbons for the Development of Advanced Catalysts. *Chem. Rev.* 2013, 113, 5782-5816.
4. Su, C.; Loh, K. P. Carbocatalysts: Graphene Oxide and Its Derivatives. *Acc. Chem. Res.* 2013, 46, 2275-2285.
5. Navalon, S.; Dhakshinamoorthy, A.; Alvaro, M.; Garcia, H. Carbocatalysis by Graphene-Based Materials. *Chem. Rev.* 2014, 114, 6179-6212.
6. Dhakshinamoorthy, A.; Latorre-Sanchez, M.; Asiri, A. M.; Primo, A.; Garcia, H. Sulphur-doped graphene as metal-free carbocatalysts for the solventless aerobic oxidation of styrenes. *Catal. Commun.* 2015, 65, 10-13.
7. Dhakshinamoorthy, A.; Primo, A.; Concepcion, P.; Alvaro, M.; Garcia, H. Doped Graphene as a Metal-Free Carbocatalyst for the Selective Aerobic Oxidation of Benzylic Hydrocarbons, Cyclooctane and Styrene. *Chemistry-a European Journal* 2013, 19, 7547-7554.
8. Hayashi, M. Oxidation using activated carbon and molecular oxygen system. *Chemical Record* 2008, 8, 252-267.
9. Lv, G.; Wang, H.; Yang, Y.; Deng, T.; Chen, C.; Zhu, Y.; Hou, X. Graphene Oxide: A Convenient Metal-Free Carbocatalyst for Facilitating Aerobic Oxidation of 5-Hydroxymethylfurfural into 2, 5-Diformylfuran. *Acs Catalysis* 2015, 5, 5636-5646.
10. Dreyer, D. R.; Jia, H. P.; Bielawski, C. W. Graphene Oxide: A Convenient Carbocatalyst for Facilitating Oxidation and Hydration Reactions. *Angewandte Chemie-International Edition* 2010, 49, 6813-6816.
11. Long, J. L.; Xie, X. Q.; Xu, J.; Gu, Q.; Chen, L. M.; Wang, X. X. Nitrogen-Doped Graphene Nanosheets as Metal-Free Catalysts for Aerobic Selective Oxidation of Benzylic Alcohols. *Acs Catalysis* 2012, 2, 622-631.
12. Patel, M. A.; Luo, F.; Khoshi, M. R.; Rabie, E.; Zhang, Q.; Flach, C. R.; Mendelsohn, R.; Garfunkel, E.; Szostak, M.; He, H. P-Doped Porous Carbon as Metal Free Catalysts for Selective Aerobic Oxidation with an Unexpected Mechanism. *ACS Nano* 2016, 10, 2305-15.
13. Watanabe, H.; Asano, S.; Fujita, S.; Yoshida, H.; Arai, M. Nitrogen-Doped, Metal-Free Activated Carbon Catalysts for Aerobic Oxidation of Alcohols. *Acs Catalysis* 2015, 5, 2886-2894.
14. Cheon, J. Y.; Kim, J. H.; Goddeti, K. C.; Park, J. Y.; Joo, S. H. Intrinsic Relationship between Enhanced Oxygen Reduction Reaction Activity and Nanoscale Work Function of Doped Carbons. *J. Am. Chem. Soc.* 2014, 136, 8875-8878.
15. Meng, Y.; Voiry, D.; Goswami, A.; Zou, X.; Huang, X.; Chhowalla, M.; Liu, Z.; Asefa, T. N-, O-, and S-tridoped nanoporous carbons as selective catalysts for oxygen reduction and alcohol oxidation reactions. *J. Am. Chem. Soc.* 2014, 136, 13554-7.

16. Dreyer, D. R.; Jia, H. P.; Bielawski, C. W. Graphene oxide: a convenient carbocatalyst for facilitating oxidation and hydration reactions. *Angew. Chem. Int. Ed. Engl.* 2010, 49, 6813-6.
17. Boukhvalov, D. W.; Dreyer, D. R.; Bielawski, C. W.; Son, Y. W. A Computational Investigation of the Catalytic Properties of Graphene Oxide: Exploring Mechanisms by using DFT Methods. *Chemcatchem* 2012, 4, 1844-1849.
18. Patel, M.; Luo, F.; Khoshi, M. R.; Rabie, E.; Zhang, Q.; Flach, C. R.; Mendelsohn, R.; Garfunkel, E.; Szostak, M.; He, H. P-Doped Porous Carbon as Metal Free Catalysts for Selective Aerobic Oxidation with an Unexpected Mechanism. *ACS Nano* 2016, 10, 2305-2315.
19. Choi, C. H.; Park, S. H.; Woo, S. I. Phosphorus-nitrogen dual doped carbon as an effective catalyst for oxygen reduction reaction in acidic media: effects of the amount of P-doping on the physical and electrochemical properties of carbon. *J. Mater. Chem.* 2012, 22, 12107-12115.
20. Li, R.; Wei, Z. D.; Gou, X. L. Nitrogen and Phosphorus Dual-Doped Graphene/Carbon Nanosheets as Bifunctional Electrocatalysts for Oxygen Reduction and Evolution. *Acs Catal* 2015, 5, 4133-4142.
21. Shi, Q. Q.; Peng, F.; Liao, S. X.; Wang, H. J.; Yu, H.; Liu, Z. W.; Zhang, B. S.; Su, D. S. Sulfur and nitrogen co-doped carbon nanotubes for enhancing electrochemical oxygen reduction activity in acidic and alkaline media. *Journal of Materials Chemistry A* 2013, 1, 14853-14857.
22. Wang, X.; Sun, G.; Routh, P.; Kim, D. H.; Huang, W.; Chen, P. Heteroatom-doped graphene materials: syntheses, properties and applications. *Chem. Soc. Rev.* 2014, 43, 7067-98.
23. Patel, M.; Savaram, K.; Keating, K.; He, H. Rapid Transformation of Biomass Compounds to Metal Free Catalysts via Short Microwave Irradiation. *Journal of Natural Products Research Updates* 2015, 1, 18-28.
24. Dhakshinamoorthy, A.; Primo, A.; Concepcion, P.; Alvaro, M.; Garcia, H. Doped Graphene as a Metal-Free Carbocatalyst for the Selective Aerobic Oxidation of Benzylic Hydrocarbons, Cyclooctane and Styrene. *Chemistry – A European Journal* 2013, 19, 7547-7554.
25. Fung, W.-H.; Yu, W.-Y.; Che, C.-M. Chemoselective Oxidation of Alcohols to Aldehydes and Ketones by tert-Butyl Hydroperoxide Catalyzed by a Ruthenium Complex of N,N',N''-Trimethyl-1,4,7-triazacyclononane. *The Journal of Organic Chemistry* 1998, 63, 2873-2877.
26. Poreddy, R.; Engelbrekt, C.; Riisager, A. Copper oxide as efficient catalyst for oxidative dehydrogenation of alcohols with air. *Catalysis Science & Technology* 2015, 5, 2467-2477.
27. Yamaguchi, K.; Mizuno, N. Scope, Kinetics, and Mechanistic Aspects of Aerobic Oxidations Catalyzed by Ruthenium Supported on Alumina. *Chemistry – A European Journal* 2003, 9, 4353-4361.
28. Dijksman, A.; Marino-González, A.; Mairata i Payeras, A.; Arends, I. W. C. E.; Sheldon, R. A. Efficient and Selective Aerobic Oxidation of Alcohols into Aldehydes and Ketones Using Ruthenium/TEMPO as the Catalytic System. *J. Am. Chem. Soc.* 2001, 123, 6826-6833.

29. El-Sawy, A. M.; Mosa, I. M.; Su, D.; Guild, C. J.; Khalid, S.; Joesten, R.; Rusling, J. F.; Suib, S. L. Controlling the Active Sites of Sulfur-Doped Carbon Nanotube–Graphene Nanolobes for Highly Efficient Oxygen Evolution and Reduction Catalysis. *Advanced Energy Materials* 2016, 6, n/a-n/a.
30. Hsi, H.-C.; Rood, M. J.; Rostam-Abadi, M.; Chen, S.; Chang, R. Effects of Sulfur Impregnation Temperature on the Properties and Mercury Adsorption Capacities of Activated Carbon Fibers (ACFs). *Environmental Science & Technology* 2001, 35, 2785-2791.
31. Huffman, G. P.; Mitra, S.; Huggins, F. E.; Shah, N.; Vaidya, S.; Lu, F. Quantitative analysis of all major forms of sulfur in coal by x-ray absorption fine structure spectroscopy. *Energy & Fuels* 1991, 5, 574-581.
32. Zhang, L.; Niu, J.; Li, M.; Xia, Z. Catalytic Mechanisms of Sulfur-Doped Graphene as Efficient Oxygen Reduction Reaction Catalysts for Fuel Cells. *The Journal of Physical Chemistry C* 2014, 118, 3545-3553.
33. Li, W.; Gao, Y.; Chen, W.; Tang, P.; Li, W.; Shi, Z.; Su, D.; Wang, J.; Ma, D. Catalytic Epoxidation Reaction over N-Containing sp² Carbon Catalysts. *Acs Catal* 2014, 4, 1261-1266.
34. Gao, Y.; Hu, G.; Zhong, J.; Shi, Z.; Zhu, Y.; Su, D. S.; Wang, J.; Bao, X.; Ma, D. Nitrogen-Doped sp²-Hybridized Carbon as a Superior Catalyst for Selective Oxidation. *Angew. Chem. Int. Ed.* 2013, 52, 2109-2113.
35. Lai, L.; Potts, J. R.; Zhan, D.; Wang, L.; Poh, C. K.; Tang, C.; Gong, H.; Shen, Z.; Lin, J.; Ruoff, R. S. Exploration of the active center structure of nitrogen-doped graphene-based catalysts for oxygen reduction reaction. *Energy & Environmental Science* 2012, 5, 7936-7942.
36. Yuan, H.; He, Z. Graphene-modified electrodes for enhancing the performance of microbial fuel cells. *Nanoscale* 2015, 7, 7022-7029.
37. Patel, M.; Feng, W.; Savaram, K.; Khoshi, M. R.; Huang, R.; Sun, J.; Rabie, E.; Flach, C.; Mendelsohn, R.; Garfunkel, E.; He, H. Microwave Enabled One-Pot, One-Step Fabrication and Nitrogen Doping of Holey Graphene Oxide for Catalytic Applications. *Small* 2015, 11, 3358-3368.
38. Ravel, B.; Newville, M. ATHENA, ARTEMIS, HEPHAESTUS: data analysis for X-ray absorption spectroscopy using IFEFFIT. *Journal of synchrotron radiation* 2005, 12, 537-541.